Dissertation

Next scale Chemical Looping Combustion

-

Overall Plant Design

ausgeführt zum Zwecke der Erlangung des akademischen Grades eines
Doktors der technischen Wissenschaften unter der Leitung von

Univ. Prof. Dipl.-Ing. Dr. Hermann Hofbauer
Univ. Prof. Dipl.-Ing. Dr. Tobias Pröll

E166
Institut für Verfahrenstechnik, Umwelttechnik und Technische Biowissenschaften der
Technischen Universität Wien

eingereicht an der Technischen Universität Wien

Fakultät für Maschinenwesen und Betriebswissenschaften

Von

Dipl.-Ing. Klemens Marx
Matr. Nr.: 0426116
Herklotzgasse 13/8
1150-Wien

Wien, am 29.Juli.2013

.....
Klemens Marx

Abstract

Chemical looping combustion is a second generation carbon capture technology. The process features the concept of unmixed combustion where fuel and combustion air are never directly mixed. This is established by using a metal oxide as a carrier and conducting a continuous reduction-oxidation cycle to transfer the oxygen needed for combustion in the solid phase between two separate reactors, i.e. the air reactor and the fuel reactor. A properly functioning chemical looping combustion system provides fuel reactor exhaust ideally containing only CO_2 and H_2O, where after water vapor condensation a CO_2-rich stream is obtained, ready for sequestration. Compared to first generation carbon capture processes, energy intensive gas-gas separation is avoided and thus costs related to CO_2 mitigation are considerably reduced. The technology has been demonstrated for gaseous fuels in the past in numerous laboratory test facilities at scales of up to 140 kW. Very promising results have been obtained using nickel-based oxygen carriers. To gain sufficient confidence in the application of this technology at larger scales, a demonstration at an industrial scale is necessary.

This thesis aims to perform scale-up of the technology from a small laboratory pilot setup to the industrial demonstration scale at 10 MW thermal input using natural gas and nickel-based oxygen carriers. The demonstration plant is integrated into an existing combined heat and power cycle where a natural gas combined cycle with supplementary firing is located. The chemical looping combustion unit is designed to substitute the energy input of supplementary firing, which in turn can easily compensate for fluctuations during demonstration plant operation. Sharing the existing infrastructure will allow for a significant reduction in capital costs. A heat integration setup was proposed and tested against part load operation. The setup allows for operation from 55-110%, referring to the nominal load (10 MW) typical for steam generators. The chemical looping combustion boiler allows for efficiency values of 87.7-96.1% in terms of fuel-to-steam conversion with reference to lower heating values. Such values are typical in small-scale steam generation although, in fact, chemical looping combustion allows for carbon capture. However, improvements can be made using advanced oxygen carriers with improved fuel conversion performance.

The dual circulating fluidized bed concept for chemical looping systems was applied to the design of the demonstration unit. In this thesis, the dimensions of the reactor system are presented, including all parts such as the risers, loop seals and cyclones. Based on this, a cold flow model was designed, built and put into operation, allowing for testing of fluidized bed hydrodynamics and operation considering the similarity between the hot demonstration unit and cold model. Improvements were made with respect to cyclone separation performance and loop seal operation. The cold flow model studies underline the hydrodynamic feasibility of the design and verify a high degree of flexibility with respect to system control, part load operation and performance of the oxygen carrier.

The performance of the chemical looping combustion for steam generation at 100 MW in the heavy oil sands industry was compared to state-of-the-art technology without carbon capture and two first generation CCS technologies; namely, post-combustion capture and oxy-fuel combustion. Chemical looping combustion technology is capable of providing steam with very little energy penalty compared to state-of-the-art boilers. In practice, only about 1.1-2.5%-pts. is lost owing to carbon capture. Even for high-performance solvents in post-combustion capture,

this loss is considerably higher. For this reason, chemical looping combustion is considered the ideal solution for the supply of industrial process steam whenever carbon capture is necessary.

Kurzfassung

Bei dem "chemical looping combustion" (CLC) Verfahren handelt es sich um eine "carbon capture and storage (CCS)" Technologie der zweiten Generation. Der Prozess erlaubt die Verbrennung von Brennstoff ohne direkten Kontakt zwischen Verbrennungsluft und Brennstoff. Dies wird erreicht indem ein Metalloxid in einem kontinuierlichen Reduktions-Oxidations-Zyklus zum Transport von Sauerstoff zwischen zwei physisch getrennten Reaktoren, dem Luftreaktor und dem Brennstoffreaktor, genutzt wird. Das dabei im Brennstoffreaktor entstehende Gas besteht daher, idealerweise, nur aus CO_2 und H_2O. Nach Kondensieren des Wassersdampfs steht ein mit CO_2 angereicherter Strom zur Verfügung, welcher sich zur Speicherung eignet. Im Vergleich zu CCS Verfahren der ersten Generation wird hier eine Gas-Gas Trennung vermieden, was zu einer deutlichen Kostensenkung im Zusammenhang mit CO_2 Emissionsvermeidung führt. In der Vergangenheit wurde die Technologie für gasförmige Brennstoffe in etlichen Laboranlagen in einem Maßstab von bis zu 140 kW erfolgreich getestet. Im speziellen wurden mit auf Nickel basierenden Sauerstoffträgern herausragende Ergebnisse erzielt. Um die Technologie großtechnisch Verfügbar zu machen ist eine Demonstration in industriellem Maßstab notwendig.

Diese Arbeit befasst sich mit der Maßstabsvergrößerung der Technologie vom Labormaßstab zu industrieller Größe mit 10 MW thermischer Leistung unter Verwendung von Erdgas und eines nickelbasierten Sauerstoffträgers. Die Demonstrationsanlage wird dabei an einen bestehenden Standort eines Gas-Kombikraftwerks mit Zusatzfeuerung und Kraft-Wärmekopplung integriert. Die CLC Anlage wird dabei so eingegliedert, dass sie die durch die Zusatzfeuerung eingebrachte Leistung substituiert. Die Zusatzfeuerung ermöglicht es, schnell auf Laständerungen im CLC Demonstrationsbetrieb zu reagieren um so die Leistungsabgabe des Standortes konstant zu halten. Durch die gemeinsame Nutzung der vorhandenen Infrastruktur erreicht man eine wesentliche Reduktion der anfallenden Investitionskosten. Die Anordnung der Wärmetauscher wurde vorgeschlagen und hinsichtlich Teillastverhalten untersucht. Es stellt sich heraus, dass die Demonstrationsanlage die Möglichkeit bietet einen weiten Teillastbereich von 55-110% der Nominallast (10 MW) abzudecken welcher typisch für Dampferzeuger ist. Dabei werden Effizienzen von 87.7-96.1% im Sinne der Umwandlung von Brennstoff zu Dampf (bezogen auf den unteren Heizwert) erreicht. Solche Werte sind typisch für Dampferzeuger kleiner Größe, wobei man beachten muss, dass bei CLC Kohlenstoff bereits konzentriert vorliegt. Es besteht aber weiterhin ein Entwicklungspotential wenn Sauerstoffträger mit verbessertem Potenzial betreffend Brennstoffumsatz zum Einsatz kommen.

Das Zweibett-zirkulierende-Wirbelschicht-Konzept für CLC wurde auf das Design der Demonstrationsanlage angewendet. Im Rahmen der Arbeit wurden die Anlagenteile, darunter die Riser, Siphon und die Zyklone, dimensioniert. Darauf basierend wurde ein Kaltmodell entwickelt, gebaut und in Betrieb genommen welches die Untersuchung der Fluiddynamik und des Betriebs unter Berücksichtigung von Ähnlichkeitsbeziehungen zwischen heißer Demonstrationsanlage und Kaltmodell ermöglicht. Im speziellen wurden Verbesserungen im Bereich der Abscheideleistung der Zyklone und dem Betrieb des Siphons erreicht. Die Kaltmodellstudien unterstreichen die Anwendbarkeit des entwickelten Designs und untermauern die Flexibilität des Systems hinsichtlich Betrieb, Teillastverhalten und sich ändernder Effizienz des Sauerstoffträgers.

Die Effizienz von CLC in einer Größe von 100 MW zur Bereitstellung von Dampf in der Schwerölgewinnung aus Ölsanden wurde ermittelt und dem aktuell eingesetzten Prozess ohne

CCS und zwei CCS Verfahren der ersten Generation (Luftverbrennung mit anschließender CO_2 Wäsche und Oxy-fuel Verbrennung) gegenübergestellt. Es stellt sich heraus, dass mit dem CLC Verfahren, im Vergleich zum heutigen Stand der Technik, Dampf mit einem geringfügigen Wirkungsgradverlust bereitgestellt werden kann. In der Praxis ergibt sich ein Verlust von 1.1-2.5% Punkten aufgrund der Abtrennung von CO_2. Selbst neuartige Hochleistungslösungsmittel die für die CO_2 Wäsche vorgeschlagen werden bewirken einen wesentlich höheren Wirkungsgradverlust. Aus diesem Grund kann "chemical looping combustion" wenn CO_2 abgetrennt werden soll als die ideale Lösung zur Bereitstellung von industriellem Prozessdampf angesehen werden.

List of Publications

Reviewed papers

- Marx, K., Bolhàr-Nordenkampf, J., Pröll, T., Hofbauer, H., **2011**. Chemical looping combustion for power generation—Concept study for a 10MW_{th} demonstration plant. *International Journal of Greenhouse Gas Control 5(5)*, pp. 1199-1205, doi: 10.1016/j.ijggc.2011.05.012.
- Marx, K., Pröll, T., Hofbauer, H., Hohenwarter, U., Horn, V., Sit, S.P., **2011**. Chemical looping combustion for industrial steam generation from natural gas with inherent CO_2 capture. in: Reis, A. (Ed.), Proceedings of the 9th European Conference on Industrial Furnances and Boilers (INFUB-9), Estoril, Portugal.
- Marx, K., Pröll, T., Hofbauer, H., **2011**. Design requirements for pressurized chemical looping reforming. in: Pugsley, T. (Ed.), Proceedings of the 10th International Conference on Circulating Fluidized Bed Technology (CFB10), Sunriver, Oregon, USA.
- Guío-Pérez, D.C., Marx, K., Pröll, T., Hofbauer, H., **2011**. Fluid dynamic effects of ring-type internals in a dual circulating fluidized bed system. in: Pugsley, T. (Ed.), Proceedings of the 10th International Conference on Circulating Fluidized Bed Technology (CFB10), Sunriver, Oregon, USA.
- Marx, K., Pröll, T., Hofbauer, H., **2012**. Next scale chemical looping combustion: Fluidized bed system design for demonstration unit. Proceedings of the 21st International Conference on Fluidized Bed Combustion (FBC), Naples, Italy.
- Sit, S.P., Reed, A., Hohenwarter, U., Horn, V., Marx, K., Pröll, T., **2012**. 10 MW CLC Field Pilot. Proceedings of the 2nd International Conference on Chemical Looping, Darmstadt, Germany.

Abstract reviewed papers

- Marx, K., Bertsch, O., Pröll, T., Hofbauer, H., **2013**. Next scale chemical looping combustion: Process integration and part load investigations for a 10MW demonstration unit. *Energy Procedia submitted for publication*.
- Sit, S.P., Reed, A., Hohenwarter, U., Horn, V., Pröll, T., Marx, K., **2013**. Cenovus 10 MW CLC Field Pilot. *Energy Procedia submitted for publication*.

Abstract reviewed conferences

- Pröll, T., Bolhàr-Nordenkampf, J., Kolbitsch, P., Marx, K., Hofbauer, H., **2009**. Pure hydrogen and pure carbon dioxide from gaseous hydrocarbons by chemical looping reforming. Proceedings of the 2009 AIChE Spring National Meeting and 5th Global Congress on Process Safety, Tampa, Florida, USA.
- Marx, K., Bertsch, O., Pröll, T., Hofbauer, H., **2012**. Next scale chemical looping combustion: Process integration and part load investigations for a 10MW demonstration unit. Proceedings of the International Conference on Greenhouse Gas Technology 11 (GHGT11), Kyoto, Japan.
- Sit, S.P., Reed, A., Hohenwarter, U., Horn, V., Pröll, T., Marx, K., **2012**. Cenovus 10 MW CLC Field Pilot. Proceedings of the International Conference on Greenhouse Gas Technology 11 (GHGT11), Kyoto, Japan.

Related technical reports

- Marx, K., Pröll, T., Hofbauer, H., **2010**. CO_2 free Heavy Oil Extraction using Chemical Looping Combustion. Final report of the project CLCSG-Encana. *Institute of Chemical Engineering*.
- Marx, K., Pröll, T., Hofbauer, H., **2011**. Next Scale Chemical Looping Combustion. Project Report "CLCSG PreFEED". *Institute of Chemical Engineering, Vienna University of Technology*.
- Bertsch, O., Marx, K., Sprachmann, G., Williams, G., **2011**. INNOCUOS DL 5.1: Next scale CLC plant, report on deployment potential and technical feasibility. Deliverable of the EU financed project INNOCUOUS (FP7 Contract No. 241401), coordinated by Chalmers University of Technology.
- Marx, K., Pröll, T., Hofbauer, H., Bertsch, O., **2012**. INNOCUOUS DL 5.2: Integrated process model of a next scale CLC power plant. Deliverable of the EU financed project INNOCUOUS (FP7 Contract No. 241401), coordinated by Chalmers University of Technology.
- Mayer, K., Schöny, G., Marx, K., Schlapansky, F., Pröll, T., **2012**. INNOCUOS DL 4.1: Evaluated results from mixed oxide testing at 120 kW. Deliverable of the EU financed project INNOCUOUS (FP7 Contract No. 241401), coordinated by Chalmers University of Technology. *Insitute of Chemical Engineering, Vienna University of Technology*.
- Marx, K., Pröll, T., Schinninger, M., Hofbauer, H., **2012b**. Chemical Looping Combustion DL T2: Cold flow model built. Deliverable of the CCP Phase 3 financed project Chemical Looping Combustion an amendment of the EU financed project INNOCUOUS (FP7 Contract No. 241401).
- Marx, K., Pröll, T., Hofbauer, H., **2013**. Chemical Looping Combustion DL T4: Feasibility study for large scale CLC steam generation. Deliverable of the CCP Phase 3 financed project Chemical Looping Combustion an amendment of the EU financed project INNOCUOUS (FP7 Contract No. 241401).

Books

- Marx, K., **2010**. Hydrogen and power generation using chemical looping: Potential of hydrogen and power generation from natural gas with quantitative carbon capture using chemical looping technology. *VDM Verlag Dr. Müller*, ISBN: 978-3639159301.

Patents

- Pröll, T., Kolbitsch, P., Bolhàr-Nordenkampf, J., Hofbauer, H., Marx, K., **2010**. Verfahren zur Herstellung von Kohlendioxid und Wasserstoff auf Kohlenwasserstoffen unter Verwendung von "Chemical Looping Reforming" (Method for producing carbon dioxide and hydrogen from hadrocarbons using chemical looping reforming). Austria, written in German language.

Directed Master and Bachelor thesis's

- Schlapansky, F., **2012**. Performance of mixed oxides in chemical looping – The case of Ilmenite/Ni-19γ-Al_2O_3. Institute of Chemical Engineering. *Vienna University of Technology*, Vienna, Austria.

- Radulovic, M., **2013**. Potenzial von Chemical Looping Combustion zur Bereitstellung von Prozessdampf. Institute of Chemical Engineering. *Vienna University of Technology*, Vienna, Austria, written in German.
- Schinninger, M., **2013**. Commissioning and operation of a scaled cold flow model of a 10MW chemical looping combustion demonstration unit. Institute of Chemical Engineering. *Vienna University of Technology*, Vienna, Austria.

Conference posters

- Marx, K., Pröll, T., Bertsch, O., Hofbauer, H., **2011**. Next scale chemical looping combustion- Design evaluation. Poster at the 3rd IEAGHG High Temperature Solids Looping Cycles Network Meeting, Vienna, Austria.

Invited speeches

- Marx, K., Pröll, T., Hofbauer, H., **2010**. Chemical looping combustion for carbon capture – Research and Development at Vienna University of Technology. Invited speech at: 2010 International Symposium on Sustainable Clean Coal Technology, Taipei, Taiwan.

ACKNOWLEDGEMENT

On the long way in preparation of a scientific thesis like this there are several people supporting in one way or another to whom I would like to take the chance to express my gratitude.

First of all, I like to thank Univ.Prof. Dipl.-Ing. Dr.techn. Hermann Hofbauer for giving me the opportunity to work at the Institute of Chemical Engineering. For providing the environment where people from several disciplines can freely interact in an amicable way giving a high potential of individual development of everyone involved.

My deep gratitude to Univ.Prof. Dipl.-Ing. Dr.techn. Tobias Pröll for the excellent supervision of my work. For his capability of guidance through difficult topics in discussions where he always was able to support me with valuable advice giving me the chance to broaden my knowledge and experience.

It is important for me to mention the outstanding work of Dipl.-Ing. Dr.techn. Johannes Bolhàr-Nordenkampf and Mag. Dipl.-Ing. Dr.techn. Philipp Kolbitsch in the field of chemical looping combustion and chemical looping reforming. Their endurance in supporting me during my master thesis and their enthusiasm in introducing me into the topic. As such, they provided the cornerstone which allowed me to prepare this thesis.

My colleagues in the chemical looping team for the pleasurable team-work and open-minded discussions. Particularly, I would like to highlight the discussions with Dipl.-Ing. Karl Mayer. His enthusiasm in supporting me in finding technical solutions and endurance in making me familiar with the "secrets" of chemistry.

My parents Ludmilla and Eduard for supporting me whenever possible. For giving me the chance to grow up in an protected but open-minded environment where I was able to shape my personality.

My brother, sisters their families and friends who always make me feel that whatever happens there is a place where I can return.

A special thank to my wife Kathrin which is the most important person in my life. Your remarkable mindset and on how you life your live filled my life with wonder; and still continues to do. Day-by-day I feel like I fall in love with you again, and again ... .

TABLE OF CONTENT

1 Introduction

1.1 Motivation for this work

Social and economic development and improved human welfare and health are based on the utilization of natural resources. Among these resources primary, energy resources, i.e. fossil fuels, are the most important. This is because most of nowadays products are derived either directly or indirectly, via by-products, from these resources. Moreover, global trading would not be possible without the use of fossil fuels for transportation. With the continuous increase in the global population, the demand for primary energy will grow too.

The utilization of fossil fuels is accompanied by the emission of carbon dioxide (CO_2), which gas caused the concentration of this gas in the atmosphere to increase significantly in recent decades. The physical properties of the atmosphere have thus changed with the increased presence of CO_2, promoting the absorption of long wavelength radiation emitted by the planet's surface. This effect, generally known as the greenhouse gas effect, made life on Earth possible but today is discussed as being problematic and the cause of climate change. Increased occurrence of climate events such as coastal flooding and winter extremes on continental Europe have been discussed as a result of this causing harm to humans either directly or indirectly, e.g. harvesting losses. Mitigation of anthropogenic emissions of greenhouse gases, primarily CO_2, is therefore crucial to inhibit the destabilization of the global climate.

Sustainable use of natural resources, including a switch from fossil fuels to renewable sources, implies a significant re-structuring of contemporary industries. Therefore, the use of renewables is inevitable on a long-term basis, but also requires a mid-term strategy to effectively reduce anthropogenic greenhouse gas emissions. Carbon capture and storage (CCS), where CO_2 is isolated from the atmosphere by injecting the CO_2 into adequate storage facilities, is capable of closing the gap between current energy use and a sustainable future. Since power generation is the most important contributor to CO_2 emissions, such sources are the most feasible for the application of CCS technologies. In general, three CCS processes have been discussed: post-combustion capture, pre-combustion capture and oxy-fuel. All these processes have in common that energy intense gas-gas separation is needed, which not only causes an energy penalty but also increases the formation of CO_2 to provide the necessary energy.

1.2 Chemical looping combustion

Chemical looping combustion is an advanced CCS technology that may potentially reduce CCS related costs. The process features the concept of unmixed combustion where fuel and combustion air are never directly mixed. Thus, two separate gas streams are obtained where one is oxygen-depleted air and the other contains oxidized fuel (ideally CO_2 and H_2O). Hence, in this process, two physically separated reactors are needed: the air reactor (AR) and the fuel reactor (FR). Gas-gas separation is inherently accomplished by the use of a metal oxide that selectively transports oxygen and heat between the reactors. The metal oxide, also called an oxygen carrier, is oxidized in the air reactor by combustion air. Then, the oxidized oxygen carrier is transported to the fuel reactor where it is subsequently used for fuel oxidation. CCS can be easily applied to this process by condensation of the water vapor from the fuel reactor exhaust to obtain a concentrated CO_2 stream ready for sequestration.

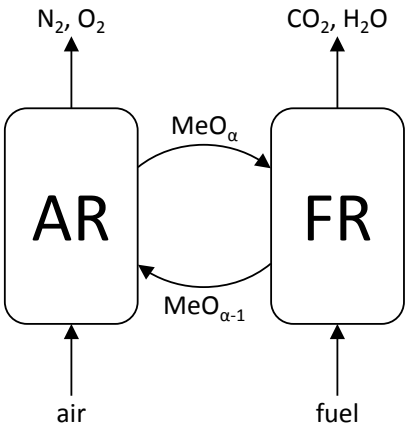

Fig. 1 Basic chemical looping combustion process setup. AR - air reactor, FR - fuel reactor, Me - metal.

Although the combustion process takes place in two reactors, the overall energy release remains the same compared to direct combustion. The main efficiency loss in chemical looping combustion thus is due to the slightly increased auxiliary energy required to run the process.

1.3 Objective of this work

Chemical looping combustion can be used for CO_2-free utilization of fossil fuels when sequestration is included. In practice, any kind of hydrocarbon fuel can be used in the process, but most experience has been gained with gaseous fuels. Natural gas combined cycles (NGCC) is state-of-the-art in power generation, where fuel to electricity conversion factors of up to 60% can be reached. Thus, chemical looping combustion for power generation has to compete with the NGCC cycle requiring pressurization of the process. Pressurized chemical looping combustion seems promising on a theoretical basis, but realization seems difficult. However, industrial steam is often generated in atmospheric natural gas boilers where chemical looping combustion has the potential to perform equally well as the conventional combustion processes, but CO_2 capture can be applied. Atmospheric chemical looping combustion application can involve small-scale combined heat and power generation as well as the production of industrial steam, e.g. in the bulk and paper industry or heavy oil extraction from in-situ oil sands production where low quality steam is injected to reduce oil viscosity.

The potential of chemical looping combustion for gaseous fuels has been successfully demonstrated in the past using numerous laboratory batch and continuous test facilities. The largest chemical looping laboratory pilot for gaseous fuels is located at the Vienna University of Technology with a nominal fuel power input of 140 kW which was put in operation in 2008. The unit features the use of a dual circulating fluidized bed reactor system specifically designed for chemical looping purposes. Very promising results have been obtained with natural gas using a nickel-based oxygen carrier. For this reason, the next logical step in the evolution of the process is the demonstration of the technology at an industrial scale to gain sufficient confidence in chemical looping for further up-scaling.

In this thesis, research is performed in preparation for up-scaling the chemical looping technology from the 140 kW laboratory pilot to the 10 MW demonstration scale. Up-scaling by a similar factor from 100 kW to 8 MW was successfully accomplished in 2002 at the combined heat and power biomass gasification plant located in Güssing, Austria, also using dual fluidized bed

technology. A similar up-scaling factor for chemical looping combustion seems to be feasible. The development path includes the design and construction phase with the accompanying fluid dynamic proof of concept in cold flow model investigations followed by experiments at the laboratory pilot unit. A similar approach was applied in the development of the design of the 8 MW combined heat and power biomass gasification plant in Güssing, Austria and for the 140 kW chemical looping laboratory pilot unit. This work includes the up-scaling of chemical looping starting with the experimental proof of the process at the 140 kW scale performed in late 2008. It includes:

- a techno-economic evaluation of the process at the next scale,
- the design of the next scale demonstration plant,
- the design of a scaled cold flow model of the demonstration plant,
- the experimental proof of the fluid dynamics of the demonstration plant design, and
- a determination of the potential of the process at a larger scale.

A schematic drawing of the scale-up path is provided in Fig. 2.

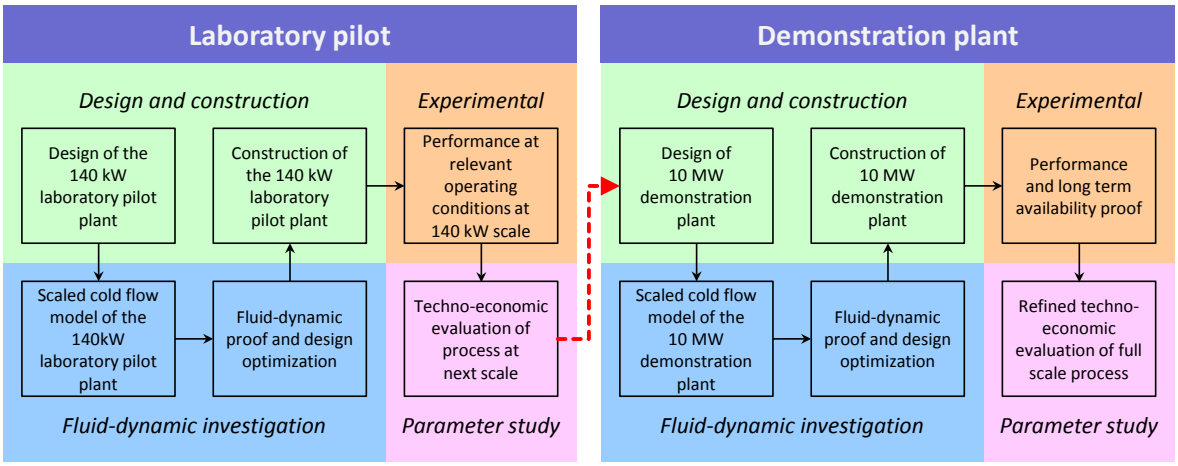

Fig. 2 Selected scale-up strategy.

The thesis is structured in accordance with the selected scale-up strategy.

Chapter 3 *"Process design"* includes the integration of the next scale process into a power or heat generation system, allowing for the determination of expectable performance data. It also is the basis for the design delivering occurring gas flow rates, compositions and temperatures.

Chapter 4 *"Chemical looping reactor system* design*"* includes the development of the reactor system design of the next scale unit including the quantification of dimensions and expectable operational parameters such as solid circulation rates and inventories.

Chapter 5 *"Cold flow modeling"* deals with the development of the design of a scaled cold flow model and experiments. It provides information on the feasibility of the design proposed in Chapter 4 and the implications on potentially required design modifications.

Chapter 6 *"Potential of chemical looping combustion at the large* scale*"* includes the determination of the potential of the chemical looping combustion technology at the large scale. A quantitative comparison of the process with a potential alternative CCS process is given, underlining the advantages of chemical looping combustion for carbon capture and storage.

The outcome of this work should provide a design package for the demonstration of chemical looping combustion technology with 10 MW gaseous fuel input.

2 Background

2.1 Primary energy resources and the global climate

Natural resources and our society

The development of our modern society is demanding on the availability of natural resources. Fossil fuels, such as oil or gas, are by quantity the most important of these resources. This is because nearly everything we use is either directly or indirectly, via by-products, derived from fossil-based energy resources (primary energy resources). Since the industrial revolution, energy consumption has increased, correlating with social and economic development and improved human welfare and health. Although progress has been made to reduce the amount of energy needed per unit in terms of global gross domestic product generated (global energy intensity), further growth in the use of primary energy resources is forecast. The demand is expected to increase by 36% between 2008 and 2035 from an optimistic point of view considering current policies including declared political intensions (refer to the "New Policies Scenario" IEA/OECD (2010)). Pessimistically, the growth could be as high as 47% in the same period (refer to the "Current Policies Scenario" IEA/OECD (2010)). While energy from renewable sources such as biomass, wind and solar-derived energy are discussed as a solution to meet our need for energy in a sustainable way (IPCC, 2011), fossil fuels (oil, coal and gas) will be as important in the future as they are nowadays (Fig. 3).

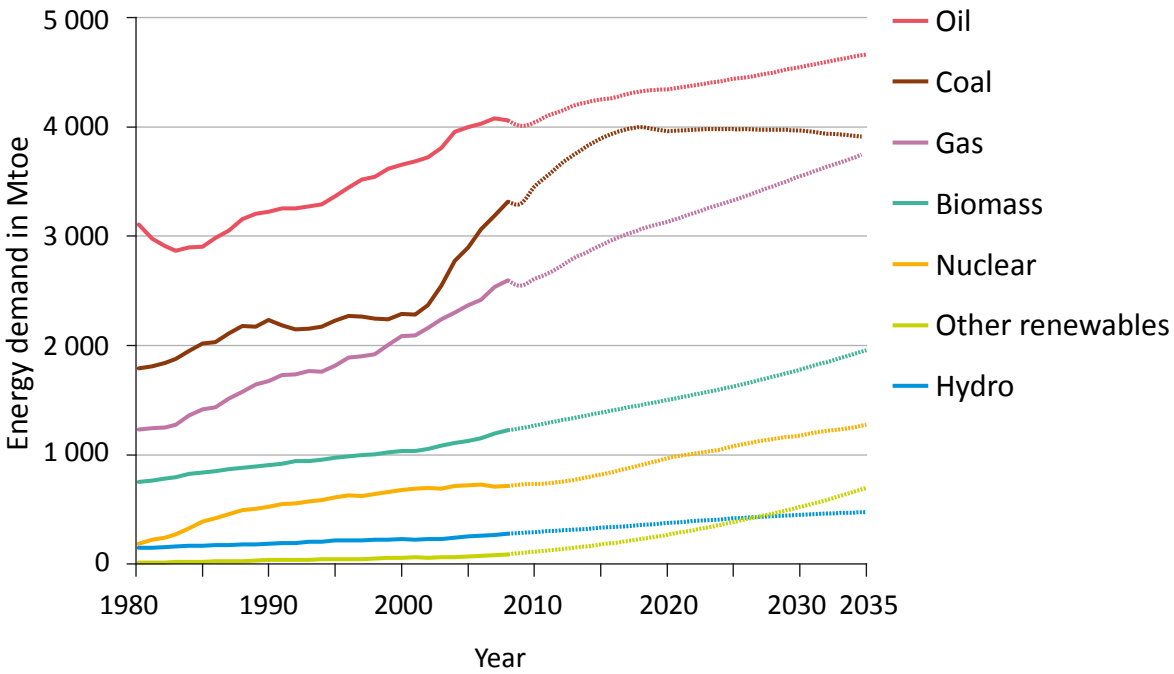

Fig. 3 World energy demand by fuel source. Adapted from (IEA/OECD, 2010).

Regionally, energy consumption differs strongly depending on the level of economic development. For example, OECD countries consumed about 44% of the world's energy in 2008, but held only about 18% of the world's population. While the increase in energy demand has leveled off in OECD countries in recent decades, it is predicted that the growth in demand of non-OECD countries will continue, reflecting faster rates of growth in population, economic activity and industrial production. Large developing economies such as China and India will dominate the annual growth in energy consumption in upcoming decades (Fig. 4).

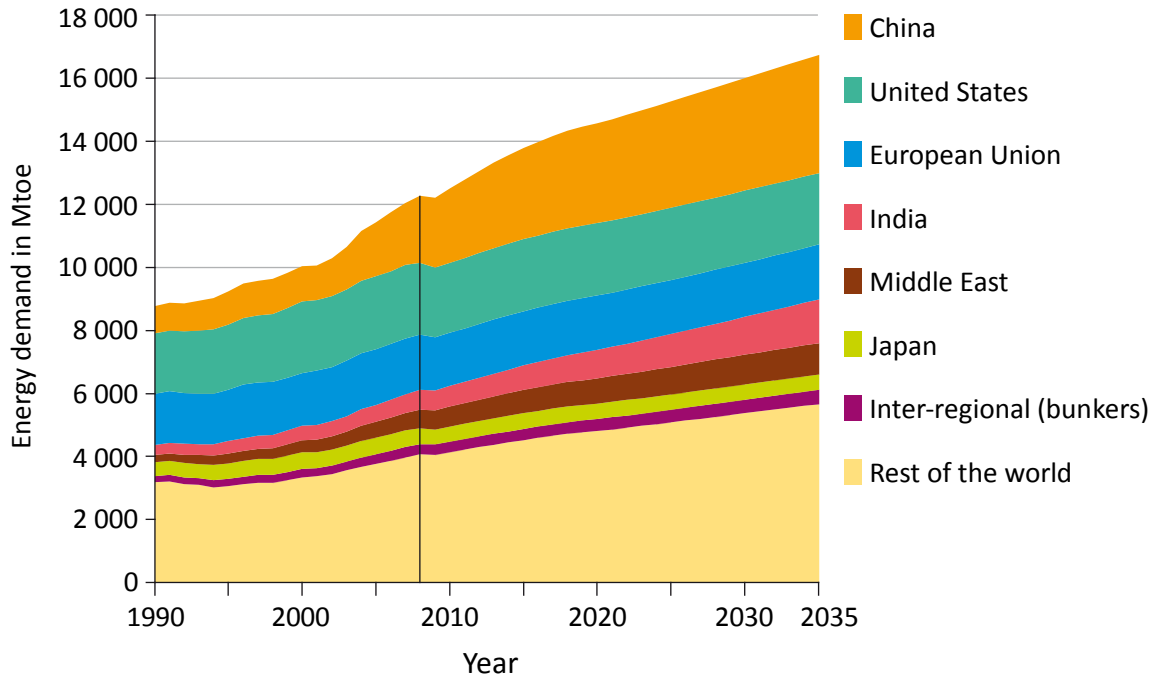

Fig. 4 World energy demand by region. Adapted from (IEA/OECD, 2010).

Among industrial sectors, power generation contributes the most to the increase in demand. Measures improving this sector are therefore considered as the most promising approach to reduce global energy consumption.

Climate change and anthropogenic activities

The global climate is controlled by the greenhouse gas effect, which describes the capability of the Earth's atmosphere to absorb long-wave radiation emitted from the Earth's surface. Without the presence of the atmosphere acting as a partial blanket, the planetary surface temperature would be as low as -19°C (IPCC, 2007b). Certain gases present in the atmosphere are responsible for this effect. The most important ones are water vapor, carbon dioxide, methane and nitrous oxide. Changes in the concentrations of greenhouse gases in the atmosphere, thus, can have a significant impact on the global climate. Long term changes in the state of the world's climate are discussed as climate change. Anthropogenic activities such as the combustion of fossil fuels have led to increased emissions of greenhouse gases. Carbon dioxide is the most important anthropogenic greenhouse gas and has risen from 280 ppm in the pre-industrial era to 379 ppm in 2005 (Fig. 5). Since then, the concentration has increased further to above 396 ppm in early 2013 (Dlugokencky and Tans, 2013).

Due to the fact that there are no appropriate models capable of reproducing all the effects contributing to the Earth's climate, there is no consensus among researchers regarding the impact of human activities on the climate. However, the IPCC Fourth Assessment Report states: *Most of the observed increase in global average temperature since the mid-20th century is very likely due to the observed increase in anthropogenic greenhouse gas concentrations* (IPCC, 2007a). This is mainly since greenhouse gas emissions correlate well with global temperature increases. Frequency, intensity, spatial extension, duration and timing of extreme weather and climate events are affected by a changing climate. There is evidence that some climate events have changed as a result of anthropogenic influences, mainly due to the increase in the atmospheric concentration of greenhouse gases. Those climate events include the overall decrease in the

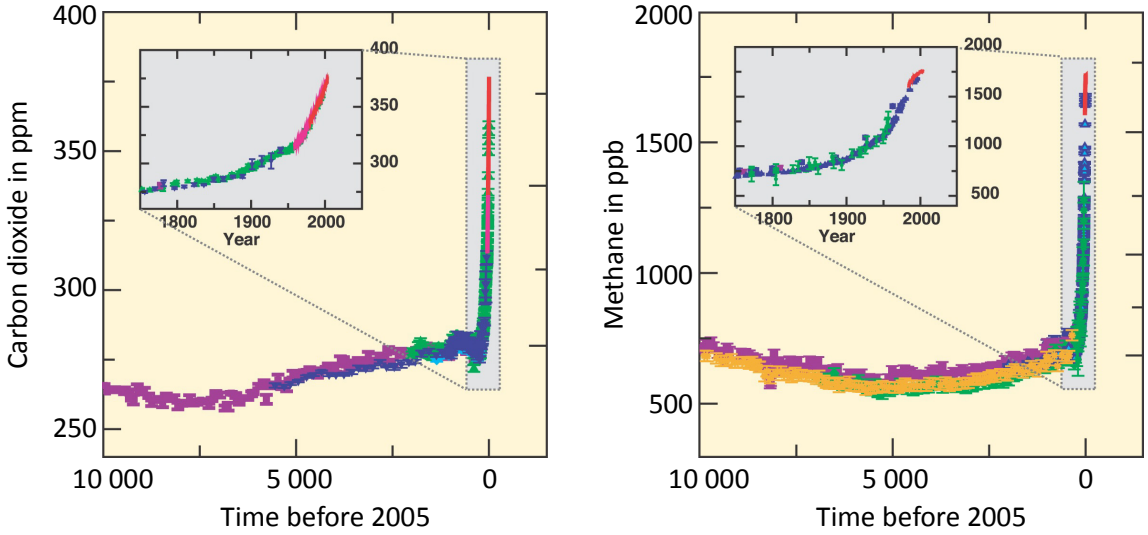

Fig. 5 Atmospheric concentrations of carbon dioxide and methane over the last 10 000 years. Adapted from IPCC (2007b).

number of cold days and nights and increasing extreme coastal high water due to an increased mean sea level (IPCC, 2012). However, the attribution of human activities on extreme events is a challenging task. The attitude of humans concerning long term consequences is a key issue for sustainable development of our world.

There are multiple options to reduce or avoid greenhouse gas emissions from energy systems while still satisfying energy demand:

- Improved conversion efficiency to reduce fuel usage.
- Switching to less carbon-intense types of fuel, e.g. from coal to gas.
- Nuclear power, which is discussed as less carbon-intense.
- Substitution of fossil fuels by renewable heat and power which, in addition, increases sustainability.
- Combined heat and power to increase fuel utilization.
- Inhibition of CO_2 emissions from stationary sources by carbon capture and storage.

2.2 Carbon capture and storage (CCS)

The shift in energy consumption towards a more sustainable use of natural resources requires major restructuring of present fossil fuel-demanding industries. Sustainability in this sense is accompanied by a reduction in anthropogenic greenhouse gas emissions. On a long-term basis, it is obvious that sustainability is the goal to be accomplished, but other measures are necessary to achieve a reduction in greenhouse gas emissions in the near future. Carbon capture and storage (CCS) has been discussed as one of the most feasible possibilities to reach the target of greenhouse gas, namely CO_2, emission reduction on a mid-term basis (IEA/OECD, 2010). In carbon capture and storage, CO_2 from anthropogenic sources is separated and put into suitable storage. CO_2 can thus be isolated from the atmosphere on a long-term basis. In practice, large stationary CO_2 emitting processes are the most relevant to be equipped with CCS technologies. These involve sources where fossil fuel is converted into CO_2; the most important industries in this regard are power generation, cement production, refineries, the iron and steel industry and the petrochemical industry. Since capturing CO_2 from such sources is energy intensive, the reduction in emissions to the atmosphere depends on the fraction of CO_2 captured, increased CO_2

production due to increased efforts required for separation, transport, storage, as well as leakage during processing and long-term leakage from storage (Fig. 6).

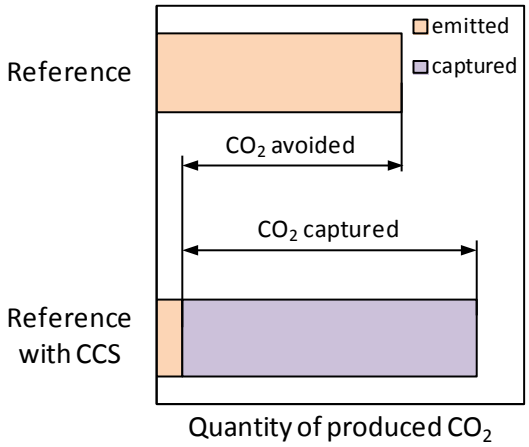

Fig. 6 CO_2 balance from carbon capture and storage with the increase in fuel consumption indicated. Adapted from (IPCC, 2005).

Since electricity and heat production is the most important contributor to CO_2 emissions with a share of about 41% in 2012 (IEA/OECD, 2012) and many of large sources are available, any attempt to mitigate CO_2 emissions will have to address CO_2 capture from such systems. The IEA/OECD (2010) estimated that the costs of electricity production increase by 12-36 US$/MWh for CCS, which is reflected by an increased fuel consumption of 11-22% for a natural gas combined cycle plant, 24-40% for a pulverized coal power plant and 14-25% for an integrated gasification combined cycle plant.

Carbon capture and storage technologies

Carbon capture and storage technologies focuses on application to large sources such as industry and power generation since applicability on the small scale is difficult and expensive. First generation CCS processes, as discussed in IPCC (2005) basically include post-combustion capture, pre-combustion capture and oxy-fuel. Capture from industrial processes is not included in this classification since CO_2 has been separated from such processes long before the discussions on climate change began. New advanced capture technologies such as unmixed combustion represent second generation CCS processes which aim for a reduction in capture-related costs. All of these approaches are illustrated in Fig. 7.

Capture of CO_2 from industrial processes has been daily practice for many years. Purification of natural gas (natural gas sweetening) and production of hydrogen-rich synthesis gas for ammonia synthesis are the most important examples. Generally, high partial pressures of CO_2 in such processes allow for relatively easy separation. However, in such cases, most of the CO_2 is vented to the atmosphere due to limited use and no requirement for storage. Integration of CCS thus can be accomplished very easily at a low cost. Among others, the cement, iron and steel industries are examples where CCS seems to be reasonable because of the large quantities of CO_2 emitted (IPCC, 2005).

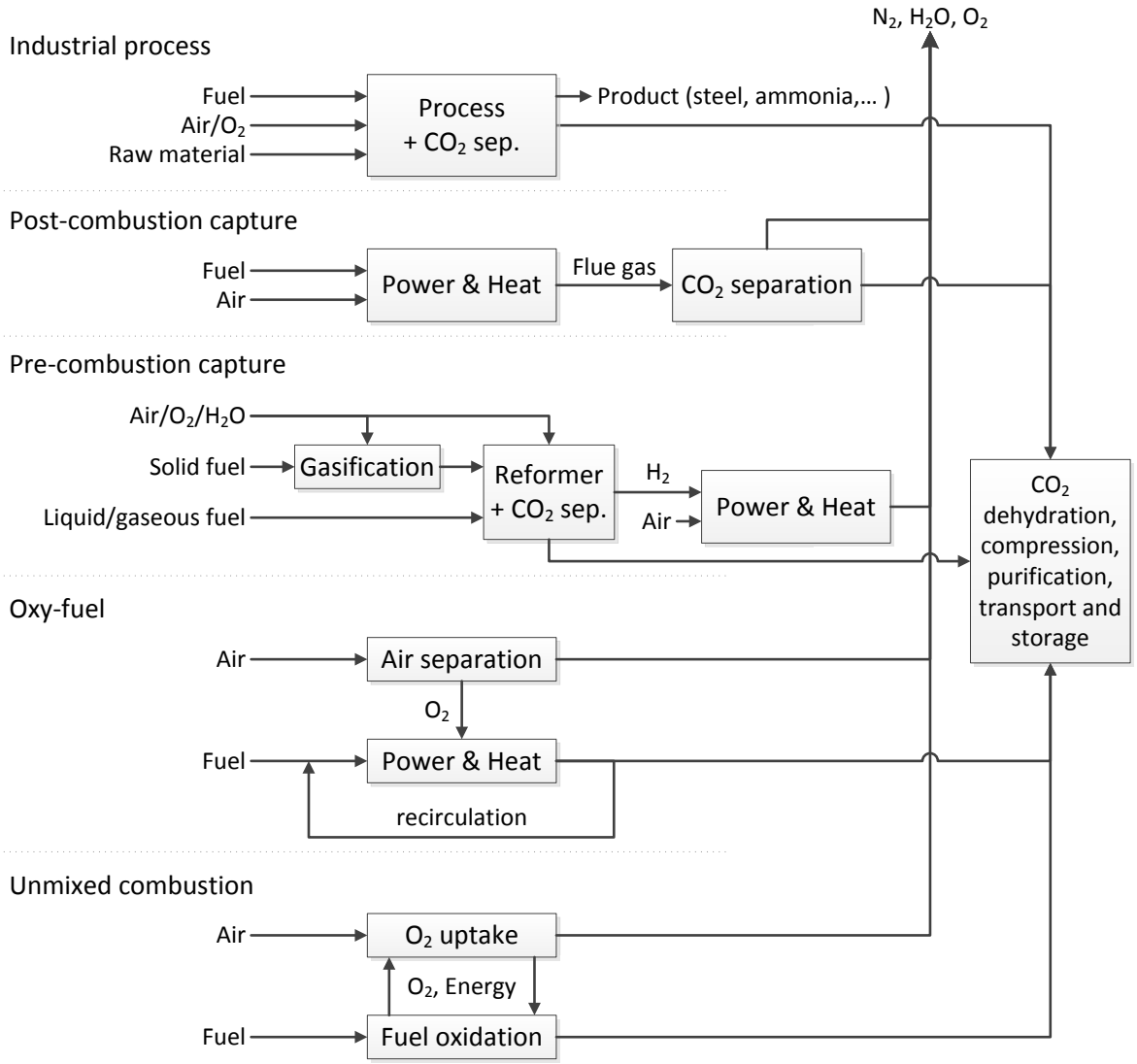

Fig. 7 CCS processes. Adapted from (IPCC, 2005).

In post-combustion capture, the CO_2 from a combustion flue gas stream is separated by means of chemical absorption. Since flue gas pressure is close to atmospheric pressure and because of the large fraction of nitrogen, huge gas flows have to be treated. Capture energy depends on the capture rate and the CO_2 partial pressure, which varies depending on the type of fuel and process from 30-150 mbar. The CO_2 concentration and presence of impurities have to be considered in the design of post-combustion capture. Primarily, post-combustion capture is discussed for coal-fired power plants where the CO_2 partial pressures are high. Furthermore, since post-combustion capture is an end-of-pipe solution, this technology is applicable for retrofitting.

In pre-combustion capture, a solid fuel is de-carbonized prior to combustion. At first, a syngas, favorably at high pressure, is produced by gasification followed by hydrogen enrichment in a reforming/CO-shift reactor. The CO_2 in this syngas can be separated easily because of the high pressure and high concentration, giving a high purity CO_2 stream and a hydrogen-rich fuel. The hydrogen then can be used in many applications such as hydrogen-fueled natural gas combined cycles where capture-related costs are the lowest.

Oxy-fuel combustion is an in-situ CO_2 separation process where a concentrated CO_2 stream is obtained by direct combustion of the fuel with nearly pure oxygen instead of air. Since the air

nitrogen is missing, the flame temperature has to be moderated by recycling of cool combustion flue gas. The required oxygen has to be produced where cryogenic air separation uses state-of-the-art technology. The main energy penalty in oxy-fuel combustion arises there. Although retrofitting of existing boilers with oxy-fuel combustion technology is discussed, challenging tasks such as air leakage, increased heat capacity of the flue gas and heat transfer rates have to be considered.

Unmixed combustion is a second generation CCS process where air and fuel are not mixed during the combustion process. Two separate gas streams thus occur where the first stream is oxygen-depleted air and the second is the oxidized fuel. In this process, therefore, CO_2 separation is inherently accomplished, avoiding energy-intense gas-gas separation. One representative of this process is chemical looping, discussed in detail in Section 2.3 *"Chemical looping technology"* (p. 11).

CO_2 transport and storage

Unless the unique situation of a CCS plant directly located above a suitable storage site occurs, the CO_2 must be transported. Basically, three transport options apply in CCS: transport by pipeline, by ship and by road or rail. Transport of gases or liquids in pipelines is a mature technology. To avoid the occurrence of two-phase flow in the pipeline, CO_2 has to be transported in a supercritical state, typically at a pressure of above 8 MPa. This makes transportation easier and less expensive. Since the first CO_2 pipeline was put into operation in Texas, USA in the early 1970s, transporting CO_2 from anthropogenic sources for use in enhanced oil recovery has been employed. A critical assessment of the required CO_2 purities is crucial to avoid damage to the pipeline. When a CCS plant is located close to a waterway, CO_2 can also be transported by ship like liquefied petroleum gas is transported today. At the very small scale, road or rail tankers can be an option, but on a large scale, this is economically unattractive compared to pipeline or ship transport. The type of transportation is based on economics, and distances play an important role (IPCC, 2005).

Once the CO_2 is at the storage site, it has to be put into suitable storage. A suitable storage site should allow for long term storage without significant leakage. It has to be reasonably close to the CCS plant to reduce transportation costs. The IPCC (2005) reported on geological and ocean storage, mineral carbonation and industrial use solutions. Depleted oil and gas reservoirs, deep saline formations and un-minable coal beds have been considered for geological storage, where the CO_2 is injected in a dense form into a rock formation. Industrially, CO_2 is currently stored in geological formations in the Sleipner project (North Sea), the Weyburn project (Canada) and the In Salah project (Algeria). Several other projects are ongoing, mainly in Texas, USA, for enhanced oil recovery. Storage in the ocean can be applied at depths greater than 1000 m where the CO_2 dissolves. Depending on depth, a sinking CO_2 plume or a CO_2 lake can occur. In any case, storage in ocean changes the ocean pH value significantly and therefore may be harmful to marine life. Therefore, ocean storage is not practically considered at present.

In CCS, the most critical task is the storage of CO_2. Legal and public opinions have imposed large uncertainties on the future of carbon capture and storage and have inhibited industrial investment into carbon capture and storage.

2.3 Chemical looping technology

The basic principle of the chemical looping process is that the overall chemical reaction is divided into two separate reaction steps that take place in two physically separate reaction zones. A suitable reactive carrier is used to selectively transport reactants from one reactor to the other in a continuous cycle, where the carrier itself is neither consumed nor produced globally. The carrier undergoes a repeating reaction and regeneration, requiring suitable carriers resistant to deactivation over several cycles. Compared to chemical processes where liquid solvents are used as a carrier, in chemical looping processes, the carrier is in the solid state.

Several chemical processes can be classified as chemical loping processes targeting different products and requiring different types of carriers. Typical chemical looping processes are:

- chemical looping combustion (CLC),
- chemical looping reforming (CLR),
- carbonate looping, and
- sorption enhanced reforming (SER).

Chemical looping combustion is a process where the main purpose of the carrier is the transport of oxygen from an air reactor to a fuel reactor. In the fuel reactor, the oxygen is used to oxidize a hydrocarbon fuel, producing a stream rich in CO_2 and H_2O. The reduced carrier leaves the fuel reactor and is regenerated (re-oxidized) in the air reactor. The basic principle of chemical looping combustion is illustrated in Fig. 8.

While full conversion of the fuel is intended in chemical looping combustion, in chemical looping reforming, a syngas is produced containing of CO and H_2 in addition to CO_2 and H_2O. This is accomplished by supplying less air than is needed for full oxidation of the fuel in a chemical looping combustion process.

In carbonate looping, calcium oxide (CaO) is used as the carrier for selective removal of CO_2 from a combustion exhaust gas by absorption and formation of limestone ($CaCO_3$). The limestone is thermally regenerated in a separate reactor requiring heat. This can be accomplished by oxy-firing to obtain a stream concentrated in CO_2 from the regenerator of the carbonate looping process. To achieve good CO_2 separation rates, it is crucial to adjust the temperatures in the absorber and the regenerator accordingly. Further details on the carbonate looping process can be found elsewhere (Dean et al., 2011).

In the sorption enhanced reforming process, calcium oxide is used for upgrading syngas by the removal of CO_2 in a syngas generation process, i.e. a gasification process. This, additionally, allows for an enhancement of the gasification reactions by the consumption of CO_2 that evolved during gasification. More specific details on the sorption enhanced reforming process can be found elsewhere (Tessie Du Motay and Maréchal, 1868; Pfeifer et al., 2007).

2.3.1 Chemical looping combustion for carbon capture

Chemical looping combustion is a two-step combustion process where mixing of combustion air and fuel is inherently avoided and therefore can be classified as “unmixed combustion” (Lyon and Cole, 2000). This process is generally established by using metal oxides as the carrier, conducting a continuous reduction-oxidation-cycle to transfer the oxygen needed for combustion in the solid phase between two separate reactors, the air reactor and the fuel reactor. The term “oxygen

carrier (OC)" has therefore been invented to describe this solid carrier. An adequately selected oxygen carrier and proper operating temperatures allow for a fuel reactor exhaust gas ideally consisting of CO_2 and H_2O. Hence, combustion flue gases are free of air nitrogen and, after water condensation, a CO_2-rich stream is obtained, ideally ready for sequestration (Fig. 8). Therefore, chemical looping combustion offers great potential compared to all other carbon capture technologies, as it avoids energy and cost intensive gas-gas separation and thus considerably reduces CO_2 avoidance costs.

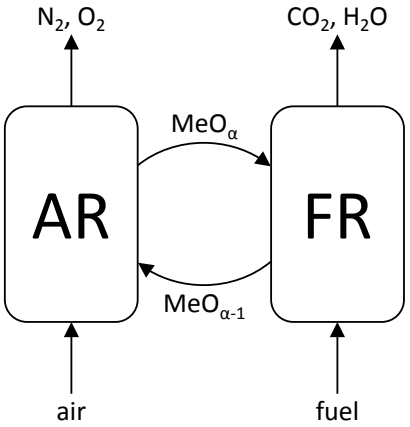

Fig. 8 Basic chemical looping combustion process setup. AR - air reactor, FR - fuel reactor, Me - metal.

In the fuel reactor, the fuel is oxidized according to the global reaction

$$C_xH_yO_z + \left(2x + \frac{y}{2} - z\right) MeO_\alpha \rightleftharpoons xCO_2 + \frac{y}{2}H_2O + \left(2x + \frac{y}{2} - z\right) MeO_{\alpha-1} \qquad \text{(reac. 2-1)}$$

where the oxygen carrier is reduced at the same time. The reduced oxygen carrier is then transported back to the air reactor where it is re-oxidized again according to

$$MeO_{\alpha-1} + \frac{1}{2}O_2 \rightleftharpoons MeO_\alpha \qquad \text{(reac. 2-2)}$$

The air reactor exhaust gas is oxygen-depleted air containing N_2 and some O_2 with the specific concentrations depending on the operation conditions. Therefore, air reactor exhaust gas does not need special treatment, except for dust removal, before it is released to the environment. While the reaction in the air reactor is always strongly exothermic, the reactions in the fuel reactor can be slightly exothermic or endothermic, depending on the active oxygen carrier material and type of fuel. This means that the air reactor is the main heat source of the chemical looping process. The sum of the reactions in the air reactor and in the fuel reactor is identical to the reaction in the direct combustion of fuel.

$$C_xH_yO_z + \left(x + \frac{y}{4} - \frac{z}{2}\right) O_2 \rightleftharpoons xCO_2 + \frac{y}{2}H_2O \qquad \text{(reac. 2-3)}$$

In practice, this means that the energy release in chemical looping combustion is the same as in direct combustion. Additionally, in chemical looping, the formation of nitrogen oxides (NO_x) is inhibited due to the absence of hot spots, evolving from flames, owing to the low temperatures in the reactors. This has been demonstrated by Ishida and Jin (1996) and Ryu et al. (2004).

Chemical looping combustion can be used for CO_2-free electricity generation. For power from natural gas, the process has to compete with natural gas combined cycle plants which can deliver electricity at very high fuel to electricity efficiency values of up to 60% (Woudstra et al., 2010). With respect to this, pressurization of the chemical looping process will be necessary where there are a lot of open questions, e.g. pressurized operation of dual fluidized bed systems and how to achieve the required oxygen carrier circulation (Marx et al., 2011b). Chemical looping for direct use with coal has been discussed as a promising option allowing for a significant reduction in the CO_2 avoidance costs compared to first generation CCS processes (Adanez et al., 2012). However, there are many industrial processes requiring steam where atmospheric driven boilers are currently being used. In such cases, chemical looping is capable of performing equally well, but is CO_2 capture ready (Lyngfelt et al., 2001; Marx et al., 2011a). Heavy oil extraction from in-situ oil sands production, where steam is injected to reduce oil viscosity, is considered a promising application for chemical looping combustion (Nikoo et al., 2010; Marx et al., 2011c).

2.3.2 Chemical looping reforming for synthesis gas generation

Hydrogen is an important raw material for the production of basic chemicals, in oil refining and many other industrial applications. Although naturally occurring, most hydrogen is produced from hydrocarbon sources. Catalytic steam reforming of hydrocarbons is currently the cheapest way to produce hydrogen and accounts for more than 90% of the world's hydrogen production (Bellona, 2002). Methane steam reforming, where the CH_4 is reformed catalytically in the presence of H_2O and heat in tubular fixed bed reactors, and auto-thermal reforming, where a part of the methane is oxidized to supply the heat for reforming, are state-of-the-art in catalytic steam reforming (Ferreira-Aparicio et al., 2005). In such systems, the catalyst and tube surface temperature as well as heat transfer are critical issues, limiting the overall process performance and the hydrogen yield (Dybkjaer, 1995).

Synthesis gas production can be applied to the concept of chemical looping when reducing the global air/fuel ratio to below 1.0, which simply means supplying less air than needed for complete combustion of the fuel. This process is called chemical looping reforming (CLR) (Fig. 11), and was discussed as a variant of chemical looping combustion by Rydén and Lyngfelt (2004) and Rydén (2008). The necessary heat for steam reforming in the fuel reactor is supplied by partial oxidation of the fuel, which means that the process is operated auto-thermally; thus, this process is often called auto-thermal chemical looping reforming (short CLR(a)).

The resulting fuel reactor exhaust gas composition depends on the global energy balance of the chemical looping reforming system, including heat loss (Fig. 10). The main advantages of chemical looping reforming compared to catalytic steam reforming is that the heat is supplied inherently to the fuel reactor with the circulating oxygen carrier. Heat transfer is therefore not limited, allowing for higher operating temperatures (Pröll et al., 2009a). It was also found that less steam is needed compared to tubular steam reforming (Pröll et al., 2010), and that the process is less sensitive to sulfur contaminants in the fuel as long as the operating temperatures are sufficiently high (García-Labiano et al., 2009).

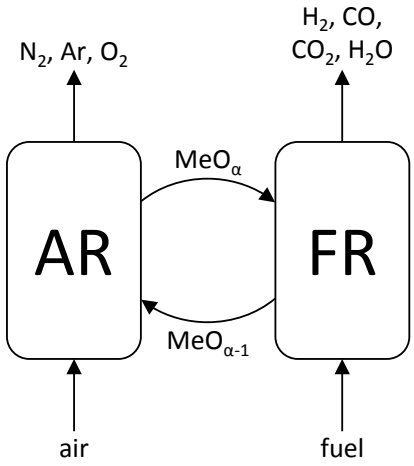

Fig. 9 Basic chemical looping reforming process setup. AR - air reactor, FR - fuel reactor, Me - metal.

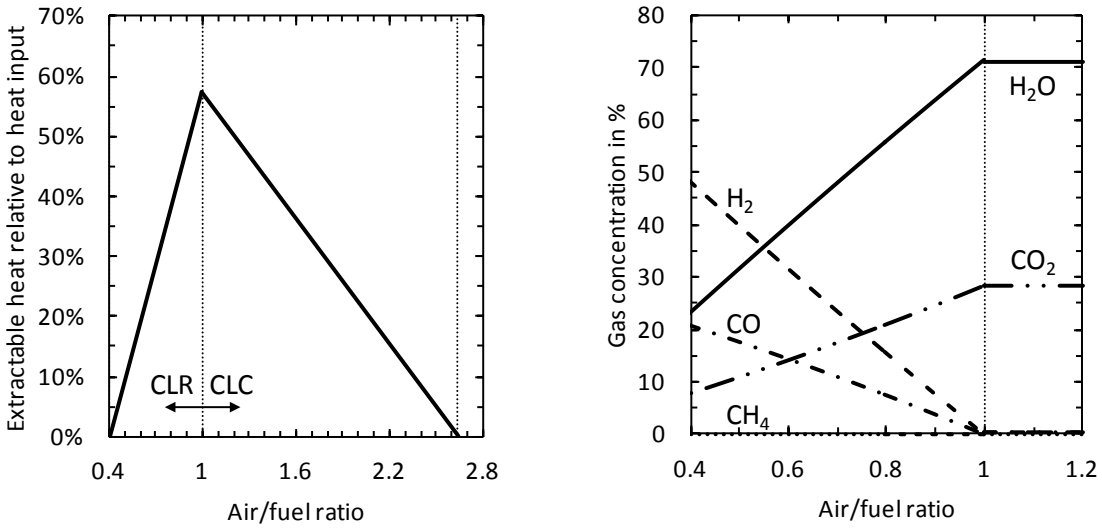

Fig. 10 Heat production and product gas composition in CLR(a) operation with methane as the fuel. Thermodynamic equilibrium is assumed for a fuel reactor temperature of ϑ_{FR} = 900°C with a steam/carbon ratio in the fuel reactor feed of 0.2 and a difference in degree of oxygen carrier oxidation between the air reactor and fuel reactor ΔX_s = 10%.

However, a key issue in chemical looping reforming is that the process must operate under pressurized conditions (PCLR). The main challenges with respect to pressurized chemical looping reforming are (Marx et al., 2011b):

- the increased gas-solids reaction intensity,
- the reduced gas velocities with pressurized operation,
- the increased ratio of solid circulation to gas flow rate, and
- proper sealing between the reactors by loop seals.

Atmospheric auto-thermal chemical looping reforming has been tested at scales of up to 140 kW at the Vienna University of Technology and showed very promising results (Mayer et al., 2010; Pröll et al., 2010). Although chemical looping reforming is expected to be capable of revolutionizing hydrogen production, the process has been investigated to a lesser extent than chemical looping combustion.

2.3.3 Chemical looping combustion of solid fuels

Solid fuels are cheaper and more abundant than gaseous fuels and therefore are very interesting for use in chemical looping systems. For solid biomass, chemical looping combustion is CO_2 negative since the CO_2 already was removed from the atmosphere during the growth of the plant (Chum et al., 2011). The problem with solid fuels in chemical looping is the necessary reaction time in the fuel reactor. Several minutes are usually required for the fuel to gasify, requiring long residence times in the fuel reactor.

In chemical looping combustion with the use of solid fuels, three different approaches are discussed:

- chemical looping combustion with external gasification,
- in-situ gasification chemical looping combustion, and
- chemical looping with oxygen uncoupling.

In the first, the time limiting phase of solid fuel combustion is outsourced by the use of an external gasification reactor prior to the chemical looping combustion process. The combustion of syngas has been investigated by several researchers in the past, confirming the feasibility of chemical looping combustion for coal gasification syngas (Abad et al., 2006; Adánez et al., 2009a; García-Labiano et al., 2009; Kolbitsch et al., 2010). In any case, heat has to be supplied to the gasification reactor. This is typically obtained inherently by partial oxidation of the fuel, requiring oxygen to avoid dilution of the CO_2 by nitrogen. Unfortunately, oxygen production is energy consuming and reduces the overall efficiency of the process.

In in-situ gasification chemical looping combustion, the solid fuel is fed directly into the fuel reactor. Here, the solid fuel has to undergo drying and devolatilization, char gasification and the combustion of volatiles and gasification products in a single reactor. This is accompanied by several difficulties such as providing sufficient time for gasification, sufficient oxygen carrier-volatiles contact for conversion and separation of the fuel ash from the oxygen carrier material. Special focus on the design of the reactor system is needed for the successful use of solid fuels in in-situ gasification chemical looping combustion.

In chemical looping with oxygen uncoupling (CLOU), a special oxygen carrier with the capability of spontaneous release of gaseous oxygen is necessary. It utilizes the fact that some metal oxides, e.g. CuO/Cu_2O, have suitable equilibrium partial pressures with gas phase oxygen at the chemical looping combustion temperature. This allows for direct oxidation of the fuel by gaseous oxygen, thus avoiding time consuming intermediate gasification (Mattisson et al., 2009b).

Compared to chemical looping combustion with gaseous fuels, considerable research is required before demonstrating direct solid fuel applications in chemical looping systems.

2.3.4 History of chemical looping technology

The basic idea of chemical looping combustion dates back to the year 1950 when Lewis and Gilliland presented the technology in a patent (Lewis and Gilliland, 1954). The original idea originates in finding a process capable of producing cheap CO_2 of high purity from any carbonaceous material including gaseous, liquid as well as solid fuels. They proposed the use of a copper based oxygen carrier in a multi-stage bubbling fluidized bed reactor where the solid fuel has sufficient time for the reaction when passing through the stages. In a regeneration reactor,

the spent oxygen carrier is re-oxidized. Transport of solids between the reactors was achieved by lift gases. Lewis and Gilliland also mentioned that there is the need for an inert carrier for the copper to avoid agglomeration when the system is operated at elevated temperatures. However, the process was never commercialized.

Later, the process fell into oblivion until, two decades later, it was picked up again by Richter and Knoche (Knoche and Richter, 1968; Richter and Knoche, 1983) who intended to improve the reversibility of combustion with the use of an intermediate reaction in the oxidation process of the fuel. The applicability of several other oxygen carriers than copper was discussed, such as iron or nickel. Nevertheless, Ishida et al. (1987) introduced the term “chemical looping combustion” first in their exergy analysis of a chemical looping combustion based power plant. During the 1990s, chemical looping combustion attracted attention with the beginning of the discussion on climate change where Ishida and Jin (1994b) proposed chemical looping as a potential technology for carbon capture. In the following years, the process was investigated theoretically by several researchers for carbon capture from power generation. It was concluded that when chemical looping combustion is used as a heat source in a gas turbine combined cycle, 100% carbon capture can be achieved with very little energy penalty (Ishida and Jin, 1994a; Anheden and Svedberg, 1996; Ishida and Jin, 1997; Anheden and Svedberg, 1998; Jin and Ishida, 2000).

Nevertheless, until in the early 2000 chemical looping combustion was no more than a paper concept with experimental experience limited to mainly reactivity tests of potential oxygen carriers (Ishida and Jin, 1994b, 1996; Ishida et al., 1996, 1998; Jin et al., 1998, 1999). The discussions of Lyngfelt et al. (2001) who proposed the use of fluidized bed systems for chemical looping processes can be considered as a cornerstone in the development of chemical looping systems allowing continuous operation for the first time. The proposed setup included two interconnected fluidized beds where the air reactor is operated as a high-velocity transporting riser and the fuel reactor as a bubbling fluidized bed (Fig. 11). Loop seals are placed in between the fluidized beds to allow the solids to circulate and to avoid mixing of the air reactor and fuel reactor gases. The concept was applied to an atmospheric boiler with 10 kW fuel power and CH_4 as the fuel, and the major chemical looping parameters, e.g. temperature and solids circulation rates, were investigated. Later, the concept was realized with a 10 kW laboratory pilot unit built and successfully put into operation in 2004 (Lyngfelt et al., 2004; Linderholm et al., 2008).

The unit demonstrated the feasibility of the process for more than 100 hours in first continuous operation where a fuel conversion efficiency of 99.5% was reached using a nickel-based oxygen carrier. Lifecycle assessment revealed a particle lifetime of 40 000 hours (Lyngfelt and Thunman, 2005). Since then, several continuously operating chemical looping laboratory installations have been erected, demonstrating the technology with gaseous fuels up to 140 kW fuel power (Lyngfelt et al., 2004; Ryu et al., 2004; Adánez et al., 2006; Johansson et al., 2006; Son and Kim, 2006; Adánez et al., 2009b; Mattisson et al., 2009a; Pröll et al., 2009b; Ryu et al., 2010; Wang et al., 2010; Rifflart et al., 2011) and with solid fuels up to 100 kW fuel power (Berguerand and Lyngfelt, 2008; Andrus et al., 2009; Shen et al., 2009; Wu et al., 2010; Markström et al., 2012; Thon et al., 2012). Two larger scale refractory lined units for the application of solid fuels of up to 3 MW fuel power are reported in the literature, but no operating results have been published up to now (Andrus et al., 2010; Beal et al., 2010).

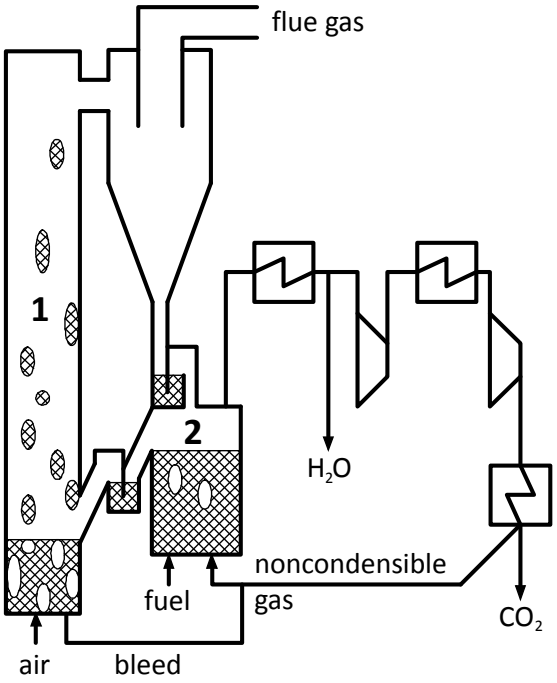

Fig. 11 Layout of the chemical-looping combustion process with two interconnected fluidized beds by Lyngfelt et al. (2001) (reproduced). 1 – air reactor, 2 – fuel reactor.

Several reviews on chemical looping have been published by Lyngfelt et al. (2008), Hossain and de Lasa (2008), Fang et al. (2009), Lyngfelt (2011), Pröll and Hofbauer (2011) and Adanez et al. (2012), highlighting the interest in chemical looping technology.

2.3.5 Oxygen carrier

The oxygen carrier is a key issue in chemical looping processes. Expectable process behavior and performance are strongly related to oxygen carrier properties. A number of metals are mentioned in the literature as potential candidates; Cu, Fe, Ni, Co and Mn are the most important ones. The following oxygen carrier requirements have to be fulfilled for successful use in chemical looping systems:

- thermodynamically suitable with respect to oxidation of the fuel in the fuel reactor and oxidation of the oxygen carrier in the air reactor,
- highly reactive towards fuel conversion in the fuel reactor and oxygen in the air reactor to keep the required solids inventories in the reactors low,
- the oxygen transport capacity should be sufficiently high to keep the required solid circulation between the air and fuel reactor within reasonable limits,
- should not suffer from degradation over repeated cycles of reduction and oxidation, thus should have a high cyclic stability,
- high structural stability to reduce attrition and, thus, required material make up rate,
- good fluidization properties (avoidance of agglomeration) at high temperature,
- the oxygen carrier should allow safe handling, avoiding negative impacts on human health and the environment, and
- be cost effective at a low price and high lifetime.

Pure metals suffer from degradation and agglomeration, showing that there is the need for an inert support (de Diego et al., 2004). Using a porous support provides a higher surface area for the reaction and improves the mechanical properties, thus improving the lifetime and avoiding the

occurrence of agglomeration. Supporting materials can be Al_2O_3, $MgAl_2O_3$, SiO_2, TiO_2, ZrO_2 and many others. Such synthetic oxygen carriers can be prepared by different methods, including spray drying, spin flash and impregnation (Adanez et al., 2012). The properties of the oxygen carrier are strongly affected by the preparation method. In general, spray dried particles have a higher attrition resistance while impregnated particles typically have a higher surface area. Since particle preparation is a cost factor, natural minerals as an alternative are often discussed. Minerals such as iron ore, ilmenite, manganese ore or waste materials from the steel industry and alumina production have been considered (Leion et al., 2009; Cuadrat et al., 2011). Often, the use of such materials with solid fuels is discussed, mainly due to the low price (Ishida et al., 1987) and limited reactivity towards CH_4 conversion (Pröll et al., 2009c).

The driving force of a reaction is governed by the distance from equilibrium. While in direct combustion with air the reactants are far from equilibrium and, thus, the driving force is high, in chemical looping combustion, this force diminishes depending on the oxygen carrier material. A significant amount of unconverted fuel can be left in the fuel reactor even when chemical equilibrium is reached (Fig. 12). There are oxygen carriers with very high redox potential inside the fuel reactor, i.e. Mn_2O_3/Mn_3O_4 and CuO/Cu_2O, where only very little fuel is lost compared to direct oxidation with air.

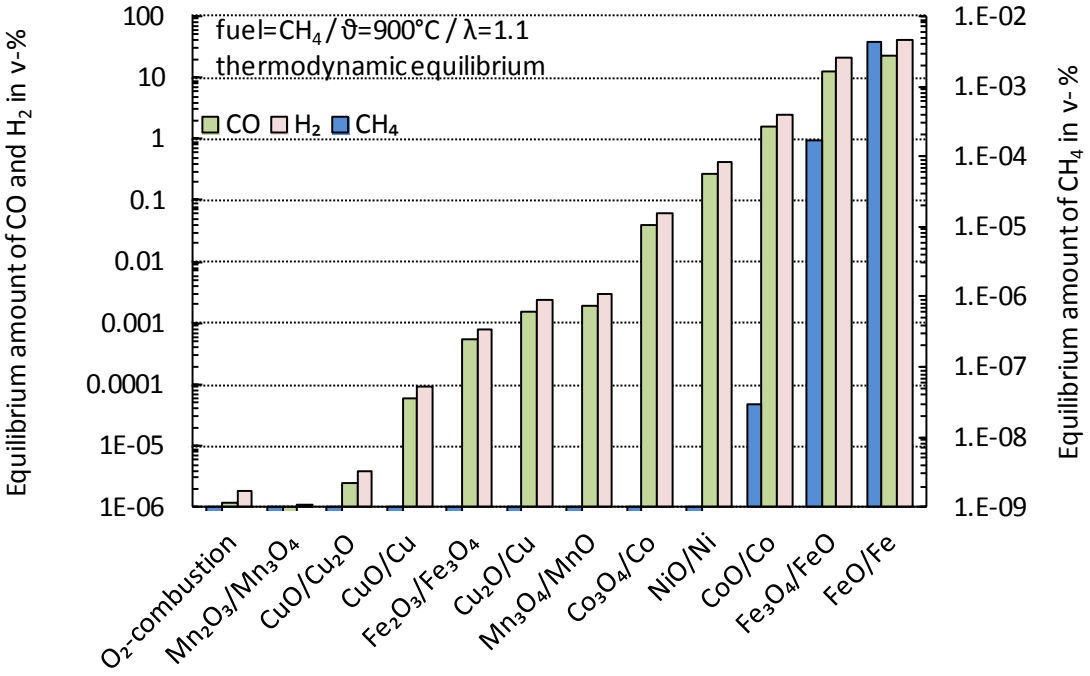

Fig. 12 Thermodynamic limitation of the fuel conversion of direct combustion and in chemical looping combustion for different redox reaction schemes. Database: HSC Chemistry 6.1.

Apart from the reaction potential in the fuel reactor, it is important to consider the situation in the air reactor where the oxygen carrier is re-oxidized. It was found that an oxygen carrier having a high thermodynamic driving force for fuel conversion in the fuel reactor shows limitations with respect to re-oxidation in the air reactor (Fig. 13). An oxygen carrier following the redox oxidation of Mn_2O_3/Mn_3O_4, which has the potential to outperform direct combustion, exhibits limitations when re-oxidized in air.

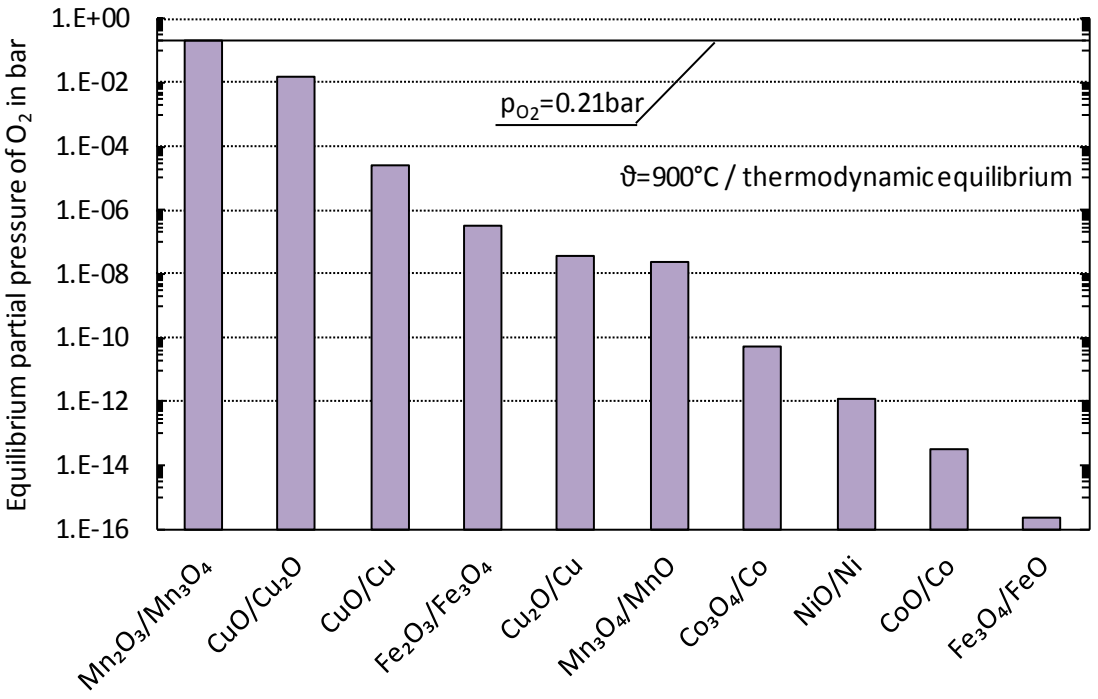

Fig. 13 Thermodynamic limitation of oxygen carrier oxidation in the air reactor for different oxygen carrier redox reaction schemes. Database: HSC Chemistry 6.1.

When ranking oxygen carriers from a thermodynamic point of view, it is thus important to consider both the air rector and fuel reactor reactions. The optimal oxygen carrier should allow for high fuel conversion in the fuel reactor and sufficiently high potential for re-oxidation in the air reactor at reasonably low O_2 concentrations. Nevertheless, in practice, fuel conversion is governed by reactivity rather than by thermodynamics. This is why nickel-based oxygen carriers, which obviously have thermodynamic restrictions, are still among the best performing candidates when a methane rich fuel is used.

The oxygen carrier circulation rate between the air and the fuel reactor can be determined by the oxygen mass balance of the system. The actual oxidation state of the oxygen carrier is determined by the degree of oxidation, X_s.

$$X_s = \frac{m - m_{red}}{m_{ox} - m_{red}} \qquad \text{(eqn. 2-1)}$$

It relates the actual amount of oxygen on the partially oxidized state (m-m_{red}) to the potential amount of oxygen (m_{ox}-m_{red}) on the oxygen carrier. The required minimal solids circulation is reached when the oxygen carrier is fully oxidized in the air reactor and fully reduced in the fuel reactor. The oxygen transport capacity R_0 is a useful indicator for ranking oxygen carriers (Lyngfelt et al., 2001).

$$R_0 = \frac{m_{ox} - m_{red}}{m_{ox}} \qquad \text{(eqn. 2-2)}$$

Typical oxygen transport capacities for different oxygen carrier redox systems are listed in Table 2-1.

Table 2-1 Oxygen transport capacity R_0 of different oxygen carrier redox systems.

Redox system	R_0
$CaMnO_{3-0}$/ $CaMnO_{3-1}$	0.112
Co_3O_4/Co	0.266
CoO/Co	0.214
CuO/Cu	0.201
CuO/Cu_2O	0.101
Fe_2O_3/Fe_3O_4	0.033
Fe_2TiO_5+TiO_2/$FeTiO_3$	0.05
Fe_2O_3/FeO	0.10
Mn_2O_3/Mn_3O_4	0.034
Mn_3O_4/MnO	0.070
NiO/Ni	0.214

The necessary oxygen carrier circulation rate diminishes with an increase in R_0. In practice, it was found that the required solids circulation rate is usually not critical. It must be considered that the inert support significantly reduces the effective oxygen transport capacity of the carrier.

Oxygen carriers with oxygen uncoupling (CLOU)

The so-called CLOU effect describes the capability of an oxygen carrier to decompose, spontaneously releasing gaseous oxygen. The CLOU effect utilizes the fact that some metal oxides have a suitable equilibrium partial pressure of gas-phase oxygen at typical chemical looping operating temperatures. For such metals to be used, it is important that this reaction is reversible in chemical looping, which means that the oxygen carrier should be re-oxidizable in the air reactor at reasonably low oxygen partial pressures. So far, three single-metal systems that are theoretically suitable have been identified: CuO/Cu_2O, Mn_2O_3/Mn_3O_4 and Co_3O_4/CoO (Mattisson et al., 2009b). Fig. 14 shows the thermodynamic redox potential of these oxygen carriers. The thermodynamics reveal that CuO is capable of releasing oxygen above 1028°C in air (p_{O2}=0.21). Thus, when using particles with CLOU properties, the temperature in the air reactor should be kept low to promote re-oxidation while the fuel reactor temperature has to be high to promote O_2 release.

In addition to these single-metal systems, several combined metals with a perovskite structure, e.g. $CaMnO_{3-\delta}$, have been shown to exhibit CLOU properties (Källén et al., 2013). Although CLOU particles are mainly discussed for solid fuels, such particles do have excellent potential for use with gaseous fuels as well.

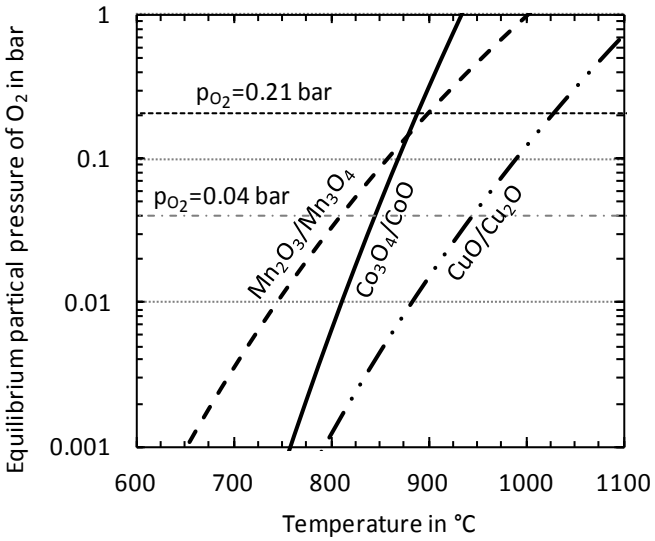

Fig. 14 Equilibrium partial pressure of discussed CLOU oxygen carriers. Reproduced after Mattisson et al. (2009b). Database: HSC Chemistry 6.1.

2.3.6 Chemical reactions in chemical looping systems

The most relevant reactions in chemical looping combustion and reforming are listed below. The oxygen carrier is oxidized in a strongly exothermal reaction following:

$$MeO_{\alpha-1} + \frac{1}{2}O_2 \rightleftharpoons MeO_{\alpha} \qquad \text{(reac. 2-4)}$$

In the fuel reactor, hydrocarbon fuel is oxidized while the oxygen carrier is reduced. Many subsequent or parallel reactions occur. For catalytically inactive oxygen carriers, the fuel is expected to be oxidized in direct interaction with the oxygen carrier where the partial oxidation of the fuel follows a reaction (reac. 2-5) which can be slightly exothermal or endothermal depending on the metal and the type of fuel.

$$C_xH_yO_z + (x-z)MeO_{\alpha} \rightleftharpoons xCO + \frac{y}{2}H_2 + (x-z)MeO_{\alpha-1} \qquad \text{(reac. 2-5)}$$

Subsequent to partial oxidation, or in cases when syngas is used as the fuel, the oxidation of CO and H_2 with the oxygen carrier occurs in a slightly exothermal reaction.

$$CO + MeO_{\alpha} \rightleftharpoons CO_2 + MeO_{\alpha-1} \qquad \text{(reac. 2-6)}$$

$$H_2 + MeO_{\alpha} \rightleftharpoons H_2O + MeO_{\alpha-1} \qquad \text{(reac. 2-7)}$$

In parallel to the reactions mentioned above, the catalytically activated steam reforming reaction occurs in the presence of water which can be introduced either externally or from the oxidation of CO or H_2. In chemical looping reforming, oxygen carriers that promote steam reforming are beneficial where the temperature should be high for high hydrocarbon conversion.

$$C_xH_y + xH_2O \overset{cat.}{\longleftrightarrow} xCO + \left(x + \frac{y}{2}\right)H_2 \qquad \text{(reac. 2-8)}$$

Subsequently to partial oxidation (reac. 2-5) or in cases of a syngas fueled chemical looping process, oxidation of CO can occur via the catalytically activated CO-shift reaction instead of direct

oxidation by the oxygen carrier (reac. 2-6). Compared to direct oxidation of CO with the metal oxide, oxidation of CO via the CO-shift reaction is promoted at low temperatures.

$$CO + H_2O \overset{cat.}{\longleftrightarrow} CO_2 + H_2 \qquad \text{(reac. 2-9)}$$

Both the steam reforming reaction (reac. 2-8) and the CO-shift reaction (reac. 2-9) are catalyzed at metallic surfaces. In chemical looping reforming, therefore, oxygen carriers capable of offering catalytically active sites are very attractive candidates.

The reaction scheme in the fuel reactor for oxygen carriers with CLOU properties is significantly different to the reactions mentioned above. For CLOU oxygen carriers, the oxygen carrier is spontaneously reduced by thermodynamics, releasing gaseous oxygen. This is essentially the backward reaction of the air reactor reaction (reac. 2-4), and is highly endothermic.

$$MeO_\alpha \rightleftharpoons MeO_{\alpha-1} + \frac{1}{2}O_2 \qquad \text{(reac. 2-10)}$$

Subsequently, the hydrocarbon fuel reacts with this free oxygen in an exothermic combustion reaction:

$$C_xH_yO_z + \left(x + \frac{y}{4} - \frac{z}{2}\right)O_2 \rightleftharpoons xCO_2 + \frac{y}{2}H_2O \qquad \text{(reac. 2-11)}$$

Since oxygen carrier oxidation and reduction equalize at the same temperature, the overall reactions in the fuel reactor for CLOU property oxygen carriers are typically slightly exothermic. The main benefit of CLOU in chemical looping combustion processes is that the fuel does not have to react directly with the metal oxide. This is especially important for solid fuels, since slow intermediate gasification reactions are eliminated. In any case, CLOU property oxygen carriers are also very interesting for gaseous fuels since reactions are generally much faster with gaseous oxygen. Lower solids inventories and smaller fuel reactors could therefore be applied when using such particles.

However, the global reaction in a chemical looping combustion reactor system is independent of whether the oxygen carrier has CLOU properties or not, and is the same as for direct combustion with air.

$$C_xH_yO_z + \left(2x + \frac{y}{2} - z\right)MeO_\alpha \rightleftharpoons xCO_2 + \frac{y}{2}H_2O + \left(2x + \frac{y}{2} - z\right)MeO_{\alpha-1} \qquad \text{(reac. 2-12)}$$

3 Process design

3.1 Introduction

A key issue for the successful demonstration of a new technology is the selection of an adequate site for effective and long term demonstration. To keep the investment costs low, integration of the demonstration unit into an existing site is beneficial over green field installation. Utilizing the present infrastructure is therefore essential for successful operation within the scope of the selected site. Hence, the optimal site should allow for the introduction of the demonstration unit at the selected size while keeping the existing site infrastructure untouched. For this reason, a site is selected where a natural gas combined cycle heat and power cogeneration plant with supplementary firing before the heat recovery section is installed. In such units, the site output can be adapted very quickly to the actual demand by supplementary firing. District heating is accomplished by taking intermediate pressure bleeding steam from the steam turbine. This allows for variable adjustment of the ratio of electric power to district heat output. Such a cycle is illustrated in a process flow diagram in Fig. 15.

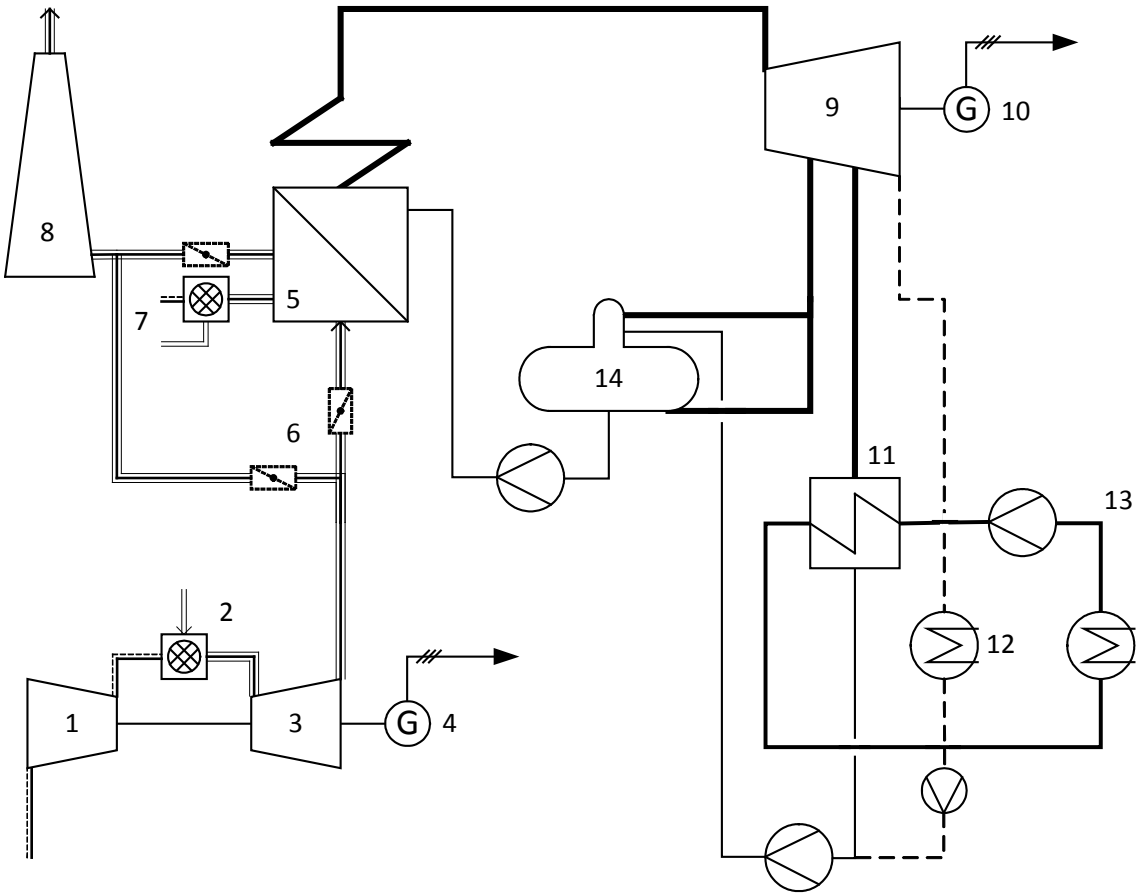

1. Gas turbine compressor
2. Gas turbine combustion chamber
3. Gas turbine expander
4. Electricity generator
5. Heat recovery steam generator (HRSG)
6. HRSG emergency bypass
7. Supplementary firing
8. Stack
9. Steam turbine
10. Electricty generator
11. District heating condenser
12. Steam turbine condenser
13. District heating cycle
14. Boiler feedwater deaerator

Fig. 15 Process flow diagram of a natural gas combined cycle heat and power cogeneration plant with supplementary firing. Adapted from (Schmitz and Schaumann, 2005).

The attached chemical looping combustion demonstration plant is designed to substitute the energy input of supplementary firing, which in turn can easily compensate for fluctuations in demonstration plant operation with very little response time. Moreover, the overall site output can be increased when operating the chemical looping combustion plant and supplementary firing in parallel. Such a system exhibits the advantage that power output from the chemical looping combustion unit would not contribute to the CO_2 footprint of the site, thus improving the CO_2 output balance. A schematic process flow diagram of the overall process, including the steam from the chemical looping combustion demonstration unit, is given in Fig. 16. The arrows indicate the possibility of switching between supplementary firing and the chemical looping combustion plant.

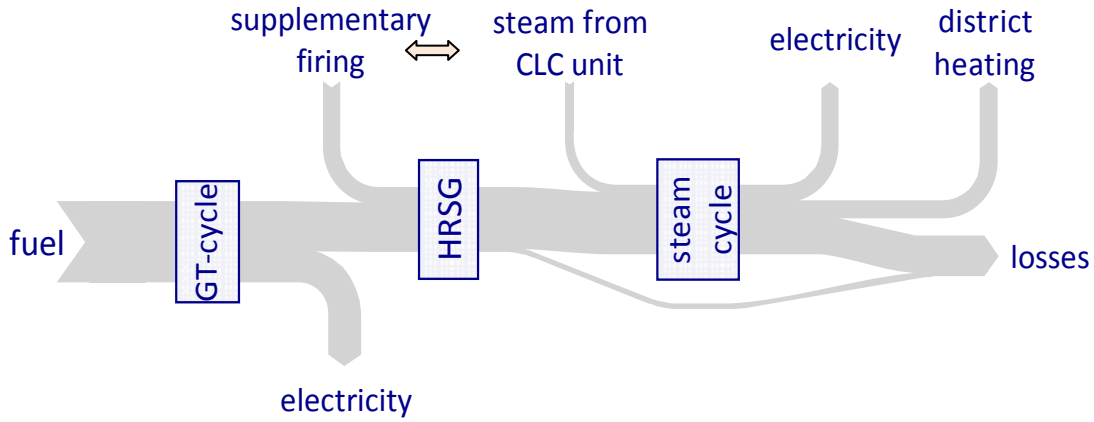

Fig. 16 Schematic overall process flow diagram of the site including steam from the chemical looping combustion demonstration unit. GT - gas turbine, HRSG - heat recovery steam generator.

In the following, the integration of a chemical looping combustion demonstration unit at a scale of 10 MW thermal input using gaseous fuel into the steam generating system of such a commercial natural gas combined cycle plant is discussed. The demonstration unit shares the steam cycle, including i.e. the steam turbine, condenser, boiler feedwater deaerator and district heating cycle, with the existing plant. This allows for a significant reduction in the investment costs. Expectable demonstration plant performance data were determined considering experimental data obtained in 140 kW chemical looping combustion laboratory pilot testing at the Vienna University of Technology.

3.2 Theoretical background

3.2.1 The mass and energy balance investigation software IPSEPro

The SimTech Simulation Technology IPSEpro is a stationary, equation oriented simulation software for use in the simulation of power generation cycles and chemical processes. Such simulations can involve:

- calculation of heat balances, prediction of design and off design performance,
- verification and validation of measurements during acceptance tests,
- monitoring and optimization of plant performance on-line, and
- estimation of design costs.

The software is structured in modules sketched in Fig. 17 and was built with respect to transparency and easy user interaction.

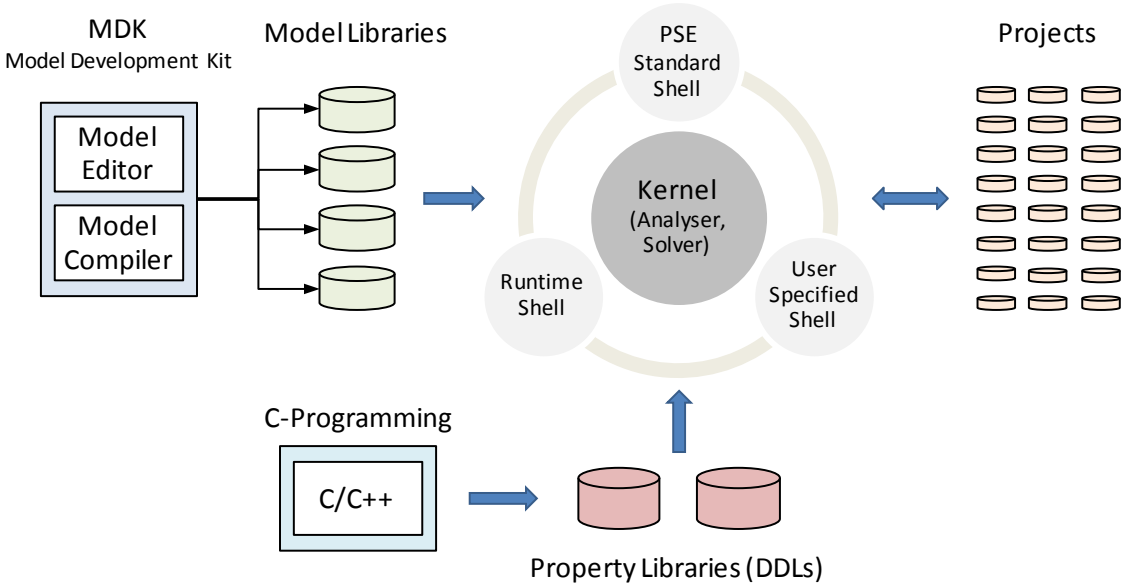

Fig. 17 Modular structure of the IPSEpro process simulation software. Adapted from (SimTech, 2011).

The central component of IPSEpro is the Kernel where the system of equations is analyzed and solved. During the calculations, data are taken from the user interface, i.e. the process simulation environment (PSE). The PSE is the module of the program where the process is modeled and data are entered and read and, as such, is the user interface. The inner structure of the models and apparatuses is contained in the model libraries. The model library is developed or changed in the model development kit (MDK) in the model editor where the equations describing the models are deposited. The model compiler translates these model equations into a machine executable code collected in the model libraries. During a calculation, thermodynamic data are taken from the properties libraries in the format of a dynamic link library (DLL). The property libraries were developed in the C/C++ program language and are converted into machine readable code in the C-programming software. The power of the software is its open structure which enables quick and effective introduction of new user-defined models and substances, introducing a unique level of flexibility.

The software uses the Newton-Raphson algorithm to solve the multidimensional system of equations where the system of equations is solved by separation into small groups. This allows for fast convergence with an average calculation time of a few seconds.

IPSEpro solving mechanism – the Newton-Raphson method

There are two possibilities for handling non-linear equations. The first is to find the minimum of the associated root description of the equation. The problem is solved by finding the steepest descent of the associated function. The second possibility is the Newton-Raphson method, names after Sir Isaac Newton (Whiteside, 1967-1976) and Joseph Raphson (Raphson, 1690) which has undergone remarkable development (Ypma, 1995).

The method of steepest descent nearly always results in a minimum at the cost of higher calculation times. In comparison, the Newton-Raphson method converges very quickly and,

therefore, has evolved as the mathematical standard procedure for solving non-linear equations. The convergence radius of the Newton-Raphson method is small, requiring very good starting values in order to find the solution.

In the following, the Newton-Raphson method is discussed for a single equation (a one-dimensional case) and then extended to equation systems of n dimensions.

The Newton-Raphson method for an one-dimensional equation system

In the case of a one-dimensional problem, the root $x_0 \in \mathbb{R}$ of a twice continuously differentiable function $R(x)$: $\mathbb{R} \rightarrow \mathbb{R}$ is approximated by $x^* \in \mathbb{R}$ where it applies that:

$$x_0 \neq x^* \qquad \text{(eqn. 3-1)}$$

The approximation of the function $R(x)$ by a first-order Taylor series

$$R(x) = R(x_0) + \frac{dR(x)}{dx}(x_0) \cdot (x - x_0) + \mathcal{O}[(x - x_0)^2] \qquad \text{(eqn. 3-2)}$$

causes an error of the magnitude of $(x\text{-}x_0)^2$ with a reasonably accurate approximation in the region close to the arbitrarily selected development point x_0. The root x_1 of this approximation is found by substituting x in (eqn. 3-2) by x_1

$$R(x_1) = R(x_0) + \frac{d}{dx}R(x_0) \cdot (x_1 - x_0) + \mathcal{O}[(x_1 - x_0)^2] \qquad \text{(eqn. 3-3)}$$

and prescribing $R(x_1) = 0$. Applying this and by rearrangement (eqn. 3-3), the associated root of the approximation x_1 is derived from

$$x_1 = x_0 - \frac{R(x_0)}{R'(x_0)} \qquad \text{(eqn. 3-4)}$$

The value of x_1 is used in (eqn. 3-4) as a new starting point $x_1 \rightarrow x_0$ to determine a new root x_2 with $x_2 \rightarrow x_1$. In an iterative procedure the values of x_n aspire after the root x^* of the original function $R(x)$. This procedure is the Newton-Raphson method, for which the general formulation is:

$$x^{(n+1)} = x^{(n)} - \frac{R(x^{(n)})}{R'(x^{(n)})} \qquad \text{(eqn. 3-5)}$$

A graphical interpretation is given in Fig. 18.

The Newton-Raphson method for a n-dimensional equation system

To apply the Newton-Raphson solving algorithm to an n-dimensional equation system, the associated system of equations has to be transformed into a zero point search problem to obtain the residual $\boldsymbol{R}^{(n)} = \boldsymbol{R}(\boldsymbol{x}^{(n)})$: $\mathbb{R}^n \rightarrow \mathbb{R}^n$. From this, the Newton-Raphson procedure is derived to

$$\boldsymbol{x}^{(n+1)} = \boldsymbol{x}^{(n)} - \boldsymbol{J}^{(n)^{-1}} \times \boldsymbol{R}(\boldsymbol{x}^{(n)}) \qquad \text{(eqn. 3-6)}$$

where the Jacobian matrix $\boldsymbol{J}^{(n)}$ is

$$J_{ij}^{(n)} = \frac{\partial R_j^{(n)}}{\partial x_{ij}} \qquad \text{(eqn. 3-7)}$$

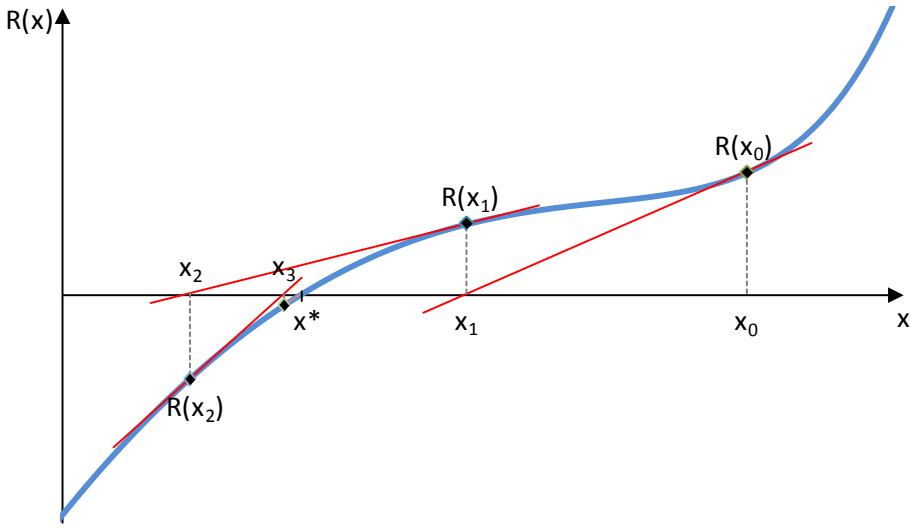

Fig. 18 Graphical interpretation of the Newton-Raphson root iteration procedure.

Constraints and drawbacks of the Newton-Raphson solving algorithm

To make use of the local at least quadratic convergence (Schaback and Werner, 1992) of the Newton-Raphson algorithm, the starting conditions of the iteration have to be selected carefully. Poorly selected starting conditions could lead to almost anything, including alternation or infinite growth of the solution. Another disadvantage of the procedure is that for every single iteration, the Jacobian matrix $\boldsymbol{J}^{(n)}$ have to be recalculated and inverted, which requires considerable calculation effort for matrices of high bandwidth.

3.2.2 Model structure in simulation

A model in practice can include an arbitrary selected description of any occurring process of interest. The only requirement is that the description of the process is adequate enough to deduce the phenomena appearing in reality. The proposition after which a model is developed is to keep the description as simple as possible without critically falsifying the model outputs. When modeling chemical processes, such simplifications can include formulation of conversion rates instead of formulation of reaction kinetics. However, there are minimal requirements when describing naturally occurring processes, e.g. the reaction of two species. It is evident that any model of such kind has to include a description of the conservation of mass and energy. The models used here are based on this, fulfilling at least these two conditions. In the following, the approach is discussed and a generalized model is presented. This model is then applied to stationary flow processes where the typical representatives are chemical processes, i.e. chemical looping combustion.

When considering an arbitrary natural process where several streams are entering (1, 2 … g) and exiting (g+1, g+2 … j), energy can be extracted from the process P_{out}, e.g. mechanical energy from a stirrer, or can be lost to the surrounding $\dot{Q}_{out}$, e.g. heat loss. A representative schematic of such a process is given in Fig. 19.

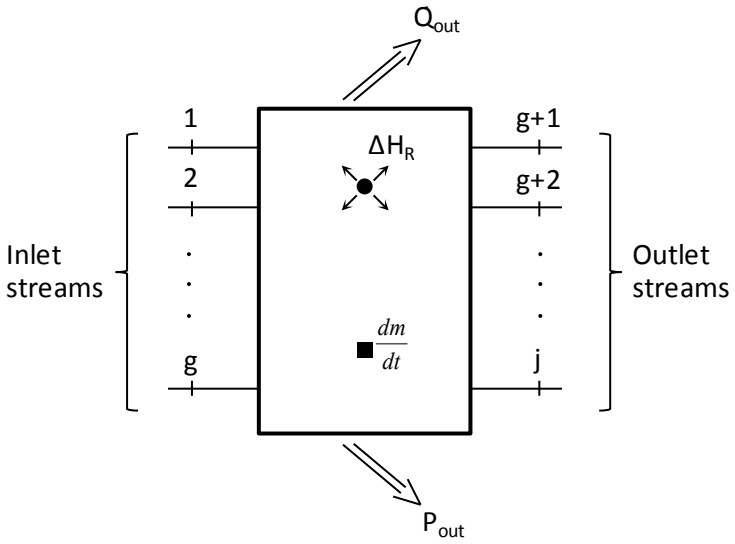

Fig. 19 Schematic flow diagram of an arbitrary chemical process with a potential mass accumulation (dm/dt) and a reaction indicated (ΔH_R).

In chemical engineering, such streams are typically composed of a mixture of many components in any condition of aggregation. Natural gas is a typical representative of such where, apart from CH_4, many other components are present. Considering a stream *g* consisting of *n* components, the sum of the molar fractions y_i of all components included in the stream equals unity.

$$\sum_{i=1}^{n} y_i = 1 \qquad \text{(eqn. 3-8)}$$

With a known mass-flow rate of a stream $\dot{m}_g$, the mass-flow rate of a certain element *k*, $\dot{m}_{k,g}$, in this stream is calculated by

$$\dot{m}_{k,g} = \dot{m}_g \cdot w_{k,g} = \dot{m}_g \cdot M_k \cdot \sum_{i=1}^{n} \frac{\nu_{k,i} \cdot y_i}{M_i} \qquad \text{(eqn. 3-9)}$$

where $w_{k,g}$ is the mass fraction of element *k* in stream *g*, M_k is the molar mass of the element *k*, M_i the molar mass of component *i* and $\nu_{k,i}$ is the quantity of element *k* in component *i*. For example, when determining the amount of carbon in C_2H_6, the value of $\nu_{k,i}$ will be $\nu_{C,C2H6} = 2$.

The accumulation of a certain element *k* inside of the process dm_k/dt is derived by subtracting the sum of the elements of type *k* leaving the process from the sum of elements *k* entering the process. Entering streams have a positive sign and streams leaving the process have a negative algebraic sign; dm_k/dt is

$$\frac{dm_k}{dt} = \sum_{g=1}^{g} \left|\dot{m}_{k,g}\right| - \sum_{g=g+1}^{j} \left|\dot{m}_{k,g}\right| = \sum_{g=1}^{j} \dot{m}_g \cdot w_{k,g} = \sum_{g=1}^{j} \dot{m}_g \cdot M_k \cdot \sum_{i=1}^{n} \frac{\nu_{k,i} \cdot y_i}{M_i} \qquad \text{(eqn. 3-10)}$$

With knowledge of the elementary based mass-flow rates the mass-flow rate of a stream g, $\dot{m}_g$, follows from

$$\dot{m}_g = \sum_{k=1}^{k} \dot{m}_{k,g} \qquad \text{(eqn. 3-11)}$$

The total mass accumulated in the process is then

$$\frac{dm}{dt} = \sum_{g=1}^{g} |\dot{m}_g| - \sum_{g=g+1}^{j} |\dot{m}_g| = \sum_{g=1}^{j} \sum_{k=1}^{k} \dot{m}_{k,g} \qquad \text{(eqn. 3-12)}$$

In stationary flow processes, no accumulation occurs which means that

$$\frac{dm_k}{dt} = \frac{dm}{dt} = 0 \qquad \text{(eqn. 3-13)}$$

The models in the IPSEpro environment are based on (eqn. 3-13), allowing for handling of stationary flow processes in chemical engineering.

The representing energy balance of such a process with $\dot{Q}_{out}$ as sensible heat and P_{out} as mechanical energy released to the surrounding is given as

$$\sum_{g=1}^{j} \dot{m}_g \cdot h_t(p,T)_g = \dot{Q}_{out} + P_{out} \qquad \text{(eqn. 3-14)}$$

where h_t is the conventional enthalpy

$$h_t(p,T) = \Delta h_{f,298}^0 + h(p,T) - h(p_0 = 1.01325bar, T_0 = 298K) \qquad \text{(eqn. 3-15)}$$

including the specific enthalpy of formation $\Delta h^0_{f,298}$ at 25°C as well as the specific thermal enthalpy $h(p,T)$ (difference in thermo-chemical standard conditions). Using this formulation of the enthalpy allows for simple handling of the energy balance of any process occurring in nature. This is that even if reactions are involved reaction enthalpies do not have to be considered separately since they are covered by the formulation of the conventional enthalpy.

3.2.3 The advanced energy technology library (AET-Lib)

The advanced energy technology library (AET-Lib) has been developed to model chemical looping based processes (Bolhàr-Nordenkampf et al., 2009a). It is based on experience gained in the modeling of biomass gasification processes used to assess plant performance (Pröll, 2004). The chemical looping models have been cross-correlated to performance tests at the 140 kW chemical looping testing rig at the Vienna University of Technology (Bolhàr-Nordenkampf et al., 2009b; Kolbitsch et al., 2009a; Kolbitsch et al., 2009b; Kolbitsch et al., 2010), verifying that the models are capable of predicting the behavior of chemical looping systems sufficiently well. In the following, the AET-Lib is described in more detail.

Substance classes and thermodynamic properties

Several types of substances with specific compositions are considered in the AET-Lib including:

- pure water/steam,
- mixtures of ideal gases,
- mixtures of real gases,
- organic substances, and
- inorganic substances.

The International Association for the Properties of Water and Steam formulation IAPWS-IF97 after Wagner et al. (Wagner and Kruse, 1998) is used to calculate the properties of water and steam including the description to the two-phase region. The formulation is an industrial standard covering a validity range of 273.15 K ≤ T ≤ 1073.15 K / 0 < p ≤ 100 MPa and 1073.15 K ≤ T ≤ 2273.15 K / 0 < p ≤ 50 MPa. The properties of ideal gas mixtures are calculated from data collected by Burcat and McBride (Burcat and McBride, 1997) using seven-term polynomials of the NASA type. Real gas property data are calculated using the reference equation of state GERG-2004 XT08 for natural gas and other mixtures (Kunz et al., 2007). The formulation includes 21 components and allows for the calculation of thermodynamic properties in the homogeneous gas, liquid and supercritical regions and allows performing vapor-liquid equilibrium calculations in the validity range of the formulation of 60 K ≤ T ≤ 700 K / p ≤ 70 MPa. Using this, flash vapor-liquid equilibrium, phase envelope, dew point and bubble point (even for multi-component mixtures) can be calculated with high accuracy. The organic substances modeled include the elements C, H, O, N, S and Cl with the properties also calculated from seven-term NASA polynomial fits of the data tables by Barin and Platzki (1995). Additionally, 41 inorganic substances are included, composed of the elements Al, Ca, Cl, Co, Cu, Fe, K, Mg, Mn, Na, Ni, S, Si, Ti, Zn and Zr with property data taken from Barin and Platzki (1995). This allows for modeling of nearly all the oxygen carrier materials used in chemical looping processes.

Thermodynamic equilibrium formulation

The thermodynamic equilibrium of a chemical reaction is reached when any further change in the composition would increase the Gibbs free enthalpy. This means that the chemical equilibrium of a reaction is found by minimization of the Gibbs free enthalpy.

$$G \rightarrow min \qquad \text{(eqn. 3-16)}$$

The equilibrium constant K_p of a reaction, assuming ideal substances, is a function of temperature only and is found via minimization of the Gibbs free enthalpy.

$$\ln\big(K_p(T)\big) = -\frac{\Delta G_R^0(T)}{R \cdot T} \qquad \text{(eqn. 3-17)}$$

With the general form of a reaction equation

$$\sum_{\mathrm{i}} \nu_i \cdot A_i = 0 \qquad \text{(eqn. 3-18)}$$

where A_i are all the species taking part in the reaction and ν_i are the stoichiometric coefficients, with ν_i being negative for reactants and positive for reaction products. The equilibrium constant K_p expressed by the equilibrium partial pressures p_i^* then is defined by

$$K_p = \prod_i p_i^{*\nu_i} \qquad \text{(eqn. 3-19)}$$

The actual state of a gas composition with respect to the thermodynamic equilibrium of a specified chemical reaction is determined by relating the actual composition to the chemical equilibrium composition. This is expressed by formulating the logarithmic deviation from the equilibrium $p\delta_{eq}$

$$p\delta_{eq}(p_i, T) = \log_{10} \frac{\prod {p_i}^{\nu_i}}{\prod p_i^{*\nu_i}} = \log_{10} \frac{\prod {p_i}^{\nu_i}}{K_p(T)} \qquad \text{(eqn. 3-20)}$$

Negative values of $p\delta_{eq}<0$ mean that the actual composition has a surplus of reactants where $\nu_i<0$, i.e. the reaction did approach the equilibrium and further reaction in the direction of the products is thermodynamically possible. A positive value of $p\delta_{eq}>0$ means that the actual composition has an excess of reaction products where $\nu_i>0$ which indicates that the reaction can only proceed towards the reactants. Thermodynamic equilibrium is prescribed by setting the logarithmic deviation from the equilibrium to zero ($p\delta_{eq} = 0$), which requires adjustment of the actual composition to reach a state of minimal Gibbs free enthalpy. This formulation of chemical equilibrium allows for comfortable handling of chemical equilibria in modeling.

Modeled chemical reactions

The AET-Lib includes six main redox systems basing on Cu, Fe, Mn, Ni, Co and CaS. Practically, any kind of redox reaction including these elements can be described since the thermodynamic data are accessible. A list of the included redox systems is provided in Table 3-1.

Table 3-1 Redox systems implemented in the AET-Lib.

Cu	Fe	Mn	Ni	Co	CaS
Cu/CuO	Fe/FeO	Mn/MnO	Ni/NiO	Co/CoO	$CaS/CaSO_4$
Cu/Cu_2O	FeO/Fe_3O_4	MnO/Mn_3O_4	Support material implemented: Al_2O_3, $CaAl_2O_4$, $MgAl_2O_4$, $CuAl_2O_4$, $NiAl_2O_4$, SiO_2, TiO_2, ZrO_2		
Cu_2O/CuO	Fe_3O_4/Fe_2O_3	Mn_3O_4/Mn_2O_3			
		Mn_2O_3/MnO_2			

While in the air reactor the oxidation reaction

$$MeO_{\alpha-1} + \frac{1}{2}O_2 \rightleftharpoons MeO_\alpha \qquad \text{(reac. 3-1)}$$

is formulated directly from the fuel reactor reactions

$$C_xH_yO_z + (x-z)MeO_\alpha \rightleftharpoons xCO + \frac{y}{2}H_2 + (x-z)MeO_{\alpha-1} \qquad \text{(reac. 3-2)}$$

$$CO + MeO_\alpha \rightleftharpoons CO_2 + MeO_{\alpha-1} \qquad \text{(reac. 3-3)}$$

$$H_2 + MeO_\alpha \rightleftharpoons H_2O + MeO_{\alpha-1} \qquad \text{(reac. 3-4)}$$

that have to be separated into more elementary steps. Conversion of hydrocarbons (CH_4, C_2H_4, C_2H_6 and C_3H_8) is described by prescribing conversion rates, since thermodynamic equilibrium will

lead to full conversion at typical chemical looping operating temperatures and atmospheric pressure. Oxidation of CO and H_2 is determined by using the CO-shift reaction and direct oxidation of CO with the oxygen carrier.

$$CO + H_2O \overset{cat.}{\longleftrightarrow} CO_2 + H_2 \qquad \text{(reac. 3-5)}$$

$$CO + MeO_\alpha \rightleftharpoons CO_2 + MeO_{\alpha-1} \qquad \text{(reac. 3-6)}$$

For cases with no CO in the fuel reactor, the direct oxidation of H_2 (reac. 3-4) is modeled instead of reactions (reac. 3-5) and (reac. 3-6). Alternatively, for chemical looping reforming, the steam reforming reaction is included.

$$C_xH_y + xH_2O \overset{cat.}{\longleftrightarrow} xCO + \left(x + \frac{y}{2}\right) H_2 \qquad \text{(reac. 3-7)}$$

It is important to note that this simplified reaction scheme requires experimental validation to allow for sound conclusions.

3.2.4 Definition of relevant parameters

The performance of chemical looping systems with respect to combustion efficiency is described by the use of two significant parameters: the fuel specific conversion and the carbon dioxide yield.

The fuel specific conversion X_i indicates the extent to which a specific fuel compound is converted in the fuel reactor. It is determined by relating the flow of the fuel compound in the fuel reactor exhaust $\dot{m}_i|_{FR\ exhaust}$ to the fuel compound in the fuel reactor feed $\dot{m}_i|_{FR\ feed}$. Full conversion of a specific fuel thus means that the conversion reaches 100%.

$$X_i = 1 - \frac{\dot{m}_i\big|_{FR\ exhaust}}{\dot{m}_i\big|_{FR\ feed}} \qquad \text{(eqn. 3-21)}$$

For natural gas, the most important fuel specific conversion is methane conversion X_{CH4} describing how much of the CH_4 in the fuel reactor is converted to species other than CH_4.

$$X_{CH_4} = 1 - \frac{\dot{m}_{CH_4}\big|_{FR\ exhaust}}{\dot{m}_{CH_4}\big|_{FR\ feed}} \qquad \text{(eqn. 3-22)}$$

Note that a value of 100% for X_i does not mean complete conversion of the fuel, since X_i only describes the specific conversion of a species *i* to any other species, including species other than CO_2.

The carbon dioxide yield Y_{CO2} is an indicator of the completeness of fuel combustion. The carbon dioxide yield is determined by the amount of CO_2 in the fuel reactor exhaust $\dot{V}_{CO2}|_{FR\ exhaust}$ compared to the theoretical amount of CO_2 $\dot{V}_{CO2}|_{FR\ exhaust\text{-}theoretic}$ when complete conversion of the fuel is reached. For completeness, the amount of CO_2 in the fuel $\dot{V}_{CO2}|_{FR\ feed}$ has to be considered.

$$Y_{CO_2} = \frac{\dot{V}_{CO_2}\big|_{FR\ exhaust} - \dot{V}_{CO_2}\big|_{FR\ feed}}{\dot{V}_{CO_2}\big|_{FR\ exhaust-theoretic}} = \frac{\dot{V}\cdot y_{CO_2}\big|_{FR\ exhaust} - \dot{V}\cdot y_{CO_2}\big|_{FR\ feed}}{\dot{V}\cdot \sum_{i=1}^{n} \nu_{CO_2,i}\cdot y_i\big|_{FR\ feed}} \qquad \text{(eqn. 3-23)}$$

The capability of the process to convert the energy input by the fuel into thermal energy is expressed by the combustion efficiency η_{comb}, where a value of 100% means complete conversion.

$$\eta_{comb} = \frac{P_{fuel} - P_{exhaust}}{P_{fuel}} = 1 - \frac{\dot{V} \cdot LHV\big|_{exhaust}}{\dot{V} \cdot LHV\big|_{fuel}} = 1 - l_u \qquad \text{(eqn. 3-24)}$$

The definition of η_{comb} includes the losses due to unburnt fuel l_u, which is a well-known characteristic parameter in power plant performance characterization.

$$l_u = \frac{P_{exhaust}}{P_{fuel}} = \frac{\dot{V} \cdot LHV\big|_{exhaust}}{\dot{V} \cdot LHV\big|_{fuel}} = 1 - \eta_{comb} \qquad \text{(eqn. 3-25)}$$

The oxygen supplied in chemical looping systems has to be adapted accordingly to meet the specific requirements of the oxygen carrier. For this reason, the commonly used definition of the air/fuel ratio λ is adapted to chemical looping systems by relating the oxygen flow to the air reactor to the oxygen required for complete combustion of the fuel.

$$\lambda = \frac{O_{2-available}}{O_{2-necessary}} = \frac{\dot{m}_{O_2}\big|_{AR\ inlet}}{\dot{m}_{O_2,FR-fuel}\big|_{FR\ inlet}} \qquad \text{(eqn. 3-26)}$$

X_i, Y_{CO2}, η_{comb}, l_u and λ comprise a comprehensive set of parameters that effectively describe the performance and operating conditions of a chemical looping system.

The performance of heat and power cogeneration plants is determined in the following according to the VDI guideline for power plants (VDI, 2003, 2005). One difficulty when evaluating the efficiency of such plants is the appearance of different types of useable energies, namely thermal energy and electrical energy. This is because the quality of electrical energy is considerably different than the quality of thermal energy, for example in district heating. Additionally, depending on the site and location, the monetary value of both can differ significantly. Thus, the optimal operation of such plants depends strongly on the conditions of the local demand.

The boiler efficiency η_b describes the performance of the boiler itself. It includes information on the ability of the boiler to convert the chemical energy input by the fuel P_{fuel} into thermal energy in the water/steam $\dot{Q}_{wat/st}$.

$$\eta_b = \frac{\dot{Q}_{wat/st}}{P_{fuel}} = \frac{\dot{m}_{wat/st} \cdot \left(h_{wat/st} - h_{BFW}\right)}{\dot{V}_{fuel} \cdot LHV_{fuel}} \qquad \text{(eqn. 3-27)}$$

To assess the efficiency of the steam cycle (steam turbine and district heating cycle), the energy output in the form of district heating and net electricity is related to the energy input by the water/steam coming from the boiler. This gives the process efficiency η_p.

$$\eta_p = \frac{\dot{Q}_{DH} + \sum P_{el,i}}{\dot{Q}_{wat/st}} = \frac{\dot{Q}_{DH} + \sum P_{el,i}}{\dot{m}_{wat/st} \cdot \left(h_{wat/st} - h_{BFW}\right)} \qquad \text{(eqn. 3-28)}$$

The product of the boiler efficiency η_b and the process efficiency η_p is the fuel utilization factor ω.

$$\varpi = \eta_b \cdot \eta_p = \frac{\dot{Q}_{DH} + \sum P_{el,i}}{P_{fuel}} = \frac{\dot{Q}_{DH} + \sum P_{el,i}}{\dot{V}_{fuel} \cdot LHV_{fuel}} \quad \text{(eqn. 3-29)}$$

As a criterion for evaluation, the information of ω is limited to the quantification of energetic loss. In heat and power cogeneration, it is useful to consider each, i.e. district heating and electricity, separately to make a clearer difference between the efficiency of the power plant and the boiler. These variables are thermal efficiency η_{th} and electric efficiency η_{el}.

$$\eta_{th} = \frac{\dot{Q}_{DH}}{P_{fuel}} = \frac{\dot{m}_{DH} \cdot \left(h_{DH,s} - h_{DH,r}\right)}{\dot{V}_{fuel} \cdot LHV_{fuel}} \quad \text{(eqn. 3-30)}$$

$$\eta_{el} = \frac{\sum P_{el,i}}{P_{fuel}} = \frac{\sum P_{el,i}}{\dot{V}_{fuel} \cdot LHV_{fuel}} \quad \text{(eqn. 3-31)}$$

It follows that the sum of η_{th} and η_{el} equals ω.

$$\varpi = \eta_{th} + \eta_{el} \quad \text{(eqn. 3-32)}$$

When comparing cogeneration plants and power stations, it must be kept in mind that when extracting heat for heating purposes from steam power stations, the generation of electrical energy is reduced. The relation of generated electricity and heat is called the power index of the combined heat and power plant σ_{CHP}.

$$\sigma_{CHP} = \frac{\sum P_{el,i}}{\dot{Q}_{DH}} \quad \text{(eqn. 3-33)}$$

The inverse of σ_{CHP} is called the heat index of the combined heat and power plant ϕ_{CHP}.

$$\Phi_{CHP} = \frac{\dot{Q}_{DH}}{\sum P_{el,i}} = {\sigma_{CHP}}^{-1} \quad \text{(eqn. 3-34)}$$

Often, when evaluating the performance of a cogeneration plant, the electric efficiency is weighted to account for the difference in the quality of the energies. Therefore, the effective efficiency η_{eff} is introduced. It is an extension of the fuel utilization factor ω where the electricity is weighted by σ.

$$\eta_{eff} = \eta_{th} + \sigma \cdot \eta_{el} \quad \text{(eqn. 3-35)}$$

In addition to the thermodynamic analysis, an economic evaluation is inevitable when comparing combined heat and power plants.

3.3 Site conditions and selected chemical looping parameter values

Chemical looping combustion performance parameters

In a chemical looping combustion system, the fuel combustion efficiency to CO_2 is subjected to uncertainties. Achievable fuel conversion rates can vary strongly depending on, gas-solids contact efficiency and time, solids inventory and distribution in the system, oxygen carrier age distribution, the solids circulation rate and many other parameters. This means that it is hard to predict the performance of chemical looping combustion at the next scale since the reactor

system behavior may differ significantly from the laboratory pilot to the demonstration scale. For this reason, three cases are considered.

- An experimental related case ① where fuel conversion is considered which has been determined in experiments at the 140 kW chemical looping pilot at the Vienna University of Technology,
- an ideal case ② where chemical equilibrium in the fuel reactor exhaust is assumed, and
- an average case ③ where the fuel conversion is assumed to be the arithmetic average of ① and ②.

It is expected that the performance data determined by case ① will underestimate the performance at the demonstration scale. This is because, in the chemical looping testing pilot, the riser heights are low with respect to typical circulating fluidized beds; the air reactor has a height of 4 m and the fuel reactor a height of 3 m. Furthermore, solids inventories in such small units are considerably less than in large scale units. Gas residence time and gas-solids contact time therefore are significantly less in the laboratory pilot than in a respective demonstration plant. The limited reaction time in the pilot setup is expected to restrict the combustion performance.

While the data determined in case ② represent the theoretical potential of chemical looping combustion systems, case ③ can be used as a basis for the determination of bulk dimensions such as reactor cross-sections and heat exchanger dimensions.

Oxygen carrier definition

The oxygen carrier is a key issue in chemical looping processes. Adequate selection is critical for successful demonstration of the chemical looping combustion technology. In addition to the general requirements for oxygen carriers, listed in Section 2.3.5 *"Oxygen carrier"* (p. 17), it is important to use an oxygen carrier which has been tested intensively and, thus, can be considered be to mature. For gaseous fuels, the most investigated oxygen carriers are based on nickel and show, in general, excellent performance. Among these, a physical mixture of two nickel-based oxygen carriers has shown outstanding properties in terms of fuel conversion and endurance. The mixture is so far the most intensively tested oxygen carrier with in total, with more than thousand hours in continuous chemical looping operation, at scales of up to 140 kW (Bolhàr-Nordenkampf et al., 2009b; Kolbitsch et al., 2009a; Linderholm et al., 2009; Kolbitsch et al., 2010). The first ingredient of the mixture, in the following designated NiO-VITO I, is a nickel oxide (NiO) supported by nickel aluminate ($NiAl_2O_4$) which shows high fuel conversions and high oxygen carrying capacity R_0 but a limited activity towards methane conversion (in Jerndal et al. (2010) compare to NOV1T1450sd). The second oxygen carrier, in the following designated NiO-VITO II, is a nickel oxide where a part of the nickel on the inert support ($NiAl_2O_4$) is substituted by magnesium, forming $MgAl_2O_4$. Jerndal et al. (2009) reported that the magnesium in the inert support decreases oxygen diffusion at the oxygen carrier surface, generating free nickel sites at the oxygen carrier surface. These sites promote the methane steam reforming reaction, significantly improving the methane conversion X_{CH4}. By this, the effective oxygen carrying capacity R_0 is limited. More specific details on the oxygen carrier NiO-VITO II can be found elsewhere (in Jerndal et al. (2009) compare to S1T1400). Mixing these two oxygen carriers in a ratio of 1:1, based on weight, promotes a synergetic effect where NiO-VITO II acts as a reforming catalyst while NiO-VITO I is responsible for the conversion of the steam reforming reaction products (CO and H_2). An overview of the oxygen carrier characteristics is provided in Table 3-2. More detailed

information can be found in Appendix Section 12.1 (p. 159), including information on the particle size distribution.

Table 3-2 Key oxygen carrier properties.

Item	Symbol	NiO-VITO I	NiO-VITO II	1:1 mixture	Unit
Support material	-	$NiAl_2O_4$	$NiAl_2O_4$ + $MgAl_2O_4$	$NiAl_2O_4$, $NiAl_2O_4$ + $MgAl_2O_4$	-
Active nickel oxide content	-	40	41.3	40.6	wt%
Mean particle diameter	d_p	149	129	139	µm
Apparent density	ρ_p	3600	3250	3425	kg/m^3

The performance data used in case ② were determined by testing the oxygen carrier mixture in the 140 kW chemical looping pilot. A summary of the relevant experimental parameters and conditions is given in Table 3-3.

Table 3-3 Relevant experimental conditions and data measured in the 140 kW chemical looping pilot at the Vienna University of Technology using a physical mass-based 1:1 mixture of the NiO-VITO I and NiO-VITO II oxygen carriers.

Item	Symbol	Value	Unit
Fuel	-	natural gas	-
Fuel reactor exhaust gas temperature	ϑ_{FR}	905	°C
Air reactor exhaust gas temperature	ϑ_{AR}	907	°C
Methane conversion	X_{CH4}	99.39	%
CO_2 yield	Y_{CO2}	92.2	%
Change in degree of oxidation in the fuel reactor	ΔXs	9.94	%
Fuel reactor superficial gas velocity	Us_{FR}	2.8	m/s
Air reactor superficial gas velocity	Us_{AR}	8.1	m/s
Mean gas residence time in the fuel reactor	$\tau_{g,FR}$	1.0	s
Mean gas residence time in the air reactor	$\tau_{g,AR}$	0.5	s
Active solids inventory in the fuel reactor	$m_{s,FR}$	20.0	kg
Active solids inventory in the air reactor	$m_{s,AR}$	10.3	kg
Mean solids residence time in the fuel reactor	$\tau_{s,FR}$	17.3	s
Mean solids residence time in the air reactor	$\tau_{s,AR}$	8.9	s
Oxygen carrier global mass-flow rate	$\dot{m}_{OC}$	4170	kg/h

Site conditions and selected chemical looping combustion reactor system parameter values

At the selected site, fuel is delivered at ambient temperature and pressurized from the grid. For simplicity, the fuel is considered to be composed only of methane. Boiler feedwater is delivered saturated from the boiler feedwater deaerator. The steam grid is operated at 450°C and 65 bara, which is typical for small size power plants. The site conditions are summarized in Table 3-4 .

Table 3-4 Summary of site conditions.

Item	Symbol	Value	Unit
Fuel type	-	CH_4	-
Fuel temperature	ϑ_{fuel}	25	°C
Fuel pressure	p_{fuel}	300	mbarg
Boiler feedwater temperature	ϑ_{BFW}	105	°C
Boiler feedwater pressure	p_{BFW}	saturated water	bara
Live steam temperature	ϑ_{LS}	450	°C
Live steam pressure	p_{LS}	65	bara
Ambient conditions			
Ambient temperature	ϑ_{amb}	25	°C
Ambient pressure	p_{amb}	1013.25	mbara
Ambient relative humidity	φ_{amb}	60	%
District heating			
Supply water temperature	$\vartheta_{DH,s}$	170	°C
Return temperature	$\vartheta_{DH,r}$	70	°C

The considered size of the next scale chemical looping combustion demonstration unit is 10 MW thermal input. Chemical looping reactor system operation parameters are selected considering the experience gained from 140 kW laboratory pilot testing. The specific chemical looping reactor system operation parameters are listed in Table 3-5.

Table 3-5 Selected chemical looping combustion system parameter values.

Item	Symbol	Value	Unit
Chemical looping combustion plant thermal input (based on LHV)	P_{fuel}	10	MW
Global air/fuel ratio	λ	1.1	-
Fuel reactor gas outlet temperature	ϑ_{FR}	900	°C
Air reactor relative heat loss	$\dot{q}_{AR,loss}$	1.5	%
Fuel reactor relative heat loss	$\dot{q}_{FR,loss}$	1.5	%
Air reactor solids flux	Gs_{AR}	50	kg/m^{2}s
Air reactor riser system pressure loss	Δp_{AR}	200	mbar
Fuel reactor riser system pressure loss	Δp_{FR}	200	mbar
Mean oxygen carrier oxidation state at the air reactor outlet	Xs_{AR}	50	%

3.4 Heat integration

In chemical looping systems, the temperature in the reactors is limited by acceptable oxygen carrier operation temperatures. Therefore, excess heat has to be withdrawn from the system, which can be done at three different locations: the air reactor, the fuel reactor and heat extraction from the circulating solids. The selected system includes an air reactor equipped with water-cooled walls and a bed material cooler. While the heat extraction rate from the water-cooled wall is governed by riser hydrodynamics, the cooling duty of the bed material cooler (a bubbling bed) is controllable by using a solids flow control valve. A schematic of the setup is shown in Fig. 20. More specific details of the reactor system design and heat integration setup can be found in Chapter 4 *"Chemical looping reactor system* design*"* (p. 53).

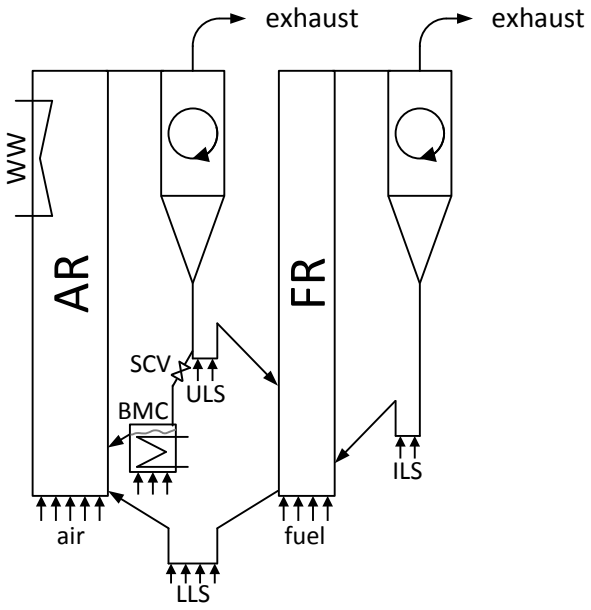

Fig. 20 Reactor system with heat exchanger arrangement based on the dual circulating fluidized bed concept. Locations where fluidization is applied are indicated by arrows. AR - air reactor, FR - fuel reactor, LLS - lower loop seal, ULS - upper loop seal, ILS - internal loop seal, BMC - bed material cooler, WW - water cooled walls, SCV - solids flow control valve.

3.5 Process integration

The process flow diagram, shown in Fig. 21, represents the entire chemical looping combustion plant, including the steam generation section, but without the steam turbine and condenser part. The input streams, i.e. fuel, air, boiler feedwater (BFW) and fluidization steam (support steam) as well as the output streams, i.e. superheated steam, AR exhaust and FR exhaust, are the system boundaries of the plant. Air is provided at ambient conditions and is preheated by air reactor exhaust gas (air ph) for energy recovery after compression (air blower) to the air reactor riser system inlet pressure. Natural gas is provided at elevated pressure and is used as the fuel. The boiler feedwater is supplied pressurized from the boiler feedwater deaerator and the boiler feedwater pump. Fluidization steam is taken from the corresponding steam cycle.

A common natural circulation steam cycle is integrated where steam is produced utilizing thermal forces to overcome the pressure drop within the evaporative heat exchanger surfaces. At the chosen operating parameters, the amount of heat produced in the reactors is greater than the sensible heat in the exhaust gas streams. Therefore, a bed material cooler (BMC) and water walls inside the air reactor (AR_clg) have been arranged to act as evaporative heat exchangers. Only a part (S3) of the elutriated solids from the air reactor (S1) are taken and directed to the bed material cooler. The solids flow rate is controlled using a hot sand valve commonly used in circulating fluidized bed applications. The setup of the heat recovery steam generator includes the air reactor and fuel reactor heat recovery boiler, the air reactor water walls and the bed material cooler. The proposed heat recovery boiler setup consists of two steam super heaters (SH_I and SH_II), two economizers (ECO_AR and ECO_FR) and a recuperative air pre-heater (air ph). To control the output steam temperature (W12), a drum heat exchanger is arranged where a part of the superheated steam is used to evaporate additional water in the drum. The quantity of steam passing the drum heat exchanger depends on the load and operating conditions. To overcome the pressure drop in the heat recovery boiler, two induct fans are used: the fuel reactor induct fan

and the air reactor induct fan (AR ID fan). The fuel reactor induct fan is not shown in Fig. 21 since it is shown in the steam cycle flow diagram in Fig. 22.

The process flow diagram of the corresponding steam cycle is provided in Fig. 22. It covers electricity production in the steam turbine, the district heating cycle and the support steam generator. Superheated steam is taken from the chemical looping combustion boiler and used in an extraction-type condensation turbine for electricity production. Steam is extracted from the steam turbine at two ports: the high pressure port (C2) and the low pressure port (C3). High pressure extraction steam is used to preheat the boiler feedwater and in the high pressure district heating heat exchanger (HP heater). Steam taken from the low pressure port is used for boiler feedwater deaeration, to produce the necessary support steam and in the low pressure district heating heat exchanger (LP heater). Using high and low pressure district heaters allows for optimized heat integration. District heat is extracted from the district heating cycle where a pump (DH pump) is placed to account for the pressure loss in the district heating cycle.

Low calorific heat is recovered from the fuel reactor exhaust gas, including the heat of condensation (FR condenser), allowing for improved process efficiency. To overcome the pressure drop in the fuel reactor heat recovery section, a fuel reactor induct fan is put in place (FR ID fan). The necessary pressure in the steam cycle is supplied by the boiler feedwater pump (BFW pump) and the low pressure pump (LP pump). To further improve the process efficiency, a boiler feedwater preheater (BFW preheater) is present, which can be used optionally.

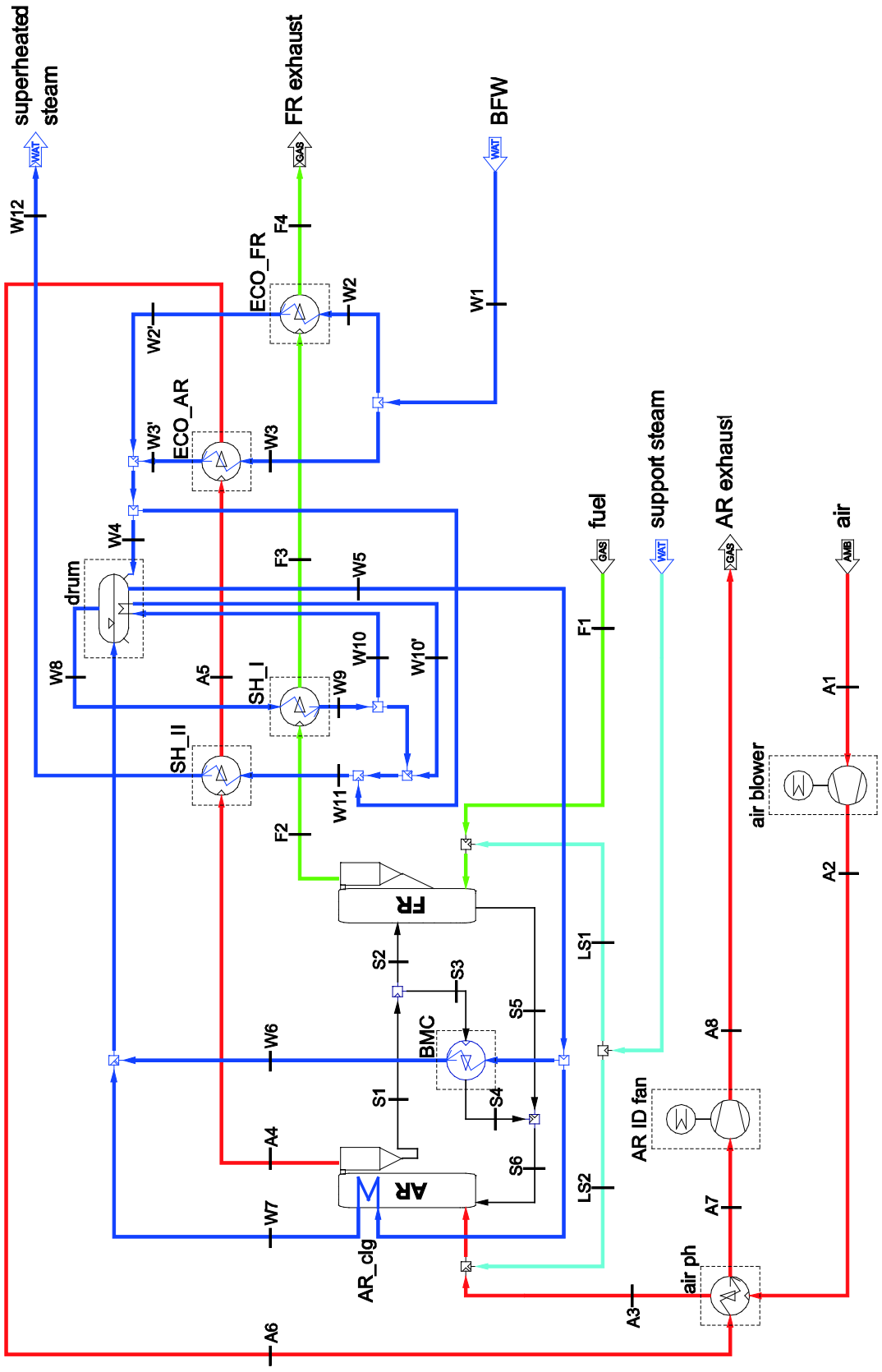

Fig. 21 Process layout of the chemical looping combustion process including the heat recovery steam generator.

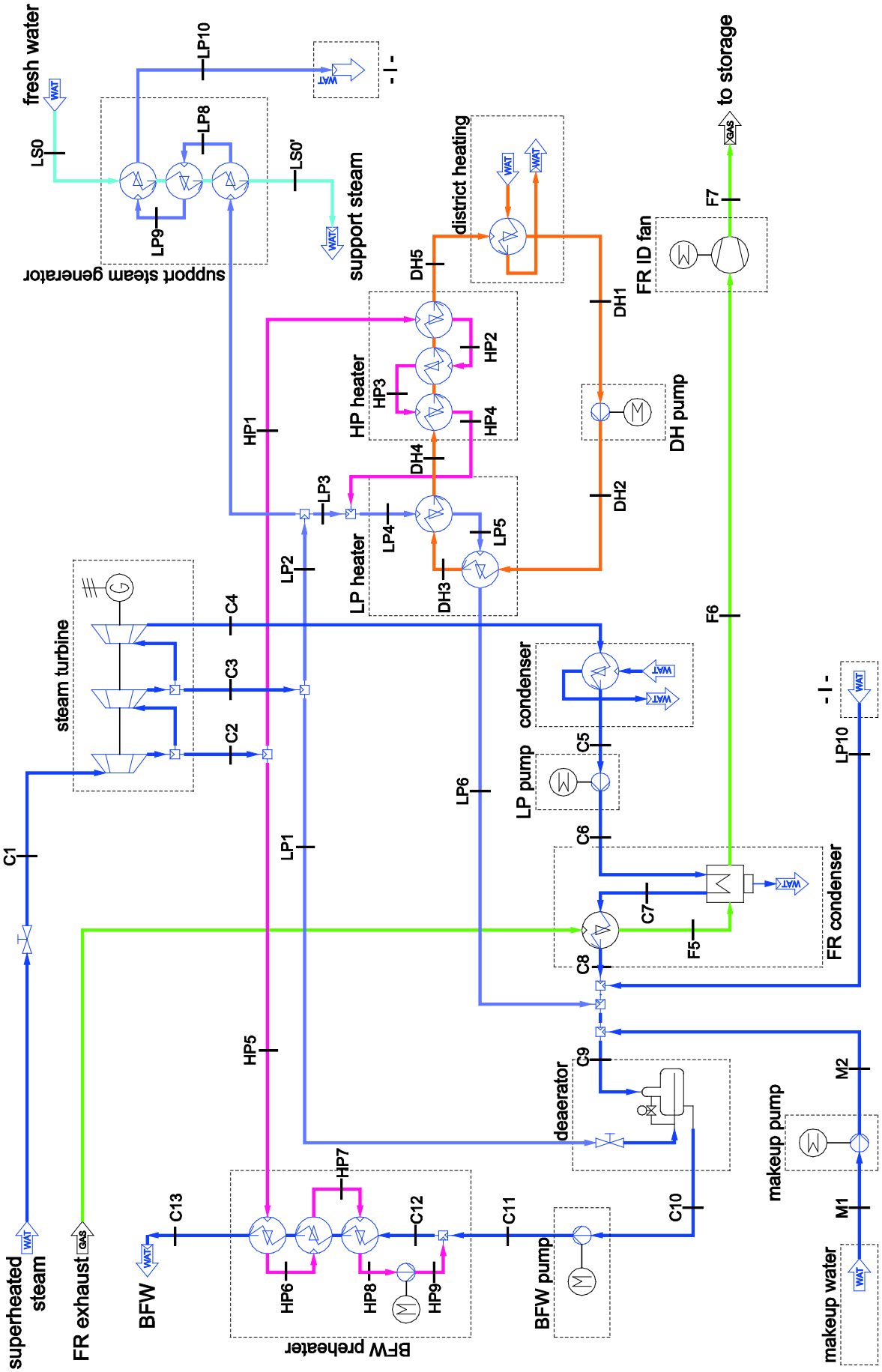

Fig. 22 Process layout of the steam and district heating cycle.

The parameters used in the mass and energy balance investigation are typical for the size of the unit; a summary is given in Table 3-6.

Table 3-6 Selected apparatus parameter values.

Item	Symbol	Value	Unit
Heat exchangers			
Superheaters pressure loss water side	$\Delta p_{SH,w}$	3	bar
Superheaters pressure loss gas side	$\Delta p_{SH,g}$	5	mbar
Economizer pressure loss water side	$\Delta p_{ECO,w}$	0.1	bar
Economizer pressure loss gas side	$\Delta p_{ECO,g}$	5	mbar
Economizer minimal temperature difference	$\Delta\vartheta_{ECO,min}$	25	°C
Recuperative air preheater pressure loss gas side	$\Delta p_{air\_ph,g}$	5	mbar
Recuperative air preheater minimal temperature difference	$\Delta\vartheta_{air\_ph}$	30	°C
FR condenser pressure loss water side	$\Delta p_{FR\text{-}cond,w}$	0.1	bar
FR condenser pressure loss gas side	$\Delta p_{FR\text{-}cond,g}$	5	mbar
FR condenser minimal temperature difference	$\Delta\vartheta_{FR\text{-}cond}$	15	°C
Steam-water heat exchangers minimal temperature difference	$\Delta\vartheta_{wat\text{-}st}$	15	°C
Steam turbine			
Isentropic efficiency first stage	$\eta_{s,I}$	88	%
Isentropic efficiency second stage	$\eta_{s,II}$	84.6	%
Isentropic efficiency third stage	$\eta_{s,III}$	84.6	%
Outlet pressure first stage	p_I	12	bar
Outlet pressure second stage	p_{II}	4	bar
Outlet pressure third stage	p_{III}	0.1	bar
Blowers			
Isentropic efficiency	$\eta_{s,ID}$	82	%
Mechanic efficiency	$\eta_{m,ID}$	100	%
Water pump			
Isentropic efficiency	$\eta_{s,p}$	85	%
Mechanic efficiency	$\eta_{m,p}$	100	%
Electric motor			
Isentropic efficiency	$\eta_{s,M}$	96	%
Mechanic efficiency	$\eta_{m,M}$	99	%
Electricity generator			
Isentropic efficiency	$\eta_{s,G}$	95	%
Mechanic efficiency	$\eta_{m,G}$	99	%
Boiler feedwater deaerator outlet temperature	$\vartheta_{BFW,dea}$	105	°C

3.6 Results

Using advanced mass and energy balance investigations allows for the determination of chemical looping combustion system parameters such as gas flow rates and performance values. This investigation is an essential basis for economic evaluation as well as for design. This includes the design of fluidized bed apparatuses, e.g. fluidized bed cross-section areas, and heat exchangers. Table 3-7 provides the relevant demonstration unit parameters useful for determining the required dimensions of the chemical looping reactor system. These parameters distinguish between the three cases, i.e. ①, ② and ③, allowing for the inclusion of deviation in combustion efficiency in the design of the unit.

Table 3-7 Summary of relevant demonstration unit parameters.

Item	Symbol	Case ①	Case ②	Case ③	Unit
Fuel thermal input power	P_{fuel}	10	10	10	MW
Methane conversion	X_{CH4}	99.39	100.0	99.70	%
CO_2 yield	Y_{CO2}	92.20	99.11	95.65	%
Fuel reactor temperature	ϑ_{FR}	900	900	900	°C
Air reactor temperature	ϑ_{AR}	949	964	955	°C
Air/fuel ratio	λ	1.1	1.1	1.1	-
Fuel flow rate	$\dot{V}_{fuel}$	1006	1006	1006	Nm^3/h
Air flow rate	$\dot{V}_{air}$	10768	10768	10768	Nm^3/h
Fuel reactor exhaust gas flow rate	$\dot{V}_{FR\text{-}exh}$	13804	13857	13830	m^3/h
Air reactor exhaust gas flow rate	$\dot{V}_{AR\text{-}exh}$	40687	40738	40649	m^3/h
Air reactor solids flux	Gs_{AR}	50	50	50	kg/m^2s
Steam production					
temperature	ϑ_{LS}	450	450	450	°C
pressure	p_{LS}	65	65	65	bara
mass-flow rate	$\dot{m}_{LS}$	11090	11879	11485	kg/s
CLC boiler system electric power demand	P_{el}	86.5	86.6	86.6	kW

Considering the three fuel conversion cases, it was found that with the proposed setup, the boiler efficiency ranges from 87.7% to 93.9%, which is the amount of steam produced in the boiler setup (see Fig. 21) referred to as the fuel input. Bearing in mind the small size of the unit, these values are in the typical range of small-scale steam boilers without carbon capture; improvements will require increasing the heat exchanger size, which in turn increases the investment costs. It is obvious that a significant amount of energy is lost via unconverted fuel (l_u), even if ideal conditions are assumed (case ②). It is expected that improvements are necessary for economically successful use of chemical looping combustion technology in the near future. Treatment of the fuel reactor exhaust is therefore crucial to the technology. One option is to separate the combustibles during compression of the fuel reactor exhaust gas by cryogenic CO_2 purification, which then can be recycled to the fuel reactor. Another possibility is to reduce the heat content of the fuel reactor exhaust in a post-combustion boiler. This requires using high purity oxygen to avoid the dilution of CO_2 by air nitrogen. Both options are costly and require either energy during CO_2 liquefaction or for producing the necessary oxygen. Mitigation of the occurrence of combustibles is therefore considered to be essential. Advanced oxygen carriers, currently being developed within the EU financed project INNOCUOUS (FP7 Contract No. 241401), are expected to be a significant driver to overcome this challenge (Jing et al., 2012; Jing et al., 2013; Källén et al., 2013). A summary of expectable demonstration unit performance values is given in Table 3-8.

Table 3-8 Expectable demonstration unit performance values.

Item	Symbol	Case ①	Case ②	Case ③	Unit
Combustion efficiency	η_{comb}	93.0	99.2	96.1	%
Losses due to unburnt fuel	l_u	6.96	0.78	3.87	%
Boiler efficiency	η_b	87.7	93.9	90.8	%

A simple energy flow diagram of case ③ is shown in Fig. 23. The values of sensible heat (sens.) are calculated with reference to 0.0°C, 1.0 bara and gaseous species. The chemically bound energy is calculated based on lower heating values and, additionally, the heat of condensation is indicated. In the energy of the water/steam streams, there is a distinction between excess energy with

reference to the boiler feedwater (e) and energy with reference to thermodynamic standard conditions (E0). This allows for a quick assessment of process performance data when relating the relative energy values in the water/steam to fuel input data.

In the energy flow diagram, the input streams, i.e. air, fuel, electricity, support steam and boiler feedwater (BFW), and the output streams, i.e. stack loss, loss (heat and mechanical losses) and superheated steam are presented. Non-utilizable energy leaves the boiler via the stack in the form of chemical energy, caused by incomplete combustion, and as sensible heat as well as reactor system heat loss and mechanical losses in the blowers. Energy is recovered prior to the stack in an air preheater allowing for efficiency improvements. As depicted, the major amount of the energy input is converted to steam. Further improvements to the process may include a reduction in losses due to unburnt fuel and improved utilization of the sensible heat of the exhaust gases.

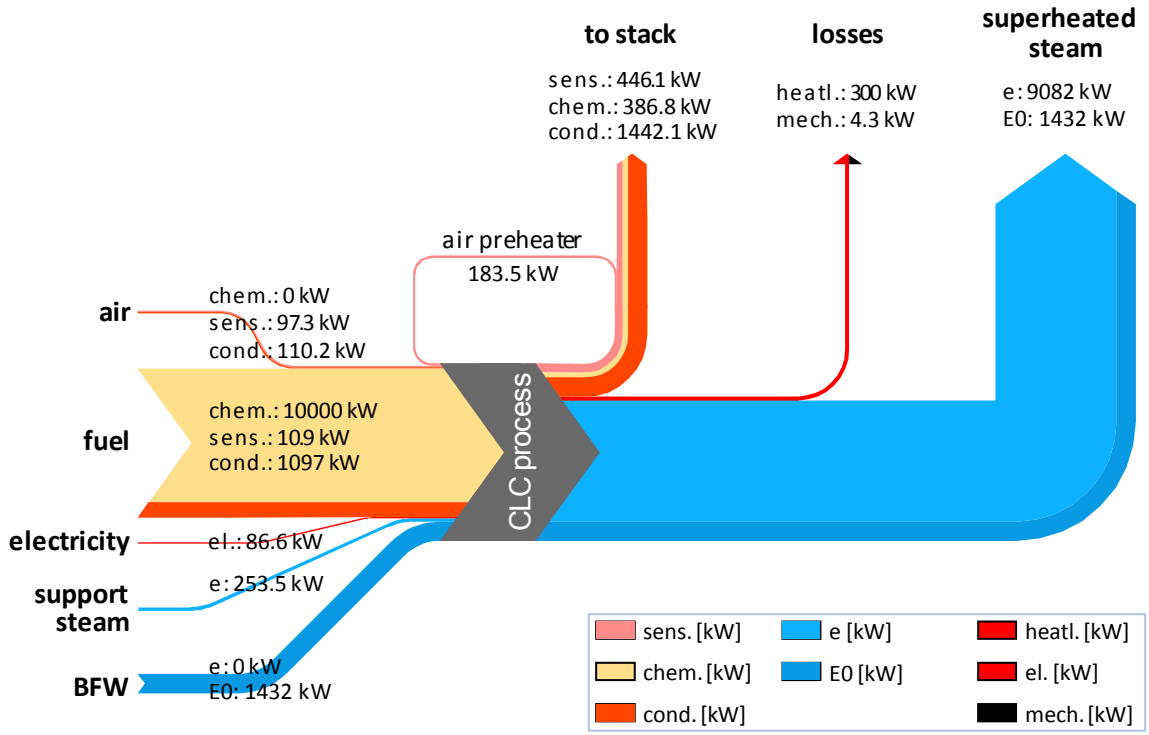

Fig. 23 Energy flow diagram of the chemical looping case ③. The values of sensible heat (sens.) are calculated with reference to 0.0°C and 1.0 bara. The values of chemical energy (chem.) are based on the lower heating value at 25.0°C and 1.0 bara. The condensation heat (cond.) reflects the energy of condensation, defined as the difference between the higher and lower heating values at 25.0°C and 1.0 bara. The values of E0 describe the energy in the water/steam streams in the state of the feedwater inlet conditions (71.2 bara/105°C) and thermodynamic data based on 0.0°C and 1.0 bara. The values of the energy (e) in the water/steam streams indicate the excess energy with reference to the boiler feedwater inlet conditions, indicating the generated steam power. The heat loss via radiation (heatl.) as well as mechanical losses (mech.) are also indicated.

The gas temperature and water/steam cycle temperature profiles for case ③ are shown in Fig. 24 as a Q-T diagram. Conservative pinch point temperatures are assumed considering the small scale of the plant. The analysis reveals that more than 50% of the totally transferred heat has to be withdrawn from the reactor system itself using the bed material cooler and the water cooled walls in the air reactor. The remaining energy leaves the system via the reactor system exhaust

gases where it is used for steam superheating and preheating of boiler feedwater in the economizers. With the chosen steam parameters, the greatest amount of energy (52.5%) is needed to evaporate the water, while only about 20% is needed for superheating. Heat recovery boiler improvement will require a reduction in the exhaust gas temperature after the fuel reactor economizer and after the air preheater. This can be achieved by a greater heat exchanger surface area or via a reduction in the temperature of the boiler feedwater, which will be discussed later. Both measures depend on an economic evaluation of the process, including the steam utilization process.

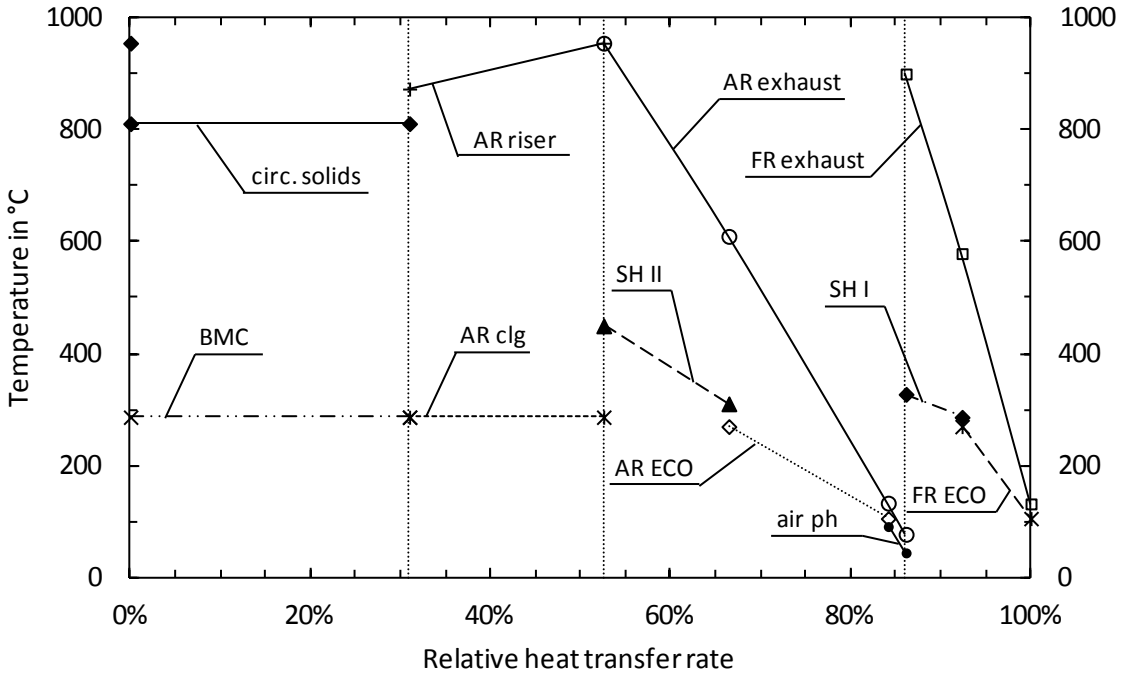

Fig. 24 Temperature profiles of the heat recovery boiler (Q-T diagram) for case ③. SH I - steam superheater I, SH II - steam superheater II, BMC - bed material cooler, AR clg - air reactor water walls, AR ECO - air reactor economizer, FR ECO - fuel reactor economizer, and air ph - air preheater.

The flow of energy in the steam cycle including the steam turbine and the district heating cycle is shown in Fig. 26. The input streams, steam and fuel reactor exhaust (FR exh), coming from the chemical looping boiler and electrical energy and the useable output streams, electricity from the steam turbine electricity generator, district heating and support steam, as well as non-useable outputs, i.e. mechanical losses, steam condenser duty and boiler feedwater are presented. Depending on the actual demand, the system allows for adaption of the ratio of district heating to the electrical energy output; this is indicated by the heat index ϕ_{CHP}. With the proposed setup, the heat index can reach values of zero, but is limited by the maximal extractable steam from the steam turbine. The sensible heat of condensation in the fuel reactor exhaust gas is used to preheat the low temperature condensate after the LP condensate pump. This allows for an improvement in the overall efficiency due to a reduction in fuel reactor stack loss.

When the steam turbine is operated without the extraction of steam, the heat index is $\phi_{CHP} = 0$ and no district heat is delivered (see Fig. 26a). In this case, the fuel utilization factor ω equals the electric efficiency η_{el} and with a steam cycle efficiency of η_p = 31.7-31.8%, the fuel utilization factor was found to be ω = 27.8-29.9%, depending on the chemical looping combustion efficiency.

The energy flow diagram with maximum heat output to the district heating cycle is shown in Fig. 26b. In this case, 7300 kW are delivered to the district heating grid and the corresponding heating index is ϕ_{CHP} = 5.4. Then, the fuel utilization factor reaches values of ω = 85.5-87.5%. It is important to note that these high values are caused by low quality energy extracted from the water/steam cycle. Such high values are typical for combined heat and power plants.

The effect of the heat index ϕ_{CHP} on the thermal efficiency η_{th}, electric efficiency η_{el} and fuel utilization factor ω for case ③ is illustrated in Fig. 25. The thermal efficiency increases with the heating index while the electric efficiency drops slightly. This is because the fuel utilization factor increases with the heat index. The fuel utilization factor value ranges from 28.8% when no heat is delivered to the district heating cycle and up to 84.5% for ϕ_{CHP} = 5.

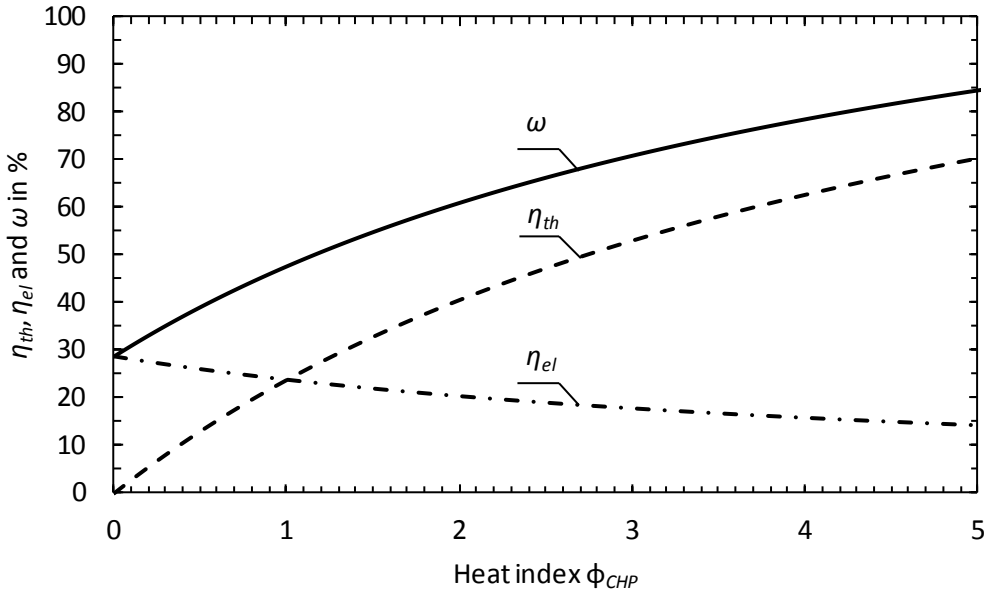

Fig. 25 Thermal efficiency η_{th}, electric efficiency η_{el} and fuel utilization factor ω depending on the heat index ϕ_{CHP} for case ③.

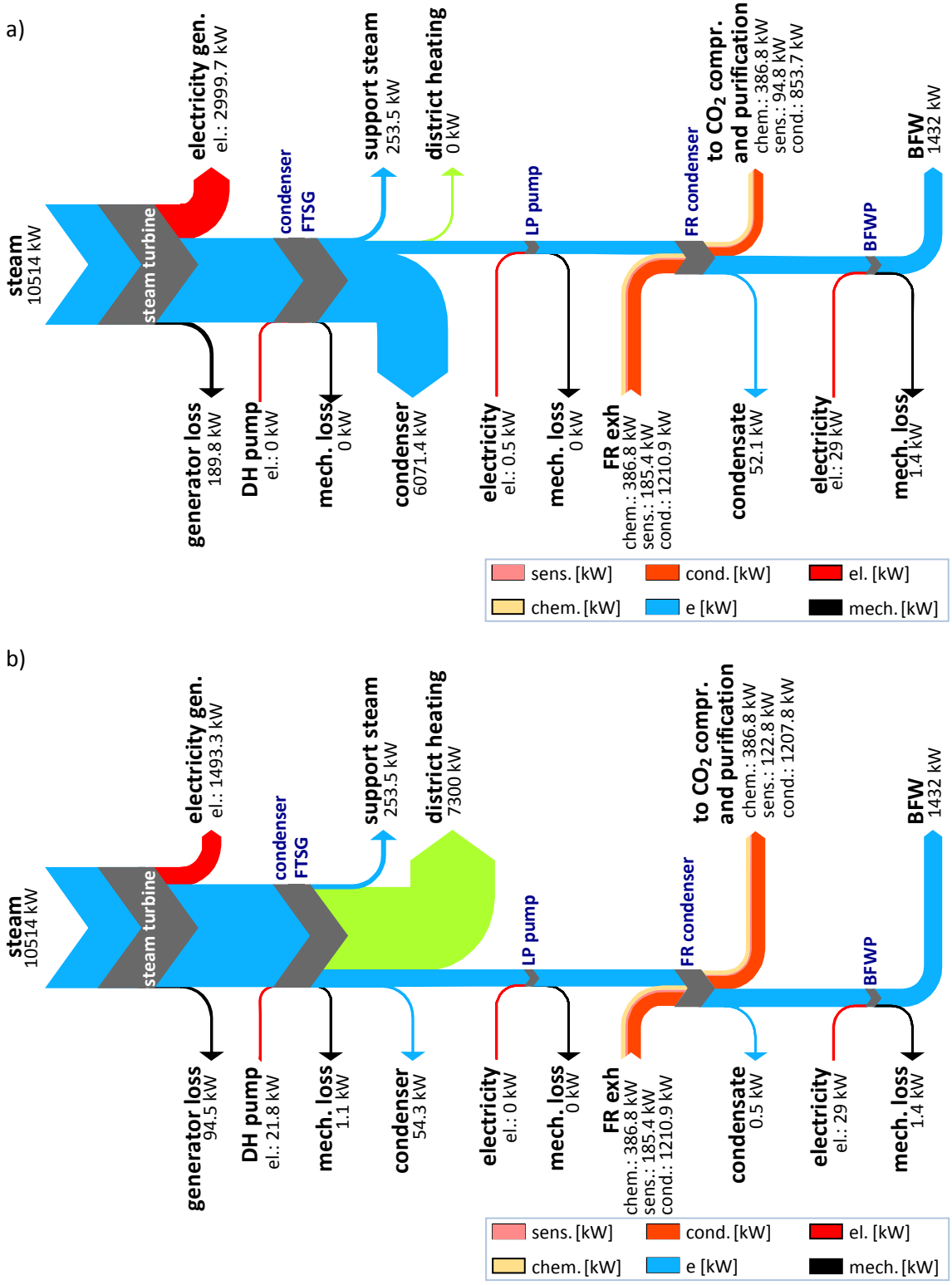

Fig. 26 Energy flow diagram of the steam and district heat generation for chemical looping case ③. Depicted in a), the process operated in power production mode and in b) in combined heat and power production mode with maximum district heat production. The values of sensible heat (sens.) are calculated with reference to 0.0°C and 1.0 bara. The values of chemical energy (chem.) are based on the lower heating value at 25.0°C and 1.0 bara. The condensation heat (cond.) reflects the energy of condensation, and is the difference between the higher and lower heating values at 25.0°C and 1.0 bara. The energy in the water/steam streams (e) is calculated with reference to the thermodynamic standard conditions (0.0°C and 1.0 bara). el. - electrical energy, mech. - mechanical energy.

3.6.1 Part load operation

In chemical looping combustion systems, the energy to be withdrawn from the reactors has to be adapted accordingly to keep the desired reactor temperatures. The energy extraction rate depends on the reactor temperatures, the air/fuel ratio, the combustion efficiency of the chemical looping process and the total thermal energy input. While the reactor temperature and combustion efficiency is an extensive process parameter, the air/fuel ratio can be set arbitrarily. In general, the energy to be extracted from the reactor system decreases with a rising air/fuel ratio and lower combustion efficiency.

In the proposed reactor system arrangement, the heat extraction rate can be influenced through the air/fuel ratio and through solids flow to the bed material cooler. This flow of solids is controlled using the solids flow control valve. The heat extraction rate from the bed material cooler increases with solids flow through the heat exchanger. This allows for controlling the energy balance and operation in part load when the necessary heat extraction rate from the chemical looping system diminishes. To quantify the amount of solids flowing to the bed material cooler, the solids split-up ratio X_{BMC} is defined.

$$X_{BMC} = \frac{\dot{m}_{BMC}}{\dot{m}_{s,AR}} \qquad \text{(eqn. 3-36)}$$

X_{BMC} describes the amount of solids flowing to the bed material cooler $\dot{m}_{BMC}$ relative to the total amount of solids entrained from the air reactor passing through the upper loop seal downcomer $\dot{m}_{s,AR}$. Given that proper loop seal operation requires keeping a certain solids level in the loop seal, in practice, X_{BMC} is limited. To maintain continuous operation, X_{BMC} is additionally limited by the necessary oxygen transport to the fuel reactor.

A part load operation diagram for case ③ is given in Fig. 27 to map the operating range of the reactor system setup. It shows how the solids flow to the bed material cooler X_{BMC} has to be adapted for a given fuel input, air/fuel ratio λ and fuel reactor temperature ϑ_{FR}. For high fuel inputs, X_{BMC} has to be increased to adapt the energy balance of the system. However, high air/fuel ratios can compensate an increment of X_{BMC} by increasing the sensible heat at the air and fuel reactor exit. Furthermore, the diagram shows how the air reactor gas exit temperature ϑ_{AR} and the superficial gas velocity in the air reactor Us_{AR} adapt to changes in reactor system operation. It was found that, at an air/fuel ratio of $\lambda = 1.1$ and a fuel power input of 10 MW, the air reactor temperature is expected to be $\vartheta_{AR} = 955$°C and approximately 30% (i.e. X_{BMC}) of the solids entrained by the air reactor have to pass through the bed material cooler.

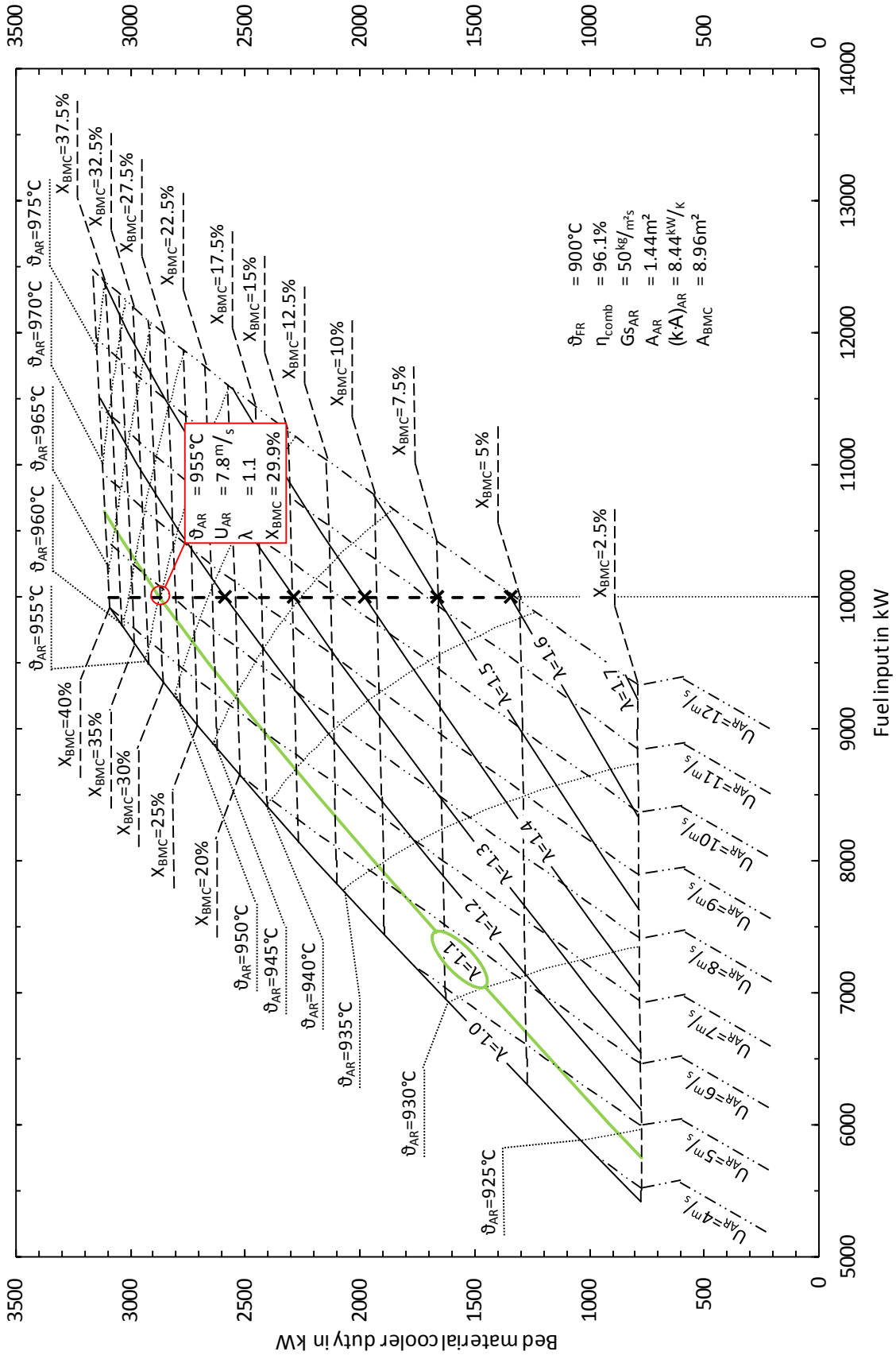

Fig. 27 Part load diagram of the chemical looping combustion plant with the combustion efficiency in case ③ and the design operating point indicated.

3.6.2 Overall process optimization potential

While the chemical looping system performance itself is characterized by the combustion efficiency of the process, the setup of the overall process can be optimized with respect to efficiency. Boiler setup efficiency depends on the ability to transfer thermal energy to steam. Generally, boiler efficiency increases with lower loss of sensible heat through the stack. This means that it is necessary to reduce the stack entrance temperature as much as possible. This can be achieved by the use of preheaters, e.g. an air preheater, larger heat exchanger surfaces, i.e. an economizer, and or by lower boiler feedwater temperatures. In any case, the process efficiency of the water/steam cycle η_p increases with increased mean temperature of the heat supply. This temperature can be increased by shifting energy from the steam to the feedwater by use of recuperative boiler feedwater preheating or increased boiler feedwater deaerator pressure. Fig. 28 and Fig. 29 show the dependence of the boiler and process efficiency, the fuel utilization factor and the relative improvement of the fuel utilization factor for standalone power generation ($\phi_{CHP} = 0$). While the boiler efficiency decreases with deaerator pressure and boiler feedwater temperature, an over-proportional increase in process efficiency occurs. Therefore, the fuel utilization factor is also improved. Hence, when applicable, boiler feedwater preheating and deaerator pressure should be increased for improved overall process operation.

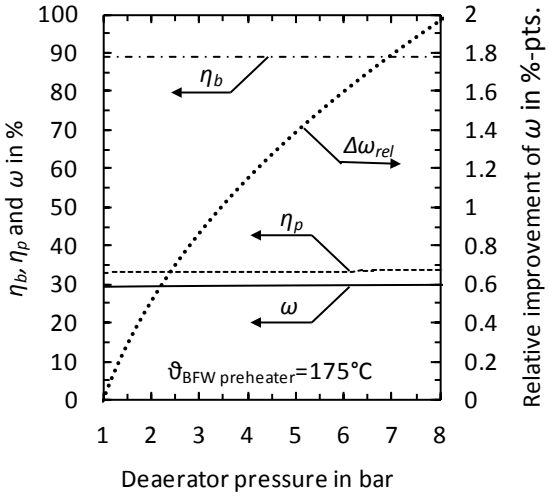

Fig. 28 Boiler efficiency η_b, process efficiency η_p, fuel utilization factor ω and relative improvement of the fuel utilization factor $\Delta\omega_{rel}$ depending on the deaerator pressure at a boiler feedwater preheater exit temperature of 175°C and a heat index of $\phi_{CHP} = 0$.

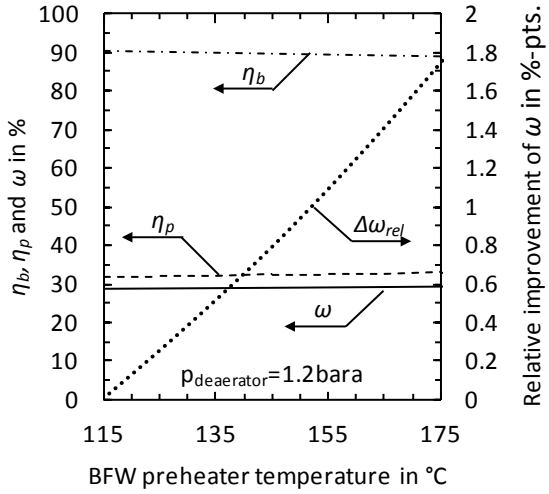

Fig. 29 Boiler efficiency η_b, process efficiency η_p, fuel utilization factor ω and relative improvement of the fuel utilization factor $\Delta\omega_{rel}$ depending on the boiler feedwater preheater exit temperature at a deaerator pressure of 1.2 bara and a heat index of $\phi_{CHP} = 0$.

3.7 Summary and discussion

The potential next scale of the chemical looping combustion process at 10 MW thermal input using gaseous fuels was integrated into a commercial natural gas combined cycle plant with supplementary firing before the heat recovery section. The attached chemical looping combustion demonstration unit was designed to substitute the energy input of supplementary firing, which in turn can easily compensate for fluctuations in demonstration plant operation with very little response time. The chemical looping combustion demonstration unit is integrated into the existing infrastructure and shares the water steam cycle with the existing plant, allowing for a

significant reduction in chemical looping combustion demonstration-related costs. At the selected site, heat for district heating and power is produced by cogeneration, allowing for high utilization of the fuel.

To account for the uncertainties in the expectable fuel conversion performance when going from the laboratory to the industrial scale, three cases have been considered:

- Case ①: Chemical looping combustion operation experience at 140 kW pilot testing is used to determine expectable process combustion efficiency.
- Case ②: Ideal performance of chemical looping combustion is determined by assessing the chemical equilibrium in the fuel reactor.
- Case ③: The combustion efficiency is selected by the arithmetic mean between case ① and ②.

It is expected that case ① represents a worst case scenario with respect to process performance considering the short residence time of the gas in the relative short risers of the 140 kW pilot at the Vienna University of Technology. In the demonstration unit, the overall performance is believed to increase given a tall fuel reactor riser where gas-solids contact times are greater. To allow the demonstration unit to be flexible with respect to fuel conversion, case ③ is expected to be the most meaningful for the selection of reactor and heat exchanger dimensions.

The selected oxygen carrier, which is a key issue in chemical looping, is based on nickel as this specific type is the one best known and most promising carriers for gaseous fuels. The oxygen carrier is supported by nickel-aluminate and magnesium-aluminate with an active nickel content of 40.6 wt%.

By detailed mass and energy balance investigations, it was found that the chemical looping boiler efficiency can reach values of 87.7% to 96.1%, which is the amount of steam produced in the boiler setup relative to the thermal energy input by the fuel (based on LHV). Bearing in mind the small size of the unit, these values are in the typical range of small-scale steam boilers without carbon capture. Improvement will require increased heat exchanger size which in turn increases the investment costs. However, there is a significant amount of energy lost due to incomplete combustion. This is true in case ③, i.e. 3.87% of the chemical energy remains in the fuel reactor exhaust. The energy penalty is expected to be barely tolerable for economically successful operation of the chemical looping combustion process. Treatment of the fuel reactor exhaust is therefore crucial to make use of the energy. One option is to separate the combustibles during compression of the fuel reactor exhaust gas by cryogenic CO_2 purification. This then can be recycled to the fuel reactor. Another possibility is to reduce the heat content of the fuel reactor exhaust in a post-combustion boiler. This requires using high purity oxygen to avoid the dilution of CO_2 by air nitrogen. Both options are costly and require either considerable amounts of energy during CO_2 liquefaction or to produce the necessary oxygen. Advanced oxygen carriers, currently being developed within the EU financed project INNOCUOUS (FP7 Contract No. 241401), are expected to be a significant driver to overcome this challenge. However, although it is expected that there will be a certain amount of fuel left in the fuel reactor exhaust, the calculated efficiencies are high considering that the setup is carbon capture and storage ready.

The chemical looping combustion reactor system setup has been investigated with part load operation. The proposed arrangement of heat exchangers, i.e. the bed material cooler and water

walls in the air reactor, allow for operation of the plant over a wide operating range. The system can easily handle loads from 55% to more than 110% referring to nominal load (10 MW).

The setup of the water/steam cycle allows for flexible adaption of the ratio of useable heat (district heating) to power output. The fuel utilization factor can range from 27.8-29.9% in single power generation or 85.5-87.5% for combined heat and power generation.

The overall setup (chemical looping boiler and water/steam cycle) performance optimization potential has been investigated. Shifting energy from the steam to the water in the water/steam cycle allows for an improvement in the overall process by increasing the mean temperature of the heat supply. This can be achieved by recuperative boiler feedwater preheating or increased boiler feedwater deaerator pressure.

The investigation reveals that even with nickel-based oxygen carriers, the chemical looping combustion process has a high potential for carbon capture and storage. The performance loss can potentially be as low as 0.78% in terms of sensible heat loss when the combustion proceeds ideally (thermodynamic equilibrium in the fuel reactor with NiO/Ni as the governing redox system). This is comparable to standard steam boiler technology without carbon capture. Demonstration of the technology at the industrial scale is crucial to gain sufficient confidence in chemical looping combustion up-scaling.

4 Chemical looping reactor system design

4.1 Introduction

Apart from the oxygen carrier material, the design of the reactor system is a key issue in chemical looping applications. In the development of a successful reactor system, it is necessary to consider the specific requirements of the process, which are discussed in the following section.

It is required that the driving forces for the reaction of both gas and solids should be high, thus promoting conversion rates. While solids conversion is governed by the composition of the gas surrounding the oxygen carrier, gas conversion is limited by the presence of reactive oxygen. The oxygen can be available in the solid phase within the oxygen carrier or as gaseous O_2 for CLOU particles. Therefore, excellent gas and solids contact and good gas-gas mixing in both reactors as well as prolonged contact times is crucial to achieve high gas conversion rates, thus high process efficiency.

To avoid the limitation of gas conversion by oxygen availability in the fuel reactor, the oxygen delivery rate should be sufficiently high. To meet this requirement, the solids circulation rate between the air reactor and the fuel reactor has to be sufficiently high. High solids circulation rates furthermore improve the heat transport between the reactors. For some oxygen carriers, it is, however, beneficial that a specific solids circulation rate occurs. The reactor system should be adaptable with respect to the circulation rate to agree with the specific requirements of the oxygen carrier.

Leakage from the fuel reactor CO_2 to the air reactor and the dilution of fuel reactor gas with air nitrogen must be avoided. Proper sealing between the two reactors is therefore needed. This includes avoiding direct mixing of the reactor gases and gas carryover by physical adsorption.

Since chemical looping process performance depends on the solids inventory, the reactor system has to be able to handle required solids inventories. Good flexibility of the system with respect to changed inventories is beneficial. Effective gas-solids separation at the reactor exits is necessary to keep the inventory stable over long operating periods.

The heat extraction rate from the reactor system has to be controllable to allow for part load operation. The setup should, furthermore, be stable in operation, avoiding undesirable operating conditions such as uncontrolled accumulation of solids in any part of the system.

Supplementary energy demand such as blower duty and potentially necessary sealing gas has to be minimized, which otherwise would cause a potential loss in process efficiency.

Finally, the design of the reactor system should allow for scale-up to a larger size.

This multitude of requirements is unique for chemical looping systems and, thus, presents a challenge in the design of chemical looping reactor systems. Fluidized beds which have outstanding properties with respect to gas mixing and gas-solids contact as well as heat transfer are therefore considered to best suit the requirements of chemical looping. Properly designed fluidized beds are capable of providing high solids entrainment and thus solids circulation. Apparatuses, e.g. loop seals capable of sealing gases between two zones, are commonly used in fluidized beds. Chemical looping systems are therefore a typical application of dual fluidized bed (DFB) systems where two fluidized beds are connected to each other.

This chapter describes the design of a chemical looping combustion reactor system with 10 MW fuel input based on fluidized bed technology. Applicable gas flow rates are taken the mass and energy balance investigations as described in Chapter 3 *"Process design"* (p. 23).

4.2 Fluidized bed technology

When solids, collected in a vertically aligned column, are exposed to an upwards flowing gas stream, several hydrodynamic conditions occur depending on the amount of gas. Solids remain in a fixed position (fixed bed) with very low gas flow rates. When the gas flow is increased, the ratio of weight forces relative to drag and buoyancy decreases until identity is reached where particles become fluidized. A further increase in gas flow leads to an expansion of the bed accompanied in most cases by the formation of bubbles (bubbling regime). Particles with certain properties exhibit a regime of homogenous bubble-free expansion, which is discussed later. Bubbles grow with gas velocity and axial distance from the gas injection point. For columns with a sufficiently small diameter and certain particle properties, bubbles can reach diameters close to the column diameter and a slugging regime occurs. Break-up of such large bubbles at the surface of the bed causes the bulk of particles to freely fall onto the top of the bed, provoking large pressure fluctuations. This may cause serious structural damage to the apparatus. When the forces on the particles exposed by the gas outbalance their weight, particles start to elutriate from the surface of the bed. Separation and recycling of elutriated particles is necessary to keep the solids inventory constant. The onset of the turbulent regime is characterized by the point where the pressure fluctuations from the bed caused by bubble break-up reach a maximum. Increasing the gas velocity further leads to a point where the entrainment of solids starts to be significant, which characterizes the appearance of fast fluidization. Still, the axial solids profile along the height is pronounced with a dense region at the bottom of the bed and exponential decay above. The solids profile loses this shape at an even higher gas velocity, which is then called pneumatic conveying. The discussed gas-solids flow patterns as well as axial solids profiles of the different fluidization regimes are illustrated in Fig. 30.

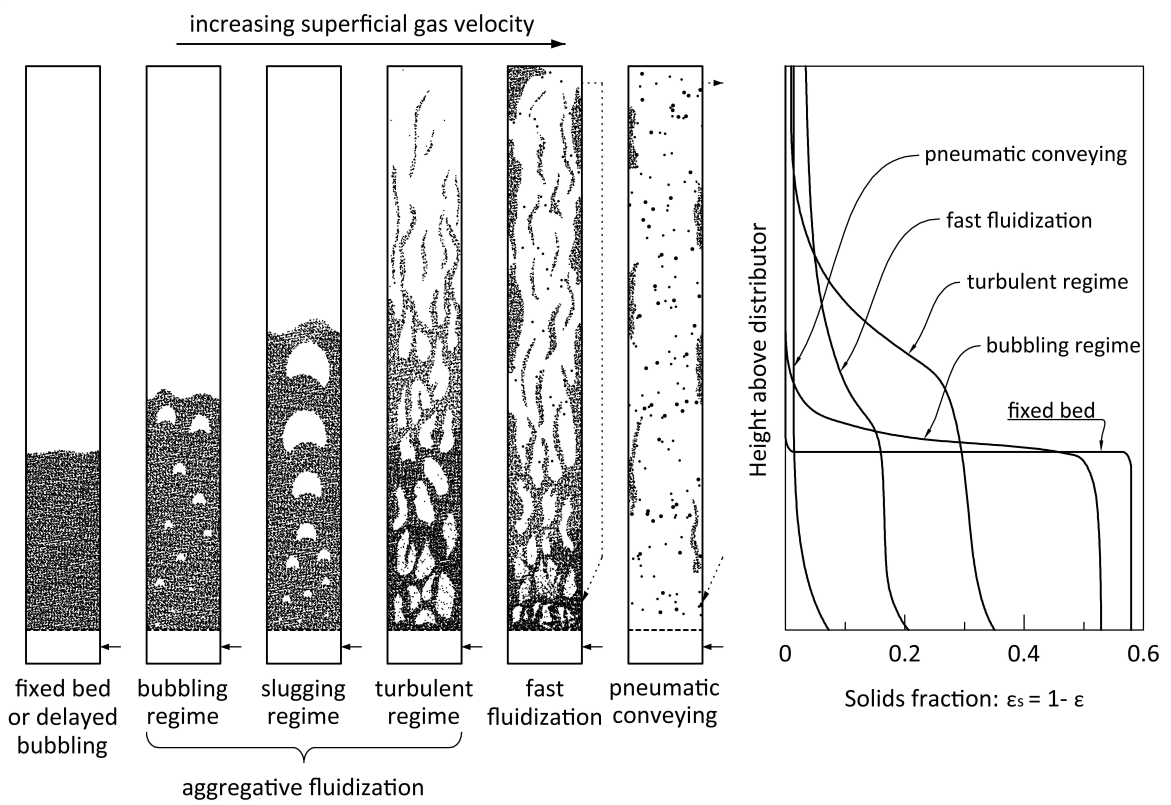

Fig. 30 Gas-solids flow patterns in fluidized beds and solids distribution over column height. Reproduced after Grace (1986) (flow patterns) and Kunii and Levenspiel (1991) (solids profiles).

4.2.1 Fluidized bed regimes

Incipient fluidization

A gas stream passing through a packed bed causes a pressure gradient due to frictional losses. The pressure gradient depends on the height of the bed and can be described by the equation after Ergun (1952):

$$\frac{\Delta p}{H} = 150 \cdot \frac{(1-\varepsilon)^2}{\varepsilon^3} \cdot \frac{\mu_g \cdot U_s}{\left(\phi \cdot d_p\right)^2} + 1.75 \cdot \frac{1-\varepsilon}{\varepsilon^3} \cdot \frac{\rho_g \cdot U_s^2}{\phi \cdot d_p} \qquad \text{(eqn. 4-1)}$$

The equation includes a linear gas velocity dependent term accounting for viscous flow and a quadratic term accounting for turbulent flow. The onset of fluidization occurs when the forces of weight, buoyancy and fluid drag are in balance.

$$\frac{\Delta p}{H} = \left(\rho_p - \rho_g\right) \cdot \left(1 - \varepsilon_{mf}\right) \cdot g \qquad \text{(eqn. 4-2)}$$

At this point, the particle to particle friction diminishes and the particles start to move more freely. This is when the bulk of particles begins to behave like a fluid. At the transition from fixed bed to fluidized bed, (eqn. 4-1) and (eqn. 4-2) equalize giving

$$\left(\rho_p - \rho_g\right) \cdot \left(1 - \varepsilon_{mf}\right) \cdot g = 150 \cdot \frac{(1-\varepsilon)^2}{\varepsilon^3} \cdot \frac{\mu_g \cdot U_s}{\left(\phi \cdot d_p\right)^2} + 1.75 \cdot \frac{1-\varepsilon}{\varepsilon^3} \cdot \frac{\rho_g \cdot U_s^2}{\phi \cdot d_p} \qquad \text{(eqn. 4-3)}$$

Extending the equation by the factor

$$\frac{\rho_g \cdot (\phi \cdot d_p)^3}{{\mu_g}^2}$$

and introducing the Archimedes number

$$Ar = \frac{\rho_g \cdot d_p^3 \cdot (\rho_p - \rho_g) \cdot g}{{\mu_g}^2} \quad \text{(eqn. 4-4)}$$

and the particle specific Reynolds number

$$Re_p = \frac{U_s \cdot d_p \cdot \rho_g}{\mu_g} \quad \text{(eqn. 4-5)}$$

leads to

$$Ar = C_1 \cdot Re_{p_{mf}} + C_2 \cdot {Re_{p_{mf}}}^2 \quad \text{(eqn. 4-6)}$$

with

$$C_1 = 150 \cdot \frac{1 - \varepsilon_{mf}}{{\varepsilon_{mf}}^3 \cdot \phi^2} \quad \text{(eqn. 4-7)}$$

$$C_2 = \frac{1.75}{{\varepsilon_{mf}}^3 \cdot \phi} \quad \text{(eqn. 4-8)}$$

With knowledge of the voidage at incipient fluidization ε_{mf}, the minimum fluidization velocity U_{mf} can be determined from

$$Re_{p_{mf}} = \sqrt{\left(\frac{C_1}{2 \cdot C_2}\right)^2 + \frac{Ar}{C_2}} - \frac{C_1}{2 \cdot C_2} \quad \text{(eqn. 4-9)}$$

Since direct experimental quantification of ε_{mf} is difficult, it is typically derived by the determination of U_{mf} following

$${\varepsilon_{mf}}^3 - \frac{150}{\phi^2} \cdot \frac{Re_{p_{mf}}}{Ar} \cdot (1 - \varepsilon_{mf}) - \frac{1.75}{\phi} \cdot \frac{{Re_{p_{mf}}}^2}{Ar} = 0 \quad \text{(eqn. 4-10)}$$

The coefficient of correlation (eqn. 4-6) can be assessed experimentally. It was found that C_1 and C_2 stay constant over a wide range of operating conditions (Wen and Yu, 1966). Therefore, the onset of fluidization only depends on the Archimedes number and thus only on the particle and fluid properties. Several researchers have reported on C_1 and C_2 with a comprehensive overview given by Löffler (2001). The correlation after (Grace, 1982) is most often used

$$Re_{p_{mf}} = \sqrt{27.2^2 + 0.0408 \cdot Ar} - 27.2 \quad \text{(eqn. 4-11)}$$

which corresponds to a voidage at incipient fluidization of ε_{mf} =0.429 and a particle sphericity of ϕ=0.898. Such values are typical for particles used in fluidized beds. With increasing gas velocity above U_{mf}, the bed expands while the pressure drop remains practically unchanged. This can be

explained by using the analogy of a liquid where the pressure at the bottom only depends on the static pressure, which itself is independent of whether gas is introduced or not.

Bubbling regime

Bed expansion can happen uniformly or through the appearance of bubbles. The velocity at which bubbles first occur is called minimum bubbling velocity, U_{mb}. While for very coarse particles, incipient fluidization coincides with the appearance of bubbles, delayed bubbling appears for very fine, light particles where homogeneous bed expansion can be observed. The appearance of bubbles is related to the instability of homogeneous fluidization. The minimum bubbling velocity after Geldart and Abrahamsen (1978) is

$$U_{mb} = 33 \cdot d_p \cdot \left(\frac{\rho_g}{\mu_g}\right)^{0.1} \qquad \text{(eqn. 4-12)}$$

Homogenous fluidization occurs in the superficial gas velocity range $U_{mf}<U_s<U_{mb}$.

Slugging regime

For very deep and narrow beds, the bubbles can grow to diameters close or equal to the bed diameter or width. Large and fairly regular pressure fluctuations are typical for this regime, caused by collapsing bubbles at the top of the bed. The slugging regime occurs at velocities above the minimum slugging velocity (Stewart and Davidson, 1967).

$$U_{ms} = U_{mf} + 0.07 \cdot \sqrt{g \cdot D} \qquad \text{(eqn. 4-13)}$$

Operation of fluidized beds in the slugging regime should be avoided due to the appearance of mechanical stress at the bottom of the bed, which can lead to mechanical disintegration of the fluidized bed apparatus.

Terminal velocity and solids entrainment

At the terminal velocity, U_t, the fluid force (drag) on the particle outbalances the forces of effective particle weight and the particles start to float. The terminal velocity can thus be related to the free-falling velocity of a single particle. The terminal velocity is derived from the force balance of an un-accelerated floating particle

$$U_t = \sqrt{\frac{4}{3} \cdot \frac{\rho_p - \rho_g}{\rho_g} \cdot \frac{d_p \cdot g}{C_D}} \qquad \text{(eqn. 4-14)}$$

where C_D, the drag coefficient, is determined experimentally in wind tunnel tests. Such a drag coefficient curve is illustrated in Fig. 31 with the correlations given in Table 4-1.

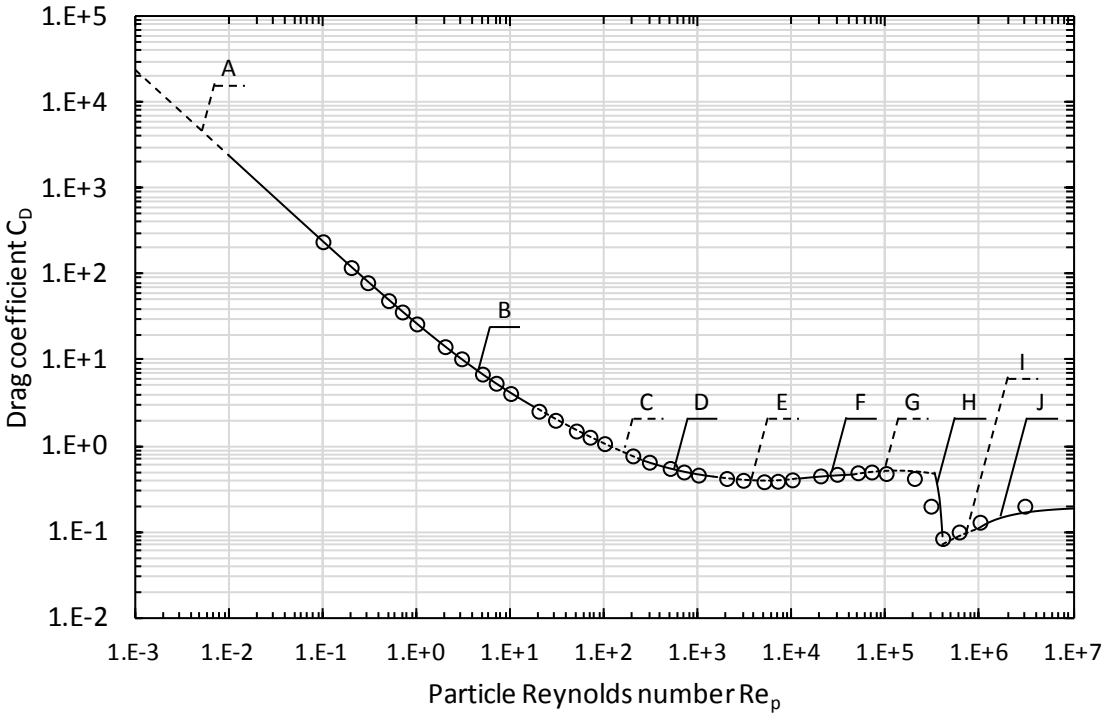

Fig. 31 Drag coefficient of a sphere as a function of the Reynolds number (standard drag curve). Data calculated after Clift et al. (1978); correlations can be found in Table 4-1. Experimental data indicated by circles (○) are taken from Lapple and Shepherd (1940).

Table 4-1 Drag coefficient correlations of a sphere by Clift et al. (1978), $w = \log_{10} Re_p$.

Range	Correlation
A $Re_p < 0.01$	$C_D = \frac{3}{16} + \frac{24}{Re_p}$
B $0.01 \leq Re_p < 20$	$C_D = \frac{24}{Re_p} \cdot \left[1 + 0.1315 \cdot Re_p^{\,0.82-0.05 \cdot w}\right]$
C $20 \leq Re_p < 260$	$C_D = \frac{24}{Re_p} \cdot \left[1 + 0.1935 \cdot Re_p^{\,0.6305}\right]$
D $260 \leq Re_p < 1500$	$\log_{10} C_D = 1.6435 - 1.1242 \cdot w + 0.1558 \cdot w^2$
E $1500 \leq Re_p < 1.2x10^4$	$\log_{10} C_D = -2.4571 + 2.5558 \cdot w - 0.9295 \cdot w^2 + 0.1049 \cdot w^3$
F $1.2x10^4 \leq Re_p < 4.4x10^4$	$\log_{10} C_D = -1.9181 + 0.6370 \cdot w - 0.0636 \cdot w^2$
G $4.4x10^4 \leq Re_p < 3.38x10^5$	$\log_{10} C_D = -4.3390 + 1.5809 \cdot w - 0.1546 \cdot w^2$
H $3.38x10^5 \leq Re_p < 4x10^5$	$C_D = 29.78 - 5.3 \cdot w$
I $4x10^5 \leq Re_p < 10^6$	$C_D = -0.49 + 0.1 \cdot w$
J $10^6 \leq Re_p$	$C_D = 0.19 - \frac{8x10^4}{Re_p}$

Entrainment of solids generally starts when the gas velocity exceeds U_t. However, the formation of clusters can provoke a delay in entrainment since the hydrodynamic effective diameter increases with cluster size.

Turbulent regime

If the gas velocity is increased further, a turbulent regime emerges. Turbulent fluidized beds are characterized by bubble break-up instead of bubble growth as in bubbling fluidized beds. Small

voids and particle clusters dart to and from on a now indistinct bed surface. The critical velocity U_c marks the onset of the turbulent regime and is defined where the standard deviation of the pressure fluctuation reaches a maximum. It is believed that this point reflects a dynamic balance between bubble coalescence and break-up. The critical velocity can be determined after Abba et al. (2003) from

$$Re_c = 0.74 \cdot Ar^{0.426} \quad \text{(eqn. 4-15)}$$

which is the advanced formulation after Bi and Grace (1995a, 1995b) obtained from absolute pressure fluctuation measurement data.

Fast fluidization regime

At the transition from a turbulent to a fast fluidization regime, solids entrainment starts to increase significantly. The superficial velocity U_{se} marks this changeover and is determined by measuring the emptying time of fluidized particles inside a vessel. At U_{se}, the emptying time starts to be significantly lower than before. Therefore, U_{se} is often called "blow-out velocity" and is calculated after Abba et al. (2003) from

$$Re_{se} = 1.68 \cdot Ar^{0.469} \quad \text{(eqn. 4-16)}$$

which is the enhanced formulation of the extensively used formula after Bi et al. (1995) allowing for a more precise prediction of U_{se}.

Pneumatic conveying

At even higher velocities than U_{se}, the dense region at the bottom section of the bed disappears, marking the onset of the pneumatic conveying regime. Pneumatic conveying is governed by large pressure fluctuations at the bottom of the bed. The onset of pneumatic conveying appears at V_{CA} and is not discussed here. For more detailed information, refer to Grace et al. (1997).

4.2.2 Particle classification

In gas-solids fluidized beds, the behavior of particles differs significantly depending on particle diameter and density and gas density. Fluidized bed regimes, such as homogenous fluidization, appear only for particles of a certain type. Geldart (1973) identified four specific groups of powders for fluidized beds.

Group C particles are cohesive or very fine powders. Fluidization is extremely difficult since particle-particle forces are greater than the forces induced by the gas. The appearance of channels and plug-type slugging is typical for this type of particle. The particles can be fluidized under certain circumstances, e.g., when applying external vibration.

Group A particles are characterized by the appearance of a velocity range with bubble-free (homogeneous) expansion. At higher velocities, bubbles appear that rise faster than the gas. Particles of this group can be fluidized very easily.

Group B, often referred to as "sand-like" particles, fluidize with the instantaneous appearance of bubbles at the onset of fluidization. Bubbles grow large with the size increasing nearly linearly with distance from the gas distributor.

Group D particles have very large diameters where bubbles rise slower than the gas percolating through the bed. Bubbles grow quickly with large exploding bubbles at the top of the bed. For very deep beds, difficulties in fluidization may appear.

The diagram after Geldart (1973) includes the classification of powders depending on particle, and gas density and particle diameter (Fig. 32).

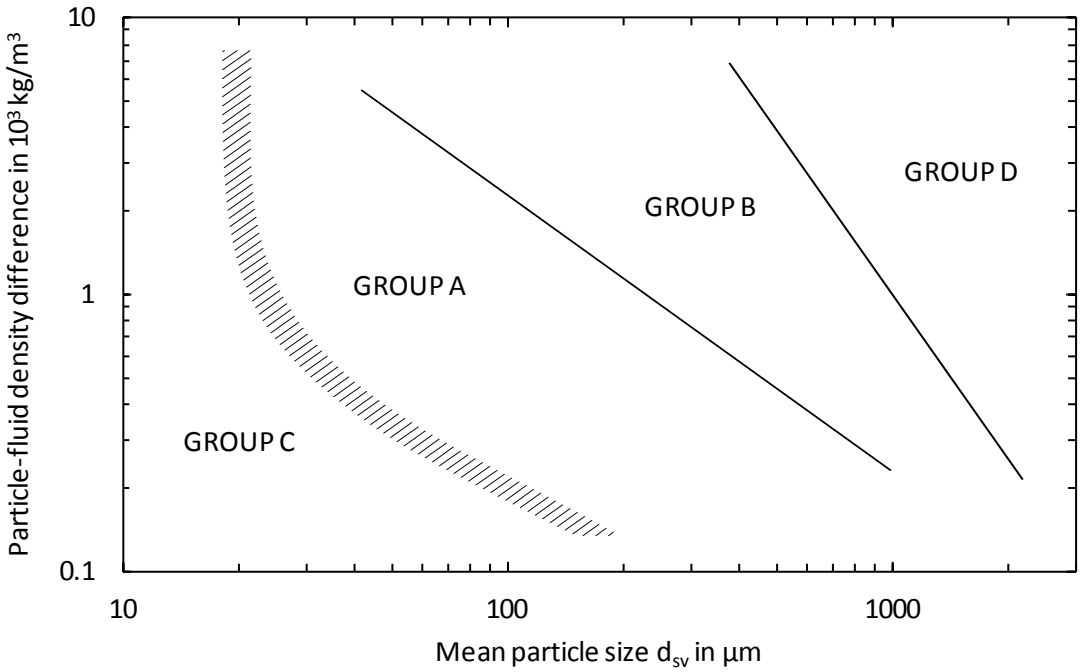

Fig. 32 Powder classification diagram after Geldart (1973).

Geldart determined the properties of powders under atmospheric conditions with air. Fluidization behavior at elevated temperature and pressure has been the focus of several researchers, i.e. Yates (1996) and Sidorenko and Rhodes (2003), where powders behaved differently than shown by Geldart. However, it was found that when substituting the particle-fluid density difference in the Geldart diagram (Fig. 32) by dimensionless density, the Geldart diagram can be applied to fluidized beds operating at elevated temperature and pressure (Yang, 2007).

4.2.3 Flow regime maps

A flow regime maps illustrates the regime of a fluidized bed depending on the gas and solids flow conditions. Several flow regime maps are mentioned in the literature where some of them specifically focus on certain fluidized bed regimes, e.g. pneumatic conveying. Among these, the contributions from Reh and Grace are outstanding in terms of applicability for fluidized bed engineers and scientists and are, therefore, discussed in more detail.

The regime map after Reh is based on the idea that a fluidized bed can ideally be described by single particles where the fluid-particle drag coefficient and the particle Reynolds number are deterministic for the particle state. The fixed bed, fluidized bed and conveying mode are distinguished by introducing a load factor *n* describing the ratio of fluid to particle forces relative to the particle weight. Fluidized beds are found for *n=1* where the effective particle weight (gravity minus buoyancy) equals the fluid forces. Conveying of particles occurs for *n>1* and particles remain at rest for *n<1*. Under ideal flow conditions, the load factor *n* is calculated from

$$n = \frac{3}{4} \cdot {Fr_p}^2 \cdot \frac{\rho_g}{\rho_p - \rho_g} \cdot C_D\left(Re_p\right) \qquad \text{(eqn. 4-17)}$$

where $C_D = f(Re_p)$ is the drag coefficient of a single sphere or a bulk of particles. To account for solids motion in fluidized beds, C_D has to be extended to include specific fluidized bed information. Reh concluded that bed porosity is useful to determine the effective drag coefficient $C_D = f(Re_p, \omega)$. The Reh diagram illustrates the effective drag coefficient for gas-solids flow including fluidized beds depending on the Reynolds number. The specific selection of dimensionless parameters means that the Archimedes number, a particle-fluid characteristic value, and the Beranek number, a particle diameter independent value, appear as straight lines. The Beranek number Ω is calculated from

$$\Omega = \frac{{\rho_g}^2 \cdot {U_s}^3}{\left(\rho_p - \rho_g\right) \cdot g \cdot \mu_g} \qquad \text{(eqn. 4-18)}$$

The discrepancy of the model of an equivalent single particle fluidized bed is presented in the diagram by the area between the solid lines applicable to particulate fluidization and the dotted lines representing the drag coefficients of single particles. Regimes with entrainment, e.g. turbulent regimes and fast fluidized beds, can therefore be found in the area between the solid line $\varepsilon \rightarrow 1$ $n=1$ and the associated dotted line for a single particle. It is important to mention that the Reh diagram includes information on the absolute gas velocity in fluidized beds by including information of the average bed porosity ε. The regime map after Reh (1961) is illustrated in Fig. 33.

Grace (1986) discussed the appearance of fluidization regimes basing on similarity rules where he concluded that the fluidization state can be described by a dimensionless particle diameter ${d_p}^*$ and a dimensionless superficial gas velocity U^*.

$${d_p}^* = Ar^{1/3} \qquad \text{(eqn. 4-19)}$$

$$U^* = \frac{Re_p}{{d_p}^*} \qquad \text{(eqn. 4-20)}$$

The Grace diagram, shown in Fig. 34, includes information on the classification of powders after Geldart (1973) and the fluidization regimes as discussed in Section 4.2.1. *"Fluidized bed regimes"* (p. 55). Although the borders between fluidization regimes are indicated as clear lines, it is important to note that, in reality, a fluent transition appears. This is why care has to be taken when identifying the state of a fluidized bed in the region of the borders. Especially, application of the diagram to fluidized beds with significant entrainment, e.g. fast fluidization and pneumatic conveying, is considered critical since these regimes are very much dependent on the actual solids entrainment rates. This is why fast fluidized beds can appear as pneumatic conveying when using

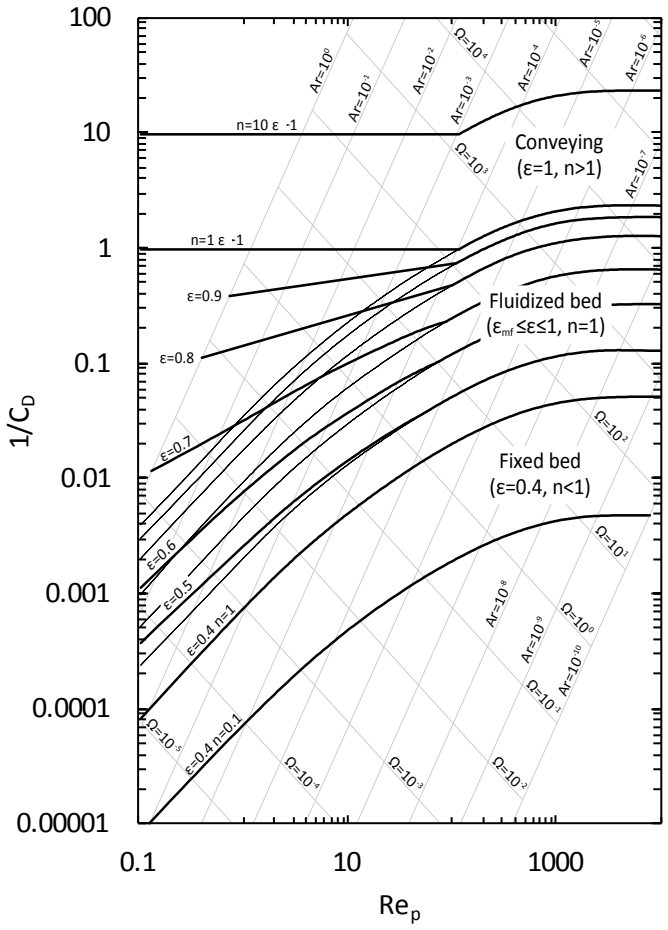

Fig. 33 Flow regime map after Reh (1961). See also Reh (1968, 1971).

very low solids inventories causing the disappearance of the lower dense bed typical of fast fluidization.

Later, Bi and Grace (1995b) modified the original Grace (1986) diagram by substituting the superficial velocity in U^* by absolute velocities which certainly improved the validity of the diagram for fast fluidized beds and pneumatic conveying. Remarkably, Reh included this information in 1961 with the bed porosity ε and the load factor n. He furthermore extended his diagram by substituting the superficial velocity in his original approach with relative gas velocities (Reh, 1996), introducing a new unique coverage of the diagram for all types of fluidized beds. It also turned out that the Grace diagram is included in the Reh diagram and vice versa.

For practical engineering purposes, neither the absolute nor the relative gas velocities are known and therefore these extended diagrams are of limited use in such cases. However, they can be useful in describing certain phenomena, especially with respect to high solids entrainment in more detail.

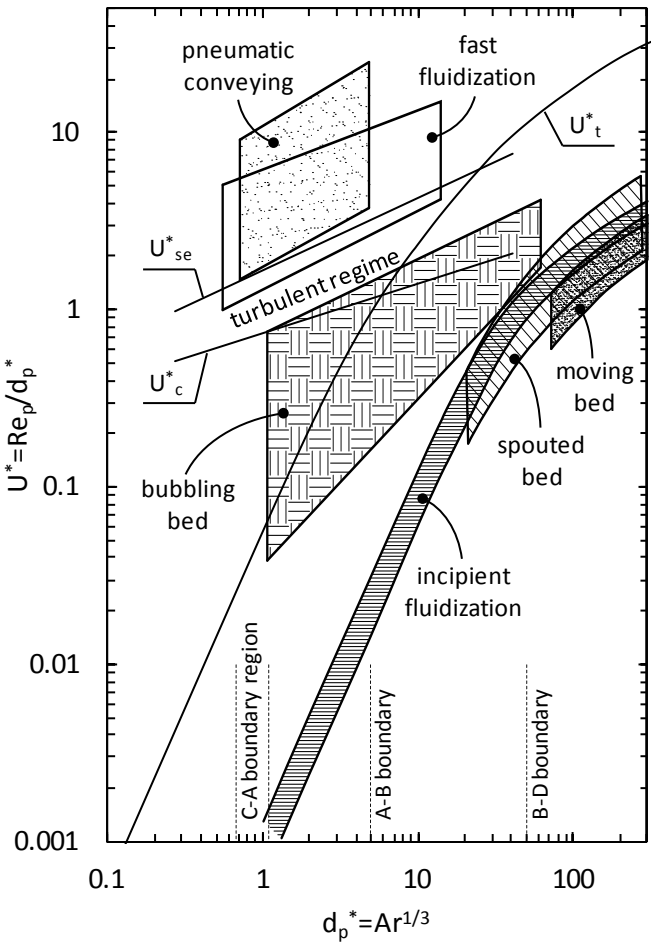

Fig. 34 Flow regime map after Grace (1986) with U_{se}^* and U_c^* after Abba et al. (2003) and U_t^* determined by the equations given in Table 4-1.

4.3 General design considerations

4.3.1 Chemical looping reactor systems

The multitude of requirements to the reactor systems in chemical looping is a challenge in the design. Rotating bed reactors, alternating fixed bed vessels and moving beds have been discussed. However, chemical looping is a typical fluidized bed application. Fluidized beds with two separate fluidized beds are often discussed as dual fluidized beds. Fluid catalytic cracking (FCC) is a typical application of such systems which is nowadays state-of-the-art even at the very large scale in the petrochemical industry. Several chemical looping units based on fluidized bed technology are currently in operation at scales of up to 140 kW gaseous fuel input (Pröll et al., 2009b) and 100 kW solid fuel input (Markström et al., 2012). While basically all of these systems have in common that the air reactor is operated in the transporting regime, two fuel reactor concepts are applied. Historically, the first chemical looping units were designed with bubbling fluidized bed fuel reactors where the fuel reactor is placed in the return leg of the air reactor. Similar systems for allothermic biomass gasification are today in operation at scales of up to 8 MW_{th} (Hofbauer et al., 2002). However, there is a limitation with respect to large scale due to the very large cross-section areas and limited lateral solids mixing. Fuel passing through the bubble phase exhibiting insufficient solids contact may leave the reactor unconverted and no considerable gas conversion occurs in the particle-free freeboard. Expanded fluidized beds, e.g. turbulent and fast fluidized beds, where solids are present over the whole reactor height, are therefore considered beneficial

for chemical looping applications. Such dual circulating fluidized beds are therefore discussed in more detail in the following section.

The dual circulating fluidized bed reactor system

Based on the chemical looping reactor system requirements mentioned in Section 4.1, the dual circulating fluidized bed (DCFB) reactor concept for chemical looping applications has been developed at the Vienna University of Technology (Pröll et al., 2008; Kolbitsch, 2009; Pröll et al., 2009b). It is composed of two interconnected circulating fluidized bed reactors. The design focuses on scale-up related issues such as low solids inventories and low reactor footprint, while maintaining the focus on high gas-solids contact. The principle is shown in Fig. 35. The DCFB system involves two solids loops: the global loop and the internal loop. The solids entrained from the air reactor are separated by a cyclone and sent to the upper loop seal. The upper loop seal, fluidized by steam, provides proper sealing between the reactors to avoid gas leakage. The entrained solids are then transported back to the air reactor by the lower loop seal, closing the global solids loop. The fuel reactor includes an internal solids loop, which is closed by the fuel reactor cyclone, and the internal loop seal. A key feature of the dual circulating reactor system concept is the lower loop seal. Solids inventories are inherently stabilized by the lower loop seal which acts as a hydraulic link. Solids accumulation in any part of the system is avoided as long as proper fluidization is provided to the loop seals. To avoid dilution of air and fuel reactor gases by undesired gases, the loop seals are fluidized with steam. One feature of the dual circulating fluidized bed reactor system is that the two solids loops are largely independent of each other, and, as such, the fuel reactor can be operated with respect to maximum fuel conversion. Since this design introduced a new age in terms of applicability to large scales, the design of the 10 MW chemical looping combustion demonstration unit is based on the DCFB concept.

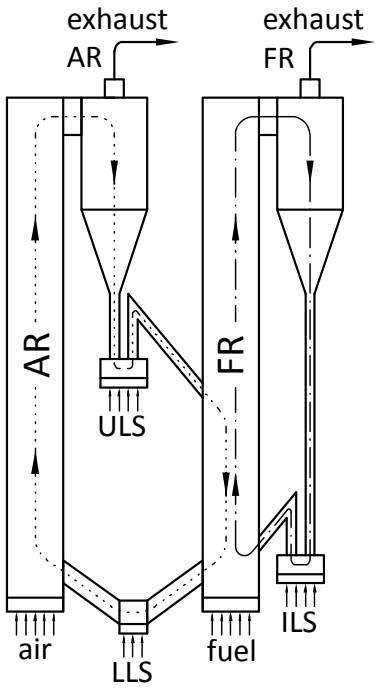

Fig. 35 Principle setup of the dual circulating fluidized bed reactor system, with the global solids loop indicated by the dotted line and the internal solids loop indicated by the dash-dotted line. AR – air reactor, FR – fuel reactor, LLS – lower loop seal, ULS – upper loop seal, ILS – internal loop seal.

4.3.2 The 10 MW scale chemical looping combustion reactor system setup

In chemical looping systems, the temperature is limited by the specific properties of the oxygen carrier, such as the material melting point and agglomeration tendency. Typical maximal operating temperatures range from 800 to 1000°C, while the adiabatic combustion temperature is roughly 1900°C at an air/fuel ratio of 1.1. This excess energy has to be withdrawn from the reactor system, which in addition is dependent on the completeness of the combustion, described by the combustion efficiency η_c (Fig. 36). Depending on the selected air/fuel ratio, a great percentage of the total heat release has to be extracted directly from the reactor system. This can be done by direct cooling of the reactor vessels and/or by cooling the bed material in an external heat exchanger. At typical chemical looping operating conditions (air/fuel ratio = 1.1-1.2 and η_c = 90-100%), this means that about 50% of the heat input has to be extracted from the reactor system itself.

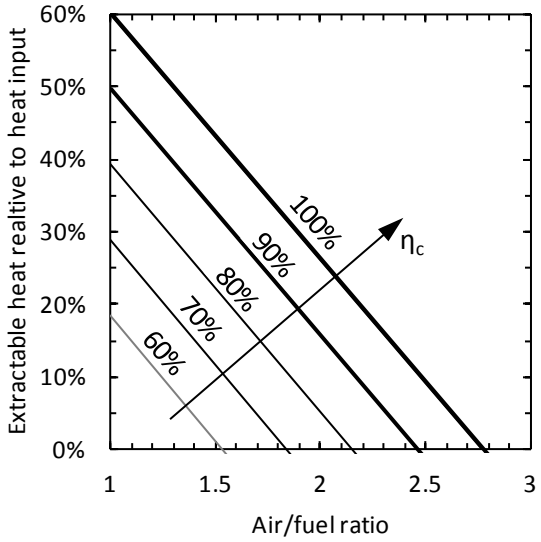

Fig. 36 Required cooling of the reactor system dependent on the global air/fuel ratio and the combustion efficiency η_c (based on lower heating values) with no air and fuel preheating and a fuel reactor temperature of ϑ_{FR} = 900°C.

While the quantity of heat directly extracted from the reactor system is not limited with respect to net plant efficiency, the air/fuel ratio has to be selected considering the specific oxygen carrier requirements and stack loss. In fluidized bed applications, the vessel can be cooled using evaporative water walls. The heat extraction ratio varies with vessel temperature and solids-wall contact behavior (Hamdan and Al-qaq, 2008), and thus cannot be significantly influenced by the operator. For this reason, stable off-design load operation is difficult to obtain when only water walls are used. Therefore, there is a strong demand for a controllable heat extraction device for start-up and off-design load operation. In circulating fluidized bed applications, this is typically obtained by using external fluidized bed heat exchangers, where the flow of solids to the heat exchanger is controlled, e.g. by a solids flow control valve (Basu and Fraser, 1991). In order to keep the size of this heat exchanger within reasonable limits, a combination of both is assumed to be the most effective. An overly large bed material cooler could additionally reduce the oxygen carrier lifetime attributable to the high thermal stress when particles are repeatedly exposed to large temperature gradients.

In general, both reactors can be equipped with water walls. However, in chemical looping, the reactions within the air reactor are always strongly exothermic while the fuel reactor reactions can be, depending on the oxygen carrier used, either slightly exothermic or endothermic. For this reason, a setup where only the air reactor is equipped with water walls was chosen.

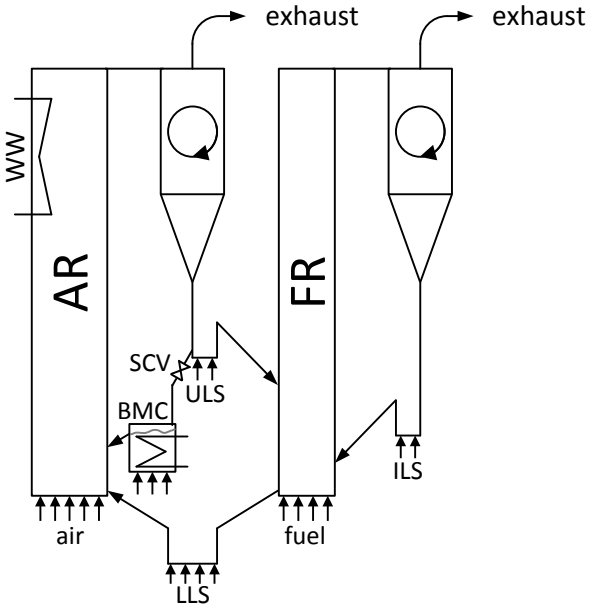

Fig. 37 Proposed reactor system arrangement based on the dual circulating fluidized bed concept. Locations where fluidization is applied are indicated by arrows. AR - air reactor, FR – fuel reactor, LLS – lower loop seal, ULS – upper loop seal, ILS – internal loop seal, BMC – bed material cooler, WW – water walls, SCV – solids flow control valve.

The proposed reactor system heat exchanger arrangement is shown in Fig. 37. It includes an external fluidized bed heat exchanger, the bed material cooler and water walls in the air reactor. The bed material cooler is placed in a return loop of the air reactor where only part of the air reactor entrained solids are directed to the bed material cooler controlled by a solids flow control valve.

The advantage of this arrangement is that:

- part load operation is possible,
- only a small fraction of the air reactor solids entrainment has to pass the bed material cooler, thus only a minor loss of global solids circulation is expected,
- the function of the bed material cooler has a minor effect on the fuel reactor operation,
- the bed material cooler can be fluidized by air, and as a result
- the bed material cooler fluidization air takes part in the air reactor oxidation reaction, and thus
- no additional supplementary air is needed for bed material cooler fluidization.

A detailed part load operation analysis was performed using mass and energy balance investigations provided in Section 3.6.1 *“Part load operation”* (p. 48). The specific design of the fluidized beds is discussed in the following section.

4.4 Design of a 10 MW CLC demonstration plant

The design is based on the dual circulating fluidized bed concept for chemical looping systems. The main design parameters are shown in Table 4-2. Air is used in the air reactor as the fluidization agent while the fuel reactor is fluidized by gaseous fuel. To avoid fuel reactor exhaust gas dilution by, e.g., nitrogen, the loop seals are fluidized by superheated steam.

Table 4-2 Site conditions/design parameters for the CLC reactor system.

Item	Symbol	Value	Unit
Fuel power input (based on LHV)	P_{fuel}	10	MW
Lower heating value of the fuel	LHV	50	MJ/kg
Stoichiometric combustion oxygen demand	O_{min}	4.1	kg/kg
Stoichiometric combustion air demand	l_{min}	17.4	kg/kg
Design air/fuel ratio	λ	1.1	-
Design fuel reactor temperature	ϑ_{FR}	900	°C
Design air reactor temperature	ϑ_{AR}	960	°C
Oxygen carrier			
active material	-	Ni/NiO	-
active NiO content	-	40	wt%
oxygen transport capacity	R_0	0.084	kg/kg
mean particle size	d_p	200	µm
particle apparent density	ρ_p	3425	kg/m^3
sphericity	ϕ	0.9	-

Air and fuel reactor design

The air reactor is designed based on three requirements:

- sufficient oxygen carrier entrainment for oxygen transport,
- oxidation of the reduced oxygen carrier coming from the fuel reactor, and
- controllability of the solids entrainment rates.

Therefore, the air reactor is designed as a transporting fluidized bed, i.e. a fast fluidized bed, where the superficial gas velocity at the riser exit is selected as the design velocity. The onset of fast fluidization after (eqn. 4-16) appears at a superficial gas velocity of

$$U_{se-AR} = 7.25 \frac{m}{s} \quad \text{(eqn. 4-21)}$$

Thus, the air reactor design outlet superficial gas velocity is selected in the range

$$U_{AR-design} = 7.5 - 8.0 \frac{m}{s} \quad \text{(eqn. 4-22)}$$

To control the solids entrainment rates in circulating fluidized beds, gas is supplied at different heights of the riser. Shifting gas from the top stages to the lower stages causes the gas velocities at the bottom to increase, provoking solids carryover to the upper, lean region of the riser. Thus, the solids fraction at the riser exit increases as does the solids circulation rate. The air reactor is equipped with three gas introduction stages; most of the gas is introduced at the primary stage. To keep the gas velocities within a similar range, a diffuser is placed in the lower section of the riser. The bottom part of the air reactor is designed as a continuation of the lower loop seal and

operates in a high velocity bubbling fluidized bed regime. An overview of the applicable gas mass-flow rates and design superficial gas velocities is given in Table 4-3.

Table 4-3 Gas distribution and design superficial gas velocities along the air reactor riser height.

Stage	Present relative quantity of gas based on mass	Effective mass-flow rate of gas in kg/h	Design superficial gas velocity
Bottom	5 %	690	$30 \cdot U_{mf}\vert_{inlet}$
Primary	55 %	8290	$120\% \cdot U_{se}\vert_{inlet}$
Secondary	20 %	11053	$120\% \cdot U_{se}\vert_{inlet}$
Tertiary	20 %	11029	$120\% \cdot U_{se}\vert_{outlet}$

The air reactor has a rectangular cross-section allowing for simple construction of the water walls necessary for cooling.

The consumption of oxygen in the air reactor by oxygen carrier oxidation causes a reduction in the effective gas flow rates. The resulting fluidized bed regimes with respect to gas quantities at the inlet (no oxygen uptake) and outlet are depicted in Fig. 38, revealing that the air reactor operates in a fast fluidized bed regime close to U_{se}^*.

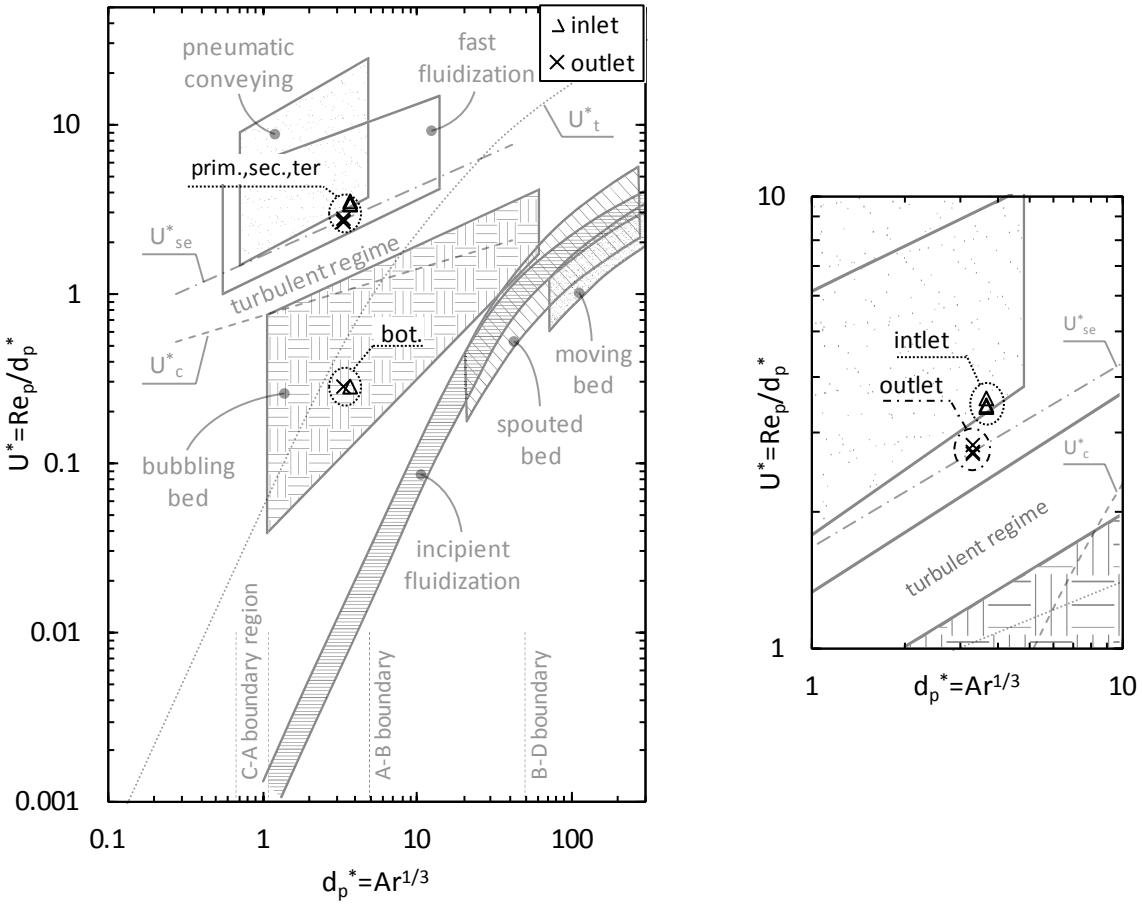

Fig. 38 Air reactor fluidized bed operating state with respect to the quantities at the inlet and outlet depicted in the Grace diagram. Left: Operating conditions in the bottom, primary, secondary and tertiary fluidization stages. Right: Detailed operating conditions in the primary, secondary and tertiary fluidization stages. bot. - bottom, prim. - primary, sec. - secondary, ter. - tertiary.

Compared to the air reactor, the reaction rate in the fuel reactor is an order of magnitude slower. Gas-solids contact is therefore significantly more important in this reactor. Bubbling fluidized bed fuel reactors suffer from the risk of gas bypassing through the bubble phase, which can be minimized by low fluidization numbers and deep beds. The applicability of very deep beds is limited due to the large pressure differences between the bottom and the top of the bed, which runs the risk of de-fluidized dead zones at the bottom of the bed or slugging in the upper region of the bed. However, low fluidization numbers will result in large fuel reactor cross-sectional areas, high solids inventories and large bed pressure drops. Additionally, most of the reactor volume will be lost because no relevant reaction can be expected in the practically particle-free freeboard of the bed. Turbulent fluidized bed or fast fluidized bed regimes allow for gas-solids contact over the entire height of the reactor and permit operation with lower solids inventories, which is particularly important for increased plant capacity. However, finding the optimum solution between reduced gas residence time at an increased gas velocity and less intensive solids distribution over the reactor is a key issue in fuel reactor design.

The main design criterion of the fuel reactor is to maximize the gas-solids contact while keeping the solids inventory low. Turbulent fluidized beds are characterized by bubble break-up instead of bubble growth as in bubbling fluidized beds. Small voids and particle clusters dart to and from the indistinct top surface of the bed. Thus, potential gas-slip through the bubble phase is minimized, while gas-solids contact is expected to increase. Solids are also present over the entire height of the riser, allowing for an improved gas-solids reaction time. The onset of turbulent and fast fluidization under fuel reactor operating conditions according to (eqn. 4-15) and (eqn. 4-16) at a superficial gas velocity of

$$U_{c-FR} = 2.74 - 2.80\frac{m}{s} \quad \text{(eqn. 4-23)}$$

$$U_{se-FR} = 7.45 - 8.59\frac{m}{s} \quad \text{(eqn. 4-24)}$$

where the lower values correspond to the conditions (gas properties) at the fuel reactor exit. The fuel reactor design superficial gas velocity is chosen to be in the middle of the turbulent regime. Thus, the fuel reactor superficial gas velocity range is

$$U_{FR-design} = 5.25 - 5.75\frac{m}{s} \quad \text{(eqn. 4-25)}$$

The fuel reactor has a circular shape, similar to the air reactor, with a dense bottom bubbling bed as an extension of the lower loop seal. To account for the increase in gas volume by fuel combustion, a diffuser is placed above the primary gas injection stage. Table 4-4 summarizes the gas flow rates and design superficial gas velocities in the fuel reactor riser.

Table 4-4 Gas distribution and design superficial gas velocities along the fuel reactor riser height.

Stage	Present relative quantity of gas based on mass	Effective mass-flow rate of gas in kg/h	Design superficial gas velocity
Bottom	20 %	144	$25 \cdot U_{mf}\big\vert_{inlet}$
Primary	80 %	3607	$resulting$

Compared to the air reactor gas, staging is not necessary in the fuel reactor, so the fuel gas is introduced at low levels to reach high gas phase residence times. The fluidized bed regimes

appearing in the fuel reactor are illustrated in the regime map after Grace in Fig. 39. Owing to combustion where the gas volume triples, the theoretical gas velocities with respect to complete combustion (outlet) differ significantly from flow rates at the inlet. In practice, the appearance of such high gas velocities (bot. outlet and prim. outlet) is not expected since gas velocity will gradually increase with reaction in the riser. However, for completeness, these theoretical fluidized bed conditions are included in the regime map.

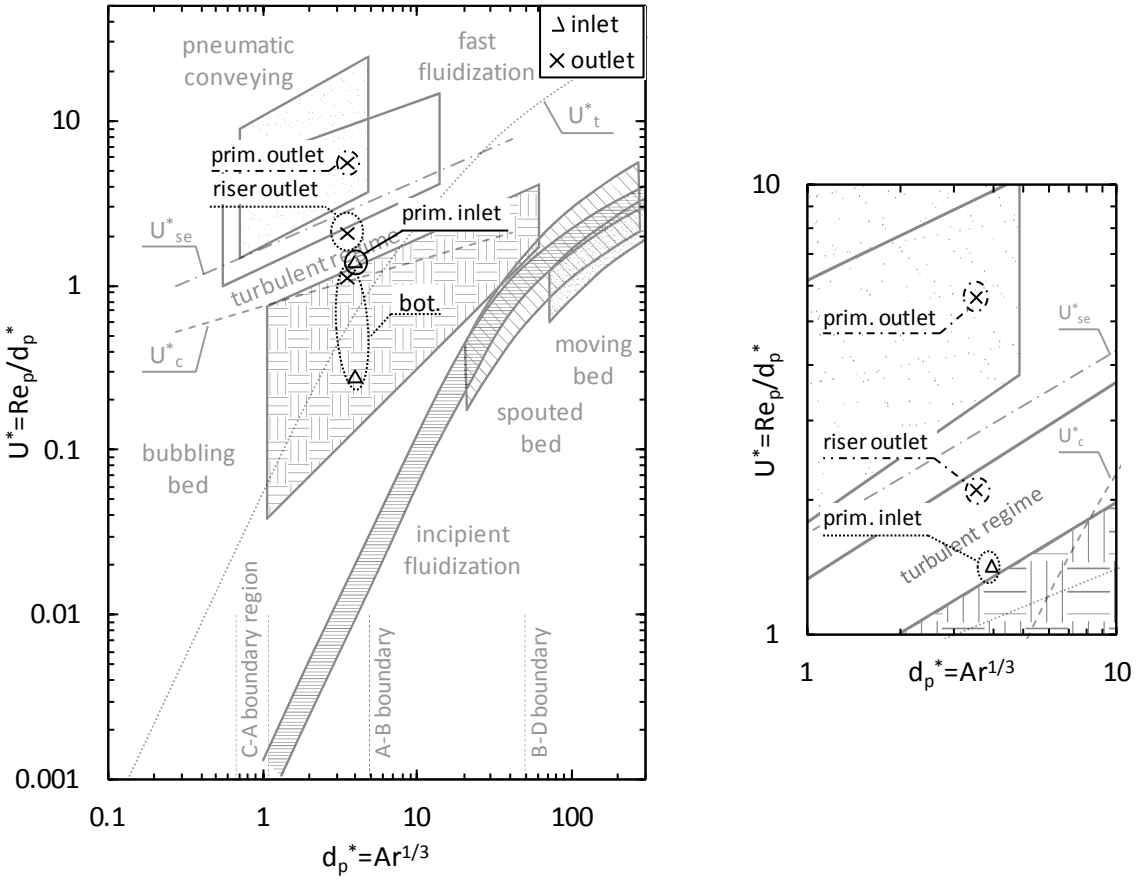

Fig. 39 Fuel reactor fluidized bed operating state with respect to quantities at the inlet and outlet depicted in the Grace diagram. Left: Operating conditions in the bottom, primary stage and at the riser outlet. Right: Detailed operating conditions in the primary stage and at the riser outlet. bot. - bottom, prim. - primary.

Detailed information on the fluidized bed cross-section and superficial gas velocities in the air reactor and fuel reactor are given in Table 4-5.

Table 4-5 Air and fuel reactor riser cross-sections and gas velocities.

Stage	Effective cross-section in mm	Superficial gas velocity in m/s with respect to the		U_s/U_{mf}		U_s/U_c		U_s/U_{se}	
		inlet	outlet	inlet	outlet	inlet	outlet	inlet	outlet
Air reactor									
bottom	900 x 900	0.65	0.62	29	28	0.31	0.22	0.10	0.08
primary	900 x 900	7.8	7.4	351	338	3.7	2.7	1.2	1.0
secondary	1044 x 1044	7.7	7.3	348	335	3.7	2.6	1.2	1.0
tertiary	1200 x 1200	8.0	7.7	364	350	3.8	2.7	1.3	1.03
Fuel reactor									
bottom	Ø 550	0.85	3.0	25	125	0.3	1.1	0.01	0.4
primary	Ø 550	4.2	15.1	126	625	1.5	5.4	0.5	2.0
riser top	Ø 900	1.6	5.6	47	234	0.6	2.0	0.18	0.76

Fluidized bed height

To obtain high gas conversion in chemical looping systems, it is necessary that the reactions proceed with excess oxygen carrier and sufficient residence time. Maximization of the gas-solids contact time is therefore crucial. The actual contact time, often referred to as space time, is difficult to assess in circulating fluidized bed applications. However, assuming very simplified conditions, the model of plug flow is applied where the residence time is computed from superficial gas velocity and height. This means that the residence time is the same for equally high risers with the same superficial gas velocity, which then also applies for the gas conversion. This means that the optimal height when comparing two chemical looping plant plants of similar capacity is, more or less, independent of thermal duty.

However, heat integration has to be kept in mind. Risers are typically equipped with evaporative water walls where the extractable heat depends on the surface area. Assuming that the quantity of energy transferred to the water walls relative to system heat input is independent of size, the surface area *S* has to increase linearly with plant capacity for similar heat transfer rates. Since the gas flow rates $\dot{V}$ correlate well with capacity, this can be expressed by:

$$\frac{S}{\dot{V}} = k \qquad \text{(eqn. 4-26)}$$

where *k* is an unknown constant quantity mainly depending on the heat transfer rate. Using

$$\dot{V} = U_g \cdot A_{riser}$$
$$S = 4 \cdot \sqrt{A_{riser}} \cdot h_{riser} \qquad \text{(eqn. 4-27)}$$

for rectangular cross-section risers and (eqn. 4-32) allows for the determination of the required riser height, h_{riser}

$$h_{riser} = k \cdot \sqrt{\dot{V} \cdot U_g} = f\left(\sqrt{\dot{V} \cdot U_g}\right) = f\left(\sqrt{P_{fuel} \cdot U_g}\right) \qquad \text{(eqn. 4-28)}$$

where P_{fuel} is the capacity of the plant. To evaluate the constant term in (eqn. 4-28), the heat transfer coefficient has to be known as postulated in (eqn. 4-26). Heat transfer rates in circulating

fluidized bed applications are subject to uncertainties where only experienced manufacturers have detailed knowledge (Basu and Fraser, 1991). However, with knowledge of the dependencies as described in (eqn. 4-28), published data can be used to find an applicable correlation for the riser height. It is assumed that the riser height follows the most generalized form of a root function as discussed above.

$$h_{riser} = \sqrt{a \cdot P_{fuel} + b} + c \qquad \text{(eqn. 4-29)}$$

Using the published data from existing circulating fluidized bed boilers summarized in Appendix Section 12.2, it was found that meaningful parameters are:

$$a = 1.523,\ b = -0.052,\ c = 9.678 \qquad \text{(eqn. 4-30)}$$

A graphical interpretation of the fitted curve is illustrated in Fig. 40.

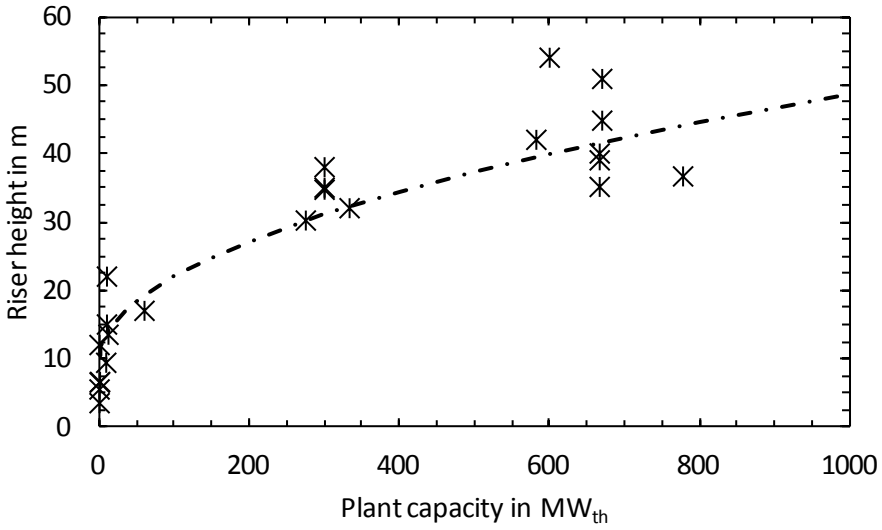

Fig. 40 Typical riser heights of circulating fluidized bed boilers and the fitted curve according to (eqn. 4-29). References are summarized in Appendix Section 12.2.

While for low riser heights, a limitation of chemistry is expected and thus the riser height has to be selected with respect to residence time, for large units, heat integration is critical. Applying the found correlation to a 10 MW_{th} boiler returns a required riser height of 13.6 m. Thus, the riser height of the 10 MW_{th} chemical looping combustion demonstration unit h_{CLC} is selected to be:

$$h_{CLC} = 15\ m \qquad \text{(eqn. 4-31)}$$

This corresponds to a plug flow equal gas residence time of $\tau_{g,AR}$ = 2 s in the air reactor and $\tau_{g,FR}$ = 2.7 s in the fuel reactor. Compared to the 140 kW chemical looping laboratory pilot at the Vienna University of Technology, this is an increase of a factor of 3.5 in the air reactor and 2.7 in the fuel reactor.

Estimation of solids entrainment rates

The solids circulation rate is an important parameter in circulating fluidized bed applications, and specific knowledge of the magnitude is of certain interest. The dimensions of the solids return loop parts are governed by the solids throughput, and heat exchange rates depend on the solids distribution. In chemical looping systems, solids circulation is of great importance as it governs

oxygen transport from the air reactor to the fuel reactor. Bai and Kato (1999) observed that solids circulation is cross-linked to the solids distribution along the axis of the fluidized bed. Li and Kwauk (1980) proposed a model describing the axial mean voidage by an exponential decay function. The model distinguishes between a lower dense section of nearly constant solids fraction ε_{sd} and a freeboard where the solid fraction ε_s decreases exponentially with freeboard height z_f.

$$\frac{\varepsilon_s(z_f) - \varepsilon_s^*}{\varepsilon_{sd} - \varepsilon_s^*} = e^{-a \cdot z_f} \qquad \text{(eqn. 4-32)}$$

In spite of the complex nature of fluidized beds, this simple approach has been found to describe reality quite well and is therefore often used in modeling. The parameters in the model have to be obtained experimentally either in cold flow models or in existing hot units. Many such studies are available in the literature and are used here to estimate these parameters.

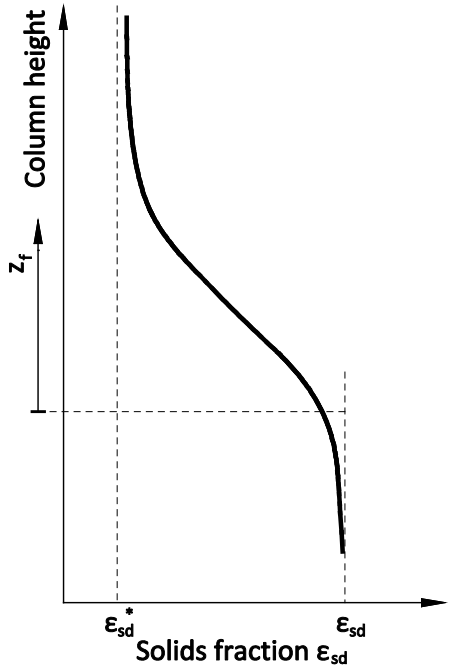

Fig. 41 Axial solids distribution in circulating fluidized bed applications. Adapted from (Kunii and Levenspiel, 1991).

The bed in the dense region can be described by the two-phase theory of Toomey and Johnstone (1952) which distinguishes between a particle-free bubble phase and an emulsion phase at minimum fluidization conditions. To account for the overestimation of the bubble volume by the two-phase theory, a correction term has to be included, e.g. Grace and Clift (1974). From this, the bed porosity can be estimated by

$$\varepsilon = \delta_b + (1 - \delta_b) \cdot \varepsilon_{mf} \qquad \text{(eqn. 4-33)}$$

where the bubble fraction δ_b quantifies the volumetric part of the bubbles. The equation proposed by Johnsson et al. (1991)

$$\delta_b = \frac{1}{1 + \frac{1.3}{f_2} \cdot \left(U_s - U_{mf}\right)^{-0.8}}$$
$$f_2 = \frac{0.26 + 0.70 \cdot e^{-3.3 \cdot d_p}}{\left(0.15 + \left(U_s - U_{mf}\right)\right)^{0.33}} \qquad \text{(eqn. 4-34)}$$

allows for an estimation of the bubble fraction. For the lower, dense section of a turbulent or fast fluidized bed, similar behavior as in a highly expanded bubbling bed is assumed, and it follows that

$$\varepsilon_{sd} = 1 - \varepsilon \qquad \text{(eqn. 4-35)}$$

At the transition from the dense bed to the lean phase of the bed, a splash zone is considered where the model of Li and Kwauk (1980) applies. The decay constant *a* in (eqn. 4-32) determines the curvature of the curve. Values ranging from 0.5 m^{-1} (Kunii and Levenspiel, 1991) to 6.4 m^{-1} (Wen and Chen, 1982) can be found in the literature. The correlation proposed by Choi et al. (1999) for the decay coefficient has improved validity for elevated temperatures. It involves gas and particle properties as well as fluidized bed dimensions.

$$a \cdot d_p = e^{-11.2 + 210 \cdot \frac{d_p}{D - d_p}} \cdot A^{-0.492} \cdot B^{0.725} \cdot C^{0.731} \cdot {C_d}^{-1.47}$$
$$A = \frac{d_p \cdot \rho_g \cdot \left(U_s - U_{mf}\right)}{\mu} \quad B = \frac{\rho_p \cdot g \cdot d_p}{\rho_g \cdot \left(U_s - U_{mf}\right)^2} \qquad C = \frac{\rho_p - \rho_g}{\rho_g} \qquad \text{(eqn. 4-36)}$$
$$C_d = \begin{cases} 24/Re_p & for\ Re_p \leq 5.8 \\ 10/{Re_p}^{0.5} & for\ 5.8 < Re_p \leq 540 \\ 0.43 & for\ 540 < Re_p \end{cases}$$

While the correlation after Choi et al. (1999) focuses on stationary fluidized beds and is used to model the splash zone, the correlation after Lei and Horio (1998) uses a large database from several researchers and is also valid for higher gas velocities. Therefore, this decay coefficient correlation was used to model the lean upper section of the expanded fluidized bed.

$$a \cdot D = 0.019 \cdot \left(\frac{G_s}{U_s \cdot \rho_g}\right)^{-0.22} \cdot \left(\frac{U_s}{\sqrt{g \cdot D}}\right)^{-0.32} \cdot \left(\frac{\rho_p - \rho_g}{\rho_g}\right)^{0.41} \qquad \text{(eqn. 4-37)}$$

The so-called saturation carrying capacity, ε_s^*, describes the extent to which an upward flowing gas is capable of carrying solids against gravitation at an infinite height. It depends on the properties of the particles and on the flow conditions. A comprehensive overview of formulations for the saturation carrying capacity can be found in Löffler et al. (2003). The saturation carrying capacity can be derived from the equilibrium elutriation constant, K_i

$$\varepsilon_s^* = \frac{K_i}{\rho_p \cdot (U_s - U_t)} \qquad \text{(eqn. 4-38)}$$

where K_i is defined according to (Colakyan and Levenspiel, 1984)

$$K_i = 0.011 \cdot \rho_p \cdot \left(1 - \frac{U_t}{U_s}\right)^2 \quad \text{(eqn. 4-39)}$$

Knowledge of ε_{sd}, ε^* and a allows for determination of the solids concentration profile where the solids hold-up follows from

$$m_{sol} = \int_0^{h_{riser}} \rho_p \cdot A_{riser}(z) \cdot \varepsilon_s(z)\, dz \quad \text{(eqn. 4-40)}$$

To estimate the solids circulation rate, it is assumed that the gas-solids suspensions density at the exit is equal to that at the top of the column. With knowledge of the solids upwards traveling velocity, $v_{sol\text{-}upward}$, the solids circulation is

$$G_s = \varepsilon_s(h_{riser}) \cdot \rho_p \cdot v_{sol-upward} \quad \text{(eqn. 4-41)}$$

The force balance of a single upward traveling particle in the fully developed zone of a circulating fluidized bed shows that the actual solids velocity is lower than the gas velocity, resulting from the necessity of relative gas-solid movement to exert a frictional force. This velocity, in terms of fluidization engineering, is referred to as the slip velocity. When assuming steady flow conditions (no particle acceleration), the slip velocity is equal to the terminal velocity U_t for single particles. The formation of particle clusters with a greater diameter means that the true slip velocity is slightly higher than the terminal velocity. Thus, the solids upward traveling velocity is assumed to be

$$v_{sol-upward} = U_s - 1.25 \cdot U_t \quad \text{(eqn. 4-42)}$$

This model allows for an estimation of the solids circulation in fluidized beds. With the proposed operating conditions, expectable solids entrainment rates from the air reactor and fuel reactor as well as solids inventories are determined. The calculated values are summarized in Table 4-6.

Table 4-6 Calculated solids entrainment rates from the air reactor and fuel reactor riser and solids inventories.

Item	Symbol	Air reactor	Fuel reactor	Unit
Solids flux	G_s	74	26	kg/m^{2}s
Solids inventory	m_{sol}	2400	1560	kg

With respect to reality, model parameters are subject to uncertainties. To cover this issue, the model was analyzed by a linear sensitivity analysis, shown in (Fig. 42). The sensitivity values, ξ_i, were calculated according to

$$\xi_i = \frac{\Delta G_i / G_0}{\Delta P_i / P_0} \quad \text{(eqn. 4-43)}$$

where the relative change in the solids circulation rate $\Delta G_i/G_0$ is evaluated in terms of relative changes in the control value, P_i. It was found that among the extensive parameters U_s, ρ_p and d_p, the superficial gas velocity effects the solids entrainment the most. Heavier and larger particles have a negative impact on solids circulation. Errors the in estimation of $v_{sol\text{-}upward}$, ε_{sd}, U_t, a and z_f

may cause significant deviation of model predicted values from reality. Thus, experimental verification is essential to avoid design errors.

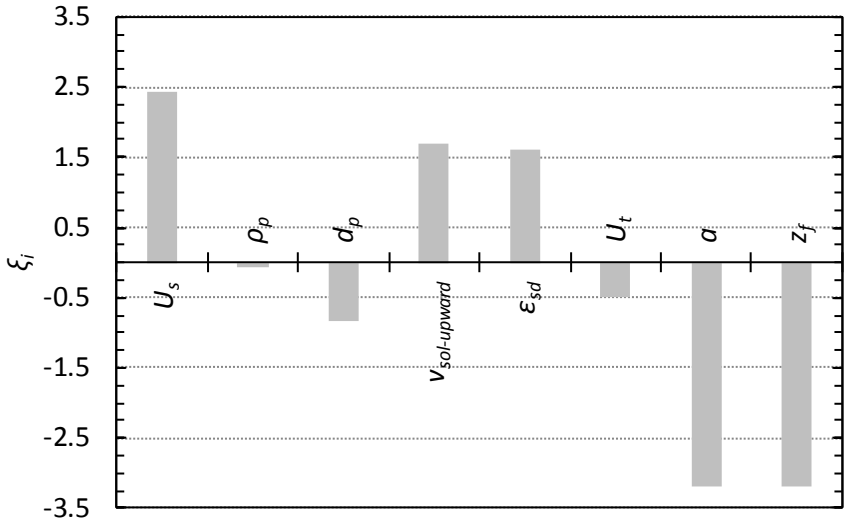

Fig. 42 Sensitivity of the solids circulation, G_s, rate with respect to relative changes in the control value P_i of ±5%.

Air and fuel reactor cyclone

The gas-solids separation at the exit of an entrainment riser is important for the performance of circulating fluidized bed systems. Such separators should provide high separation efficiency while incurring only minor pressure losses. The separation of solids can be based on either external, e.g. gravity or electrostatic, or internal, e.g. inertia or centrifugal forces. Cyclone separators are typically used in circulating fluidized beds since they are simple and provide a high degree of separation. The separation principle is based on centrifugal forces acting on the solids. Although the shape of cyclone separators is simple, computation of the specific performance is difficult. Several dimensional ratios for cyclone separators can be found in the literature (Hoffmann and Stein, 2002) where the design of Hugi (1997) (see also Hugi and Reh (1998)) focuses on cyclones with high solids entrance loads. Due to the high solids circulation rates, high solids entrance loads appear at the inlet of the cyclones in chemical looping applications. Therefore, the design is based on the cyclone separator geometry, which showed the best performance in Hugi's tests. The specific shape of this cyclone separator, including the dimensions, is given in Appendix Section 12.3 (p. 160). The Reynolds, Stokes and Froude numbers as constitutive parameters are used for scaling as described by Hoffmann and Stein (2002)

$$Re = \frac{D_a \cdot U_i}{\mu_g / \rho_g} \qquad \text{(eqn. 4-44)}$$

$$Stk = \frac{(\rho_p - \rho_g) \cdot d_p \cdot U_i}{18 \cdot \mu_g \cdot D_a} \qquad \text{(eqn. 4-45)}$$

$$Fr = \frac{U_i \cdot \frac{A_i}{A_o}}{\sqrt{D_o \cdot g}} \qquad \text{(eqn. 4-46)}$$

where D_a is the outer diameter of the cylindrical part of the cyclone separator body and U_i is the inlet gas velocity. These parameters allowed for the calculation of the cyclone dimensions of the chemical looping combustion demonstration unit.

Trefz (1992) found in his studies that the ideally centric vortex in a cyclone separator is disturbed by the gas stream entering tangentially to the cyclone body. This causes a displacement of the vortex to an eccentric position. To avoid radial acceleration of solids and gas towards the vortex finder, the position of the outlet should be readjusted to meet the new position of the occurring vortex, thus preventing the detachment of flow. For high performance, Trefz concluded that the eccentricity Δr should be

$$\Delta r / r_i = 0.2 \qquad \text{(eqn. 4-47)}$$

where r_i is the radius of the vortex finder tube and at an angular position of

$$\alpha = 225° \qquad \text{(eqn. 4-48)}$$

as depicted in Fig. 43. Later, Muschelknautz and Muschelknautz (1996, 1999) confirmed the findings of Trefz in general; however, their optimal position shifted towards 255°.

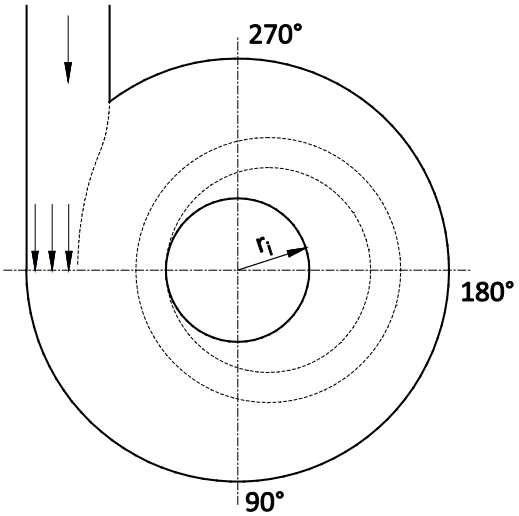

Fig. 43 Flow conditions at the vortex tube of a cyclone. Reproduced after Trefz (1992).

The design of air reactor and fuel reactor cyclones is derived from Hugi (1997) including the findings of Trefz (1992). Detailed drawings of both cyclones can be found in Appendix Section 12.4 (p. 161).

Loop seals

A loop seal is a non-mechanical device that allows the flow of solids from an entrance to an outlet while providing a sealing function. For proper operation, aeration gas has to be applied to the loop seal to produce a friction force, thereby provoking the motion of the solids. The loop seal is the central component of the return system of a circulating fluidized bed. Different types of loop seals are used in circulating fluidized bed applications, with loop seals of the L- and J-types being the most commonly used. A rectangular J-shaped loop seal was applied to the design of the upper and internal loop seal, while a modified V-shaped version of a J-shape loop seal was used in the lower loop seal section. Such loop seals are composed of two vertical parts connected by a horizontal passage. In loop seal operation, the horizontal part is critical where solids motion is

governed by the pressure gradient between the inlet and the outlet. Thus, this part contributes the most to the pressure drop across the loop seal and therefore has to be kept small in size (Basu and Butler, 2009). The pressure balance and typical vertical and horizontal solids velocities are considered with the minimum free cross-section, and are determined for a critical solids flux of

$$Gs_{critical} = 300 \frac{kg}{m^2 s} \quad \text{(eqn. 4-49)}$$

Such values, and even higher, have been appeared in the 140 kW chemical looping combustion pilot at the Vienna University of Technology and are in the range proposed by Basu and Fraser (1991). The length of the loop seal is divided into three parts: the inlet, the center and the outlet parts. While the inlet area covers the area below the downcomer, the outlet area covers the area below the outlet tube. Separate wind boxes supplying the necessary fluidization gas are employed, allowing for optimization of the gas demand of the loop seal. A well-operated loop seal should allow the solids to pass from the inlet to the outlet without limiting the solids throughput while providing proper sealing. This is of special importance in chemical looping systems where gas leakage may cause either a dilution of the CO_2 when nitrogen passes through the upper loop seal from the air reactor to the fuel reactor or a loss of carbon if CO_2 leaks through the lower loop seal from the fuel reactor to the air reactor.

The loop seal fluidization gas demand is determined by prescribing a ratio of superficial to minimum fluidization velocity of

$$Us_{loop\ seal} = 10 \cdot U_{mf-loop\ seal} \quad \text{(eqn. 4-50)}$$

Such high values are typical for high solids throughput small-scale circulating fluidized bed boilers. The solids inventory in the loop seals is determined using equation (eqn. 4-33) and (eqn. 4-34). To avoid mixing of fuel reactor CO_2 with undesired gas components, the loop seals are fluidized with steam. A summary of calculated loop seal cross-section areas, fluidization gas demands and solids inventories is given in Table 4-7.

Table 4-7 Summary of loop seal dimensions, fluidization gas flow rates and solids inventories. ULS – upper loop seal, LLS – lower loop seal, ILS – internal loop seal.

Item	ULS	LLS	ILS	Unit
Inlet (downcomer) dimensions	Ø 600	550 x 550	Ø 300	mm
Outlet dimensions	Ø 600	550 x 550	Ø 300	mm
Total cross-section area	0.763	0.715	0.22	m^2
Fluidization gas demand				
inlet	54.8	64.5	13.4	kg/h
center	20.5	23.5	10.0	kg/h
outlet	54.8	64.5	13.4	kg/h
Maximum solids throughput	295	270	235	kg/m^2s
Estimated solids inventory	1440	1900	250	kg

Bed material cooler

The bed material cooler is an external bubbling fluidized bed with heat exchanger surfaces emerging into the bed. Typically, low velocity bubbling fluidized beds are used where the heat transfer coefficients are very high. Such devices can therefore be relatively compact with respect to the heat transfer rate. Compared to heat exchanger surfaces placed in the circulating fluidized

bed riser, the heat transfer rate in the bed material cooler can be controlled easily. This helps meet the varying fuel load conditions and thus increases the load control capability of the unit. The heat transfer rate can basically be influenced by the fluidization conditions and by the solids flow to the bed material cooler chamber, which is achieved by a mechanical solids flow control valve between the upper loop seal and the inlet to the bed material cooler, shown in Fig. 37. The bed material cooler (Fig. 44) basically consists of two chambers: the settling chamber and the heat exchanger chamber. Fluidization is applied to both chambers to allow for solids flow.

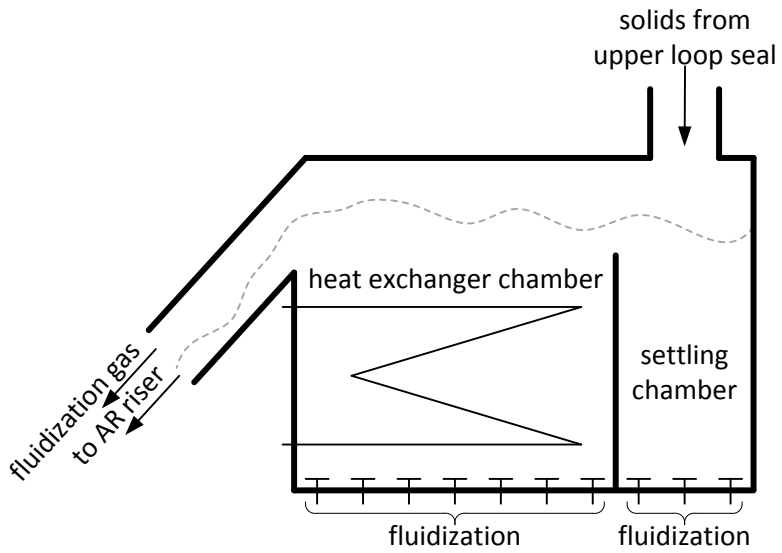

Fig. 44 Schematic setup of the bed material cooler with the settling chamber and the heat exchanger chamber indicated.

The hot solids coming from the loop seal enter the bed material cooler at the top and are directed to the settling chamber. In the settling chamber, the agitated solids are settled down in order to provide a homogeneous flow to the heat exchanger. After passing the heat exchanger, the cooled solids are directed to the circulating fluidized bed riser. The heat transfer rate in such heat exchangers is governed by the bed-to-heat exchanger wall, heat conductivity through the wall and the inner heat transfer from the wall to the cooling fluid. Applicable heat transfer rates are calculated according to VDI (2010), including all three shares, and the necessary heat exchanger surface areas are determined. A summary of the calculated bed material cooler parameters at nominal load is given in Table 4-8.

Table 4-8 Summary of bed material cooler parameters at nominal load.

Item	Symbol	Value	Unit
Heat exchanger chamber solids temperature	ϑ_{BMC_sol}	800	°C
Heat transfer coefficient bed-to-heat exchanger	α_{FB}	677	W/m^{2}K
Bed material cooler tube outer diameter	d_T	48.3	mm
Bed material cooler wall thickness	s_T	6.3	mm
Bed material cooler total k-value	k_{BMC}	610	W/m^{2}K
Required bed material cooler surface area	A_{BMC}	8.96	m^2
Heat exchanger chamber dimension			
width	a_{BMC}	1200	mm
depth	b_{BMC}	1100	mm
height	h_{BMC}	1500	mm
Settling chamber dimensions			
width	a_{set}	440	mm
depth	b_{set}	1100	mm
height	h_{set}	900	mm
Fluidization gas demand			
heat exchanger chamber	$\dot{m}_{FS\_BMC}$	360	kg/h
settling chamber	$\dot{m}_{FS\_set}$	145	kg/h
Solids inventory			
heat exchanger chamber	m_{BMC}	3700	kg
settling chamber	m_{set}	890	kg

Summary of the relevant design parameters

A summary of the most relevant 10 MW chemical looping combustion demonstration unit design parameters are summarized in Table 4-9.

A three-dimensional drawing of the overall setup, including the flue gas heat recovery section and auxiliary units, is shown in Appendix Section 12.2 (p 160). The drawing was created by BERTSCHenergy, a partner in the EU-project INNOCUOUS, based on the design presented here and the process integration presented in Chapter 3 *"Process design"* (p. 23).

Table 4-9 Summary of relevant 10 MW chemical looping combustion demonstration unit design parameters.

Item	Value	Unit
Fuel power input	10	MW
Design air/fuel ratio	1.1	-
Design fuel reactor temperature	900	°C
Design air reactor temperature	960	°C
Oxygen carrier mean particle size	200	µm
Oxygen carrier particle apparent density	3425	kg/m^3
Oxygen carrier sphericity	0.9	-
Air reactor outlet gas flow rate	39786	m^3/h
Air reactor outlet cross-section area	1.44	m^2
Air reactor outlet gas velocity	7.7	m/s
Air reactor riser height	15	m
Estimated air reactor solids entrainment	74	kg/m^2s
Fuel reactor outlet gas flow rate	12933	m^3/h
Fuel reactor outlet cross-section area	0.64	m^2
Fuel reactor outlet gas velocity	5.6	m/s
Fuel reactor riser height	15	m
Estimated fuel reactor solids entrainment	26	kg/m^2s
Fluidization gas demand		
upper loop seal (steam)	130.1	kg/h
lower loop seal (steam)	152.5	kg/h
internal loop seal (steam)	36.8	kg/h
BMC settling chamber (air)	145	kg/h
BMC heat exchanger chamber (air)	360	kg/h
Estimated solids inventories		
Air reactor riser	2400	kg
Fuel reactor riser	1560	kg
upper loop seal	1440	kg
lower loop seal	1900	kg
internal loop seal	250	kg
BMC settling chamber	890	kg
BMC heat exchanger chamber	3700	kg
Total solids inventory	12.14	to

4.5 Summary and conclusion

Based on the specific requirements, such as a prolonged gas solids contact time, the design of a 10 MW fuel power input chemical looping combustion unit was developed. The system is based on the dual circulating fluidized bed reactor system concept where both the air and the fuel reactor are operated in a circulating fluidized bed regime.

A heat integration setup was established, including a water wall cooled air reactor and an external bed material cooler in a return loop of the air reactor. The arrangement allows for part load operation while influencing the conditions in the fuel reactor only very little. Additional auxiliary energy demand is reduced by directing the bed material cooler fluidization air to the air reactor where it takes part in oxygen carrier oxidation.

A fast fluidized bed is applied to the design of the air reactor, focusing on high solids entrainment rates. Air staging is used to control the specifically occurring solids fluxes. The design of the fuel

reactor bases on a turbulent fluidized bed regime, which is expected to promote fuel conversion rates. Air and fuel reactor heights were determined by cross-correlating the capacity and height of existing circulating fluidized bed boilers. Cross-section areas, gas flow rates and expectable solids holdups were assessed.

The dimensions of the cyclone separators placed at the exit of the air reactor and fuel reactor were derived, focusing on high solids entrance loads and high performance.

The design of the three loop seals in the dual circulating fluidized bed concept was adapted to meet the demands of the size of the unit. The loop seal was split into three areas: the inlet, the center, and the outlet areas. Expected solids inventories and fluidization gas flow rates were determined.

The dimensions of the external bed material cooler were calculated by quantification of the heat transfer rates and solids inventories, and fluidization gas flow demand was determined for the bed material cooler section.

5 Cold flow modeling

In the scale-up of a new technology, a multitude of critical issues arise which have to be handled carefully by designers and engineers. The development process therefore typically involves several small enlargement steps, since important characteristics can change significantly from the small to large scale. Numerical models may assist in the process, but experimental validation is still required. Conservative scale-up ratios can help to decrease the level of uncertainty. However, large pilot plants are costly and thus an extensive experimental based scale-up program may not be feasible.

Although fluidized beds are considered a mature technology with several commercial plants operating worldwide, the hydrodynamic patterns and gas-solids mixing are often misinterpreted. Guaranteed performance data may not be reached and severe problems may appear during operation. Simplified scaled models of hot units are therefore often discussed to improve the reliability of the scale-up process. Several researchers have discussed different approaches to the development of such models; an overview has been given by Rüdisüli et al. (2012). Buckingham's π theorem (Perry, 1999) is a tool for the development of similarity rules which allows for carefully designed models to predict the behavior of a hot unit with little effort. The difficulty is that if the modeler is too precise and effects of marginal significance are included the resulting similarity rules may be overly restrictive and limit the choice of models. Glicksman (1984) proposed the most comprehensive set of similarity parameters for fluidized beds.

In the following, the Glicksman similarity parameters are applied to the design of the 10 MW chemical looping combustion demonstration unit, as described in Chapter 4 "Chemical looping reactor system design" (p. 53). A scaled cold flow model is developed which is capable of simulating the flow patterns in the hot unit. The model allows for the quantification of characteristic fluidized bed parameters such as solids circulation rates. Critical design elements can be identified and improvements can be made with very little effort. The outcome of the cold flow model study will underline the feasibility of the developed design.

5.1 The Glicksman set of scaling parameters

The Glicksman (1984) set of scaling laws allows for scaling a commercial fluidized bed. It is based on the conservation of mass (solids and gas) and on fluid-to-particle forces. It is composed of the particle Froude number, the particle-gas density ratio, the particle Reynolds number, the fluidized bed to particle diameter ratio, the bed geometry, the particle sphericity and the particle size distribution.

$$Fr_p = \frac{{U_s}^2}{g \cdot d_p}, \quad \frac{\rho_p}{\rho_g}, \quad Re_p = \frac{\rho_g \cdot U_s \cdot d_p \cdot \rho_p}{\mu_g}, \quad \frac{D}{d_p}, \quad geometry, \quad \phi, \quad PSD \qquad \text{(eqn. 5-1)}$$

This set of equations, often referred to as the full set of Glickman's scaling parameters, has been experimentally validated and shown high agreement between the model and hot unit (Nicastro and Glicksman, 1984). Later, Glicksman et al. (1993) applied the Ergun equation (eqn. 4-1) to describe the particle-gas drag in his original set of governing equations. He showed that this allows for neglecting the fluidized bed to particle diameter when the ratio of superficial to minimum fluidization velocity is similar. This introduced a new degree of freedom in scaling since the actual size of the cold flow model can be selected more arbitrarily.

$$Fr_D = \frac{{U_s}^2}{g \cdot D}, \frac{\rho_p}{\rho_g}, \frac{U_s}{U_{mf}}, geometry, \phi, PSD \qquad \text{(eqn. 5-2)}$$

It also turned out that when viscous forces are dominating, which is the case for low Reynolds numbers, the particle-gas density ratio can also be neglected.

$$Fr_D = \frac{{U_s}^2}{g \cdot D}, \frac{U_s}{U_{mf}}, geometry, \phi, PSD \qquad \text{(eqn. 5-3)}$$

Often, (eqn. 5-1) and (eqn. 5-2) are referred to as the simplified or reduced set of Glicksman's scaling parameters. The experiments of Glicksman et al. (1993) clearly underlined the validity of the simplified set of scaling laws.

5.2 Application of similarity rules

Applying the full set of scaling parameters (eqn. 5-1) to the design of the 10 MW chemical looping combustion unit revealed that a scaling factor of 1:4.7 is required for fuel reactor scaling and 1:4.9 for the air reactor. Thus, very large model geometries and high air flow rates of more than 1000 m^3/h would be needed and difficulties in air delivery would arise. However, as already mentioned above, much smaller models are also capable of describing these phenomena very well. Thus, selecting a scaling factor and applying the simplified scaling laws (eqn. 5-2) is expected to be more meaningful than erecting a large cold flow model in 1:5 scale.

A linear scaling factor of 1:10 was finally selected since the dimensions of the model are within the feasible range for small-scale laboratories. The relevant scaling parameters and the corresponding dimensionless numbers for the fuel reactor are summarized in Table 5-1 as an example. The values of the air reactor scaling can be found in Appendix Section 12.6 (p. 163). Using the simplified scaling laws led to significantly lower dimensionless particle diameters and gas flow rates in the model than in the hot unit. This circumstance is depicted in the Grace diagrams of both risers, as shown in Fig. 45. Therefore, the flow pattern may differ strongly in the model and hot unit. In the air reactor, the fluid dynamic regime will also be different. Therefore, the gas velocity and particle diameter were adjusted to fit the flow pattern in the Grace diagram.

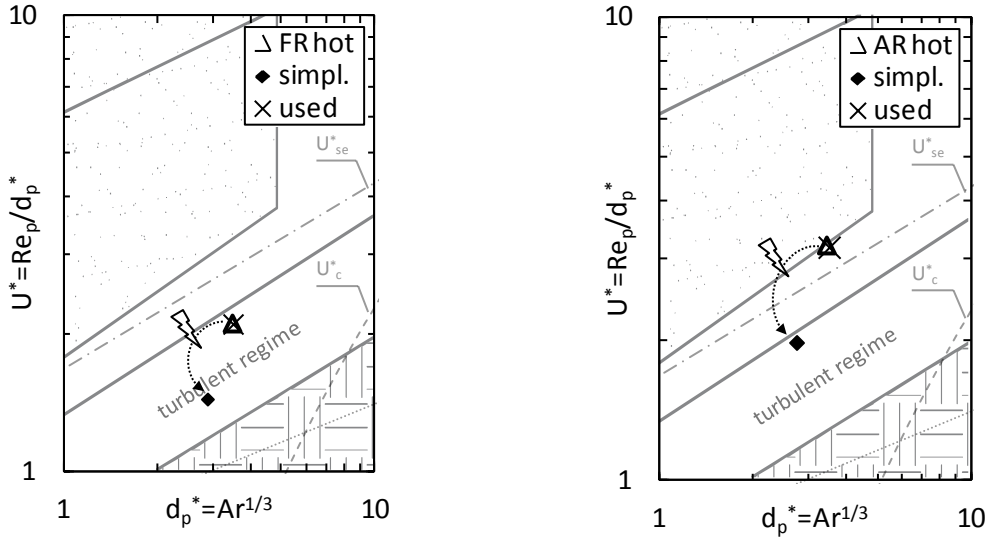

Fig. 45 Cold flow model scaling at the top of the risers illustrated in the Grace diagram. Left: Scaling of the fuel reactor outlet. Right: Scaling of the air reactor outlet.

Table 5-1 Summary of fuel reactor scaling.

Item	Unit	FR hot	Perfect match				Used	
			Full set		Simplified set			
U_s	m/s	5.65	2.61		1.79		1.78	
d_p	µm	200	42.7		35.3		50	
ρ_p	kg/m^3	3425	1.5E+4		1.5E+4		8900	
ρ_g	kg/m^3	0.27	1.19		1.19		1.19	
μ_g	Pa·s	4.2E-05	1.8E-05		1.8E-05		1.8E-05	
Dimensionless numbers			abs.	rel. ($^{hot}/_{cold}$)	abs.	rel. ($^{hot}/_{cold}$)	abs.	rel. ($^{hot}/_{cold}$)
Fr_p	-	1.6E+04	1.6E+04	1	9.2E+03	1.76	9.6E+03	1.68
Fr_D	-	3.6	3.6	1	3.6	1	5.4	0.66
ρ_p/ρ_g	-	1.26E+04	1.26E+04	1	1.26E+04	1	7.5E+03	1.68
Re_p	-	7.35	7.35	1	4.16	1.77	7.35	1
Us/U_{mf}	-	233.5	233.5	1	233.5	1	233.5	1
D/d_p	-	4.5E+03	4.5E+03	1	2.54E+03	1.77	1.8E+03	2.5
ϕ	-	0.9	0.9	1	0.9	1	0.95	0.95
$Gs{\cdot}\rho_p^{-1}{\cdot}U_s^{-1}$	-	-	-	0.49	-	0.72	-	0.99
Scale	-	-	1:4.7		1:10		1:10	
Volumetric gas flow rate	m^3/h	12933	347		52		50	

Selected particles in the cold flow model

To meet the requirement of high density particles in the cold flow model, particles made of bronze were used. The particles, manufactured by ECKA granules, were taken from an industrial sieve with a fraction size between 45-63 µm and had a globular shape. Similar particles with a different particle diameter have been used successfully in the past in cold flow model tests (Kaiser et al., 2003; Pröll et al., 2009d). Images of the particles are shown in Fig. 46.

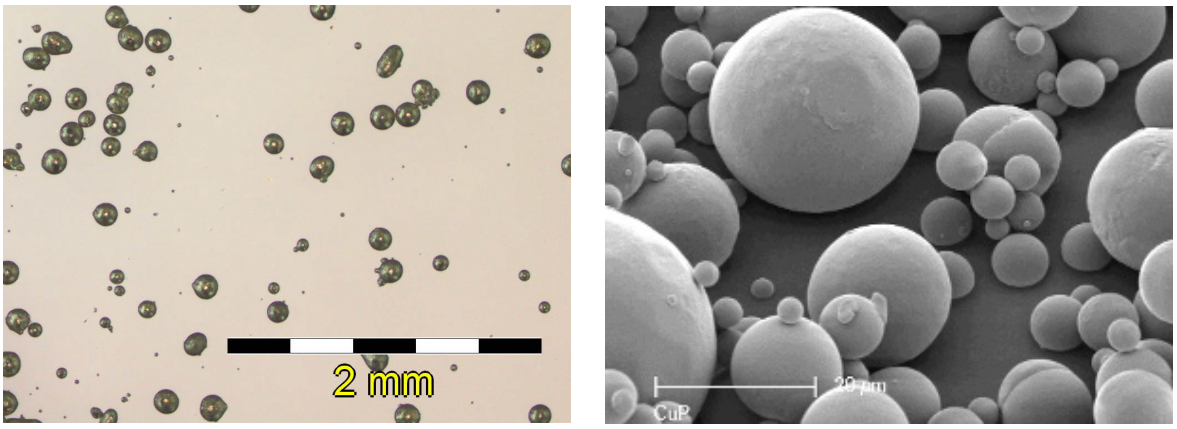

Fig. 46 Images of the bronze particles used in the cold flow model. Left: image taken using a OLYMPUS BX61 and OLYMPUS BX-UCB microscope system. Right: image taken from ECKA (2013).

The particle size distribution is determined by:

- sieve analysis using an ALPINE LS-N/AC air jet sieve and HAVER&BOECKNER DIN ISO 3310-1 sieves,
- graphic analysis of particle images using OLYMPUS BX61 and BX-UCB microscope/video equipment, and
- low angle laser light scattering using the Malvern Mastersizer 2000.

The results are shown in Fig. 47; the mean particle diameter ranged from 50-68 µm. While the optical measurement by the microscope slightly overestimated the particle diameter, likely due to un-separated particles, the sieving method led to an underestimation of the particle size compared to the Malvern Mastersizer 2000. This was probably caused by limited availability of adequate sieves. However, the particle diameters were within the expected range.

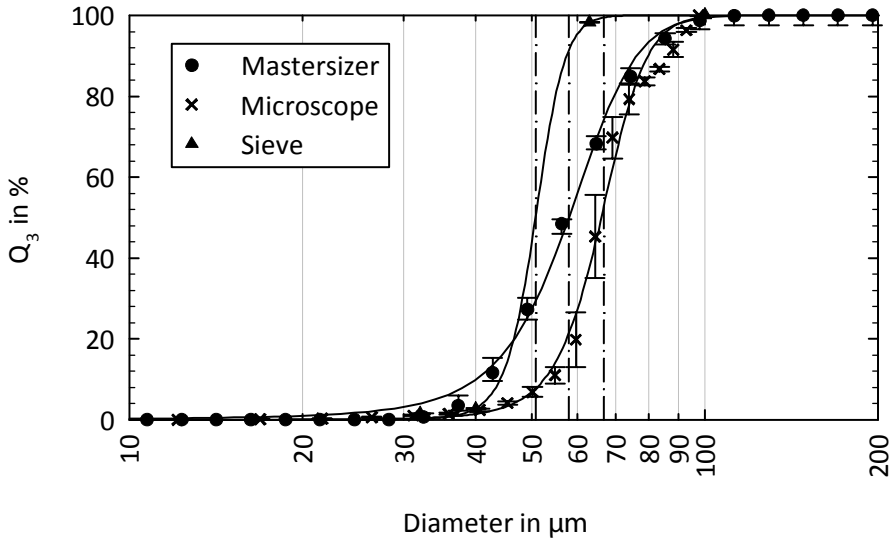

Fig. 47 Cumulative bed material size distribution depending on the measurement technique.

The bulk density of the particles was determined by weighing a specified volume of a bulk of particles. The bulk density was in the range of 5029 ±15 kg/m^3, which corresponds to a voidage of about 43%.

5.3 The cold flow model setup

A schematic drawing of the cold flow model is depicted in Fig. 48, including the air and fuel reactor risers, the cyclones, the upper, lower, and internal loop seals and the bed material cooler. The dimensions were derived from hydrodynamic scaling using a scaling factor of 1:10 from the 10 MW chemical looping combustion demonstration unit, as discussed above. The model is built of transparent acrylic glass allowing visual observation of the fluid dynamic pattern inside. Air is supplied in stages to the air reactor to control the solids flow rate to the fuel reactor. To account for the increase of the gas volume inside the fuel reactor of the hot unit, two additional gas injection ports are attached (FR exp 1 and FR exp 2). For an ideal chemical looping combustion system, the gas volume increase in the fuel reactor can be as high as three times the inlet flow rate, which will have a significant influence on the hydrodynamics.

The loop seal area is split into three parts: the inlet, center, and outlet sections. Air is provided separately to each section via separate flow meters. To control the solids flow to the bed material cooler, a solids flow control valve is attached to the upper loop seal. The solids flow control valve consists of a cone pushing against an inclined circular hole in the upper loop seal. The position of the cone and thus solids flow is adjusted by a computer controlled multiphase stepper motor. Fig 49 is a simplified sketch of the solids flow control valve and the upper loop seal.

A model of the heat exchanger tubes made of SL-TOOL® NewWhite produced by stereolithography is included, simulating the flow resistance against solids motion. The nozzle grid at the AR bottom, FR bottom, the loop seals, the bed material cooler settling chamber and the bed material cooler heat exchanger chamber are equipped with separate nozzles where each nozzle can be controlled individually.

A filter system at the outlet of the two cyclones is used to avoid emission of dust. The whole model is grounded and a self-adhesive copper tape is wrapped around the model for electric discharge.

The cold flow model was described using 3D CAD software and a virtual model is depicted in Fig. 50. A picture of the cold flow model ready for operation is included in Fig. 51, where the pressure hoses and the copper tape can be seen.

A summary of gas flow rates determined by scaling from the design are summarized in Table 5-2.

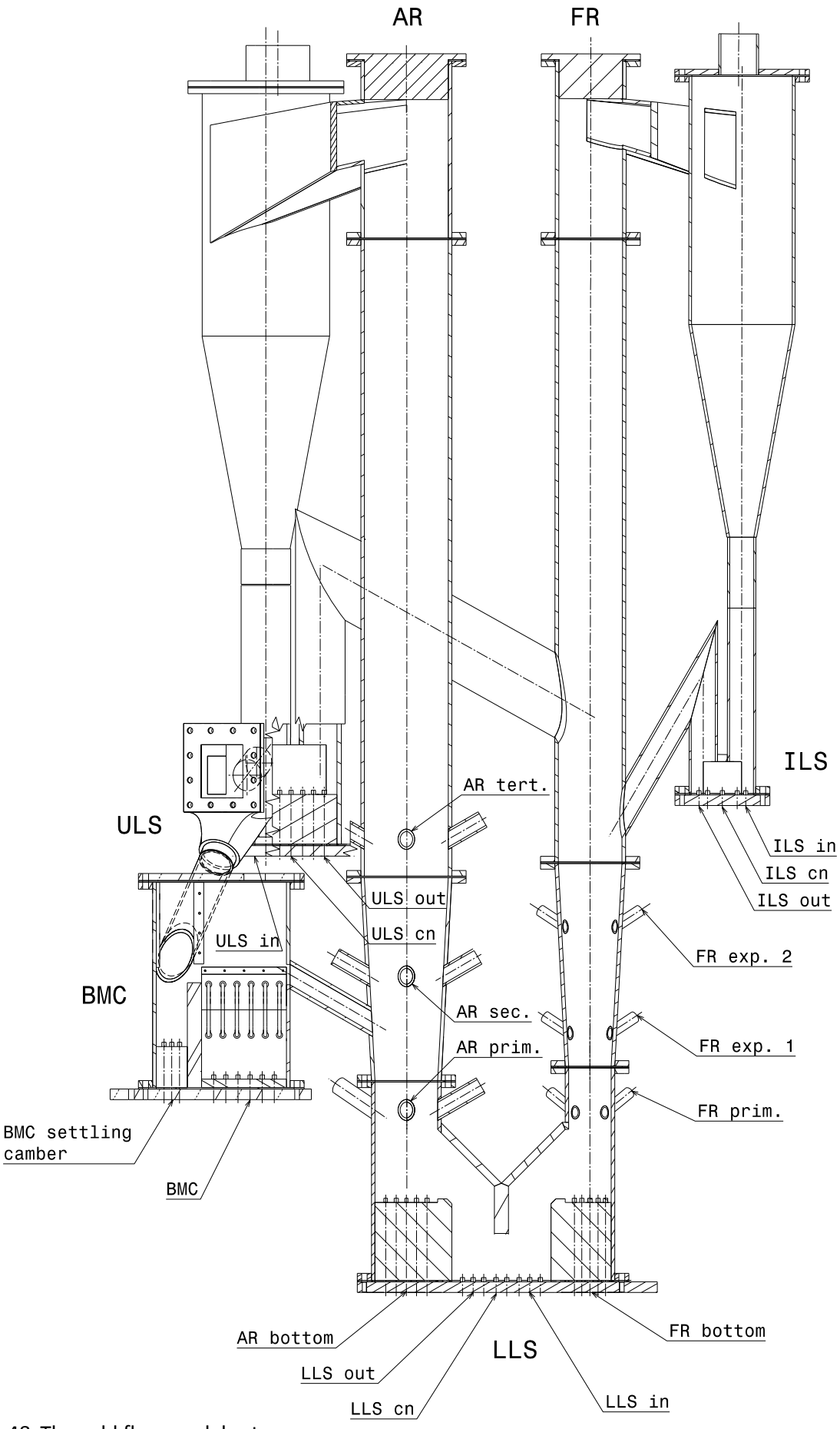

Fig. 48 The cold flow model setup.

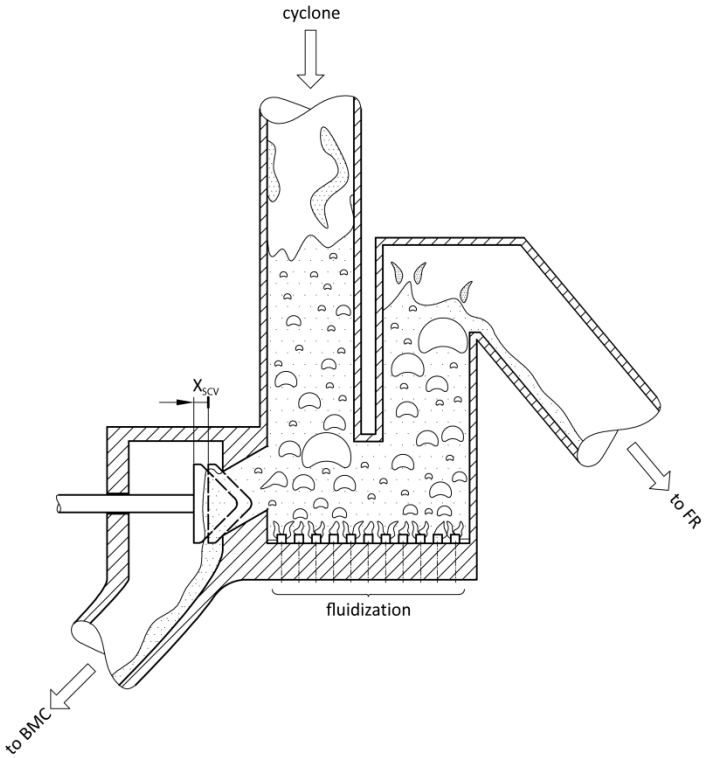

Fig 49 Setup of the solids flow control valve and the upper loop seal section. Indicated is the solids flow control valve position X_{SCV}.

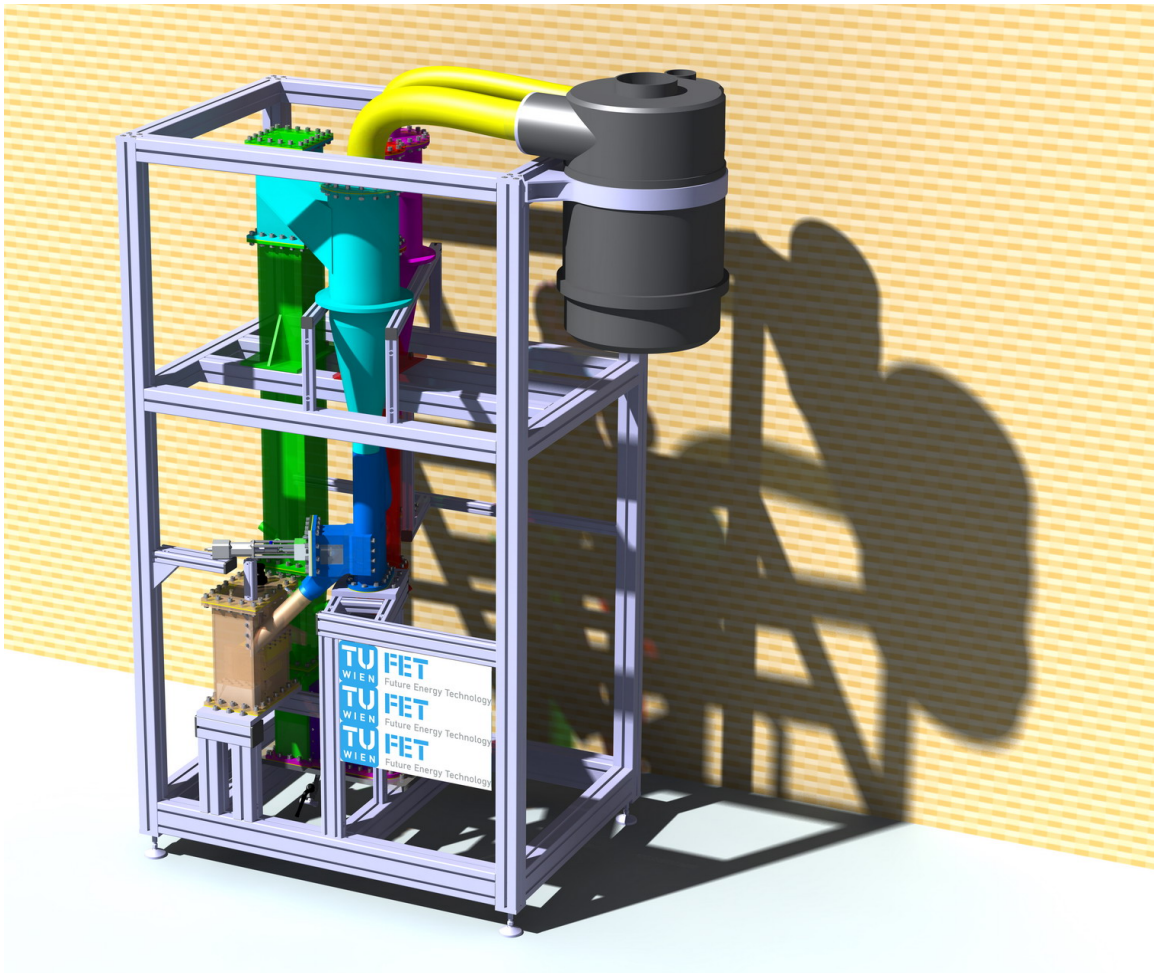

Fig. 50 Rendered 3-D model of the cold flow model including the support framework.

Fig. 51 Picture of the cold flow model ready for operation.

Table 5-2 Fluidization air flow rates in the cold flow model for simulated 10 MW hot chemical looping combustion demonstration unit operation.

Item	Value	Unit
AR bottom	9	Nm^3/h
AR prim.	85	Nm^3/h
AR sec.	35	Nm^3/h
AR ter.	35	Nm^3/h
FR bottom	3	Nm^3/h
FR prim.	13	Nm^3/h
FR exp. 1	16	Nm^3/h
FR exp. 2	16	Nm^3/h
BMC	2.8	Nm^3/h
BMC settling	1.6	Nm^3/h
ULS in	750	Nl/h
ULS cn	500	Nl/h
ULS out	750	Nl/h
LLS in	1100	Nl/h
LLS cn	400	Nl/h
LLS out	1100	Nl/h
ILS in	240	Nl/h
ILS cn	240	Nl/h
ILS out	240	Nl/h

5.3.1 Measurement setup and procedures

The measurement setup of the cold flow model includes quantification of volumetric flow rates of the inlet air, pressures, riser solids flow rates and solids elutriation rates from the cyclone. Additionally, at the outlet of the cyclones, ports are available for connection to a gas analyzer.

Volume-flow measurement

The air is delivered pressurized at 8 barg to the cold flow model air distributor system where variable area flow meters of type “KROHNE VA 40” and “KROHNE DK48” are used to quantify the air flow rates. The specific type depends on the gas flow rates, which are adjusted by hand valves. These valves also provide the necessary pressure drop to meet the pressures in the cold flow model.

Pressure measurement

The pressure measurement setup of the cold flow model includes 52 pressure measurement ports. To avoid disturbance of the hydrodynamics inside the model, very small holes, e.g. 1 mm in diameter, are used to extract the pressure information. To avoid damage to the pressure measurement system, wool is put in place. Flexible hoses connect the pressure measurement ports with a centralized pressure transmitter unit where the data acquisition system also is located. Type “Kalinsky DS2-240” pressure transmitters using a piezoresistive cell for detection of pressures relative to ambient are used. Alternatively, four pressure transmitters of the “Epcos AUR 0.100 F C4 TN H S2.0” type can be directly attached to the pressure ports, allowing for rapid detection of pressure fluctuations. Both types of pressure transmitters are temperature compensated to avoid drift of the signal.

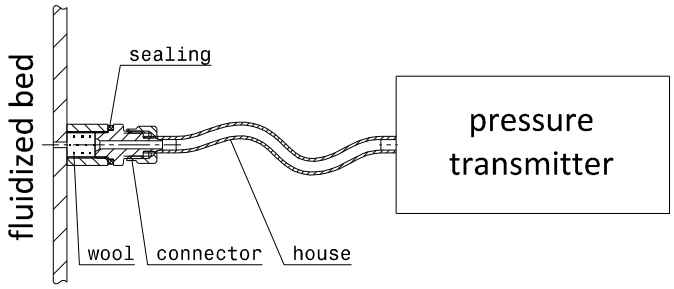

Fig. 52 Pressure measurement setup.

The pressure ports are equally distributed along the height of the two risers with a densification of ports where high pressure gradients are expected. The setup of the pressure measurement ports including detailed information on specific location and names is given in Fig. 53.

Data acquisition and recording system

The data acquisition system is equipped with two National Instruments data acquisition cards of type “NI PCIe 6323” with several analog and digital I/O ports. National Instruments LabView is used for visualization of pressure diagrams and to record the measurement signals.

Riser solids flow rate measurement

The solids flow rate measurement procedures are based on the quantification of solids accumulation and time in the downcomer when the loop seal fluidization is stopped. While for detection of the air reactor solids entrainment the upper loop seal air supply has to be stopped, the internal loop seal air supply has to be stopped for fuel reactor entrainment rate measurements.

Solid elutriation from the cyclones

The discharge of solids from the cyclone is determined by weighing the solids collected in the dust filters. The type MANN+HUMMEL Europiclon® filters are combined cyclone and paper de-dusters. The collecting containers can be dismantled and weighted, allowing for rapid quantification of the discharged material quantities.

Gas leakage and split-up measurement

For the determination of gas leakage rates and gas split-up in the upper and lower loop seals, gas tracer measurements are used. Small amounts of methane are introduced into the fluidization area of interest. The carbon concentration in the gas streams after the air and fuel reactors is detected using a flame ionization detector (TESTA FID 1230 PV) which allows for the detection of very small amounts of carbon. Specific gas leakage and gas split-up rates are determined by closing the carbon balance around the cold flow model setup.

Process flow and instrumentation diagram

A process flow and instrumentation diagram of the cold flow model is given in Fig. 54.

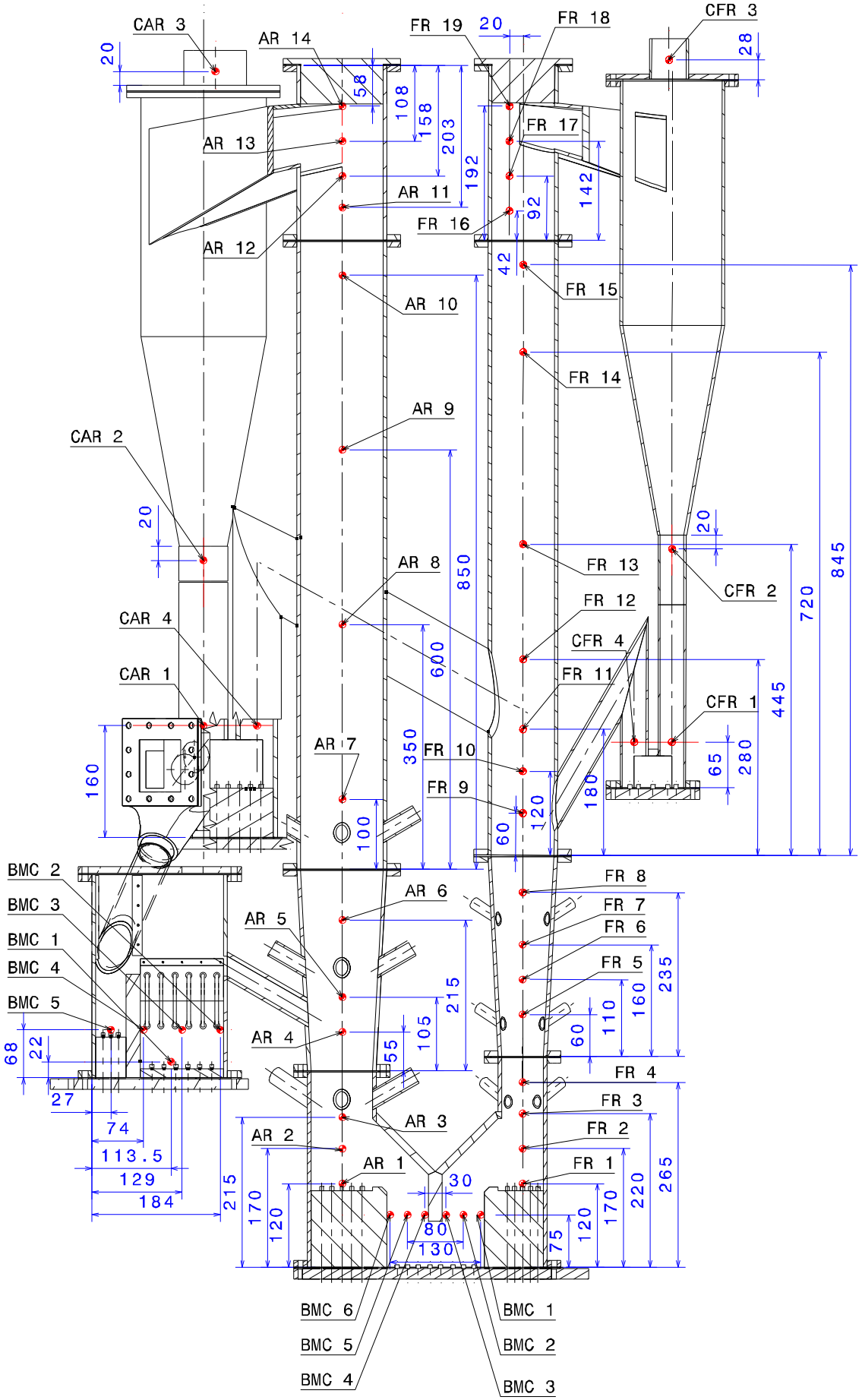

Fig. 53 Drawing of the pressure measurement ports locations with denomination.

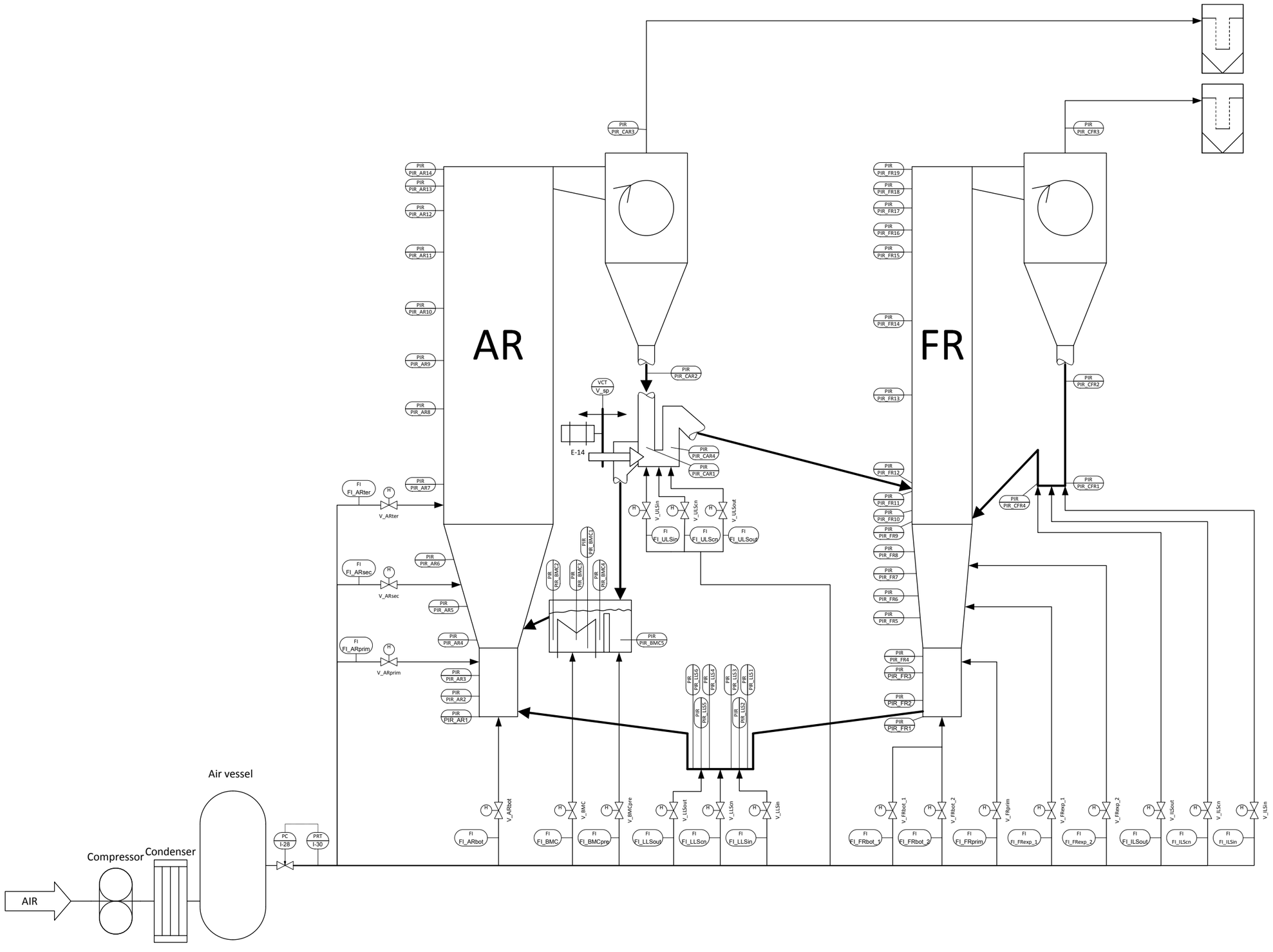

Fig. 54 The process flow and instrumentation diagram of the cold flow model.

5.4 Cold flow model testing results

5.4.1 Cyclone optimization

The cyclone is a critical part of the circulating fluidized bed system. Poorly operating cyclones may lead to severe problems in certain parts of the equipment, e.g. the filter system, when solids losses are too high. Well-operating cyclones should allow for highly efficient gas-solids separation while causing only a minimal gas pressure drop. The main parameters influencing the separation efficiency are the cyclone inlet flow pattern, inlet solids loading, the movement of the solids strand and gas in the cyclone body and the flow pattern at the gas outlet. The design of the cold flow model cyclone allows for an investigation into the effect on the inlet flow pattern by varying the gas and solids flow rates and the effect of the flow pattern at the outlet by changing the vortex finder length *l* and angular position *α* (Fig. 55).

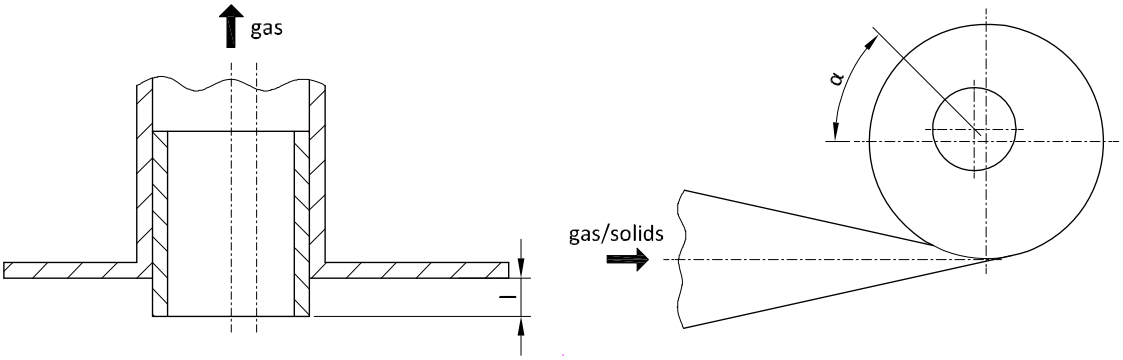

Fig. 55 Geometry of the vortex finder tube.

Air reactor cyclone performance

Solids elutriation from the air reactor cyclone is determined by weighing the solids collected in the filter system after 10 minutes of continuous operation. Since only the global solids loop is of interest, the fuel reactor is fluidized only in the bottom region to avoid solids stagnation in the air reactor solids feeding system. The upper loop seal and lower loop seal are fluidized under the design conditions (see Table 5-2) and the bed material cooler is deactivated.

For the initial setup of the air reactor, the cyclone design (l = 0 mm, α = 45°) as described in Chapter 4 was used, and the solids elutriation rates were as high as 86.2 g/min for solids fluxes of Gs_{AR} = 38 ±2 kg/m^{2}s. This means that 1 kg of solids was entrained within 11.6 minutes, which is much too high for stable operation of a circulating fluidized bed. Therefore, a vortex finder tube was introduced into the cyclone body. The effect of the vortex finder length on the separation efficiency and pressure drop of the air reactor cyclone for an angular position of the vortex finder of α = 285° is illustrated in Fig. 56. The angular position was selected since the high solids loss at α = 45° caused difficulties due to strong changes in the solids flow rates by the change in inventory. The solids loss decreased rapidly at first and leveled off at lengths of above l = 15 mm. Compared to the diameter of the cyclone body, this is only 8.7%. This means that very small vortex finders can significantly improve the performance of the cyclone.

The effect on the gas pressure drop from the cyclone inlet to the gas outlet was less pronounced than that on the separation efficiency. After an initial reduction, the pressure drop started to increase again. While the enlargement agreed well with available knowledge on cyclones, the initial decrease was probably caused by the high solids loss, as energy is needed to carry the solids

to the outlet of the cyclone. However, the relative changes in pressure drop were very small and might also have been caused by the precision of the pressure sensors.

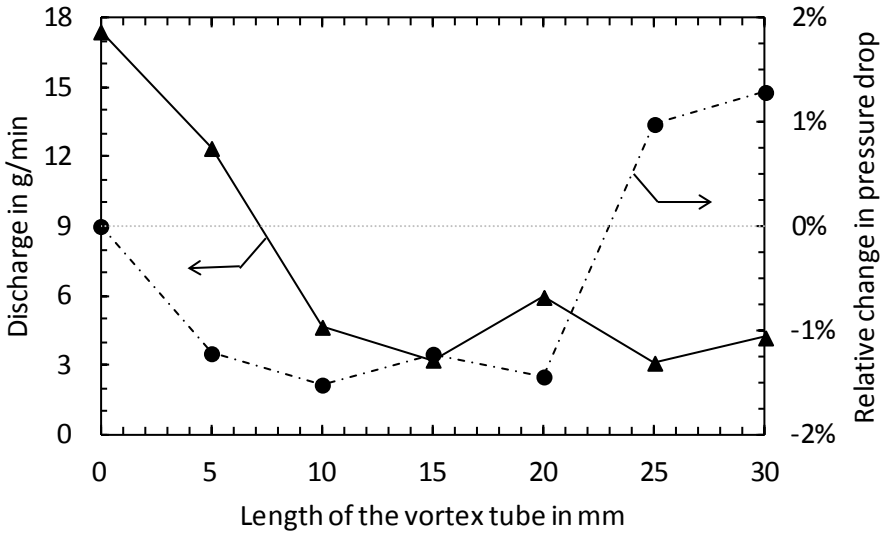

Fig. 56 Effect of the vortex finder length on the air reactor cyclone separation performance and pressure drop at a volumetric gas flow rate of $\dot{V}_{AR}$ = 164 m^3/h, a solids flow rate of Gs_{AR} = 41.5 ±2 kg/m^{2}s and an angular vortex finder position of α = 285°.

The effect of the angular position of the vortex finder and inlet solids loading on the solids discharge for a vortex finder length of l = 15 mm is shown in Fig. 57. A complete rotation of the lid was not possible because of the geometric arrangement of the exhaust filters. It was seen that selection of the angular position is crucial where significant improvements by a factor of up to 10 can be made. The optimum position was in the range between α = 245° and α = 285°, with a shift toward higher angles for lower solids loadings. This is in agreement with the visual observations. The main fraction of solids moved along a solids strand to the solids outlet at the bottom, describing a helix-like motion. A second, smaller, strand detached from the top of the cyclone inlet and traveled in a helix-like motion toward the top of the cyclone. It reached the cover of the cyclone at an approximate angle of α = 180-90°, where it was deflected downwards again. It is expected that this second solids strand is mainly responsible for the loss of solids. This is in contradiction to the findings of Trefz (1992) and Trefz and Muschelknautz (1993), who argued that the constricting effect of the gas-solids strand requires eccentric vortex finders at a position of α = 45°. It seems likely that the exact angle very much depends on the flow pattern at the cyclone inlet, which is strongly affected by the shape of the inlet duct. As expected, the absolute solids loss increased with solids entrance loading.

With respect to these investigations, the air reactor cyclone vortex finder length was adjusted to a length of l = 15 mm and to an angular position of α = 285° to ensure solids inventories during further cold flow model testing. These adjustments were maintained in all of the subsequent experiments. With this optimization of the air reactor cyclone design, the separation efficiency was increased from solids losses of 86.2 g/min to 2.16 g/min, corresponding to an improvement factor of 38.

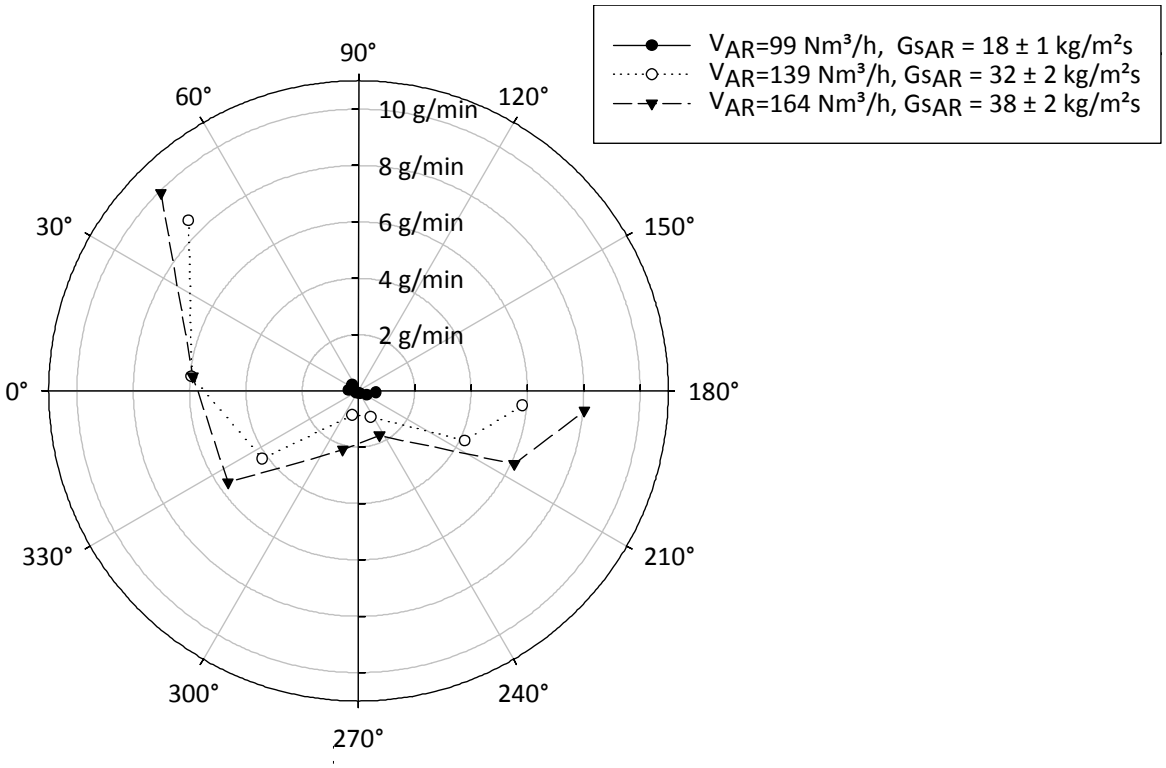

Fig. 57 Effect of the vortex finder angular position and solids entrance loading on the air reactor cyclone separation performance at a vortex finder length of *l* = 15 mm.

Fuel reactor performance

For an investigation into the fuel reactor cyclone performance, the air reactor solids loop (global loop) was deactivated and only the air reactor bottom was fluidized. The lower loop seal and internal loop seal were fluidized with flow rates given in Table 5-2.

Similar to the investigations on the air reactor cyclone, the angular position of the vortex finder was varied between $\alpha = 85°$ and $\alpha = 195°$; this was limited by the geometric settings (Fig. 58). It was found that, for the proposed design at $\alpha = 45°$, the solids discharge from the fuel reactor cyclone was 10.98 g/min for a solids inlet flux with reference to the fuel reactor cross-section of Gs_{FR} = 23.5 ±2 kg/m^{2}s. By rotation of the outlet position, the loss of solids was reduced by 65% for $\alpha = 5°$. Again, more solids were lost with higher solids entrance loads. The highest reduction was made with the introduction of a vortex finder tube. This allowed for a reduction from 3.8 g/min to 0.23 g/min for $\alpha = 5°$. This corresponds to a total reduction by a factor of 48 when the position was changed from $\alpha = 45°$ to $\alpha = 5°$ and the vortex finder was dipped into the cyclone body by *l* = 15 mm. A more detailed plot for the high solids flux and with the vortex finder is given in Fig. 59. It is clear that the optimum position of the vortex finder tube in the case of the fuel reactor cyclone is at an angular position of $\alpha = 5°$. The change in the optimal position compared to the air reactor cyclone is probably due to the different shapes of the inlet ducts and the different deflection geometry at the riser top, causing different flow patterns at the cyclone inlet.

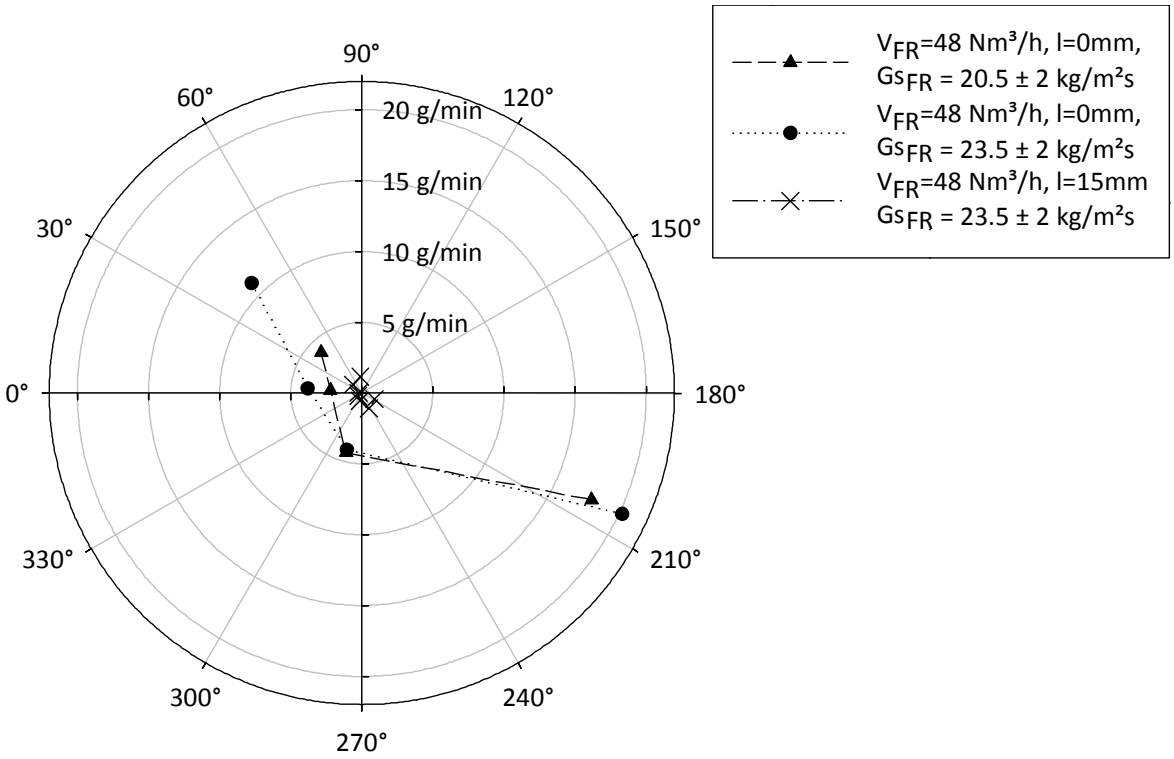

Fig. 58 Effect of the vortex finder angular position and solids entrance loading on the fuel reactor cyclone separation performance at a vortex finder length of l = 15 mm.

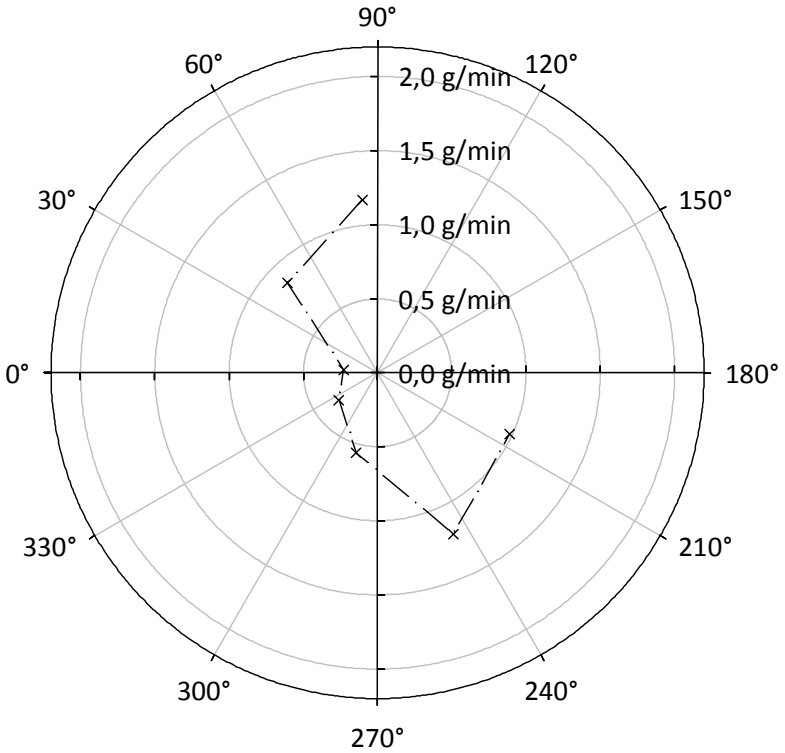

Fig. 59 Effect of the vortex finder angular position on the fuel reactor cyclone separation for a gas volume-flow of $\dot{V}_{FR}$ = 48 Nm^3/h, a vortex finder length of l = 15 mm and a solids entrainment flux of Gs_{FR} = 23.5 ±2 kg/m^{2}s.

The effect of the vortex finder on the cyclone performance was investigated for the optimum position (α = 5°). Again, the introduction of the tube caused a significant reduction in the loss of solids and the pressure drop decreased initially and then increased again. The initial higher

pressure drop was probably caused by the high elutriation rate of solids to the outlet of the cyclone.

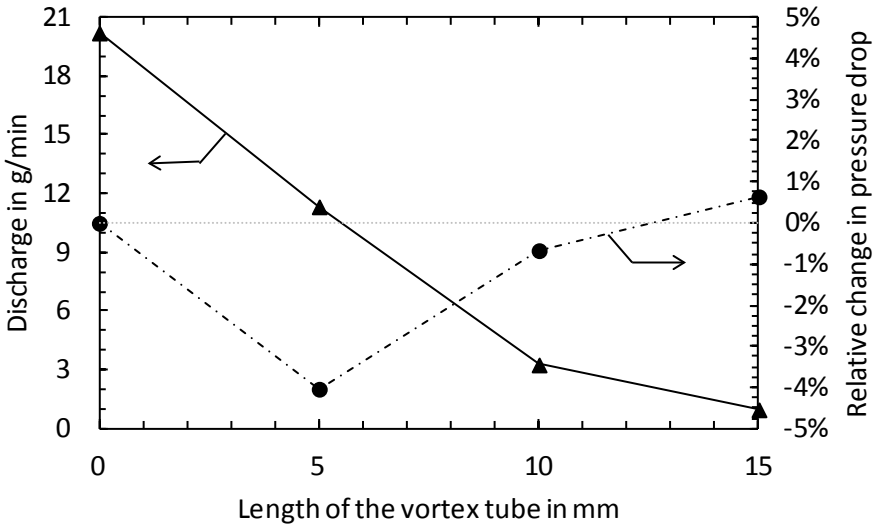

Fig. 60 Effect of the vortex finder length on the fuel reactor cyclone separation performance and pressure drop at a volumetric gas flow rate of $\dot{V}_{FR}$ = 48 m³/h, a solids flow rate of Gs_{FR} = 23.5 ±2 kg/m²s and an angular vortex finder position of α = 5°.

With respect to these investigations, the fuel reactor cyclone vortex finder length was adjusted to a length of l = 15 mm and to an angular position of α = 5°. These adjustments were maintained in all of the subsequent experiments. This allowed for an improvement by a factor of 48 compared to the initial arrangement.

5.4.2 Loop seal operation optimization

The loop seals were optimized with respect to minimization of the fluidization gas demand while avoiding the limitation of solids throughput. It is important to mention that, in a fixed inventory system like the one used here, higher flow resistance of loop seals automatically causes a drop in the solids present in the risers due to the accumulation of solids in the loop seal downcomers. This also applies to the loop seal located at the bottom of the risers whose downcomer partially includes the fuel reactor riser. The limiting effect of the loop seals was studied for all three areas (inlet, center and outlet) separately where the flow rate to the section of investigation was varied while the two other sections were held at a constant, low fluidization rate. Since the highest effect was expected for the lower loop seal, this loop seal was investigated first.

LLS

The lower loop seal directly affects the solids inventories in the fuel and air reactor by controlling the flow of solids from the fuel reactor to the air reactor risers. To investigate the function of this loop seal, similar to the investigations on the air reactor cyclone performance, only the global loop was operated. The applied fluidization rates for testing of one of the sections were $\dot{V}_{LLS\_inlet}$ = 400 Nl/h in the inlet section, $\dot{V}_{LLS\_center}$ = 200 Nl/h in the center section and $\dot{V}_{LLS\_outlet}$ = 400 Nl/h in the outlet section.

The observed behavior of the lower loop seal with respect to solids throughput is presented in Fig. 61. The quantitative flow of solids refers to the air reactor solids flux, which depends by a linear factor on the solids flux in the loop seal. Basically, in all sections, it applies that for low

fluidization rates, the increased inner loop seal friction leads to an inhibition of solids motion. Even when one of the sections is not fluidized, the inner friction is not high enough to provoke blockage of the lower loop seal. This means that the loop seal is insensitive to errors in the air supply as long as there is a minimum gas flow for fluidization available. While an increased gas flow rate does not have a negative effect on the center section and outlet section, too high fluidization rates in the inlet section can cause inhibition of solids motion. This is very likely caused by the increased dynamic pressure that solids are exposed to from the loop seal inlet section gas passing against solids motion to the fuel reactor. From an absolute point of view, center fluidization has the highest impact on solids throughput. However, the applicable cross-section area is significantly lower than that of the inlet and outlet sections. A continuous increase in solids throughput was observed for the outlet section, which was expected. Outlet section fluidization gas is very likely to proceed to the outlet (the air reactor) where it has a direct positive effect on air reactor solids entrainment.

The investigation concluded that the optimized operation conditions in the lower loop seal are when the flow rates are $\dot{V}_{LLS\_inlet}$ = 700 Nl/h in the inlet section, $\dot{V}_{LLS\_center}$ = 500 Nl/h in the center section and $\dot{V}_{LLS\_outlet}$ = 1000 Nl/h in the outlet section. Compared to the flow rates with respect to the design (see Table 5-2), this corresponds to a reduction of 15.4%. The optimized operating conditions in the lower loop seal were used in all of the following experiments.

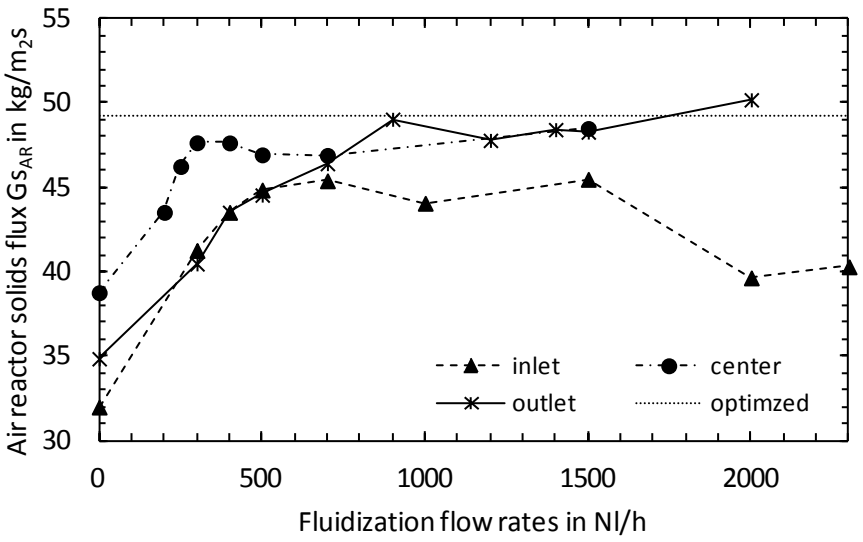

Fig. 61 Effect of the fluidization in the lower loop seal in the global solids loop (Gs_{AR}). Operating conditions for testing were: inlet fluidization $\dot{V}_{LLS\_center}$ = 200 Nl/h and $\dot{V}_{LLS\_outlet}$ = 400 Nl/h, center fluidization $\dot{V}_{LLS\_inlet}$ = 400 Nl/h and $\dot{V}_{LLS\_outlet}$ = 400 Nl/h, outlet fluidization $\dot{V}_{LLS\_inlet}$ = 400 Nl/h and $\dot{V}_{LLS\_center}$ = 200 Nl/h. For optimized operation, the following fluidization rates were used: $\dot{V}_{LLS\_inlet}$ = 700 Nl/h, $\dot{V}_{LLS\_center}$ = 500 Nl/h, $\dot{V}_{LLS\_outlet}$ = 1000 Nl/h.

ULS

For investigation into the upper loop seal, again only the global loop was operated. Operating conditions were selected as discussed for the experiments with the lower loop seal. The applied fluidization rates for testing of one of the sections were $\dot{V}_{ULS\_inlet}$ = 300 Nl/h in the inlet section, $\dot{V}_{ULS\_center}$ = 200 Nl/h in the center section and $\dot{V}_{ULS\_outlet}$ = 300 Nl/h in the outlet section.

Although gas flow to the upper loop seal does not have a direct effect on the flow pattern in the risers, a similar behavior was found when compared to the lower loop seal (Fig. 62). A higher gas flow rate in any case had a positive effect on the solids throughput. Missing fluidization in the inlet section caused failure of the loop seal due to the appearance of solids blockage in the downcomer. Only a small amount of gas was needed to avoid such a situation, while then the inlet section had only a small effect the solids throughput. Even for very high gas flow rates to the inlet, no inhibition of solids motion was observed. The effect of center fluidization on loop seal operation was less pronounced than the flow rate to the outlet section.

From this investigation, the optimal gas flow rates to the upper loop seal were found to be $\dot{V}_{ULS\_inlet}$ = 400 Nl/h in the inlet section, $\dot{V}_{ULS\_center}$ = 400 Nl/h in the center section and $\dot{V}_{ULS\_outlet}$ = 600 Nl/h in the outlet section. In comparison with the design flow rates (see Table 5-2), this corresponds to a reduction of 30%. In the following experiments, these optimized settings were used.

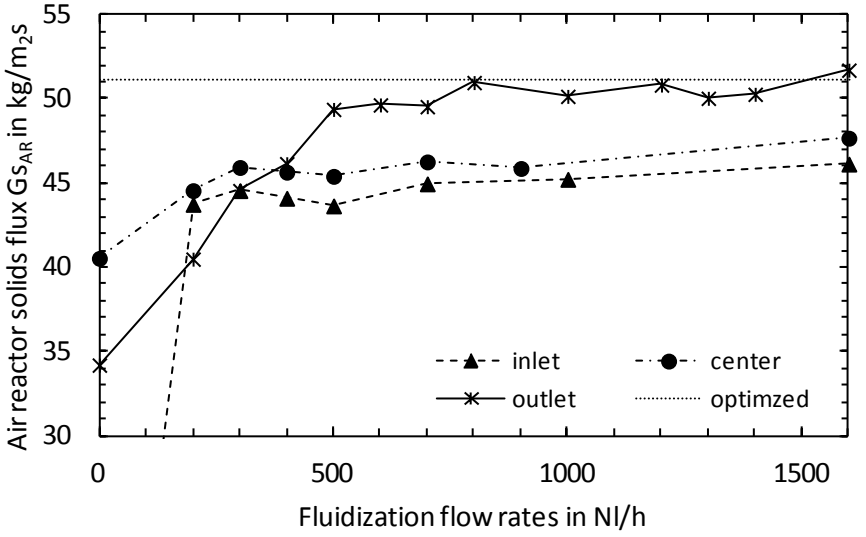

Fig. 62 Effect of the fluidization in the upper loop seal in the global solids loop (Gs_{AR}). Operating condition for testing were: inlet fluidization $\dot{V}_{ULS\_center}$ = 200 Nl/h and $\dot{V}_{ULS\_outlet}$ = 300 Nl/h, center fluidization $\dot{V}_{ULS\_inlet}$ = 300 Nl/h and $\dot{V}_{ULS\_outlet}$ = 300 Nl/h, outlet fluidization $\dot{V}_{ULS\_inlet}$ = 300 Nl/h and $\dot{V}_{ULS\_center}$ = 200 Nl/h. For optimized operation, the following fluidization rates were used: $\dot{V}_{ULS\_inlet}$ = 400 Nl/h, $\dot{V}_{ULS\_center}$ = 400 Nl/h, $\dot{V}_{ULS\_outlet}$ = 600 Nl/h.

ILS

To investigate the operation of the internal loop seal, only the internal solids loop was operated. The applied fluidization rates for testing of one of the sections were $\dot{V}_{ILS\_inlet}$ = 100 Nl/h in the inlet section, $\dot{V}_{ILS\_center}$ = 100 Nl/h in the center section and $\dot{V}_{ILS\_outlet}$ = 100 Nl/h in the outlet section.

The results of the internal loop seal optimization are shown in Fig. 63. In comparison with the other two loop seals, no saturation in solids flow was observed for fluidization of the inlet section. Very likely, this occurred because the internal loop seal cross-section is much smaller, so the gas from the inlet can travel with the solids to the outlet more easily. The same applies for the center section. Furthermore, fluidization has to be applied to the loop seal in any case to avoid operation failure. This is very probably caused by the smaller size of the internal loop seal where the surface-to-volume ratio is high, provoking higher solids flow resistance relative to size.

For optimized operation of the internal loop seal, the gas flow rates were selected as $\dot{V}_{ILS\_inlet}$ = 180 Nl/h to the inlet section, $\dot{V}_{ILS\_center}$ = 240 Nl/h to the center section and $\dot{V}_{ILS\_outlet}$ = 300 Nl/h to the outlet section. These settings were maintained in all of the following experiments.

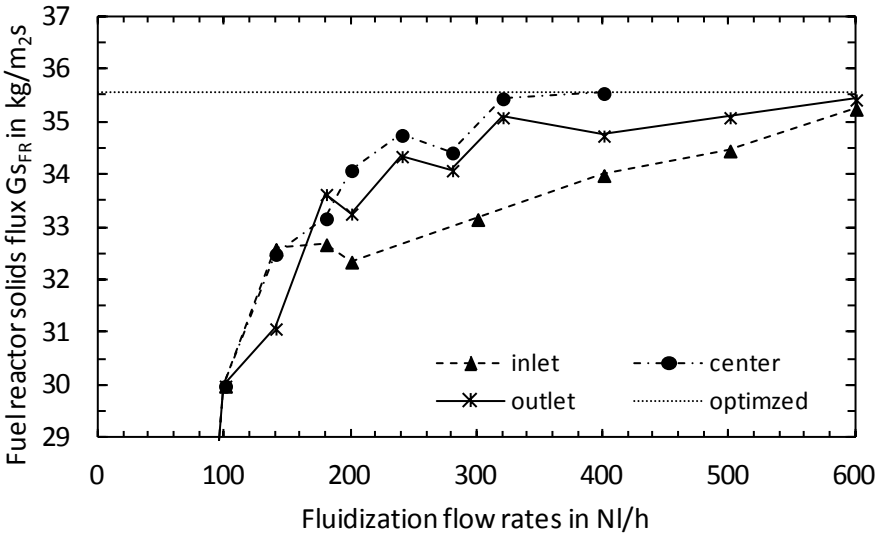

Fig. 63 Effect of the fluidization in the internal loop seal in the global solids loop (Gs_{AR}). Operating condition for testing were: inlet fluidization $\dot{V}_{ILS\_center}$ = 100 Nl/h and $\dot{V}_{ILS\_outlet}$ = 100 Nl/h, center fluidization $\dot{V}_{ILS\_inlet}$ = 100 Nl/h and $\dot{V}_{ILS\_outlet}$ = 100 Nl/h, outlet fluidization $\dot{V}_{ILS\_inlet}$ = 100 Nl/h and $\dot{V}_{ILS\_center}$ = 100 Nl/h. For optimized operation, the following fluidization rates were used: $\dot{V}_{ILS\_inlet}$ = 180 Nl/h, $\dot{V}_{ILS\_center}$ = 240 Nl/h, $\dot{V}_{ILS\_outlet}$ = 300 Nl/h.

Summary of loop seal optimization

The investigations into loop seal optimization with respect to solids and gas flow rates and the determined reduction rates are summarized in Table 5-3.

Table 5-3 Tabular summary of loop seal optimization.

	Design	Optimized	Reduction	
	Nl/h	Nl/h	Nl/h	%
Lower loop seal				
inlet	1100	700	400	36.4
center	400	500	-100	-25
outlet	1100	1000	100	9.1
sum	2600	2200	400	15.4
Upper loop seal				
inlet	750	400	350	46.7
center	500	400	100	20
outlet	750	600	150	20
sum	2000	1400	600	30
Internal loop seal				
inlet	240	180	60	25
center	240	240	0	0
outlet	240	300	-60	-25
sum	720	720	0	0
Total	5320	4320	1000	18.8

5.4.3 Investigations into solids flow control valve operation

To investigate the operation of the solids flow control valve, the riser system and bed material cooler were operated under the design conditions (see Table 5-2), while the loop seals were operated under the optimized conditions (see Table 5-3). Solids flow to the bed material cooler as well as to the upper loop seal were determined by means of measuring solids accumulation. To allow for measurement of the solids flow to the upper loop seal, the solids flow to the bed material cooler had to be stopped by quickly closing the solids flow control valve and immediate execution of the measurement. The solids split-up ratio X_{BMC} was calculated by referring the solids flow to the bed material cooler to the solids flow to the upper loop seal.

The influence of the solids flow control valve on the solids split-up ratio X_{BMC} is depicted in Fig. 64. For very small openings of the solids flow control valve, the gap was not large enough for the passage of solids. Thus, delayed solids flow occurred when the valve was opened. At an opening of X_{SCV} = 0.6 mm to X_{SCV} = 2 mm, a linear dependency of the solids split-up ration on valve opening was found. This corresponds to a split-up ratio range of X_{BMC} = 7-53%, which is in the typical range of bed material cooler operation. For valve openings larger than X_{SCV} = 3.35 mm, all of the solids were directed into the bed material cooler. Emptying of the loop seal can occur, which would cause mixing of the air reactor and fuel reactor gases. To avoid such situations, it is crucial to monitor the bed height in the upper loop seal downcomer by means of differential pressure measurements.

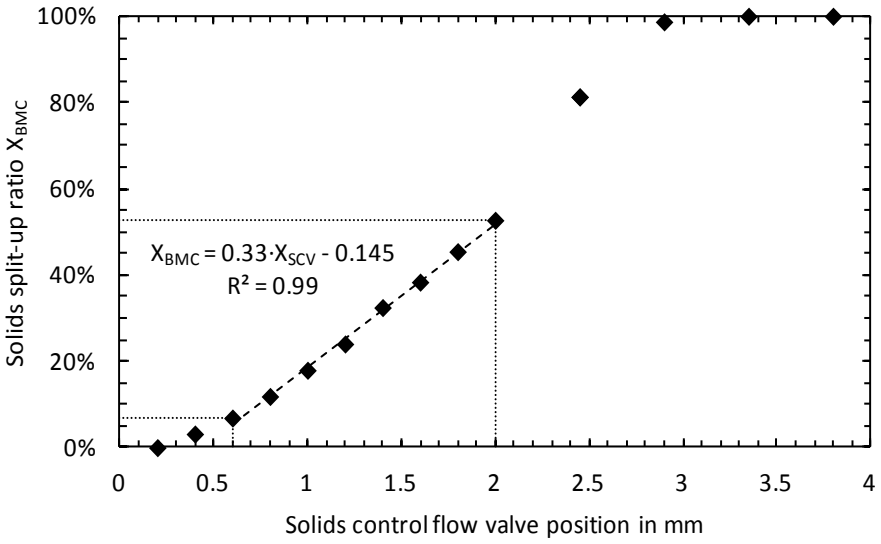

Fig. 64 Impact of the solids flow control valve position on the solids split-up ratio.

5.4.4 Effect of gas staging on the global solids loop

Gas staging is applied to circulating fluidized beds to have control over the solids entrainment rates. The effect of level of gas introduction to the air reactor on the global solids loop (Gs_{AR}) is illustrated in Fig. 65 for a total solids inventory of m_{sol} = 35 kg. The gas flow rate to the primary and the bottom fluidization has the greatest effect on the solids flux. This occurs because increased gas flow to the lower section of the riser provokes an axial expansion of the lower dense section and carryover of solids to the upper section of the riser. These solids can be then transported more easily to the exit of the riser, which increases solids flux. It is important to note that although the effect of bottom fluidization in the air reactor seems to be less pronounced in

Fig. 65, it has to be kept in mind that these are relative values. In terms of absolute flow rate, the increase in gas flow to the bottom section is small compared to the pronounced effect on the solids entrainment. It is additionally shown that the tertiary fluidization has only a minor effect on the fluid dynamics. Therefore, to reduce the costs of such units, applying only bottom, primary and secondary gas injection nozzles seems to be meaningful.

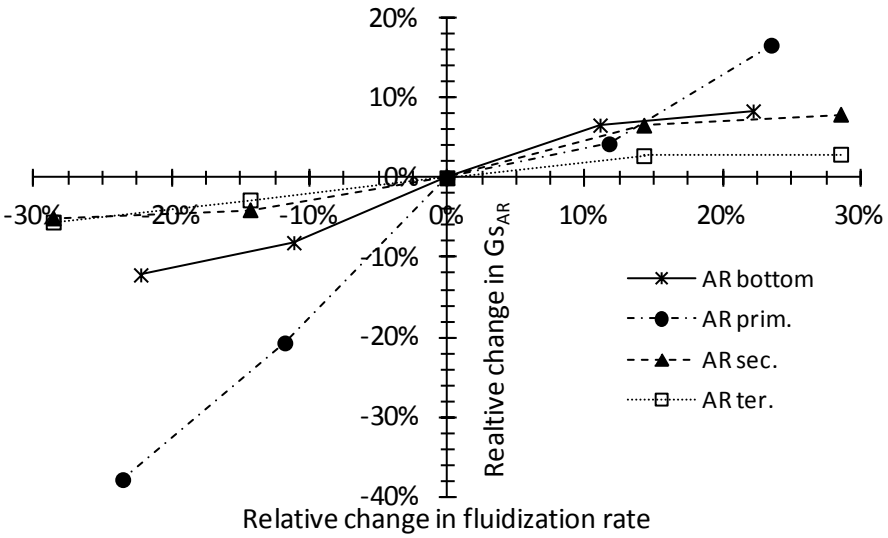

Fig. 65 Effect of gas staging in the air reactor on the global solids loop (Gs_{AR}) at a total solids inventory of m_{sol} = 35 kg. Gas flow rates to the stages under standard conditions (0%) are summarized in Table 5-2.

The fluidization of the fuel reactor only has a small influence on the global solids loop, as depicted in Fig. 66. Operation of the global solids loop is thus independent of the internal solids loop.

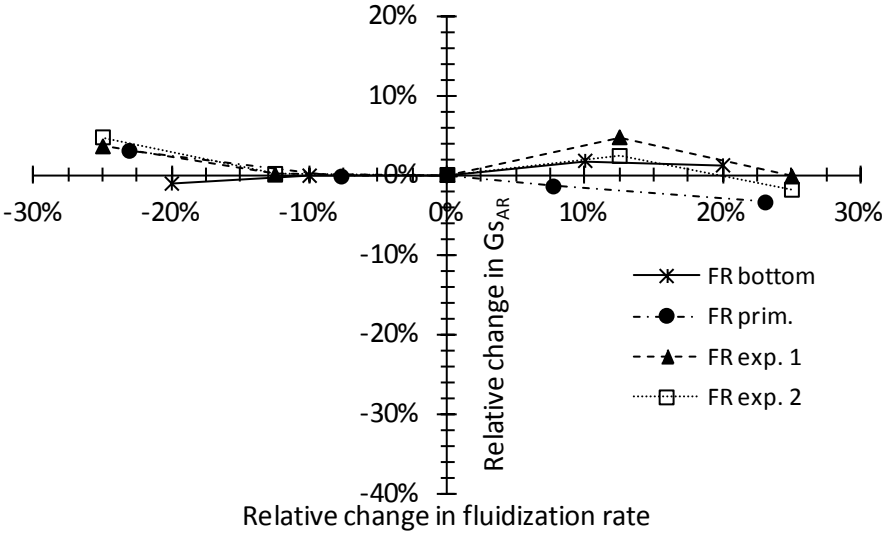

Fig. 66 Effect of gas staging in the fuel reactor on the global solids loop (Gs_{AR}) at a total solids inventory of m_{sol} = 35 kg. Gas flow rates to the stages under standard conditions (0%) are summarized in Table 5-2.

5.4.5 Effect of gas staging on the internal solids loop

The effect of gas staging in the fuel reactor on the internal solids loop is shown in Fig. 67. While gas staging in the air reactor is applied to control the solids flow, in the fuel reactor of the cold flow model, gas is introduced in a staged fashion to simulate gas production by the reactions. It is shown that the position of the reactions in the fuel reactor significantly influences the fluidized bed, while the effect is less pronounced when the reactions appear at higher levels of the riser. However, no difficulties in operation were identified. The system can easily handle both very fast and very slow reaction rates in the fuel reactor.

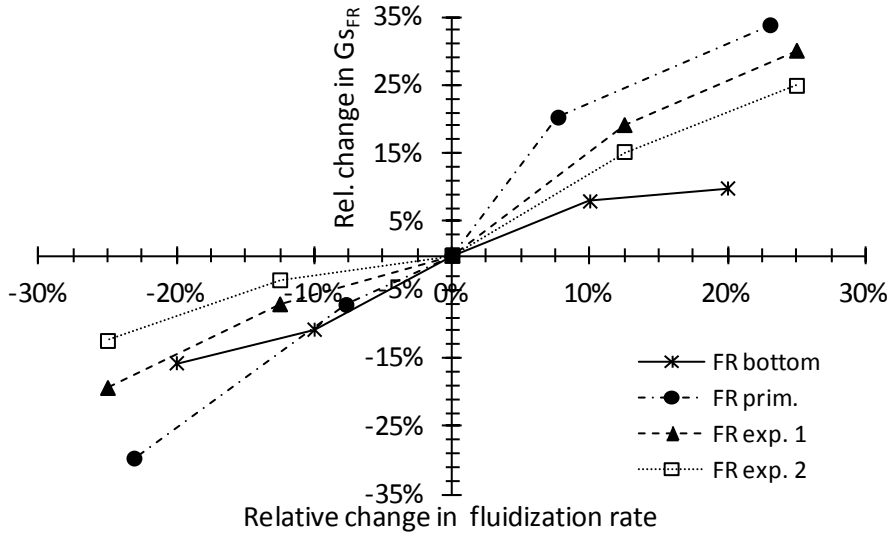

Fig. 67 Effect of gas staging in the fuel reactor on the internal solids loop (Gs_{FR}) at a total solids inventory of m_{sol} = 35 kg. Gas flow rates to the stages under standard conditions (0%) are summarized in Table 5-2.

The impact of air reactor fluidization on the internal solids loop is illustrated in Fig. 68. A reduction in the solids flux in the fuel reactor Gs_{FR} was observed with increased flow to the air reactor and thus higher air reactors solids fluxes Gs_{AR}. This is caused by the removal of solids from the internal loop by the air reactor riser.

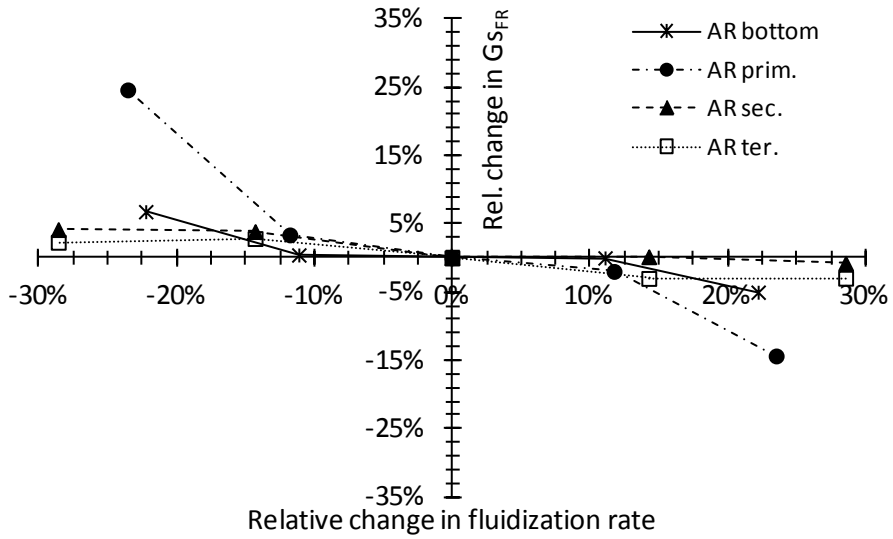

Fig. 68 Effect of gas staging in the air reactor on the internal solids loop (Gs_{FR}) at a total solids inventory of m_{sol} = 35 kg. Gas flow rates to the stages under standard conditions (0%) are summarized in Table 5-2.

5.4.6 Effect of the solids inventory

The solids inventory is a key operating parameter in fluidized bed systems. Often, control systems are based on monitoring the solids inventory. While in bubbling fluidized beds the inventory is related to bed height, in circulating fluidized beds, it has an influence on several parameters. Inadequately selected inventories can even lead to malfunction in circulating fluidized bed operation by the appearance of choking. Apart from the hydrodynamics, the solids inventory in chemical looping systems affects the chemistry. Solids residence time and thus reaction time correlates with the solids inventory. Reactor systems for chemical looping applications, therefore, should be capable of handling varying solids inventories to meet the specific requirements of the oxygen carrier.

The effect of the solids inventory on the setup was investigated for total inventories of m_{sol} = 35 ±5 kg (Fig. 69). As expected, the solids inventory had a large impact on the solids flow rates in the system. An increase of the inventory by about 15% was enough to double the solids flux in the air reactor and increase the fuel reactor solids flux by more than 50%. However, no operation difficulties were observed. If the global solids circulation rate should be limited, switching gas from lower sections in the riser to higher sections can help to meet the changed conditions and reduce the solids flux.

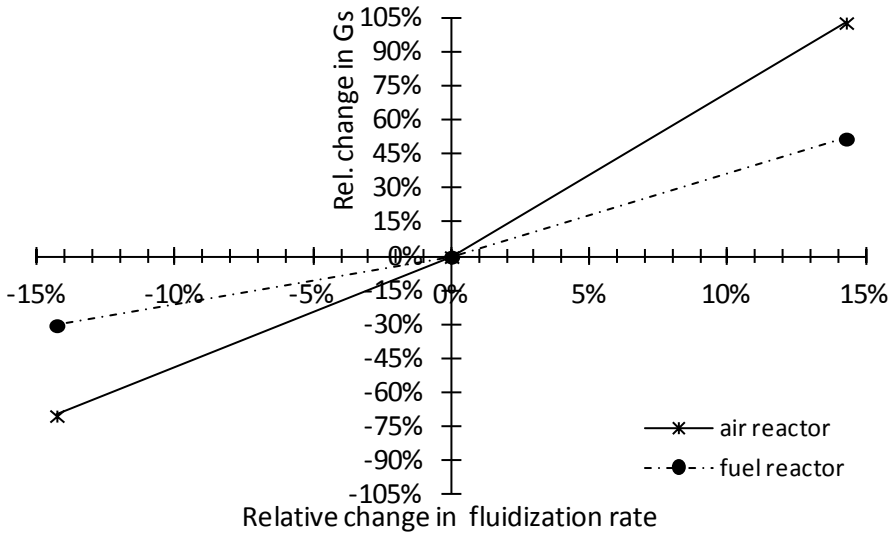

Fig. 69 Effect of the solids inventory on the global (Gs_{AR}) and internal (Gs_{FR}) solids loop with the gas flow rates in the risers under design operating conditions. The loop seals were operated under the optimized conditions and with the optimized cyclone vortex finder setup.

5.4.7 Leakage and gas splitting of loop seals

In chemical looping combustion systems, properly sealed loop seals connecting the air reactor and fuel reactor are important to avoid dilution of the exhaust gas streams. Gas bypass through the upper loop seal is often referred to as "nitrogen dilution", where air nitrogen can be found in the fuel reactor exhaust. As a consequence, the purity of the CO_2 suffers, requiring increased efforts in the purification and compression of fuel reactor gases. When fuel reactor gas passes through the lower loop seal, carbon can be found in the air reactor which is often referred to as "carbon leakage". It is not expected that gas can pass the loop seals against solids motion, which would mean that the gas flows is against a pressure gradient.

To measure the dilution rates, methane was introduced into the air reactor bottom fluidization. No carbon was detected at the fuel reactor exit even at high solids fluxes and for different upper loop seal fluidization rates. Thus, the upper loop seal design can be considered as tight against nitrogen dilution.

Introduction of methane into the fuel reactor bottom fluidization caused an increase in the carbon concentration in the air reactor gas from 0 ppmv to 0.5 ppmv for high solids throughput rates. Such small changes in these values are within the accuracy of the detector which does not allow for quantification of the actual leakage rate. Nevertheless, the trend reveals that a very small amount of fuel reactor gas can pass the lower loop seal to the air reactor.

It is important to note that carbon leakage by the formation of solid carbon in a chemical looping system cannot be quantified with this kind of measurement setup. The same applies when nitrogen is transported by absorption on particles through the lower loop seal.

The path of the gas introduced into the upper loop seal and lower loop seal inlet, center and outlet sections were investigated for three solids throughputs. To be comparable, the solids throughput is given with reference to the air reactor in terms of solids flux (Gs_{AR}). While total gas

flow rates were kept at design conditions (Table 5-2), the solids flux was adjusted by gas staging. Loop seal fluidization rates were set to the optimized conditions discussed before. The gas split-up ratio in the upper loop seal is illustrated in Fig. 70. While values of zero mean that all gas passes against solids motion to the inlet, thus the air reactor, values of one mean that the gas travels with the solids motion to the outlet, the fuel reactor. Gas split-up increases from inlet to outlet and with solids flux. Significant amounts of gas reach the air reactor against the direction of solids flow. The gas-solids counter-current flow in the air reactor downcomer guarantees that no air reactor off-gas may directly pass through the loop seal and that the downcomer is kept fluidized. This gas flow, however, has to be kept reasonably low because it can cause a reduction in cyclone performance by disturbance of the flow inside of the cyclone body. However, as expected, gas is mainly carried with the solids to the solids outlet of the upper loop seal. Gas introduced to the outlet area fully passes to the fuel reactor.

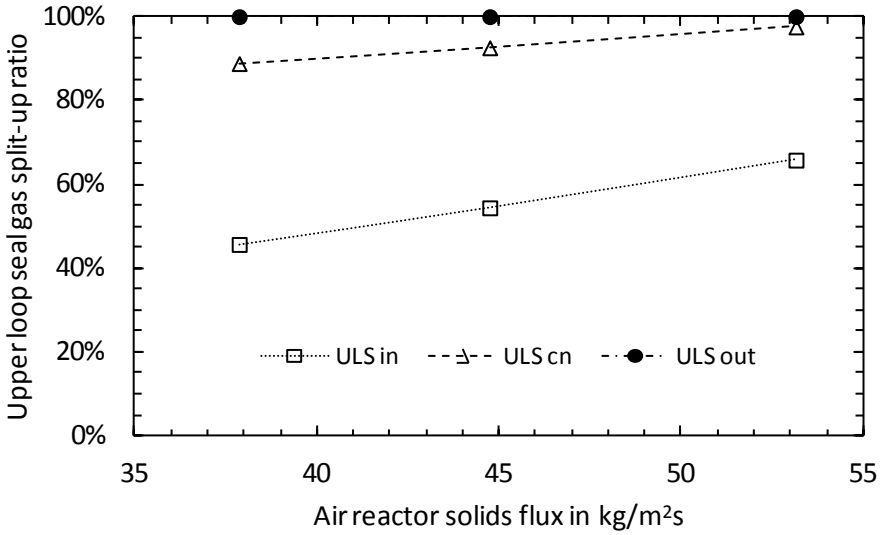

Fig. 70 Upper loop seal gas split-up ratio depending on the solids throughput with reference to the air reactor. Values of zero mean that all gas passes to the air reactor while values of unity indicate that all gas travels to the fuel reactor.

The gas split-up in the lower loop seal is depicted in Fig. 71. The lower loop seal behavior is similar that one of the upper loop seal. Interestingly, most of the gas introduced in the inlet area can pass to the fuel reactor, which is indicated by gas split-up ratios below 50%. This is very likely due to the low solids velocity in the downcomer of the lower loop seal. It also explains why there was an inhibiting effect observed for high flow rates to the inlet section of the lower loop seal, where it was noted that gas flowing against the solids motion may have an inhibiting effect.

Although both the upper loop seal and lower loop seal operates very well with respect to nitrogen dilution and carbon leakage, improvements can be made with respect to the lower loop seal depth and inlet section. Potentially, a reduction in the lower loop seal downcomer cross-section can improve the flow behavior with respect to solids flow inhibition. A deeper lower loop seal design where pressures at the bottom are higher would have a positive effect on the tightness.

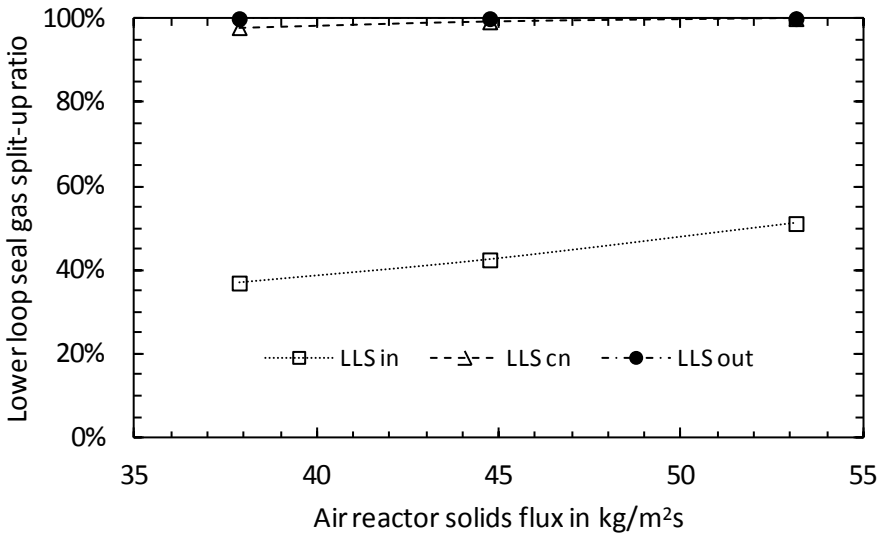

Fig. 71 Lower loop seal gas split-up ratio depending on the solids throughput with reference to the air reactor. Values of zero correspond to all gas passing to the fuel reactor while values of unity indicate that all gas travels to the air reactor.

5.4.8 Overall pressure profile

The pressure profile in fluidized bed systems is a characteristic plot which allows for the identification of design problems and an assessment of the solids distribution within the system. A typical pressure profile for operation of the risers under design conditions (listed in Table 5-2), for optimized operation of the loop seals (listed in Table 5-3) and for a solids flow control valve position of X_{SVC}=1.4 mm corresponding to a solids split-up ratio of X_{BMC} = 32% is shown in Fig. 72. High gradients were found at the bottom of the risers, corresponding to a high solids fractions, typical for bubbling fluidized beds. The solids distribution curves in the air reactor and fuel reactor at levels above the bubbling bottom are typical for circulating fluidized risers. For stable operation of loop seals, the pressure in the loop seal has to be higher than at the outlet to the riser. Additionally, the operational stability of dual circulating fluidized bed systems with respect to pressure fluctuations at the cyclone outlets is governed by the depth of the upper and lower loop seals. The pressure profile reveals that these loop seals are adequately designed and backflow of gas is unlikely to occur. In particular, the upper loop seal is capable of handling much higher backpressures from the outlet side, i.e. the fuel reactor. The pressure drop in the internal loop seal is higher than in the upper loop seal. This effect is attributable to the higher surface-to-volume ratio because of the smaller dimensions of the internal loop seal causing higher friction losses.

The pressure gradient in the bed material cooler is in accordance with the solids motion. A pressure drop is caused by the weir between the settling chamber and the heat exchanger chamber (refer to the two rightmost points in the diagram for the bed material cooler). A homogeneous flow of solids to the heat exchanger is thus expected. The pressure port in the bed material cooler BMC1 corresponds to the pressure measurement at the bottom of the heat exchanger chamber and is illustrated for completeness.

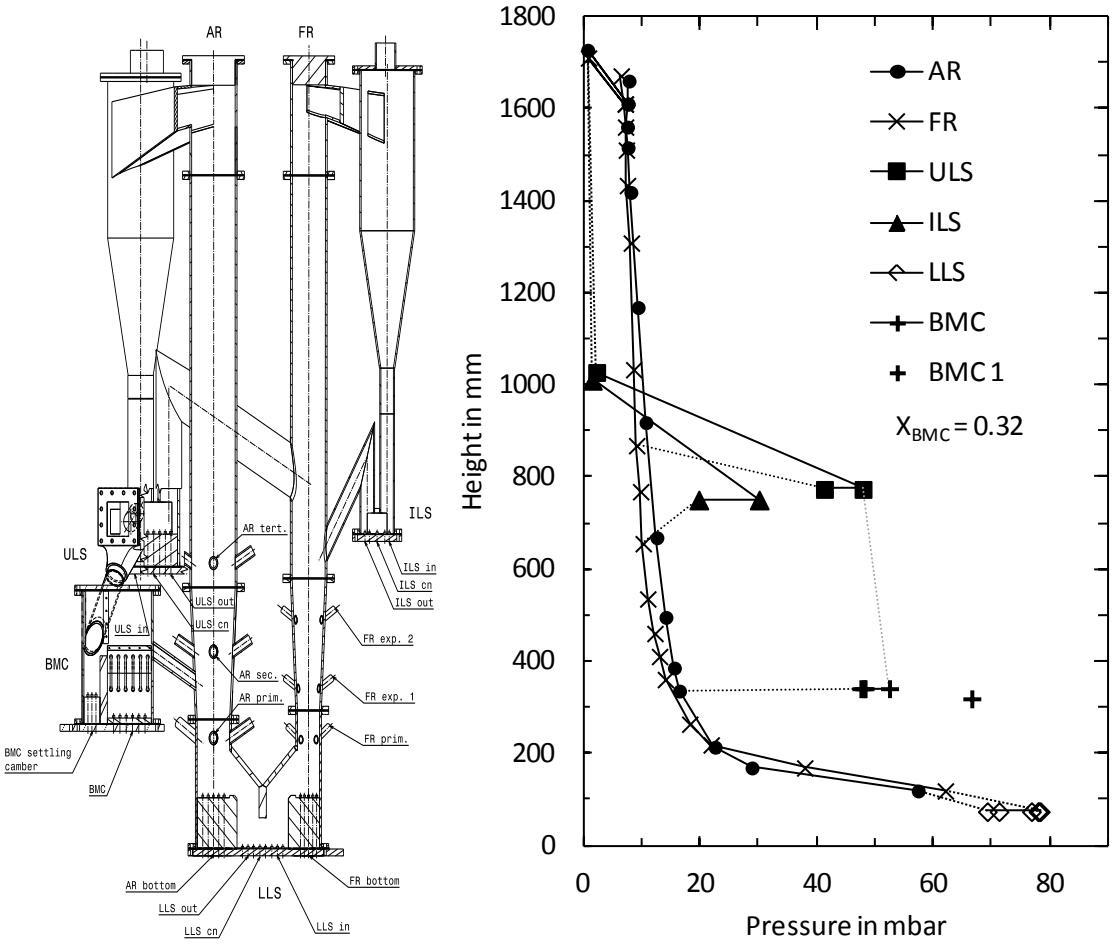

Fig. 72 Overall pressure profile of the cold flow model under design operating conditions (hot unit P_{fuel} = 10 MW, ϑ_{FR} = 900°C and λ = 1.1) and for a total solids inventory of 35 kg. Solids fluxes are Gs_{AR} = 42.3 kg/m^{2}s and Gs_{FR} = 15.6 kg/m^{2}s. Flow rates to the loop seals and vortex finder positions are set to optimized values. Total flow rates are $\dot{V}_{AR}$ = 168 Nm^3/h, $\dot{V}_{FR}$ = 48 Nm^3/h. Solids flow control vale position is X_{SCV}=1.4 mm corresponding to a solids split-up ratio of X_{BMC} = 0.32.

5.5 Summary and conclusion

Based on the design presented in Chapter 4 *"Chemical looping reactor system design"* (p. 53) of the 10 MW chemical looping combustion demonstration unit using gaseous fuels, a scaled cold flow model was designed and erected. The cold flow model allows for investigations into the hydrodynamic behavior of the hot unit by the application of similarity rules. The Glicksman set of scaling parameters, which are based on a dimensionless analysis of the governing equations in fluidized beds, was used. The parameters allow for the deduction of the dimensions of the cold flow model using 1:10 scale. Such cold models are a practicable way for the experimental validation of fluidized bed designs and are therefore often used in the engineering process. Especially in the scale-up of fluidized bed-based technologies, such cold models can be very valuable. An assessment of the issues related to scale-up can be made where potential critical parts in the design can be easily identified and corrected with very little effort.

The 1:10 cold flow model includes all parts of the hot unit design such as the riser, cyclones, loop seals as wells as the solids flow control valve and the bed material cooler. The model setup was described using 3D CAD software, state-of-the-art in mechanical engineering. It was then built and

put into operation. The model is equipped with 52 pressure measurement ports and variable area flow meters for volume-flow measurements. It allows for the quantification of solids flow rates and solids discharge rates from the cyclones.

The investigations into the performance of the cyclones revealed that, in the proposed design, the loss of solids was too high for stable operation of the circulating fluidized bed. In particular, the air reactor cyclone showed poor performance. By adjusting the vortex finder position and vortex finder tube length, considerable performance improvements were obtained. It was found that for the right position and a very short vortex finder tube length, the discharge rate from the air reactor cyclone could be reduced from 82.6 g/min to below 2.16 g/min, corresponding to an improvement by a factor of 38. Although the initial solids elutriation rates of the fuel reactor cyclone (10.98 g/min) were much lower, an improvement by a factor of 48 was found with solids loss as little as 0.23 g/min. The observed effect on the pressure drop was very small with values within the range of measurement precision.

The performance of the loop seal with respect to solids throughput was evaluated. The specific design of the loop seals allows for quantification of the effect of fluidization in the inlet area below the loop seal downcomer, the center area, the cross-section of the horizontal passage and the outlet area below the loop seal outlet. The experiments show that the lower loop seal is insensitive to operation errors even when the fluidization in one section is stopped by the allowance of flow of solids (although solids flow was reduced a little). An inhibiting effect of the inlet section for very high fluidization rates has been observed where the solids flow decreased, likely due to the increased dynamic pressure exposed against the motion of solids. The investigations into the upper loop seal revealed that fluidization to the inlet area has to be maintained in any case to avoid loop seal blockage. However, no inhibiting effect of inlet fluidization was detected, even for high fluidization gas flow. Compared to the lower and upper loop seals, the internal loop seal has to be operated with care. Blockage occurs if fluidization to one section is stopped. Also, no limitation of the inlet fluidization was observed; in contrast, an improvement was seen with increasing gas flow. The deviation in operation of the internal loop seal compared to the other loop seals was very likely due to the smaller size where the surface-to-volume ratio is much higher. This leads to increased friction relative to volumetric forces. A considerable reduction in the required fluidization rates in the lower and upper loop seals was obtained without limiting system operation over a wide solids throughput range. This allowed for a 15.4% reduction from the design flow rates in the lower loop seal, and a 30% reduction in the upper loop seal. Although the total flow to the internal loop seal has to be maintained, shifting gas from the inlet to the outlet section improved the operation.

The setup of the solids flow control valve was investigated by gradually opening the valve. The valve operation was shown to be very flexible with respect to the adjustment of solids flow rates. A linear operation range of the valve was identified for solids split-up ratios from 7-53%, which is the typical range for the operation of the valve. Emptying he upper loop seals can occur with large valve openings. In chemical looping operation, such situations have to be avoided causing the dilution of air reactor and fuel reactor gases. An automatic control setup is required, with observation of the solids inventory in the upper loop seal by means of differential pressure measurement.

Gas staging in the air reactor riser is an effective method to control the solids flow rates in the global loop. Adjustments to meet optimized operating conditions can be easily made. Since the tertiary fluidization stage only has a small effect, omission of this stage is proposed in the final setup. While gas flow rates in the fuel reactor have only a limited effect on the global loop, the air reactor riser is capable of influencing the internal solids loop by the removal of solids from this loop.

The simulated gas expansion in the fuel reactor revealed that the actual position has a significant effect on the solids distribution in the fuel reactor riser. However, no operation difficulties were identified in any case.

As expected, the solids inventory in the system had a strong effect, provoking much higher solids flow rates. Although the system was not sensitive to much higher solids fluxes, shifting fluidization gas from the bottom areas to higher levels can help to counteract this.

Gas leakage through the upper and lower loop seal was investigated using methane as a tracer gas. No leakage of gas through the upper loop seal, potentially causing the dilution of CO_2 by air nitrogen in the hot unit, was detected. The measurement of leakage through the lower loop seal which will result in leakage of carbon to the air reactor indicated that there was very minor leakage. However, the measured values were so low that actual quantification was not possible.

The path of the loop seal fluidization gases was detected by tracer gas measurement. It was found that most of the gas travels with the solids to the loop seal outlet where the actual ratio decreases in the order from inlet to outlet. However, especially in the lower loop seal, a significant amount of gas from the inlet passes against solids motion to the fuel reactor, which is the potential explanation for the observed inhibiting effect of high fluidization rates in the inlet section.

The pressure profile of the unit verifies that, with the improvements made, the system design is a success. The profile has the expected shape and the loop seals operate very well.

6 Potential of chemical looping combustion at the large scale

6.1 Introduction

The main drawback with demonstrating chemical looping combustion (CLC) for gaseous fuels in the power industry is competition with gas turbine combined cycle plants with conventional CO_2 capture as well as the large plant sizes required for economic operability. However, there are a number of possible applications in industry, especially in the oil and gas industry, in which steam is currently generated from natural gas. This can be a significant driver to overcome the need to have demonstration units in the medium size range when developing chemical looping combustion technology. One of these applications is in-situ extraction of heavy oil seams using steam. For such applications, chemical looping combustion is expected as a promising way of replacing current technology with very low capture penalties for capturing CO_2 for storage.

In this chapter, the potential of chemical looping combustion in the production of oil from heavy oil sands at a size of 100 MW is investigated. The chemical looping combustion process is compared to the base case where no carbon is captured and to two first generation carbon capture and storage processes, namely post-combustion CO_2 capture and oxy-fuel combustion.

6.1.1 Oil production and global warming

Given the fact that the greatest share of primary energy is from oil (see Fig. 73), there is a keen interest in keeping exploration rates high to meet society's needs.

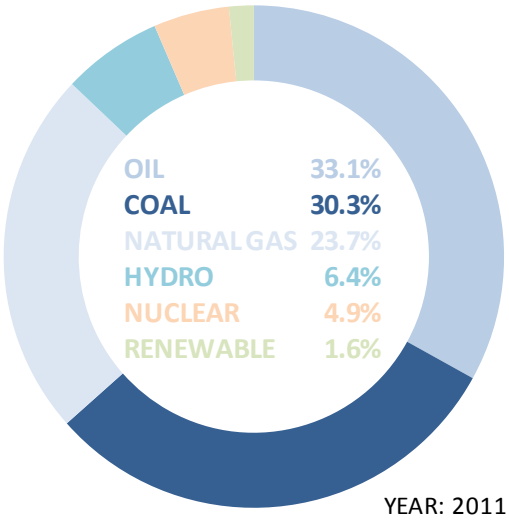

Fig. 73 Distribution of energy sources consumed in 2011. Data taken from (BP, 2011, 2012).

Crude oil can be found worldwide in reservoirs, with the Middle East (i.e. Saudi Arabia and Iran) being the most important contributors to the world's crude oil reserves, with more than 45% of total proven oil reserves. The crude oil is recovered from the reservoir in three different phases; primary oil recovery, secondary oil recovery and tertiary oil recovery. The first phase: primary oil recovery, relies on the natural pressure in the reservoir forcing the oil to the surface through the wellbore. Depending on the reservoir and the pressure, the natural pressure dissipates after a certain amount of oil has been recovered. Then, the oil has to be produced using secondary production methods. These involve methods to increase the reservoir pressure by suitable methods such as water flooding, where water is injected into the reservoir. When the oil flow diminishes using secondary methods, tertiary oil recovery methods allow for a continuation of oil

production. These methods rely on technologies that increase the flow characteristics of the oil by using steam, carbon dioxide or other gases or chemicals.

In addition to crude oil reservoirs where the oil is produced using oil wells, petroleum is also stored as unconventional oil in oil sands, heavy oil bitumen and shale oil. Among these, remarkable quantities of heavy oil and oil sands are stored in Canada in the Athabasca region and Venezuela in the Orinoco Belt territory. In total, these two sites store 390 thousand million barrels of 2011 proven reserves, contributing to approximately 19.1% of the world's oil reserves (BP, 2012). However, oil sands are currently actively developed only in Canada. Two main production methods are used commercially to recover the oil from oil sands, depending on the storage depth. Reserves that are close to the surface are collected by open-pit mining, accounting for 20% of the oil sand reserves in Canada (CAPP, 2012b; IHS-CERA, 2012b). The oil is then separated from the raw oil sand using hot water and caustic soda (NaOH). The low oil content requires processing about two tons of oil sand to extract one barrel of oil; this is 6.8% of the initial quantity. Oil sand deposits located more deeply, which do not allow for open-pit mining, are extracted by in-situ extraction methods, with cyclic steam stimulation (CSS) and steam assisted gravity drainage (SAGD) being the most important. SAGD was developed in the 1980s by Roger M. Butler (Buttler, 1980). It is based on the idea of increasing the mobility of oil stored in oil sands by exposure to thermal energy, allowing the oil to flow through the pores of the sand to an adequate collecting chamber. Two horizontally aligned wells are drilled into the deposit, where one is used to inject a heated fluid and the other is used for the production of oil. The wells are placed one over the other with an adequate vertical spacing (~5 m). The heated fluid, e.g. steam, is pumped into the upper well, forming a steam chamber that extends vertically upwards and horizontally into the formation. Within this, the oil is heated and its viscosity is reduced. Driven by gravity, oil and water flow in a countercurrent flow to the steam into the lower well. Production of steam and dissolved gases such as methane and carbon dioxide is prevented by their low density, causing them to rise in the steam chamber and fill the void space left by the oil. The water/oil mixture collected in the lower well is then pumped to the surface for processing.

Given the fact that a large amount of steam is needed for this process, emissions of greenhouse gases in producing crude oil from oil sands compared to primary oil recovery are significantly higher. The IHS Cambridge Energy Research Associates (IHS-CERA, 2012b) concluded that, depending on the selected boundary, oil from Canadian oil sands causes a 7–11% increase in greenhouse gas emissions (IHS-CERA, 2012a) compared to greenhouse gas emissions arising for an average US barrel of refined crude oil. This estimation covers all emissions from production to combustion in an engine, including oil processing and distribution. Forecasts of the Canadian Association of Petroleum Producers (CAPP) indicate that the production of oil sands by in-situ methods is expected to undergo growth from 0.8 million bbl/d in 2011 to 3.1 million bbl/d in 2030, corresponding to an annual average growth rate of 13.8% (CAPP, 2012a). This means that a significant rise in greenhouse gas emissions from oil sands production facilities is very probable in the near future. Mitigation of these emissions is a key issue in an environmentally friendly oil sands production strategy and to avoid further stressing the world's climate.

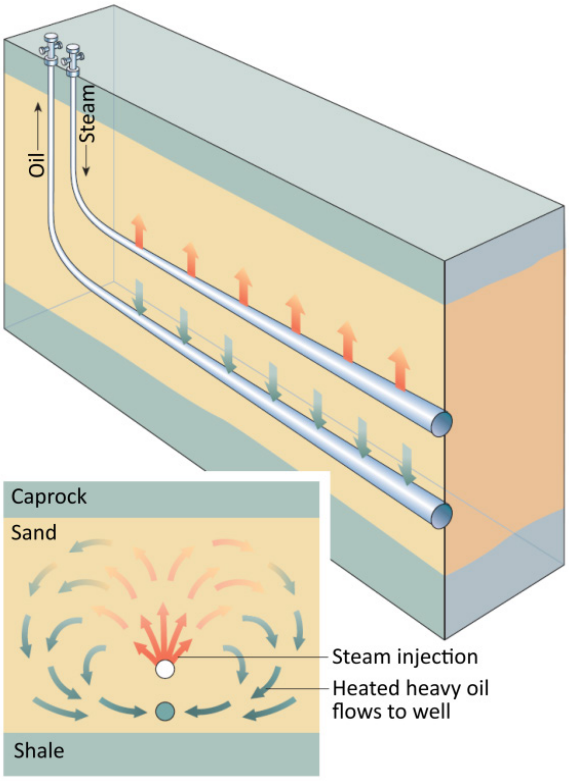

Fig. 74 Scheme of the steam assisted gravity drainage process. Adapted from Curtis et al. (2002).

6.1.2 Greenhouse gas mitigation in in-situ oil sands production

In the production of oil from oils sands by in-situ methods, most of the greenhouse gases arise during the production of the steam necessary to recover the oil from the oil sands. Primary energy resources, such as natural gas, are used in steam generators to produce the steam. The type of steam generator applicable is strongly dependent on the quality of the feedwater. Due to the fact that large quantities of steam are needed for in-situ oil recovery from oil sands, management of water usage and water processing is of significant importance. Therefore, typically low quality water is used, the trade off being that lower quality steam is produced. Once-through steam generators (OTSG) are known to be capable of handling such low purity feedwater with high availability. Buildup of inert components in the water cycle of the steam generator is prohibited by avoiding the occurrence of saturation in the steam generator. That is, the steam generator output is typically a water/steam mixture with a steam content of about 80% in terms of mass fraction (Gwak and Bae, 2010). This mixture is then sent to a water-steam separator and the steam used in the oil production process. In practice, the steam content in once-through steam generators is adjustable by the flow rate of the boiler feedwater.

In the trend of environmentally friendly oil from oil-sands, emission of greenhouse gases from the steam generator is the focus of politics and society, and actions to avoid these emissions are under discussion. For this reason, three carbon storage ready processes are compared to state-of-the-art steam generation using natural gas as the fuel. The base case is represented by a direct-fired once-through steam generator where air is used directly to combust the fuel (Fig. 75 *I.*). The first carbon capture process is derived from the base case with a CO_2 scrubber attached (Fig. 75 *II.*) in which the CO_2 is separated from the combustion gas using adequate chemical solvents such as amines or ammonia (Wang et al., 2011; Samanta et al., 2012). To avoid mixing of nitrogen in the air with combustion gases, the fuel is combusted with high purity oxygen in an

oxy-fuel combustion process from which a high purity CO_2 stream arises ready for sequestration (Fig. 75 *III.*). To limit the combustion temperature when oxy-combusting to acceptable temperatures, flue gas recycling is necessary. In addition to these first generation carbon capture and storage processes, a steam generator based on chemical looping combustion technology is considered (Fig. 75 *IV.*).

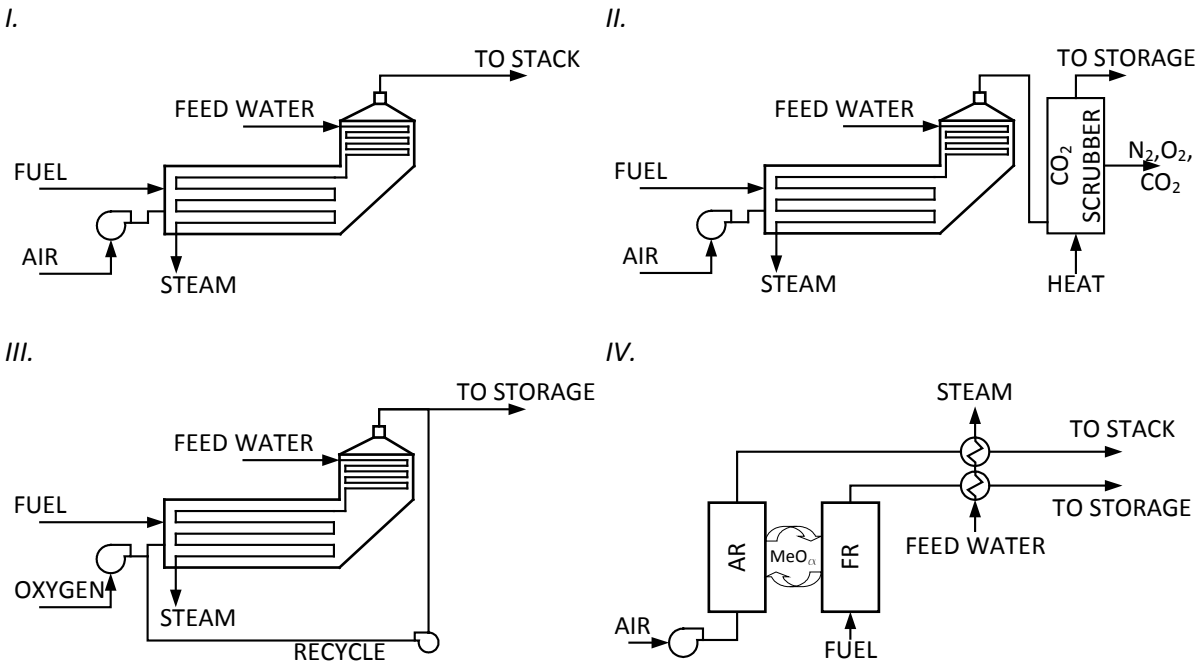

Fig. 75 Considered process cases:

I. Once-through steam generator without carbon capture.
II. Once-through steam generator with a post-carbon capture CO_2 scrubber attached.
II. Once-through steam generator with carbon capture-based on oxy-fuel combustion technology.
IV. Once-through steam generator using chemical looping combustion technology.

In the following discussion, the four processes will be compared.

6.2 Site conditions

The considered plant is to be implemented in a theoretical site located at the Athabasca oil sand deposit in Alberta, Canada. The selected site conditions are summarized in Table 6-1.

Table 6-1 Heavy oil extraction scenario site conditions.

Item	Value	Unit
Ambient		
temperature	1	°C
pressure	969	mbara
humidity	57	%
Fuel		
pressure	4	bara
temperature	1	°C
Fuel composition		
CH_4	98.87	mol%
C_2H_6	0.04	mol%
C_3H_8	0.01	mol%
N_2	0.69	mol%
CO_2	0.36	mol%
C_4H_{10}	0.01	mol%
C_6H_{14}	0.01	mol%
Boiler feedwater		
pressure	138.8	bara
temperature	190	°C
Output steam		
quality	0.8	-
pressure	110.7	bara

6.3 Process boundary conditions

To determine the performance of the processes discussed, in addition to the parameters given by the conditions at the site, more specific details are needed, e.g. parameters of the heat recovery section. These are given in Table 6-2.

Table 6-2 General process boundary conditions valid for all discussed processes.

Item	Symbol	Value	Unit
Fuel thermal input	P_{fuel}	100	MW
Weighing factor of the electric energy	σ	2	-
Minimal temperature difference of evaporative gas/water heat exchangers	$\Delta\vartheta_{min\_EVAP}$	25	°C
Minimal temperature difference of non-evaporative (e.g. economizer) gas/water heat exchangers	$\Delta\vartheta_{min\_ECO}$	15	°C
Blower			
isentropic efficiency	$\eta_{s,blower}$	82	%
mechanical efficiency	$\eta_{m,blower}$	100	%
Electric motor			
electrical efficiency	$\eta_{e,motor}$	96	%
mechanical efficiency	$\eta_{m,motor}$	99	%

6.4 Description of processes

The considered cases are:

- direct fired once-through steam generator with no carbon capture,
- direct fired once-through steam generator with post-combustion CO_2 capture,
- oxy-fuel combustion fired once-through steam generator, and
- once-through steam generator based on chemical looping combustion technology.

The details of each configuration are discussed in the following.

6.4.1 Direct-fired OTSG without carbon capture

The direct fired once-through steam generator without carbon capture is the basis for comparison since this is the most commonly used type of steam generator in this kind of application. The fuel is combusted in a cooled combustion chamber with air compressed to combustion chamber pressure using a blower. Before leaving the steam generator, heat is recovered from the combustion process exhaust gas in an evaporative heat exchanger (EVAP) and an economizer (ECO). The combustion gas is a mixture of N_2, CO_2 and O_2 and is not ready for sequestration. The simulation model of the direct fired once-through steam generator without carbon capture is depicted in Fig. 76.

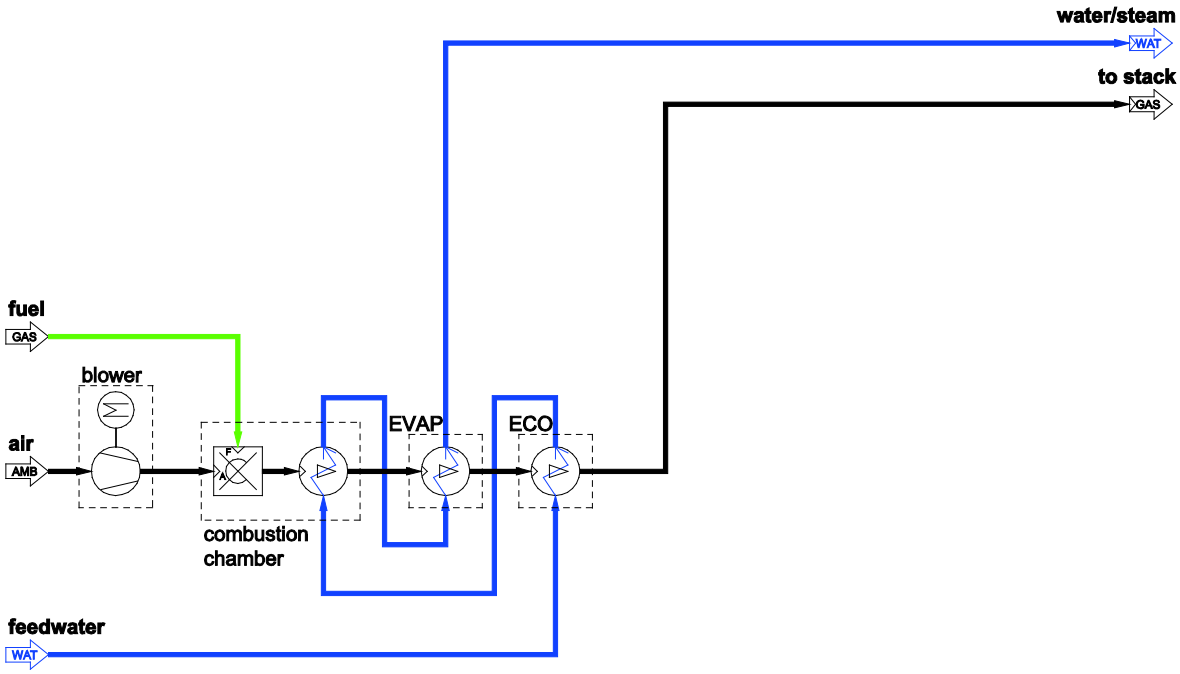

Fig. 76 Simulation model of the direct fired once-through steam generator without carbon capture.

In addition to the general process boundary conditions described in Table 6-2, selected parameters are summarized in Table 6-3.

Table 6-3 Additional boundary conditions for the direct fired OTSG without carbon capture.

Item	Symbol	Value	Unit
Combustion air/fuel ratio	λ	1.1	-
Combustion chamber burner gas pressure drop	Δp_{comb}	200	mbar
Relative heat loss of the boiler	$\dot{q}_{rel}$	3	%
Combustion chamber flue gas outlet temperature	ϑ_{comb}	1300	°C
Combustion chamber pressure drop on the flue gas side	$\Delta p_{comb,g}$	2	mbar
Combustion chamber pressure drop on the water side	$\Delta p_{comb,w}$	6.3	bar
Evaporator pressure drop on the gas side	$\Delta p_{evap,g}$	14	mbar
Evaporator pressure drop on the water side	$\Delta p_{evap,w}$	8	bar
Economizer pressure drop on the gas side	$\Delta p_{ECO,g}$	8	mbar
Economizer pressure drop on the water side	$\Delta p_{ECO,w}$	1.2	bar

6.4.2 Direct-fired OTSG with post-combustion CO_2 capture

The direct fired once-through steam generator with post-combustion capture is technically the most mature option for retrofitting an existing boiler. The process consists of a direct fired once-through steam generator described in Section 6.4.1 (p. 118) with a post-combustion CO_2 scrubber attached. The simulation model is shown in Fig. 77.

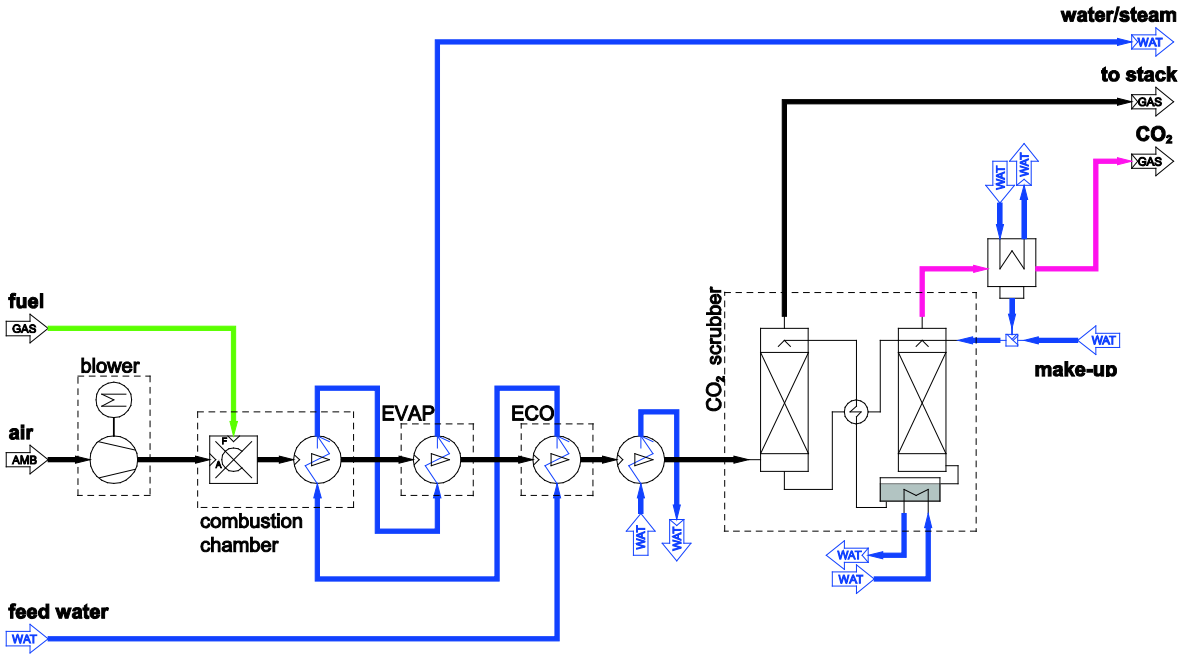

Fig. 77 Simulation model of the direct fired once-through steam generator with post-combustion CO_2 carbon capture.

In the CO_2 scrubber, the CO_2 is absorbed from the flue gas by the use of adequate solvents. For regeneration of the solvent, i.e. separation of the CO_2, thermal energy is necessary. The required amount is dependent on the type of solvent, with liquid solvents requiring 2.5-5.59 GJ/tCO_2 (Desideri and Paolucci, 1999; IPCC, 2005; Ohashi et al., 2011). If so-called solid amines, where the amines are supported by a solid carrier, are used, they allow for a significant reduction in the energy demand to 1.7 GJ/tCO_2 (Venemana et al., 2013) by avoiding the need for the energy of evaporation when using water-based solvents. To allow for a comprehensive comparison of the processes, a range of specific energy demands of CO_2 separation is considered, accounting for the different type of solvents and CO_2 separation rates. The range is specified to be $\dot{q}_{CO2\_sep}$ = 1.5-3.5 GJ/tCO_2. Further process parameters can be found in Table 6-2 and Table 6-3.

6.4.3 Oxy-fuel combustion fired OTSG

In oxy firing, the combustion air is substituted by high purity oxygen, avoiding the dilution of combustion gases by air nitrogen and leading to a CO_2 stream of high purity. The absence of nitrogen in the combustion chamber requires cooling the flame adequately to keep the material surface temperatures below reasonable limits. This is typically obtained by flue gas recycling (recycle). The simulation model of an oxy-fuel combustion fired once-through steam generator is shown in Fig. 78.

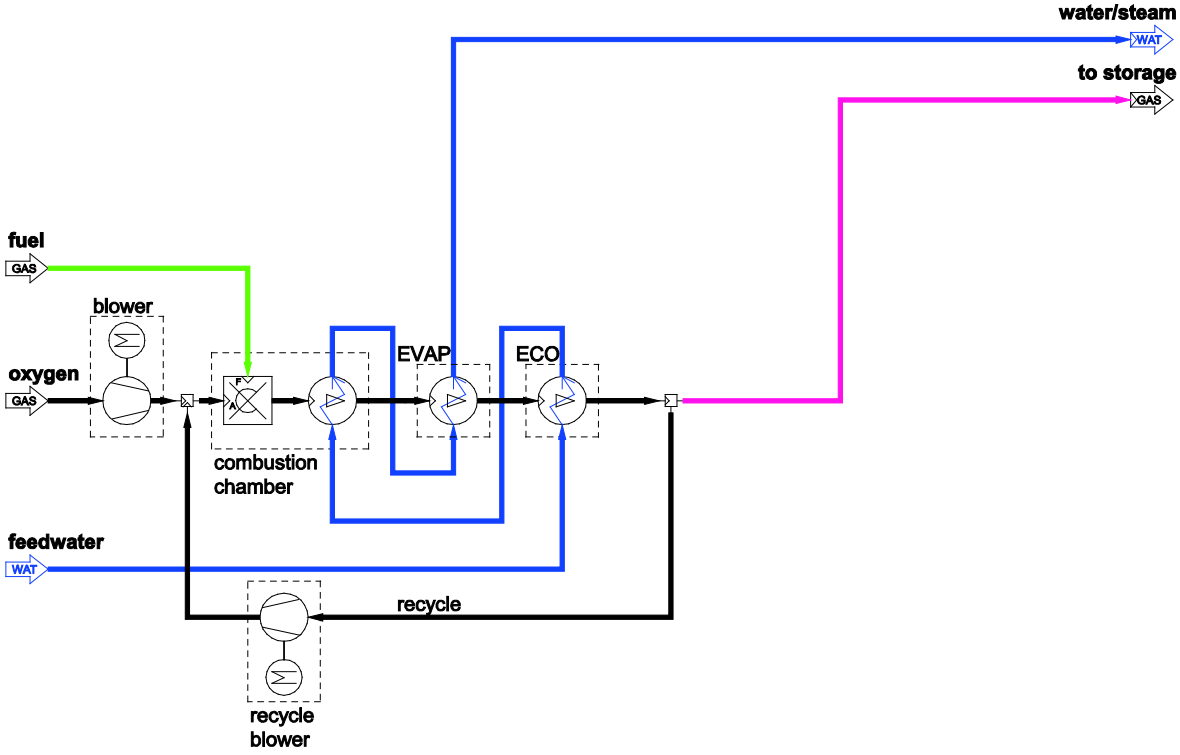

Fig. 78 Simulation model of the oxy-fuel combustion fired once-through steam generator.

The necessary oxygen is delivered from the boundary, with the delivery route outside the scope of this investigation. Currently, most of the oxygen is produced by cryogenic distillation of air in rectification-columns in the so called Linde process developed by Carl von Linde (Linde, 1905) utilizing the Joule-Thomson effect. The obtained oxygen purity is dependent on the pressure and temperature used in the process, with more energy needed for higher purity oxygen (Fig. 79).

This means that the higher the requested purity of the CO_2 for carbon capture in an oxy-fuel combustion process, the greater the need for electrical energy to supply the oxygen in the requested purity. In addition to the general boundary conditions described in Table 6-2, additional assumptions are needed, indicated in Table 6-4.

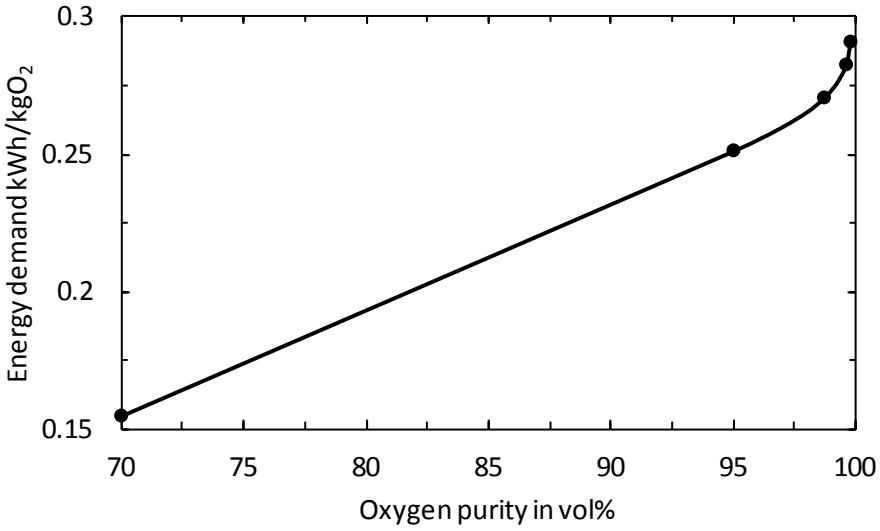

Fig. 79 Electrical energy demand for oxygen supply. Adapted from (Göttlicher, 1999; Spliethoff, 2011).

Table 6-4 Additional boundary conditions for the oxy-fuel combustion fired OTSG.

Item	Symbol	Value	Unit
CO slip in vol%	y_{CO}	1	vol%
Combustion chamber burner gas pressure drop	Δp_{comb}	200	mbar
Adiabatic combustion temperature	$\vartheta_{comb,ad}$	1900	°C
Combustion chamber flue gas outlet temperature	ϑ_{comb}	1300	°C
Relative heat loss of the boiler	$\dot{q}_{rel}$	3	%
Combustion chamber pressure drop on the flue gas side	$\Delta p_{comb,g}$	2	mbar
Combustion chamber pressure drop on the water side	$\Delta p_{comb,w}$	6	bar
Evaporator pressure drop on the gas side	$\Delta p_{evap,g}$	14	mbar
Evaporator pressure drop on the water side	$\Delta p_{evap,w}$	8.4	bar
Economizer pressure drop on the gas side	$\Delta p_{ECO,g}$	8	mbar
Economizer pressure drop on the water side	$\Delta p_{ECO,w}$	1.1	bar
Recycle blower isentropic efficiency	$\eta_{s,rec}$	82	%
Recycle blower mechanic efficiency	$\eta_{m,rec}$	100	%

6.4.4 Chemical looping combustion OTSG

The process flow diagram, shown in Fig. 80, represents the entire chemical looping combustion once-through steam generator. For reasons of clarity, the water/steam cycle is drawn as interrupted lines with numerical indicators, i.e. -1-, -2- … -5-, representing the physical connections in the cycle. The input streams of fuel, air and feedwater, as well as the output streams of water/steam, AR exhaust and FR exhaust are the system boundaries of the plant. Natural gas is provided at elevated pressure and used after throttling (V2) as a fuel. Air is provided under ambient conditions (see Table 6-1) and delivered to the air reactor riser after compression in the air blower to account for the pressure drop in the air reactor riser system, i.e. air distributor, riser and cyclone. By shifting heat from the fuel reactor and air reactor exhaust to the feed streams of fuel and air, the overall performance can be improved by including a fuel preheater (fuel_ph) and an air preheater (air_ph). The feedwater is supplied pressurized from the battery limit and is used after throttling (V1) as a boiler feedwater and to generate the necessary fluidization steam (fluidization steam generator). A throttle valve (V3) is included to reduce the feedwater pressure to riser system inlet conditions for proper loop seal fluidization.

The process flow diagram covers the chemical looping combustion reactor system and the heat recovery section. The specified steam is generated in a once-through steam generator where water is forced through the heat exchangers by applying adequate pressure. Under typical chemical looping combustion conditions, the heat produced in the reactor system is greater than the sensible heat in the two exhaust gas streams. Therefore, cooling of the air reactor riser using water walls (-2- to -3-) and the use of a bed material cooler (BMC) is foreseen. By taking only a part (S3) of the solids elutriated from the air reactor (S1), the heat/energy balance of the reactor system is controlled. This can be achieved by use of a hot sand valve, discussed in previous chapters. The setup of the once-through steam generator furthermore includes heat recovery from the fuel reactor exhaust gas (H_FR and ECO FR) and the air reactor exhaust gas (H_AR and ECO AR). The water/steam produced in the steam generator is sent to the battery limit for further processing. The pressure and steam quality is modified by adjusting the flow rate of water through the steam generator, which is achieved by adjusting the pressure at the inlet of the steam generator (V1). To account for the pressure drop in the heat exchanger, connecting pipes with pressure drops are arranged in the model.

To overcome the gas pressure drop in the heat recovery section of the fuel and air reactor, two induct fans are needed: the fuel reactor induct fan (FR ID fan) and the air reactor induct fan (AR ID fan).

The air reactor exhaust gas is oxygen-depleted air and can be released to the environment without major concerns. The gas leaving the fuel reactor is a concentrated CO_2 stream ready for sequestration after water condensation.

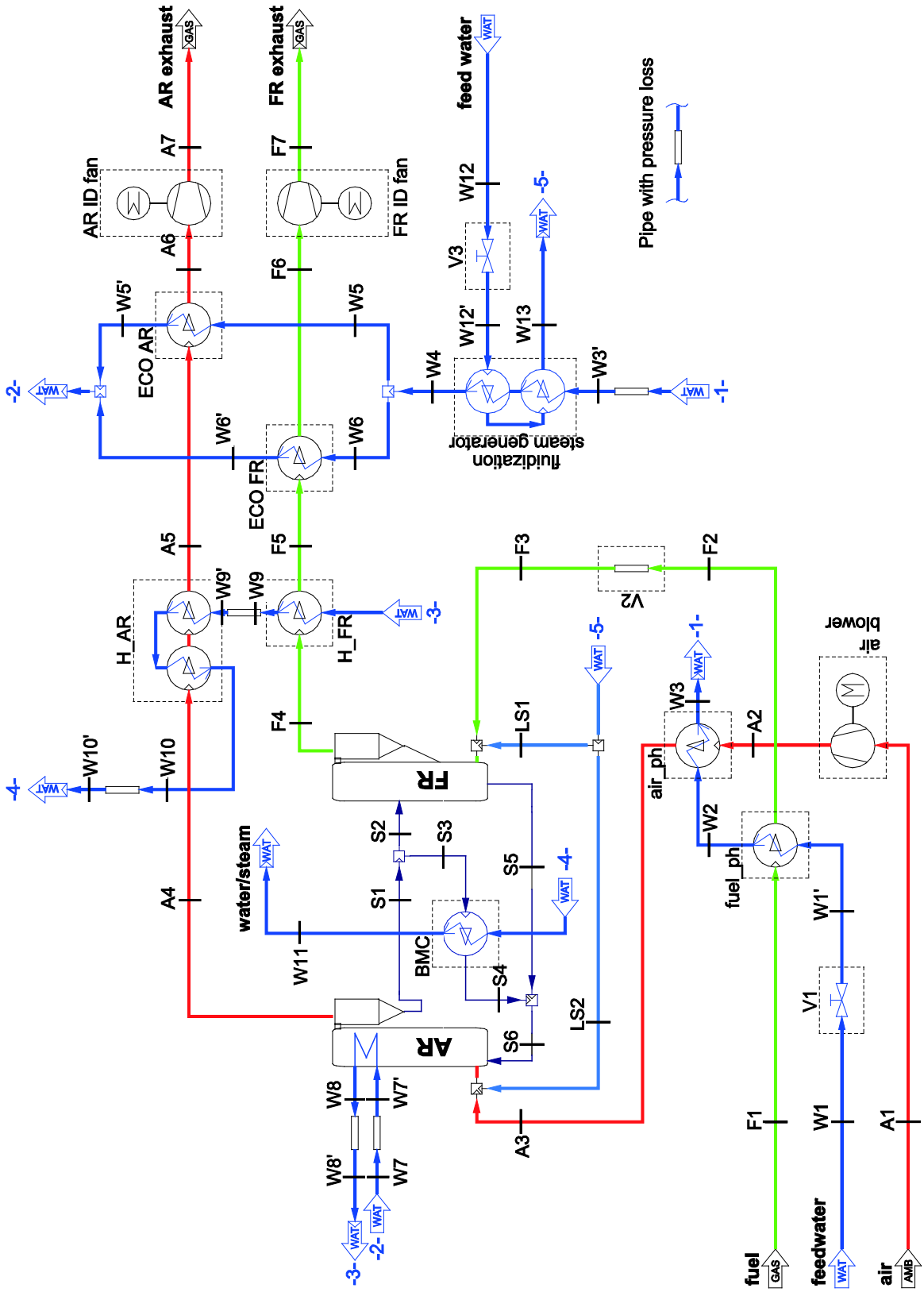

Fig. 80 Simulation model of the chemical looping combustion once-through steam generator.

In addition to the parameters given in Section 6.3 (p. 117) and Table 6-2, chemical looping combustion process-specific parameters are summarized in Table 6-5 based on operation experience gained in testing at the 140 kW chemical looping combustion laboratory pilot at the Vienna University of Technology. In this study, the theoretical performance of the chemical

looping combustion process was assessed by prescribing thermodynamic equilibrium at the fuel reactor exit when an oxygen carrier based on the NiO/Ni redox system is used.

Table 6-5 Additional boundary conditions for the chemical looping combustion OTSG.

Item	Symbol	Value	Unit
Global air/fuel ratio	λ	1.1	-
Riser pressure drop (AR and FR)	Δp_{riser}	200	mbar
AR superficial gas velocity (related to the riser exit)	Us_{AR}	7.5	m/s
Air reactor water wall cooling duty	$\dot{Q}_{AR}$	20	MW
Air reactor water wall pressure drop on the water side	$\Delta p_{AR,w}$	2	bar
Air reactor relative heat loss (based in total thermal fuel input)	$\dot{q}_{AR}$	1.5	%
FR superficial gas velocity (related to the riser exit)	Us_{FR}	5.5	m/s
Fuel reactor relative heat loss (based in total thermal fuel input)	$\dot{q}_{FR}$	1.5	%
Oxygen carrier conversion (based on degree of oxidation)	ΔXs	15	%
Fuel reactor gas exit temperature	$\vartheta_{FR,exit}$	900	°C
Solids split-up ratio to bed material cooler	X_{BMC}	30	%
AR and FR exhaust gas heat exchanger pressure drop on the water side	$\Delta p_{H,w}$	3	bar
AR and FR exhaust gas heat exchanger pressure drop on the gas side	$\Delta p_{H,g}$	8	mbar
AR and FR economizer pressure drop on the water side	$\Delta p_{ECO,w}$	2	bar
AR and FR economizer pressure drop on the gas side	$\Delta p_{ECO,g}$	4	mbar
Air preheater pressure drop on the water side	$\Delta p_{air\_ph,w}$	0.1	bar
Air preheater pressure drop on the gas side	$\Delta p_{air\_ph,g}$	5	mbar
Fuel preheater pressure drop on the water side	$\Delta p_{fuel\_ph,w}$	0.1	bar
Fuel preheater pressure drop on the gas side	$\Delta p_{fuel\_ph,g}$	0.2	bar
Connecting pipe pressure drop	Δp_{pipe}	0.1	bar
Fluidization steam generator pressure drop on the hot side	$\Delta p_{FSG,hot}$	2	bar
Fluidization steam generator pressure drop on the cold side	$\Delta p_{FSG,cold}$	2	bar
Minimal temperature difference of non-evaporative (e.g. economizer) gas/water heat exchangers	ϑ_{min_FSG}	10	°C
Pressure drop in the connecting pipes	Δp_{pipe}	100	mbar

6.5 Comparison of the four processes

The process effective efficiency (for the definition, see (eqn. 3-35)) in the base case was found to be 87%, based on natural gas input (lower heating value). This relatively low value originates from the considered site conditions, i.e. the low feedwater quality requiring high boiling water blow-down rates. Capturing carbon dioxide emissions from combustion processes is energy demanding, with the type (electrical or thermal) and intensity depending on the technology applied. Comparing the considered processes to each other (Fig. 81) reveals that, in any carbon capture and storage case, the performance of the chemical looping combustion case is significantly better. This is because only a minor amount of energy is lost compared to the base case where the greenhouse gases are emitted to the surroundings. Expressed in numbers, this means that the effective efficiency is reduced by only 1.2–2.5%-pts. in the chemical looping combustion case. The lower vale originates to the case where air and fuel preheating is applied, allowing for reduced stack losses (see Fig. 80 air_ph and fuel_ph).

In post-combustion CO_2 capture, a significant amount of heat is needed to desorb the CO_2 from the solvent after capturing it from the flue gas, depending on the type of solvent. Solid CO_2

sorbents are reputed to potentially reduce this energy demand. Regardless, even when requiring very little energy ($\dot{q}_{CO2,rel}$ = 1.5 GJ/tCO_2), a considerable reduction in process performance of 6–8%-pts. is expected referring to the base case. With typical liquid solvents ($\dot{q}_{CO2,rel}$ = 3 GJ/tCO_2), this value even doubles to 12–17%-pts..

In oxy-fuel combustion, the performance loss is caused by the energy needed to supply the necessary oxygen. Post-combustion CO_2 solvents with very low specific CO_2 capture perform better than oxy-fuel combustion.

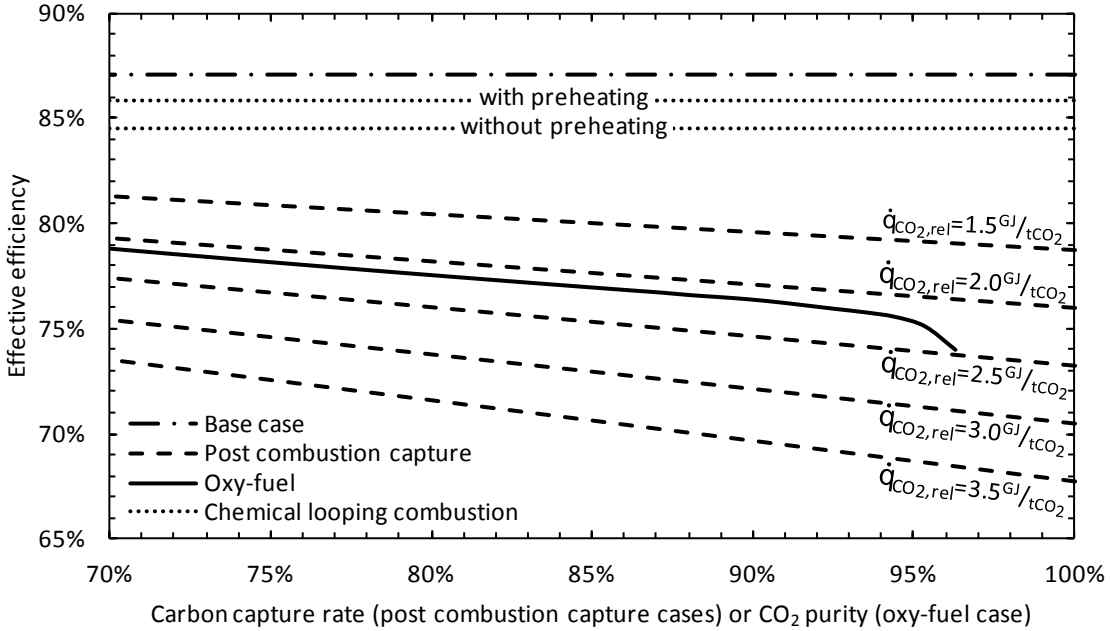

Fig. 81 Effective efficiency of the four processes with the effective efficiency of the post-combustion capture process depending on the carbon capture rate and the effective efficiency of the oxy-fuel combustion process depending on the CO_2 purity of the exhaust gas based on its water-free composition.

6.6 Summary and conclusion

Oil is the most important fossil resource, accounting for 33.1% of the world's total energy consumption. Among other sources, large quantities of oil are stored as unconventional oil in oil sands requiring advanced technologies for recovery. All these technologies have in common that a significant amount of energy, such as steam, is needed in the oil sands production process. This means that 7–11% more greenhouse gases are emitted when producing oil from oil sands compared to conventional oil production routes. Against the background of global warming and with an expected increase in oil production from oil sands, methods of limiting these emissions are required.

Three carbon capture ready processes have been compared to the state-of-the-art once-through steam generation commonly used in the production of oil sands. In the first case, a post-combustion CO_2 capture unit is attached to the conventional boiler, representing the option with the greatest potential for retrofitting. In the second case, an oxy-fuel combustion based once-through steam generator where the combustion air is substituted by oxygen is considered. In the

third case, a so-called second generation carbon capture process based on chemical looping combustion technology is presented.

The effective steam generation efficiency in the base case was found to be 87%, based on natural gas input (lower heating value). This relatively low value originates from the considered site conditions, i.e. the low feedwater quality requiring high boiling water blow-down rates. Comparison of the three carbon capture processes revealed that the loss in efficiency for carbon capture is the lowest when using chemical looping combustion technology. When compared to combustion with air only, 1.1-2.5%-pts. efficiency is lost, although 100% of the carbon is captured. The losses caused by post-combustion CO_2 capture are dependent on the capture rate and the type of solvent used, and are significantly higher in any case. Also, the oxy-fuel combustion process causes high losses, comparable to the post-combustion process with high performance solvents. Thus, chemical looping combustion for the production of industrial steam is a very promising option whenever there is the need for carbon capture. It needs to be noted that additional energy will be needed in all cases for compression and purification of the captured CO_2.

7 Summary and conclusion

The emission of greenhouse gases from combustion processes is considered one of the most significant contributors to the anthropogenic part of the greenhouse gas effect. Mitigation of emissions these is a key mid-term strategy; namely, the reduction of carbon dioxide emissions. Combustion of either fossil or fossil-derived fuels in industrial or energy production processes plays a major role when it comes to CO_2 emissions.

Chemical looping combustion is a two-step combustion process where mixing of combustion air and fuel is inherently avoided. This process is generally established by using metal oxides, conducting a continuous reduction-oxidation cycle to transfer the oxygen needed for combustion between two separate reactors; the air reactor and the fuel reactor. Hence, combustion flue gases are free from air nitrogen and, after water condensation, a CO_2-rich stream is obtained, ideally ready for sequestration. Therefore, CLC offers great potential compared to all other carbon capture technologies, as it avoids energy and cost intensive gas-gas separation steps and thus considerably reduces CO_2 avoidance costs.

The potential of chemical looping combustion for gaseous fuels has been successfully demonstrated in the past in numerous laboratory batch and continuous test facilities, at scales of up to 140 kW fuel power input. A variety of different oxygen carriers have been tested, with nickel-based ones being the most intensively studied with more than 1500 h of continuous chemical looping combustion operation. For this reason, the logical next step in the process evolution is the demonstration of the technology at an industrial scale to gain sufficient confidence in chemical looping for further up-scaling.

A potential next scale chemical looping combustion demonstration unit based on 10 MW thermal input using gaseous fuels has been integrated into a commercial natural gas combined cycle plant with supplementary firing before the heat recovery section. The chemical looping combustion unit is designed to substitute the energy input of the supplementary firing which in turn can easily compensate for fluctuations from the demonstration plant operation with very little response time. The chemical looping combustion demonstration unit is integrated into the existing infrastructure and shares the water steam cycle with the existing plant, allowing for a significant reduction in demonstration-related costs.

The selected oxygen carrier is based on nickel, as this specific type is the best known and most promising for gaseous fuels. The oxygen carrier is supported by nickel-aluminate and magnesium-aluminate with an active nickel content of 40.6 wt%. To account for uncertainties in expectable fuel conversion, fuel conversion data observed in 140 kW testing and thermodynamic equilibria were assessed to determine the effect of fuel conversion on expectable plant performance data.

It was found that the chemical looping boiler efficiency could reach values of 87.7 to 96.1%, which is the amount of steam produced in the boiler setup relative to the thermal energy input by the fuel (based on LHV). Bearing in mind the small size of the unit, these values are in the typical range of small-scale steam boilers without carbon capture. Improvements will require an increase in heat exchanger size, which in turn increases the investment costs. Moreover, there is a significant amount of energy lost by incomplete combustion when the fuel conversion is as low as in the case derived from the experimental data. Treatment of the fuel reactor exhaust is therefore crucial to make use of this energy. One option is to separate the combustibles during compression

of the fuel reactor exhaust gas by cryogenic CO_2 purification. These then can be recycled to the fuel reactor. Another possibility is to apply oxygen polishing where the remaining fuel gases are oxidized with high purity oxygen. Both options are costly and require either energy during CO_2 liquefaction or for producing the necessary oxygen. Mitigation of the occurrence of combustibles is therefore considered to be essential to be competitive with other CCS technologies. Advanced oxygen carriers, currently being developed, are expected to be a significant driver to overcome this challenge.

A heat integration setup was established, including a water wall cooled air reactor and an external bed material cooler in a return loop of the air reactor. The arrangement was tested against part-load operability. It was found that the setup is very flexible towards changed fuel inputs and is able to handle loads from 55% to more than 110%, referring to the nominal load (10 MW). Additional auxiliary energy demand (blower duty) is reduced by directing the bed material cooler fluidization air to the air reactor where it takes part in oxygen carrier oxidation.

Based on the specific requirements of chemical looping combustion, such as prolonged gas-solids contact time, the design of a 10 MW chemical looping combustion demonstration unit was pursued. The system is based on the dual circulating fluidized bed concept where both the air reactor and the fuel reactor operate in a circulating fluidized bed regime. A fast fluidized bed was applied to the design of the air reactor focusing on high solids entrainment rates. Air staging is used to control the specifically occurring solids fluxes. The design of the fuel reactor was based on a turbulent fluidized bed regime, which is expected to promote fuel conversion rates. The air and fuel reactor heights were determined by cross-correlating capacity and the height of the existing circulating fluidized bed boilers. Cross-section areas, gas flow rates and expectable solids holdups were assessed. The dimensions of the cyclone separators placed at the exit of the air reactor and fuel reactor were derived, focusing on high solids entrance loads and high performance. The design of the three loop seals in the dual circulating fluidized bed concept was adapted to meet the demands of the size of the unit. Expectable solids inventories and fluidization gas flow rates were determined. The dimensions of the external bed material cooler were derived by quantification of heat transfer.

Based on this design, a scaled cold flow model was designed and erected. The cold flow model allows for investigations into the hydrodynamic behavior of the hot unit by the application of similarity rules. The Glicksman set of scaling parameters, which based on dimensionless analysis of the governing equations in fluidized beds, was used. The cold flow model includes all parts of the design of the hot unit such as risers, cyclones, loop seals, the solids flow control valve and the bed material cooler. The model setup was described using 3D CAD software, then was constructed and put into operation. The model is equipped with 52 pressure measurement ports and variable area flow meters for volume-flow measurements. The intensive testing in the cold flow model verified the potential of the proposed design. Minor design improvements had to be made with respect to increasing the cyclones separation efficiency. Loop seal operation was investigated, which allowed a reduction in the necessary fluidization rates by 18.8% compared to the design. The solids flow control valve was successfully tested without the appearance of either blockage or any other undesired operating conditions. It was also found that, in the typical operating range, the proposed design of the solids flow control valve had a linear control characteristic. However, emptying of the upper loop seal can occur when the valve is opened too far. The automatic control setup, thus, has to include monitoring the upper loop seal downcomer

inventory by means of differential pressure measurements. Testing the gas staging applied to the air reactor was shown to be an effective mechanism to control the solids flow rate from the air rector to the fuel reactor. No flow limitations were identified, even for very high solids fluxes. The simulation of the gas envelope in the fuel reactor verified that the proposed design is capable of handling varying reaction velocities. The potential for leakage of fuel reactor gas was identified for the lower loop seal. However, the measured values were too low to allow for quantification of the specific leakage rate. The path of the gas introduced into the loop seals was determined. As expected, most of the gas travels with the solids.

The potential of chemical looping combustion at the large scale (100 MW) has been assessed and compared to first generation CCS processes; namely, post-combustion capture and oxy-fuel combustion. The units are based on once-through steam generation technology for the production of industrial steam for in-situ heavy oil extraction from oil sands. It was found that, in such cases, chemical looping combustion is the optimum application. The energy penalty is very low compared to steam generation without carbon capture where an efficiency drop of only about 1.1-2.5%-pts. can be expected. Even very efficient solid amine post-combustion sorbents, which are currently under development, are not able to compete with chemical looping combustion.

It is therefore concluded that since chemical looping performance is high compared to other CCS processes, and with this work an adequate design is available, it is only a question of time until chemical looping combustion will be demonstrated, probably in a next step at the 10 MW fuel power input as investigated in the present work.

8 Notation

8.1 Abbreviations

Symbol	Name
AET-Lib	Advanced energy technology library
air ph	Air preheater
AR	Air reactor
AR ECO	Air reactor economizer
AR ID fan	Air reactor induct fan
AR_clg	Water walls inside the air reactor
BFW	Boiler feedwater
BMC	Bed material cooler
bot.	Bottom
CAPP	Canadian Association of Petroleum Producers
cat.	Catalyst
CCS	Carbon capture and storage
chem.	Chemical energy on the lower heating value at 25.0°C and 1.0 bara
CHP	Combined heat and power plant
CLC	Chemical looping combustion
clg.	Cooling
CLOU	Chemical looping with oxygen uncoupling
CLR	Chemical looping reforming
CLR(a)	Auto-thermal chemical looping reforming
cn	Center
compr.	Compression
cond.	Condensation heat at 25.0°C and 1.0 bara
CSS	Cyclic steam stimulation
DCFB	Dual circulating fluidized bed
DFB	Dual fluidized bed
DH	District heating
DLL	Dynamic link library
e	Energy with reference to the boiler feedwater
E0	Energy with reference to thermodynamic standard conditions
ECO	Economizer
el.	Electrical energy
EVAP	Evaporator
exh	Exhaust
exp.	Expansion
FCC	Fluid catalytic cracking
FR	Fuel reactor
FR ECO	Fuel reactor economizer
gen.	Generator
GT	Gas turbine
H_AR	Heat exchanger in the air reactor exhaust gas duct
H_FR	Heat exchanger in the fuel reactor exhaust gas duct
heatl.	Sensible heat loss
HP	High pressure
HRSG	Heat recovery steam generator
IAPWS	International Association for the Properties of Water and Steam
ID	Induct
IEA	International Energy Agency
ILS	Internal loop seal

Symbol	Name
IPCC	Intergovernmental Panel on Climate Change
LLS	Lower loop seal
LP	Low pressure
MDK	Model development kit
Me	Metal
mech.	Mechanical energy
MeO_α	Metal oxide
NGCC	Natural gas combined cycle
OC	Oxygen carrier
OECD	Organization for Economic Co-operation and Development,
OTSG	Once-through steam generator
PCLR	Pressurized chemical looping reforming
ph	Preheater
prim.	Primary
PSD	Particle size distribution
PSE	Process simulation environment
SAGD	Steam assisted gravity drainage
SCV	Solids flow control valve
sec.	Secondary
sens.	Sensible heat with reference to 0.0°C and 1.0 bara
SER	Sorption enhanced reforming
SH	Superheater
SH I	Steam superheater I
SH II	Steam superheater II
ter.	Tertiary
ULS	Upper loop seal
V1	Valve
V2	Valve
V3	Valve
VDI	Verein Deutscher Ingenieure
WW	Water walls

8.2 Symbols

Symbol	Name	Unit
a	Constant for quantification of the riser height	m^2/W
a	Decay constant	m^{-1}
A_{AR}	Air reactor cross-section area	m^2
A_{BMC}	Required bed material cooler surface area	m^2
a_{BMC}	Heat exchanger chamber width	m
A_{BMC}	Bed material cooler surface area	m^2
A_i	Species *i* taking part in the chemical reaction	-
A_i	Cyclone inlet cross-section area	m^2
A_o	Cyclone vortex finder cross-section area	m^2
Ar	Archimedes number	-
A_{riser}	Riser cross-section area	m^2
a_{set}	Settling chamber width	m
b	Constant for quantification of the riser height	m^2
b_{BMC}	Heat exchanger chamber depth	m
b_{set}	Settling chamber depth	m
c	Constant for quantification of the riser height	m

Symbol	Name	Unit
C_1	Constant	-
C_2	Constant	-
C_D	Drag coefficient of a sphere	-
C_D	Drag coefficient in a fluidized bed	-
D	Fluidized bed diameter	m
D_a	Outer diameter of the cylindrical part of the cyclone	m
dm/dt	Mass accumulation	kg/s
dm_k/dt	Accumulation of a element k	kg/s
D_o	Diameter of the vortex finder	m
d_p	Mean particle diameter	m
d_p^*	Dimensionless particle diameter	-
d_T	Bed material cooler tube outer diameter	m
Fr	Froude number	-
Fr_D	Froude number based on bed diameter	-
Fr_p	Froude number based on particle diameter	-
G	Gibbs free enthalpy	J/kg
g	Gravitational constant	m/s^2
Gs	Solids flux	$kg/m^2 \cdot s$
Gs_{AR}	Air reactor solids flux	$kg/m^2 s$
$Gs_{critical}$	Critical solids flux	$kg/m^2 s$
Gs_{FR}	Fuel reactor solids flux	$kg/m^2 s$
H	Height of the fluidized bed	m
$h(p,T)$	Specific enthalpy	J/kg
h_{BFW}	Specific enthalpy of the boiler feedwater	J/kg
h_{BMC}	Heat exchanger chamber height	m
h_{CLC}	Riser height of the CLC demonstration unit	m
$h_{DH,r}$	Enthalpy of the return water in the district heating cycle	J/kg
$h_{DH,s}$	Enthalpy of the supply water in the district heating cycle	J/kg
h_{riser}	Riser height	m
h_{set}	Settling chamber height	m
h_t	Conventional enthalpy	J/kg
h_t	Conventional enthalpy	J/kg
$h_{wat/st}$	Specific enthalpy of the water/steam	J/kg
$\boldsymbol{J}^{(n)}$	Jacobian matrix	-
k	Konstant term	s/m
$(k \cdot A)_{AR}$	Heat transfer number to the air reactor water wall	W/K
k_{BMC}	Bed material cooler total k-value	W/m^2K
K_i	Equilibrium elutriation constant	$m^2 \cdot s/kg$
K_p	Equilibrium constant	$bar^{\Sigma vi}$
l	Vortex finder length	m
LHV	Lower heating value	J/kg
l_{min}	Stoichiometric combustion air demand	kg/kg
l_u	Losses due to unburnt fuel	-
m	Actual mass of the oxygen carrier	kg
m_{BMC}	Solids inventory in the heat exchanger chamber	kg
$\dot{m}_{BMC}$	Solids flowing to the bed material cooler	kg/s
$\dot{m}_{CH4}$	Mass flow rate of CH_4	kg/s
$\dot{m}_{DH}$	Mass flow rate of district heating water	kg/s
$\dot{m}_{FS\_BMC}$	Fluidization gas to the heat exchanger chamber	kg/h
$\dot{m}_{FS\_set}$	Fluidization gas to the settling chamber	kg/h
$\dot{m}_g$	Mass flow rate of stream g	kg/s
M_i	Molar mass of i	kg/kmol

Symbol	Name	Unit
$\dot{m}_i$	Mass flow rate of *i*	kg/s
M_k	Molar mass of the element *k*	kg/mol
$\dot{m}_{k,g}$	Mass flow rate of component *k* in stream *g*	kg/s
$\dot{m}_{LS}$	Live steam mass-flow rate	kg/s
$\dot{m}_{OC}$	Oxygen carrier global mass-flow rate	kg/s
m_{ox}	Mass of the oxidized oxygen carrier	kg
m_{red}	Mass of the reduced oxygen carrier	kg
$m_{s,AR}$	Active solids inventory in the air reactor	kg
$\dot{m}_{s,AR}$	Solids entrained from the air reactor	kg/s
$m_{s,FR}$	Active solids inventory in the fuel reactor	kg
m_{set}	Solids inventory in the settling chamber	kg
m_{sol}	Riser solids inventory or Riser system total inventory	kg
$\dot{m}_{wat/st}$	Mass flow rate of the water steam mixture	kg/s
n	Load factor	-
O_{min}	Stoichiometric combustion oxygen demand	kg/kg
p_{amb}	Ambient pressure	bar
p_{BFW}	Boiler feedwater pressure	bar
$p_{deaerator}$	Boiler feedwater deaerator pressure	bar
P_{el}	CLC boiler system electric power demand	kW
$P_{exhaust}$	Chemical energy of the fuel reactor exhaust gas (based on LHV)	W
p_{fuel}	Fuel pressure	bar
P_{fuel}	Fuel power or chemical energy of the fuel (based on LHV)	W
p_i	Partial pressure of component *i*	bar
P_i	Control value	-
p_i^*	Equilibrium partial pressure of component *i*	bar
P_{in}	Mechanical energy input	W
p_{LS}	Live steam pressure	bar
P_{out}	Extracted mechanical energy	W
$p\delta_{eq}$	Logarithmic deviation from the equilibrium	
Q_3	Cumulative frequency	%
$\dot{q}_{AR}$	Air reactor relative heat loss (based in total thermal fuel input)	-
$\dot{Q}_{AR}$	Air reactor water wall cooling duty	kW
$\dot{q}_{AR,loss}$	Air reactor relative heat loss	-
$\dot{q}_{CO2\_sep}$	Specific heat for CO_2 separation	GJ/tCO_2
$\dot{Q}_{DH}$	Sensible heat for district heating	W
$\dot{q}_{FR}$	Fuel reactor relative heat loss (based in total thermal fuel input)	-
$\dot{q}_{FR,loss}$	Fuel reactor relative heat loss	-
$\dot{Q}_{out}$	Sensitive heat loss or extracted sensible heat	W
$\dot{q}_{rel}$	Relative heat loss of the boiler	-
$\dot{Q}_{wat/st}$	Thermal energy in the water/steam	W
R	Universal gas constant	J/mol·K
$\boldsymbol{R}^{(n)}$	Vector of functions	-
$R(x)$	Twice continuously differentiable function	-
$R'(x)$	First order derivation of the function $R(x)$	-
R_0	Oxygen carrier oxygen transport capacity	-
Re	Reynolds number	-
Re_c	Reynolds number at the onset of turbulent fluidization	-
Re_p	Particle Reynolds number	-
Re_{pmf}	Particle Reynolds number at minimum fluidization	-
Re_{se}	Reynolds number at the onset of fast fluidization	-
r_i	Vortex finder radius	m
S	Surface area	m^2

Symbol	Name	Unit
s_T	Bed material cooler wall thickness	m
Stk	Stokes number	-
T	Temperature	K
U^*	Dimensionless superficial gas velocity	-
$U_{AR\text{-}design}$	Superficial air reactor design gas velocity	m/s
U_c	Superficial gas velocity at the onset of turbulent fluidization	m/s
U_c^*	Dimensionless superficial gas velocity at the onset of turbulent fluidization	-
$U_{c\text{-}FR}$	Superficial gas velocity in the fuel reactor at the onset of turbulent fluidization	m/s
$U_{FR\text{-}design}$	Superficial fuel reactor design gas velocity	m/s
U_g	Gas velocity	m/s
U_i	Cyclone inlet gas velocity	m/s
U_{mb}	Superficial minimum bubbling gas velocity	m/s
U_{mf}	Superficial gas velocity at minimum fluidization	m/s
$U_{mf\text{-}loop\ seal}$	Minimum fluidization superficial gas velocity in the loop seal	m/s
U_{ms}	Superficial minimum slugging gas velocity	m/s
Us	Superficial gas velocity	m/s
Us_{AR}	Air reactor superficial gas velocity	m/s
U_{se}	Superficial gas velocity at the onset of fast fluidization or blow-out velocity	m/s
U_{se}^*	Dimensionless superficial gas velocity at the onset of fast fluidization	-
$U_{se\text{-}AR}$	Superficial gas velocity in the air reactor at the onset of fast fluidization	m/s
$U_{se\text{-}FR}$	Superficial gas velocity in the fuel reactor at the onset of fast fluidization	m/s
Us_{FR}	Fuel reactor superficial gas velocity	m/s
$Us_{loop\ seal}$	Superficial gas velocity in the loop seal	m/s
U_t	Superficial terminal gas velocity	m/s
U_t^*	Dimensionless terminal superficial gas velocity	-
$\dot{V}$	Volumetric gas flow rate	m^3/h
$\dot{V}_{air}$	Air flow rate	m^3/s
$\dot{V}_{AR}$	Volumetric gas flow rate to the air reactor	m^3/s
$\dot{V}_{AR\text{-}exh}$	Air reactor exhaust gas flow rate	m^3/s
V_{CA}	Gas velocity at the onset of pneumatic conveying	m/s
$\dot{V}_{CO2}$	Volumetric flow rate of CO_2	m^3/s
$\dot{V}_{FR}$	Volumetric gas flow rate to the fuel reactor	m^3/s
$\dot{V}_{FR\text{-}exh}$	Fuel reactor exhaust gas flow rate	m^3/s
$\dot{V}_{fuel}$	Volumetric gas flow rate of the fuel	m^3/s
$\dot{V}_{ILS\_center}$	Volumetric gas flow rate to the ILS center section	m^3/s
$\dot{V}_{ILS\_inlet}$	Volumetric gas flow rate to the ILS inlet section	m^3/s
$\dot{V}_{ILS\_outlet}$	Volumetric gas flow rate to the ILS outlet section	m^3/s
$v_{k,i}$	Quantity of element k in component i	-
$\dot{V}_{LLS\_center}$	Volumetric gas flow rate to the LLS center section	m^3/s
$\dot{V}_{LLS\_inlet}$	Volumetric gas flow rate to the LLS inlet section	m^3/s
$\dot{V}_{LLS\_outlet}$	Volumetric gas flow rate to the LLS outlet section	m^3/s
$v_{sol\text{-}upward}$	Solids upwards traveling velocity	m/s
$\dot{V}_{ULS\_center}$	Volumetric gas flow rate to the ULS center section	m^3/s
$\dot{V}_{ULS\_inlet}$	Volumetric gas flow rate to the ULS inlet section	m^3/s
$\dot{V}_{ULS\_outlet}$	Volumetric gas flow rate to the ULS outlet section	m^3/s
w	Variable	-
$w_{k,g}$	Mass fraction of element k in stream g	-

Symbol	Name	Unit
x	Independent variable	-
$\boldsymbol{x}^{(n)}$	Vector of independent variables	-
x^*	Approximation of the root of a function	-
x_0	Root of a function	-
X_{BMC}	Solids split-up ratio to bed material cooler	-
X_{CH4}	Methane conversion	-
X_i	Fuel specific conversion	-
X_s	Oxygen carrier degree of oxidation	-
Xs_{AR}	Mean oxygen carrier oxidation state at the air reactor outlet	-
X_{SCV}	Solids flow control valve position	m
y_{CO}	CO slip	%
Y_{CO2}	Carbon dioxide yield	-
y_i	Mole fractions of component *i*	-
z_f	Freeboard height	m

8.3 Greek symbols

Symbol	Name	Unit
α	Vortex finder angular position	°
α_{FB}	Heat transfer coefficient bed-to-heat exchanger	$W/m^2 \cdot K$
δ_b	Bubble fraction	-
$\Delta G_i/G_0$	Relative change of the solids circulation rate	-
ΔG_R^0	Gibbs free enthalpy	J/kg
$\Delta h^0_{f,298}$	Specific enthalpy of formation at 25°C	J/kg
ΔH_R	Reaction enthalpy	J/mol
$\Delta\vartheta_{air\_ph}$	Recuperative air preheater minimal temperature difference	°C
$\Delta\vartheta_{ECO,min}$	Economizer minimal temperature difference	°C
$\Delta\vartheta_{FR\text{-}cond}$	FR condenser minimal temperature difference	°C
$\Delta\vartheta_{min\_ECO}$	Minimal temperature difference of non-evaporative (e.g. economizer) gas/water heat exchangers	°C
$\Delta\vartheta_{min\_EVAP}$	Minimal temperature difference of evaporative gas/water heat exchangers	°C
$\Delta\vartheta_{wat\text{-}st}$	Steam-water heat exchangers minimal temperature difference	°C
Δp	Pressure drop in a fixed or fluidized bed	bar
$\Delta p_{air\_ph,g}$	Air preheater pressure drop on the gas side	bar
$\Delta p_{air\_ph,w}$	Air preheater pressure drop on the water side	bar
Δp_{AR}	Air reactor riser system pressure drop	bar
$\Delta p_{AR,w}$	Air reactor water wall pressure drop on the water side	bar
Δp_{comb}	Combustion chamber burner gas pressure drop	bar
$\Delta p_{comb,g}$	Combustion chamber pressure drop on the flue-gas side	bar
$\Delta p_{comb,w}$	Combustion chamber pressure drop on the water side	bar
$\Delta p_{ECO,g}$	Economizer pressure loss gas side	bar
$\Delta p_{ECO,w}$	Economizer pressure loss water side	bar
$\Delta p_{evap,g}$	Evaporator pressure drop on the gas side	bar
$\Delta p_{evap,w}$	Evaporator pressure drop on the water side	bar
Δp_{FR}	Fuel reactor riser system pressure loss	bar
$\Delta p_{FR\text{-}cond,g}$	FR condenser pressure loss gas side	bar
$\Delta p_{FR\text{-}cond,w}$	FR condenser pressure loss water side	bar
$\Delta p_{FSG,cold}$	Fluidization steam generator pressure drop on the cold side	bar
$\Delta p_{FSG,hot}$	Fluidization steam generator pressure drop on the hot side	bar
$\Delta p_{fuel\_ph,g}$	Fuel preheater pressure drop on the gas side	bar
$\Delta p_{fuel\_ph,w}$	Fuel preheater pressure drop on the water side	bar

Symbol	Name	Unit
$\Delta p_{H,g}$	AR and FR exhaust gas heat exchanger pressure drop on the gas side	bar
$\Delta p_{H,w}$	AR and FR exhaust gas heat exchanger pressure drop on the water side	bar
$\Delta P_i/P_0$	Relative change of the control value	-
Δp_{pipe}	Connecting pipe pressure drop	bar
Δp_{riser}	Riser pressure drop (AR and FR)	bar
$\Delta p_{SH,g}$	Superheaters pressure loss gas side	bar
$\Delta p_{SH,w}$	Superheaters pressure loss water side	bar
Δr	Cyclone vortex finder eccentricity	m
$\Delta\omega_{rel}$	Relative improvement of the fuel utilization factor	-
ΔXs	Oxygen carrier conversion (based on degree of oxidation)	-
ε	Fluidized bed voidage	-
η_m	Mechanic efficiency	%
ε_{mf}	Fluidized bed voidage at incipient fluidization	-
ε_s	Solids fraction	-
ε_s^*	Solids fraction in saturation or saturation carrying capacity	-
ε_{sd}	Solids fraction in the dense zone of the fluidized bed	-
ϕ	Particle sphericity	-
φ_{amb}	Ambient relative humidity	%
ϕ_{CHP}	Heat index of the combined heat and power plant	-
η_b	Boiler efficiency	-
η_c	Combustion efficiency	-
η_{comb}	Combustion efficiency	-
$\eta_{e,motor}$	Electric motor electrical efficiency	-
η_{eff}	Effective efficiency	-
η_{el}	Electric efficiency	-
$\eta_{m,blower}$	Blower mechanical efficiency	-
$\eta_{m,G}$	Mechanic efficiency of the electricity generator	-
$\eta_{m,ID}$	Mechanic efficiency of induct fan	-
$\eta_{m,M}$	Mechanic efficiency of electric motors	-
$\eta_{m,p}$	Mechanic efficiency of water pump	-
$\eta_{m,rec}$	Recycle blower mechanic efficiency	-
η_p	Process efficiency	-
η_s	Isentropic efficiency	-
$\eta_{s,blower}$	Blower isentropic efficiency	-
$\eta_{s,G}$	Isentropic efficiency of the electricity generator	-
$\eta_{s,i}$	Isentropic efficiency of steam turbine stage *i*	-
$\eta_{s,ID}$	Isentropic efficiency of induct fan	-
$\eta_{s,M}$	Isentropic efficiency of electric motors	-
$\eta_{s,p}$	Isentropic efficiency of water pump	-
$\eta_{s,rec}$	Recycle blower isentropic efficiency	-
η_{th}	Thermal efficiency	-
ϑ	Temperature	°C
ϑ_{amb}	Ambient temperature	°C
ϑ_{AR}	Air reactor exhaust gas temperature	°C
ϑ_{BFW}	Boiler feedwater temperature	°C
$\vartheta_{BFW,dea}$	Boiler feedwater deaerator outlet temperature	°C
$\vartheta_{BFW\_preheater}$	Boiler feedwater preheater exit temperature	°C
ϑ_{BMC_sol}	Heat exchanger chamber solids temperature	°C
ϑ_{comb}	Combustion chamber flue gas outlet temperature	°C
$\vartheta_{comb,ad}$	Adiabatic combustion temperature	°C
$\vartheta_{DH,r}$	District heating return temperature	°C

Symbol	Name	Unit
$\vartheta_{DH,s}$	District heating supply water temperature	°C
ϑ_{FR}	Fuel reactor exhaust gas temperature or representative fuel reactor temperature	°C
$\vartheta_{FR,exit}$	Fuel reactor gas exit temperature	°C
ϑ_{fuel}	Fuel temperature	°C
ϑ_{LS}	Live steam temperature	°C
ϑ_{min_FSG}	Minimal temperature difference of non-evaporative (e.g. economizer) gas/water heat exchangers	°C
λ	Air/fuel ratio	-
μ_g	Viscosity of the gas	Pa·s
ν_i	Stoichiometric coefficients	-
$\nu_{k,i}$	Quantity of element *k* in component *i*	-
Ω	Beranek number	-
ρ_g	Gas density	kg/m^3
ρ_p	Apparent particle density	kg/m^3
σ	Electricity weighing factor	-
σ_{CHP}	Power index of the combined heat and power plant	-
$\tau_{g,AR}$	Mean gas residence time in the air reactor	s
$\tau_{g,FR}$	Mean gas residence time in the fuel reactor	s
$\tau_{s,AR}$	Mean solids residence time in the air reactor	s
$\tau_{s,FR}$	Mean solids residence time in the fuel reactor	s
ω	Fuel utilization factor	-
Ω	Beranek number	-
ξ_i	Sensitivity values	-

9 References

Abad, A., Mattisson, T., Lyngfelt, A., Ryden, M., **2006**. Chemical-looping combustion in a 300W continuously operating reactor system using a manganese-based oxygen carrier. *Fuel 85(9)*, pp. 1174-1185, doi: 10.1016/j.fuel.2005.11.014.

Abba, I.A., Grace, J.R., Bi, H.T., Thompson, M.L., **2003**. Spanning the flow regimes: Generic fluidized-bed reactor model. *AIChE Journal 49(7)*, pp. 1838-1848, doi: 10.1002/aic.690490720.

Adanez, J., Abad, A., Garcia-Labiano, F., Gayan, P., de Diego, L.F., **2012**. Progress in Chemical-Looping Combustion and Reforming technologies. *Progress in Energy and Combustion Science 38(2)*, pp. 215-282, doi: 10.1016/j.pecs.2011.09.001.

Adánez, J., Dueso, C., de Diego, L.F., García-Labiano, F., Gayán, P., Abad, A., **2009a**. Effect of Fuel Gas Composition in Chemical-Looping Combustion with Ni-Based Oxygen Carriers. 2. Fate of Light Hydrocarbons. *Industrial & Engineering Chemistry Research 48(5)*, pp. 2509-2518, doi: 10.1021/ie8013346.

Adánez, J., Dueso, C., de Diego, L.F., García-Labiano, F., Gayán, P., Abad, A., **2009b**. Methane Combustion in a 500 W_{th} Chemical-Looping Combustion System Using an Impregnated Ni-Based Oxygen Carrier. *Energy & Fuels 23(1)*, pp. 130-142, doi: 10.1021/ef8005146.

Adánez, J., Gayán, P., Celaya, J., de Diego, L.F., García-Labiano, F., Abad, A., **2006**. Chemical Looping Combustion in a 10 kWthPrototype Using a CuO/Al2O3Oxygen Carrier: Effect of Operating Conditions on Methane Combustion. *Industrial & Engineering Chemistry Research 45(17)*, pp. 6075-6080, doi: 10.1021/ie060364l.

Andrus, H.E., Chiu, J.H., P.R., T., A., B., **2009**. Alstom's calcium oxide chemical looping combustion coal power technology development. 34th International Technical Conference on Clean Coal & Fuel Systems, Clearwater, Florida, USA.

Andrus, H.E., Chiu, J.H., Thibeault, P.R., **2010**. Alstom's chemical looping combustion coal power technology development prototype. 1st International Conference on Chemical Looping, Lyon, France.

Anheden, M., Svedberg, G., **1996**. Chemical-looping combustion in combination with integrated coal gasification-a way to avoid CO_2 emission from coal fired power plants without a significant decrease in net power efficiency Energy Conversion Engineering Conference, 1996. IECEC 96., Proceedings of the 31st Intersociety, Washington, DC, pp. 2045 - 2050.

Anheden, M., Svedberg, G., **1998**. Exergy analysis of chemical-looping combustion systems. *Energy Conversion and Management 39(16-18)*, pp. 1967-1980, doi: 10.1016/s0196-8904(98)00052-1.

Bai, D., Kato, K., **1999**. Quantitative estimation of solids holdups at dense and dilute regions of circulating fluidized beds. *Powder Technology 101(3)*, pp. 183-190, doi: 10.1016/s0032-5910(98)00159-4.

Barin, I., Platzki, G., **1995**. Thermochemical Data of Pure Substances. 3rd ed. *VCH Publishers, Inc.*, New York, NY, USA, ISBN: 3-527-28745-0.

Basu, P., Butler, J., **2009**. Studies on the operation of loop-seal in circulating fluidized bed boilers. *Applied Energy 86(9)*, pp. 1723-1731, doi: 10.1016/j.apenergy.2008.11.024.

Basu, P., Fraser, S.A., **1991**. Circulating Fluidized Bed Boilers - Design and operations. *Butterworth-Heinemann*, Boston, USA, ISBN: 0-7506-9226-X

Beal, C., Epple, B., Lyngfelt, A., Adánez, J., Larring, Y., Guillemont, A., Anheden, M., **2010**. Development of metal oxides chemical looping process for coal-fired power plants. 1st International Conference on Chemical Looping, Lyon, France.

Bellona, **2002**. Bellona Report 6:02. *Bellona Foundation*.

Berguerand, N., Lyngfelt, A., **2008**. Design and operation of a 10kWth chemical-looping combustor for solid fuels – Testing with South African coal. *Fuel 87(12)*, pp. 2713-2726, doi: 10.1016/j.fuel.2008.03.008.

Bertsch, O., **2011**. Overall process integration and CLC next scale design. 3rd IEAGHG High Temperature Solids Looping Cycles Network Meeting, Vienna, Austria.

Bi, H.T., Grace, J.R., **1995a**. Effect of measurement method on the velocities used to demarcate the onset of turbulent fluidization. *The Chemical Engineering Journal and the Biochemical Engineering Journal 57(3)*, pp. 261-271, doi: 10.1016/0923-0467(94)02875-b.

Bi, H.T., Grace, J.R., **1995b**. Flow regime diagrams for gas-solid fluidization and upward transport. *International Journal of Multiphase Flow 21(6)*, pp. 1229-1236, doi: 10.1016/0301-9322(95)00037-x.

Bi, H.T., Grace, J.R., Zhu, J., **1995**. Regime Transitions Affecting Gas-Solids Suspensions and Fluidized-Beds. *Chemical Engineering Research & Design 73(A2)*, pp. 154-161, written in English.

Bolhàr-Nordenkampf, J., Pröll, T., Kolbitsch, P., Hofbauer, H., **2009a**. Comprehensive Modeling Tool for Chemical Looping Based Processes. *Chemical Engineering & Technology 32(3)*, pp. 410-417, doi: 10.1002/ceat.200800568.

Bolhàr-Nordenkampf, J., Pröll, T., Kolbitsch, P., Hofbauer, H., **2009b**. Performance of a NiO-based oxygen carrier for chemical looping combustion and reforming in a 120 kW unit. *Energy Procedia 1(1)*, pp. 19-25, doi: 10.1016/j.egypro.2009.01.005.

BP, **2011**. BP Statistical Review of World Energy June 2011.

BP, **2012**. BP Statistical Review of World Energy June 2012.

Burcat, A., McBride, B., **1997**. 1997 ideal gas thermodynamic data for combustion and air-pollution use. *Technion Israel Institute of Technology*, Haifa, Israel

Buttler, R.M., **1980**. Method for continuously producing viscous hydrocarbons by gravity drainage while injecting heated fluids. in: Patent, U.S. (Ed.), E21B 4324; E21B 4326 ed, p. 19.

CAPP, **2012a**. Crude Oil - Forecast, Markets & Pipelines. *CAPP - Canadian Association of Petroleum Producers*.

CAPP, **2012b**. The facts on oil sands, November 2012. *CAAP - Canadian Association of Petroleum Producers*

Choi, J.-H., Chang, I.-Y., Shun, D.-W., Yi, C.-K., Son, J.-E., Kim, S.-D., **1999**. Correlation on the Particle Entrainment Rate in Gas Fluidized Beds. *Industrial & Engineering Chemistry Research 38(6)*, pp. 2491-2496, doi: 10.1021/ie980707i.

Chum, H., Faaij, A., Moreira, J., Berndes, G., Dhamija, P., Dong, H., Gabrielle, B., Eng, A.G., Lucht, W., Mapako, M., Cerutti, O.M., McIntyre, T., Minowa, T., Pingoud, K., **2011**. Bioenergy. in: Edenhofer, O., Pichs-Madruga, R., Sokona, Y., Seyboth, K., Matschoss, P., Kadner, S., Zwickel, T., Eickemeier, P., Hansen, G., Schlömer, S., von Stechow, C. (Eds.), IPCC Special Report on Renewable Energy Sources and Climate Change Mitigation. *Cambridge University Press*, Cambridge, United Kingdom and New York, NY, USA.

Clift, R., Grace, J.R., Weber, M.E., **1978**. Bubbles, Drops, and Particles. *ACADEMIC PRESS, INC.*, New York, ISBN: 0-12-176950-X.

Colakyan, M., Levenspiel, O., **1984**. Elutriation from fluidized beds. *Powder Technology 38(3)*, pp. 223-232, doi: 10.1016/0032-5910(84)85005-6.

Cruz, E., Pugsley, T., **2008**. COMPUTATIONAL FLUID DYNAMICS MODEL OF A CIRCULATING FLUIDIZED BED LIGNITE COAL COMBUSTOR. in: Werther, J., Nowak, W., Wirth, K.-E., Hartge, E.-U. (Eds.), 9th International Conference on Circulating Fluidized Beds, Hamburg, Germany.

Cuadrat, A., Abad, A., García-Labiano, F., Gayán, P., de Diego, L.F., Adánez, J., **2011**. Ilmenite as oxygen carrier in a chemical looping combustion system with coal. *Energy Procedia 4*, pp. 362-369, doi: 10.1016/j.egypro.2011.01.063.

Curtis, C., Kopper, R., Decoster, E., Guzmán-Garcia, A., Huggins, C., Knauer, L., Minner, M., Kupsch, N., Linare, L.M., Rough, H., Waite, M., **2002**. Heavy-Oil Reservoirs. in: Garber, M., Williamson, D. (Eds.), Oilfield Review. *Schlumberger*, Sugar Land, Texas, USA, pp. 30-51.

de Diego, L.F., García-Labiano, F., Adánez, J., Gayán, P., Abad, A., Corbella, B.M., María Palacios, J., **2004**. Development of Cu-based oxygen carriers for chemical-looping combustion. *Fuel 83(13)*, pp. 1749-1757, doi: 10.1016/j.fuel.2004.03.003.

Dean, C.C., Blamey, J., Florin, N.H., Al-Jeboori, M.J., Fennell, P.S., **2011**. The calcium looping cycle for CO_2 capture from power generation, cement manufacture and hydrogen production. *Chemical Engineering Research and Design 89(6)*, pp. 836-855, doi: 10.1016/j.cherd.2010.10.013.

Desideri, U., Paolucci, A., **1999**. Performance modelling of a carbon dioxide removal system for power plants. *Energy Conversion and Management 40(18)*, pp. 1899-1915, doi: 10.1016/s0196-8904(99)00074-6.

Dlugokencky, E., Tans, P., **2013**. Link: www.esrl.noaa.gov/gmd/ccgg/trends/,

Dybkjaer, I., **1995**. Tubular reforming and autothermal reforming of natural gas — an overview of available processes. *Fuel Processing Technology 42(2-3)*, pp. 85-107, doi: 10.1016/0378-3820(94)00099-f.

ECKA, **2013**. Link: http://www.ecka-granules.com/en/products/copper-and-copper-alloys/, access date: April 28th.

Ergun, S., **1952**. Fluid Flow Through Packed Columns. *Chemical Engineering Progress 48(2)*, pp. 89-102.

Fang, H., Haibin, L., Zengli, Z., **2009**. Advancements in Development of Chemical-Looping Combustion: A Review. *International Journal of Chemical Engineering 2009*, pp. 1-16, doi: 10.1155/2009/710515.

Ferreira-Aparicio, P., Benito, M.J., Sanz, J.L., **2005**. New Trends in Reforming Technologies: from Hydrogen Industrial Plants to Multifuel Microreformers. *Catalysis Reviews 47(4)*, pp. 491-588, doi: 10.1080/01614940500364958.

García-Labiano, F., de Diego, L.F., Gayán, P., Adánez, J., Abad, A., Dueso, C., **2009**. Effect of Fuel Gas Composition in Chemical-Looping Combustion with Ni-Based Oxygen Carriers. 1. Fate of Sulfur. *Industrial & Engineering Chemistry Research 48(5)*, pp. 2499-2508, doi: 10.1021/ie801332z.

Geldart, D., **1973**. Types of Gas Fluidization. *Powder Technology 7(5)*, pp. 285-292, written in English.

Geldart, D., Abrahamsen, A.R., **1978**. Homogeneous fluidization of fine powders using various gases and pressures. *Powder Technology 19(1)*, pp. 133-136, doi: 10.1016/0032-5910(78)80084-9.

Glicksman, L., **1984**. Scaling relationships for fluidized beds. *Chemical Engineering Science 39(9)*, pp. 1373-1379, doi: 10.1016/0009-2509(84)80070-6.

Glicksman, L.R., Hyre, M., Woloshun, K., **1993**. Simplified Scaling Relationships for Fluidized-Beds. *Powder Technology 77(2)*, pp. 177-199, written in English.

Göttlicher, G., **1999**. Energetik der Kohlendioxidrückhaltung in Kraftwerken. *VDI-Verlag*, Düsseldorf, Germany, p. 202, written in German, ISBN: 3-18-342106-2.

Grace, J., Avidan, A., Knowlton, T., **1997**. Circulating Fluidized Beds. *Chapman & Hall, New York, 1997*

Grace, J.R., **1982**. Fluidized Bed Hydrodynamics. in: Hetsroni, G. (Ed.), Handbook of Multiphase Systems. *Washington Hemisphere Publishing*, Washington, USA.

Grace, J.R., **1986**. Contacting Modes and Behavior Classification of Gas - Solid and Other 2-Phase Suspensions. *Canadian Journal of Chemical Engineering 64(3)*, pp. 353-363.

Grace, J.R., Clift, R., **1974**. On the two-phase theory of fluidization. *Chemical Engineering Science 29(2)*, pp. 327-334, doi: 10.1016/0009-2509(74)80039-4.

Gwak, K.-W., Bae, W., **2010**. A Review of Steam Generation for In-Situ Oil Sands Projects. *Geosystem Engineering 13(3)*, pp. 111-118, doi: 10.1080/12269328.2010.10541317.

Hamdan, M.A., Al-qaq, A.M., **2008**. The prediction of heat transfer coefficient in circulating fluidized bed combustors. *Energy Conversion and Management 49(11)*, pp. 3274-3277, written in English, doi: 10.1016/j.enconman.2008.05.003.

Hofbauer, H., Rauch, R., Bosch, K., Koch, R., Aichernig, C., **2002**. Biomass CHP Plant Güssing - A Success Story. Proceedings of Pyrolysis and Gasification Expert Meeting, Strasbourg, France, p. 12.

Hoffmann, A.C., Stein, L.E., **2002**. Gas cyclones and swirl tubes. *Springer*, Berlin, Germany, ISBN: 3-540-43326-0.

Höltl, W., Pröll, P., Rohovec, J., Kronberger, B., Hofbauer, H., **2009**. Oxyfuel combustion of alternative fuels in a circulating fluidized bed combustor – design of a 100 kW test unit. 4th European Combustion Meeting 2009, Vienna, Austria.

Hossain, M.M., de Lasa, H.I., **2008**. Chemical-looping combustion (CLC) for inherent separations—a review. *Chemical Engineering Science 63(18)*, pp. 4433-4451, doi: 10.1016/j.ces.2008.05.028.

Hugi, E., **1997**. Auslegung hochbeladener Zyklonabscheider für zirkulierende Gas/Feststoff-Wirbelschicht-Reaktorsysteme. *VDI-Verlag*, Düsseldorf, Germany, written in German, ISBN: 3-18-350203-8.

Hugi, E., Reh, L., **1998**. Design of Cyclones with High Solids Entrance Loads. *Chemical Engineering & Technology 21(9)*, pp. 716-719, doi: 10.1002/(Sici)1521-4125(199809)21:9<716::Aid-Ceat716>3.0.Co;2-Y.

IEA/OECD, **2010**. World Energy Outlook 2010. *OECD Publishing*, ISBN: 978-92-64-08624-1.

IEA/OECD, **2012**. CO_2 emission from fuel combustion - Highlights. *OECD Publishing*

IHS-CERA, **2012a**. Appendixes to IHS CERA Special Report, Oil Sands, Greenhouse Gases, and US Oil Supply—2012 Update. *IHS Cambridge Energy Research Associates*.

IHS-CERA, **2012b**. Special Report - Oil Sands, Greenhouse Gases, and US Oil Supply. Getting the Numbers Right. *IHS Cambridge Energy Research Associates*.

IPCC, **2005**. IPCC Special Report on Carbon Dioxide Capture and Storage. *Cambridge University Press*, New York, USA, ISBN: 13 978-0-521-68551-1.

IPCC, **2007a**. Climate Change 2007: Synthesis Report, Geneva, Switzerland

IPCC, **2007b**. Contribution of Working Group I to the Fourth Assessment Report of the Intergovernmental Panel on Climate Change. in: Solomon, S., Qin, D., Manning, M., Chen, Z., Marquis, M., Averyt, K.B., Tignor, M., Miller, H.L. (Eds.), IPCC Fourth Assessment Report (AR4). *Cambridge University Press*, Cambridge, United Kingdom and New York, NY, USA, p. 996.

IPCC, **2011**. IPCC Special Report on Renewable Energy Sources and Climate Change Mitigation. *Cambridge University Press*, United Kingdom and New York, NY, USA

IPCC, **2012**. Managing the Risks of Extreme Events and Disasters to Advance Climate Change Adaptation

Ishida, M., Jin, H., **1994a**. A new advanced power-generation system using chemical-looping combustion. *Energy 19(4)*, pp. 415-422, doi: 10.1016/0360-5442(94)90120-1.

Ishida, M., Jin, H., **1994b**. A novel combustor based on chemical-looping reactions and its reaction kinetics. *Journal of Chemical Engineering of Japan 27(3)*, pp. 296-301, doi: 10.1252/jcej.27.296.

Ishida, M., Jin, H., **1996**. A Novel Chemical-Looping Combustor without NO_x Formation. *Industrial & Engineering Chemistry Research 35(7)*, pp. 2469-2472, doi: 10.1021/ie950680s.

Ishida, M., Jin, H., **1997**. CO_2 recovery in a power plant with chemical looping combustion. *Energy Conversion and Management 38*, pp. S187-S192, doi: 10.1016/s0196-8904(96)00267-1.

Ishida, M., Jin, H., Okamoto, T., **1996**. A Fundamental Study of a New Kind of Medium Material for Chemical-Looping Combustion. *Energy & Fuels 10(4)*, pp. 958-963, doi: 10.1021/ef950173n.

Ishida, M., Jin, H., Okamoto, T., **1998**. Kinetic Behavior of Solid Particle in Chemical-Looping Combustion: Suppressing Carbon Deposition in Reduction. *Energy & Fuels 12(2)*, pp. 223-229, doi: 10.1021/ef970041p.

Ishida, M., Zheng, D., Akehata, T., **1987**. Evaluation of a chemical-looping-combustion power-generation system by graphic exergy analysis. *Energy 12(2)*, pp. 147-154, doi: 10.1016/0360-5442(87)90119-8.

Jerndal, E., Mattisson, T., Thijs, I., Snijkers, F., Lyngfelt, A., **2009**. NiO particles with Ca and Mg based additives produced by spray- drying as oxygen carriers for chemical-looping combustion. *Energy Procedia 1(1)*, pp. 479-486, doi: 10.1016/j.egypro.2009.01.064.

Jerndal, E., Mattisson, T., Thijs, I., Snijkers, F., Lyngfelt, A., **2010**. Investigation of $NiO/NiAl_2O_4$ oxygen carriers for chemical-looping combustion produced by spray-drying. *International Journal of Greenhouse Gas Control 4(1)*, pp. 23-35, doi: 10.1016/j.ijggc.2009.09.007.

Jia, L., Anthony, E.J., **2009**. Combustion Of Poultry-Derived Fuel in a CFBC. in: Yue, G., Zhang, H., Zhao, C., Luo, Z. (Eds.), Proceedings of the 20th International Conference on Fluidized Bed Combustion. *Tsinghua University Press, Beijing*, pp. 271-276.

Jin, H., Ishida, M., **2000**. A novel gas turbine cycle with hydrogen-fueled chemical-looping combustion. *International Journal of Hydrogen Energy 25(12)*, pp. 1209-1215, doi: 10.1016/s0360-3199(00)00032-x.

Jin, H., Okamoto, T., Ishida, M., **1998**. Development of a Novel Chemical-Looping Combustion: Synthesis of a Looping Material with a Double Metal Oxide of CoO−NiO. *Energy & Fuels 12(6)*, pp. 1272-1277, doi: 10.1021/ef980080g.

Jin, H., Okamoto, T., Ishida, M., **1999**. Development of a Novel Chemical-Looping Combustion: Synthesis of a Solid Looping Material of NiO/NiAl2O4. *Industrial & Engineering Chemistry Research 38(1)*, pp. 126-132, doi: 10.1021/ie9803265.

Jing, D., Hermans, E.Y.S.I.M., Leion, H., Rydèn, M., Mattisson, T., Van Noyen, J., Lyngfelt, A., **2012**. Manganese-silica combined oxides as oxygen carrier for chemical-looping combustion. 2nd International Conference on Chemical Looping, Darmstadt, Germany.

Jing, D., Mattisson, T., Ryden, M., Hallberg, P., Hedayati, A., Van Noyen, J., Snijkers, F., Lyngfelt, A., **2013**. Innovative Oxygen Carrier Materials for Chemical-Looping Combustion. *Energy Procedia submitted for publication*.

Johansson, E., Mattisson, T., Lyngfelt, A., Thunman, H., **2006**. A 300W laboratory reactor system for chemical-looping combustion with particle circulation. *Fuel 85(10-11)*, pp. 1428-1438, doi: 10.1016/j.fuel.2006.01.010.

Johnsson, F., Andersson, S., Leckner, B., **1991**. Expansion of a Freely Bubbling Fluidized-Bed. *Powder Technology 68(2)*, pp. 117-123, written in English.

Kaiser, S., Loffler, G., Bosch, K., Hofbauer, H., **2003**. Hydrodynamics of a dual fluidized bed gasifier. Part II: simulation of solid circulation rate, pressure loop and stability. *Chemical Engineering Science 58(18)*, pp. 4215-4223, written in English, doi: 10.1016/S0009-2509(03)00233-1.

Källén, M., Rydén, M., Dueso, C., Mattisson, T., Lyngfelt, A., **2013**. CaMn0.9Mg0.1O3-δas Oxygen Carrier in a Gas-Fired 10 kWthChemical-Looping Combustion Unit. *Industrial & Engineering Chemistry Research*, p. 130516092125004, doi: 10.1021/ie303070h.

Knoche, K.F., Richter, H.J., **1968**. Verbesserung der Reversibilität von Verbrennungsprozessen. *Brennstoff-Wärme-Kraft 20(5)*, pp. 205-210, written in German.

Kolbitsch, P., **2009**. Chemical looping combustion for 100% carbon capture - Design, operation and modeling of a 120kW pilot rig. Institute of Chemical Engineering. *Vienna University of Technology*, Vienna Austria.

Kolbitsch, P., Bolhàr-Nordenkampf, J., Pröll, T., Hofbauer, H., **2009a**. Comparison of Two Ni-Based Oxygen Carriers for Chemical Looping Combustion of Natural Gas in 140 kW Continuous Looping Operation. *Industrial & Engineering Chemistry Research 48(11)*, pp. 5542-5547, doi: 10.1021/Ie900123v.

Kolbitsch, P., Bolhàr-Nordenkampf, J., Pröll, T., Hofbauer, H., **2010**. Operating experience with chemical looping combustion in a 120kW dual circulating fluidized bed (DCFB) unit. *International Journal of Greenhouse Gas Control 4(2)*, pp. 180-185, doi: 10.1016/j.ijggc.2009.09.014.

Kolbitsch, P., Pröll, T., Bolhàr-Nordenkampf, J., Hofbauer, H., **2009b**. Characterization of Chemical Looping Pilot Plant Performance via Experimental Determination of Solids Conversion. *Energy & Fuels 23(3)*, pp. 1450-1455, doi: 10.1021/Ef8008184.

Kunii, D., Levenspiel, O., **1991**. Fluidization Engineering, 2nd Edition. *Butterworth-Heinemann 80 Montvale Avenue Stoneham, MA 02180*

Kunz, O., Klimeck, R., Wagner, W., Jaeschke, M., **2007**. The GERG-2004 Wide-Range Equation of State for Natural Gases and Other Mixtures. *VDI Verlag GmbH*, Düsseldorf, Germany, ISBN: 978-3-18-355706-6.

Lapple, C.E., Shepherd, C.B., **1940**. Calculation of particle trajectories. *Industrial and Engineering Chemistry 32(5)*, pp. 605-617, doi: 10.1021/Ie50365a007.

Lei, H., Horio, M., **1998**. A Comprehensive Pressure Balance Model of Circulating Fluidized Beds. *Journal of Chemical Engineering of Japan 31(1)*, pp. 83-94, doi: 10.1252/jcej.31.83.

Lei, P., Yong, T., Tai-Sheng, L., Li, N., Min, H., Bei-Song, P., Jia-Xue, L., Yu-Bin, W., Qi, Z., **2005**. The design and operation of a domestic 135MW CFB boiler. in: Cen, K., Zhu, J., Rhodes, M., Hartge, E.-U., Luo, Z. (Eds.), Circulating Fluidized Bed Technology VIII, Hangzhou, China, pp. 1009-1016.

Leion, H., Mattisson, T., Lyngfelt, A., **2009**. Use of Ores and Industrial Products As Oxygen Carriers in Chemical-Looping Combustion. *Energy & Fuels 23(4)*, pp. 2307-2315, doi: 10.1021/ef8008629.

Lewis, W.K., Gilliland, E.R., **1954**. Production of pure carbon dioxide. in: Office, U.S.P. (Ed.), USA.

Li, Y., Kwauk, M., **1980**. The Dynamics of Fast Fluidization. in: Grace, J.R., Matsen, J.M. (Eds.), Fluidization. *Springer US*, New York, USA, pp. 537-544.

Linde, C., **1905**. Apparatus for producing pure nitrogen and pure oxygen. in: Office, U.S.P. (Ed.), USA.

Linderholm, C., Abad, A., Mattisson, T., Lyngfelt, A., **2008**. 160h of chemical-looping combustion in a 10kW reactor system with a NiO-based oxygen carrier. *International Journal of Greenhouse Gas Control 2(4)*, pp. 520-530, doi: 10.1016/j.ijggc.2008.02.006.

Linderholm, C., Mattisson, T., Lyngfelt, A., **2009**. Long-term integrity testing of spray-dried particles in a 10-kW chemical-looping combustor using natural gas as fuel. *Fuel 88(11)*, pp. 2083-2096, doi: 10.1016/j.fuel.2008.12.018.

Löffler, G., **2001**. A Modeling Study on Fuel-nitrogen Conversion to NO and N_2O Related to Fluidized Bed Combustion., Institute of Chemical Engineering. *Vienna University of Technology*, Vienna Austria.

Löffler, G., Kaiser, S., Bosch, K., Hofbauer, H., **2003**. Hydrodynamics of a dual fluidized-bed gasifier—Part I: simulation of a riser with gas injection and diffuser. *Chemical Engineering Science 58(18)*, pp. 4197-4213, doi: 10.1016/s0009-2509(03)00232-x.

Lyngfelt, A., **2011**. Oxygen Carriers for Chemical Looping Combustion - 4 000 h of Operational Experience. *Oil & Gas Science and Technology – Revue d'IFP Energies nouvelles 66(2)*, pp. 161-172, doi: 10.2516/ogst/2010038.

Lyngfelt, A., Johansson, M., Mattisson, T., **2008**. Chemical-looping combustion - Status of development. Proceedings of the of the 9th International Conference on Circulating Fluidized Beds (CFB-9), TU Tech, Hamburg, Germany.

Lyngfelt, A., Kronberger, B., Adanez, J., Morin, J.-X., Hurst, P., **2004**. The GRACE project. Development of oxygen carrier particles for chemical-looping combustion. Design and operation of a 10 kW chemical-looping combustion. in: Rubin, E.S., Keith, D.W., Gilboy, C.F., Wilson, M., Morris, T., Gale, J., Thambimuthu, K. (Eds.), 7th International Conference of Greenhouse Gas Control Technologies, Vancouver, Canada, pp. 115-123.

Lyngfelt, A., Leckner, B., Mattisson, T., **2001**. A fluidized-bed combustion process with inherent CO_2 separation; application of chemical-looping combustion. *Chemical Engineering Science 56(10)*, pp. 3101-3113, doi: 10.1016/s0009-2509(01)00007-0.

Lyngfelt, A., Thunman, H., **2005**. Construction and 100 h of operational experience of a 10-kW chemical looping combustor. in: Thomas, D. (Ed.), Carbon Dioxide Capture for Storage in Deep Geologic Formations - Results from the CO_2 Capture Project. *Elsevier Science*, pp. 625-645, ISBN: 9780080445700.

Lyon, R.K., Cole, J.A., **2000**. Unmixed combustion: an alternative to fire. *Combustion and Flame 121(1-2)*, pp. 249-261, doi: 10.1016/s0010-2180(99)00136-4.

Markström, P., Lyngfelt, A., Linderholm, C., **2012**. Chemical-Looping Combustion in a 100 kW unit for Solid Fuels. 21st International Conference on Fluidized Bed Combustion, Naples, Italy.

Marx, K., Bolhàr-Nordenkampf, J., Pröll, T., Hofbauer, H., **2011a**. Chemical looping combustion for power generation—Concept study for a $10MW_{th}$ demonstration plant. *International Journal of Greenhouse Gas Control 5(5)*, pp. 1199-1205, doi: 10.1016/j.ijggc.2011.05.012.

Marx, K., Pröll, T., Hofbauer, H., **2011b**. Design requirements for pressurized chemical looping reforming. in: Pugsley, T. (Ed.), Proceedings of the 10th International Conference on Circulating Fluidized Bed Technology (CFB10), Sunriver, Oregon, USA.

Marx, K., Pröll, T., Hofbauer, H., **2012**. Next scale chemical looping combustion: Fluidized bed system design for demonstration unit. Proceedings of the 21st International Conference on Fluidized Bed Combustion (FBC), Naples, Italy.

Marx, K., Pröll, T., Hofbauer, H., Hohenwarter, U., Horn, V., Sit, S.P., **2011c**. Chemical looping combustion for industrial steam generation from natural gas with inherent CO_2 capture. in: Reis, A. (Ed.), Proceedings of the 9th European Conference on Industrial Furnances and Boilers (INFUB-9), Estoril, Portugal.

Maryamchik, M., Wietzke, D.L., **2009**. B&W IR-CFB: Operating Experience and New Developments. in: Yue, G., Zhang, H., Zhao, C., Luo, Z. (Eds.), Proceedings of the 20th International Conference on Fluidized Bed Combustion. *Tsinghua University Press, Beijing*, pp. 157-161.

Mattisson, T., Adanez, J., Proell, T., Kuusik, R., Beal, C., Assinkf, J., Snijkers, F., Lyngfelt, A., **2009a**. Chemical-looping Combustion CO_2 Ready Gas Power. *Energy Procedia 1(1)*, pp. 1557-1564, doi: 10.1016/j.egypro.2009.01.204.

Mattisson, T., Lyngfelt, A., Leion, H., **2009b**. Chemical-looping with oxygen uncoupling for combustion of solid fuels. *International Journal of Greenhouse Gas Control 3(1)*, pp. 11-19, doi: 10.1016/j.ijggc.2008.06.002.

Mayer, K., Apanel, G., Pröll, T., Ibsen, M., Hofbauer, H., **2010**. Dual fluidized bed reforming pilot test results and potential commercial implications. Proceedings of the AIChE Annual Meeting 2010, Salt Lake City, Utah, USA.

Mirek, P., Czakiert, T., Nowak, W., **2009**. NO_x Emission Reduction by the Optimization of the Primary Air Distribution in the $235MW_e$ CFB Boiler. in: Yue, G., Zhang, H., Zhao, C., Luo, Z.

(Eds.), Proceedings of the 20th International Conference on Fluidized Bed Combustion. *Tsinghua University Press, Beijing*, pp. 162-166.

Muschelknautz, U., Muschelknautz, E., **1996**. Special design of inserts and short entrance ducts to recirculating cyclones., Proceedings of the International Conference on Circulating Fluidized Beds (CFB) V, Beijing, China, pp. Eq6 1-6.

Muschelknautz, U., Muschelknautz, E., **1999**. Separation Efficiency of Recirculating Cyclones in Circulating Fluidized Bed Combustions. *VGB PowerTech 4*, pp. 48-53.

Nicastro, M.T., Glicksman, L.R., **1984**. Experimental-Verification of Scaling Relationships for Fluidized-Bed. *Chemical Engineering Science 39(9)*, pp. 1381-1391.

Nikoo, M., Faltinson, J., Ordorica-Garcia, G., Chambers, A., **2010**. Application of chemical looping combustion for bitumen extraction via Steam Assisted Gravity Drainage (SAGD) in Alberta's oil sands., High Temperature Solid Looping Cycles Network Meeting, Alkmaar, Netherlands.

Ohashi, Y., Ogawa, T., Suzuki, K., **2011**. Development of Carbon Dioxide Removal System from the Flue Gas of Coal Fired Power Plant. 1st Post Combustion Capture Conference, Yas ,Abu Dhabi, VAE.

Perry, R.H., **1999**. Perry's Chemical Engineers' Handbook. 7 ed. *McGraw-Hill*, New York, USA, ISBN: 0-07-049841-5.

Pfeifer, C., Puchner, B., Hofbauer, H., **2007**. In-Situ CO_2-Absorption in a Dual Fluidized Bed Biomass Steam Gasifier to Produce a Hydrogen Rich Syngas. *International Journal of Chemical Reactor Engineering 5(1)*, doi: 10.2202/1542-6580.1395.

Pröll, T., **2004**. Potenziale der Wirbelschichtdampfvergasung fester Biomasse – Modellierung und Simulation auf Basis der Betriebserfahrungen am Biomassekraftwerk Güssing. Institute of Chemical Engineering. *Vienna University of Technology*, Vienna, Austria, written in German.

Pröll, T., Bolhàr-Nordenkampf, J., Kolbitsch, P., Hofbauer, H., **2010**. Syngas and a separate nitrogen/argon stream via chemical looping reforming – A 140kW pilot plant study. *Fuel 89(6)*, pp. 1249-1256, doi: 10.1016/j.fuel.2009.09.033.

Pröll, T., Bolhàr-Nordenkampf, J., Kolbitsch, P., Marx, K., Hofbauer, H., **2009a**. Pure hydrogen and pure carbon dioxide from gaseous hydrocarbons by chemical looping reforming. Proceedings of the 2009 AIChE Spring National Meeting and 5th Global Congress on Process Safety, Tampa, Florida, USA.

Pröll, T., Hofbauer, H., **2011**. Chemical Looping Combustion and Reforming. in: Reis, A. (Ed.), Proceedings of the 9th European Conference on Industrial Furnances and Boilers (INFUB-9), Estoril, Portugal.

Pröll, T., Kolbitsch, P., Bolhàr-Nordenkampf, J., Hofbauer, H., **2008**. Wirbelschichtreaktorsystem (Fluidized bed reactor system). in: Eigentum, W.f.g. (Ed.), Austria, written in German.

Pröll, T., Kolbitsch, P., Bolhàr-Nordenkampf, J., Hofbauer, H., **2009b**. A novel dual circulating fluidized bed system for chemical looping processes. *AIChE Journal 55(12)*, pp. 3255-3266, doi: 10.1002/aic.11934.

Pröll, T., Mayer, K., Bolhàr-Nordenkampf, J., Kolbitsch, P., Mattisson, T., Lyngfelt, A., Hofbauer, H., **2009c**. Natural minerals as oxygen carriers for chemical looping combustion in a dual circulating fluidized bed system. *Energy Procedia 1(1)*, pp. 27-34, doi: 10.1016/j.egypro.2009.01.006.

Pröll, T., Rupanovits, K., Kolbitsch, P., Bolhàr-Nordenkampf, J., Hofbauer, H., **2009d**. Cold Flow Model Study on a Dual Circulating Fluidized Bed (DCFB) System for Chemical Looping Processes. *Chemical Engineering & Technology 32(3)*, pp. 418-424, doi: 10.1002/ceat.200800521.

Raphson, J., **1690**. Analysis aequationum universalis seu ad aequationes algebraicas resolvendas methodus generalis, et expedita, ex nova infinitarum serierum doctrina ac demosntrata. *Typis T. Braddyll, prostant venales apud Johannem Taylor*, London, written in Latin

Reh, L., **1961**. Das wirbeln von körnigem Gut im schlangen Diffusor als Grenzzustand zwischen Wirbelschicht und pneumatischer Förderung. Fakultät für Maschinenwesen. *Technische Hochschule Karlsruhe*, Karlsruhe, Germany, written in German.

Reh, L., **1968**. Verbrennung in der Wirbelschicht. *Chemie Ingenieur Technik - CIT 40(11)*, pp. 509-515, written in German, doi: 10.1002/cite.330401102.

Reh, L., **1971**. Fluidized Bed Processing. *Chemical Engineering Progress 67(2)*, pp. 58-&.

Reh, L., **1996**. Fluid dynamics of CFB-Combustors. in: Kwauk, M., Li, J. (Eds.), Circulating Fluidized Bed Technology V (CFB V), Beijing, China.

Richter, H.J., Knoche, K.F., **1983**. Reversibility of Combustion Processes. *ACS Symposium Series 235*, pp. 71-85, doi: 10.1021/bk-1983-0235.ch003.

Rifflart, S., Hoteit, A., Yazdanpanah, M.M., Pelletant, W., Surla, K., **2011**. Construction and operation of a 10 kW CLC unit with circulation configuration enabling independent solid flow control. *Energy Procedia 4*, pp. 333-340, doi: 10.1016/j.egypro.2011.01.059.

Robertson, A., Goidich, S., Fan, Z., **2009**. 1300°F 800 MWe USC CFB Boiler Design Study. in: Yue, G., Zhang, H., Zhao, C., Luo, Z. (Eds.), Proceedings of the 20th International Conference on Fluidized Bed Combustion. *Tsinghua University Press, Beijing*, pp. 125-131.

Rüdisüli, M., Schildhauer, T.J., Biollaz, S.M.A., van Ommen, J.R., **2012**. Scale-up of bubbling fluidized bed reactors — A review. *Powder Technology 217*, pp. 21-38, doi: 10.1016/j.powtec.2011.10.004.

Rydén, M., **2008**. Hydrogen production from fossil fuels with carbon dioxide capture, using chemical-looping technologies. *Chalmers University of Technology*, Göteborg, Sweden.

Rydén, M., Lyngfelt, A., **2004**. Hydrogen and power production with integrated carbon dioxide capture by chemical-looping reforming. Proceedings of the 7th International Conference on Greenhouse Gas Control Technologies, Vancouver, Canada.

Ryu, H.-J., Jin, G.-T., Yi, C.-K., **2004**. Demonstration of inherent CO_2 separation and no NO_x emission in a 50 kW chemical looping combustor: continuous reduction and oxidation experiment. in: Rubin, E.S., Keith, D.W., Gilboy, C.F., Wilson, M., Morris, T., Gale, J., Thambimuthu, K. (Eds.), 7th International Conference of Greenhouse Gas Control Technologies, Vancouver, Canada, pp. 1907-1910.

Ryu, H.-J., Jo, S.-H., Park, Y.C., Bae, D.-H., Kim, S., **2010**. Long-term operation experience in a 50 kW_{th} chemical looping combustor using natural gas and syngas as fuels. 1st International Conference on Chemical Looping, Lyon, France.

Samanta, A., Zhao, A., Shimizu, G.K.H., Sarkar, P., Gupta, R., **2012**. Post-Combustion CO_2 capture using solid sorbents: A review. *Industrial & Engineering Chemistry Research 51(4)*, pp. 1438-1463, doi: 10.1021/ie200686q.

Schaback, R., Werner, H., **1992**. Numerische Mathematik. 4th ed. *Springer*, Berlin, Germany, written in German, ISBN: 3-540-54738-X

Schmitz, K.W., Schaumann, G., **2005**. Kraft-Wärme-Kopplung. 3rd ed. *Springer Berlin Heidelberg*, Berlin, Germany, written in German, ISBN: 978-3-540-20903-4.

Sciazko, M., Nowak, W., Sekret, R., **2008**. MODELLING OF TWO-PHASE FLOW IN A CIRCULATING FLUID-BED BOILER. in: Werther, J., Nowak, W., Wirth, K.-E., Hartge, E.-U. (Eds.), 9th International Conference on Circulating Fluidized Beds, Hamburg, Germany.

Shen, L., Wu, J., Xiao, J., **2009**. Experiments on chemical looping combustion of coal with a NiO based oxygen carrier. *Combustion and Flame 156(3)*, pp. 721-728, doi: 10.1016/j.combustflame.2008.08.004.

Sidorenko, I., Rhodes, M.J., **2003**. Pressure Effects on Gas-Solid Fluidized Bed Behavior. *International Journal of Chemical Reactor Engineering 1(1)*, doi: 10.2202/1542-6580.1107.

SimTech, **2011**. IPSEpro User Manual. *SimTech Simulation Technology*, Graz, Austria.

Son, S.R., Kim, S.D., **2006**. Chemical-Looping Combustion with NiO and Fe2O3in a Thermobalance and Circulating Fluidized Bed Reactor with Double Loops. *Industrial & Engineering Chemistry Research 45(8)*, pp. 2689-2696, doi: 10.1021/ie050919x.

Spliethoff, H., **2011**. Oxy-fuel combustion technology for power generation. in: Reis, A. (Ed.), Proceedings of the 9th European Conference on Industrial Furnaces and Boilers (INFUB-9), Estoril, Portugal.

Stamatelopoulos, G.-N., Darling, S., **2008**. ALSTOM´S CFB TECHNOLOGY. in: Werther, J., Nowak, W., Wirth, K.-E., Hartge, E.-U. (Eds.), 9th International Conference on Circulating Fluidized Beds, Hamburg, Germany.

Stewart, P.S.B., Davidson, J.F., **1967**. Slug flow in fluidised beds. *Powder Technology 1(2)*, pp. 61-80, doi: 10.1016/0032-5910(67)80014-7.

Tessie Du Motay, M., Maréchal, **1868**. Préparation industrielle de l'hydrogène. *Bulletin de la Société Chimique de Paris*, pp. 334-344.

Thon, A., Kramp, M., Hartge, E.-U., Heinrich, S., Werther, J., **2012**. Operational experience with a coupled fluidized bed system for chemical looping combustion of solid fuels. 2nd International Conference on Chemical Looping, Darmstadt, Germany.

Toomey, R.D., Johnstone, H.F., **1952**. Gaseous Fluidization of Solid Particles. *Chemical Engineering Progress 48(5)*, pp. 220-226, written in English.

Trefz, M., **1992**. Die verschiedenen Abscheidevorgänge im höher und hoch beladenen Gaszyklon unter besonderer Berücksichtigung der Sekundärströmung. *VDI-Verlag*, Düsseldorf, Germany, written in German, ISBN: 3-18-149503-4.

Trefz, M., Muschelknautz, E., **1993**. Extended Cyclone Theory for Gas Flows with High Solids Concentrations. *Chemical Engineering & Technology 16(3)*, pp. 153-160, doi: 10.1002/ceat.270160303.

VDI, **2003**. VDI 4661 - Energetic characteristics. *Verein Deutscher Ingenieure*, Düsseldorf, Germany

VDI, **2005**. VDI 4608 - Energy systems Combined heat and power. *Verein Deutscher Ingenieure*, Düsseldorf, Germany

VDI, **2010**. VDI heat atlas. *Springer*, Heidelberg [u.a.], ISBN: 978-3-540-77876-9.

Venemana, R., Kamphuisb, H., Brilmana, D.W.F., **2013**. Post-Combustion CO_2 capture using supported amine sorbents: A process integration study. *Energy Procedia submitted for publication*.

Wagner, W., Kruse, A., **1998**. Properties of Water and Steam: The industrial standard IAPWS-IF97 for the thermodynamic properties and supplementary equations for other properties: tables based on these equations. *Springer-Verlag*, Berlin, New York, ISBN: ISBN 3540643397.

Wang, M., Lawal, A., Stephenson, P., Sidders, J., Ramshaw, C., **2011**. Post-combustion CO_2 Capture with Chemical Absorption: A State-of-the-art Review. *Chemical Engineering Research and Design 89(9)*, pp. 1609-1624, doi: 10.1016/j.cherd.2010.11.005.

Wang, S., Wang, G., Jiang, F., Luo, M., Li, H., **2010**. Chemical looping combustion of coke oven gas by using Fe2O3/CuO with MgAl2O4 as oxygen carrier. *Energy & Environmental Science 3(9)*, p. 1353, doi: 10.1039/b926193a.

Wen, C.Y., Chen, L.H., **1982**. Fluidized bed freeboard phenomena: Entrainment and elutriation. *AIChE Journal 28(1)*, pp. 117-128, doi: 10.1002/aic.690280117.

Wen, C.Y., Yu, Y.H., **1966**. A generalized method for predicting the minimum fluidization velocity. *AIChE Journal 12(3)*, pp. 610-612, doi: 10.1002/aic.690120343.

Whiteside, D.T., ED., **1967-1976**. The Mathematical Papers Of Isaac Newton, Vol. I-VII: 1664-1695. *Cambridge University Press*, Cambridge

Woudstra, N., Woudstra, T., Pirone, A., Stelt, T.v.d., **2010**. Thermodynamic evaluation of combined cycle plants. *Energy Conversion and Management 51(5)*, pp. 1099-1110, doi: 10.1016/j.enconman.2009.12.016.

Wu, J., Shen, L., Hao, J., Gu, H., **2010**. Chemical looping combustion of coal in a 1 kW_{th} reactor. 1st International Conference on Chemical Looping, Lyon, France.

Yang, W.-C., **2007**. Modification and re-interpretation of Geldart's classification of powders. *Powder Technology 171(2)*, pp. 69-74, doi: 10.1016/j.powtec.2006.08.024.

Yates, J.G., **1996**. Effects of temperature and pressure on gas-solid fluidization. *Chemical Engineering Science 51(2)*, pp. 167-205, doi: 10.1016/0009-2509(95)00212-x.

Ypma, T.J., **1995**. Historical Development of the Newton–Raphson Method. *SIAM Review 37(4)*, pp. 531-551, doi: 10.1137/1037125.

Zhang, P., Lu, J.F., Yang, H.R., Zhang, J.S., Zhang, H., Yue, G.X., **2009**. Heat Transfer Coefficient Distribution in the Furnace of a 300MW_e CFB Boiler. in: Yue, G., Zhang, H., Zhao, C., Luo, Z. (Eds.), Proceedings of the 20th International Conference on Fluidized Bed Combustion. *Tsinghua University Press, Beijing*, pp. 167-171.

10 List of figures

11 List of tables

12 Appendix

12.1 Particle definition

NiO-VITO I

Composition			
Nickel-oxide	NiO	40	wt%
Nickel-aluminate	$NiAl_2O_4$	60	wt%
Production method			
Spray-dried, sintered at 1450°C for 4h and sieved			
Particle size			
Mean particle diameter	d_p	149	µm
Particle diameter 10%	$d_{p,0.1}$	108	µm
Particle diameter 90%	$d_{p,0.9}$	203	µm
Density			
Apparent density	ρ_p	3600	kg/m^3
Bulk density	ρ_b	1980	kg/m^3
Fluiddynamic properties			
Voidage at incipient fluidization	ε_{mf}	0.45	-
Sphericity	ϕ	0.9	-
Physical properties			
Crushing strength		2.3	N
BET surface area		0.7	m^2/g

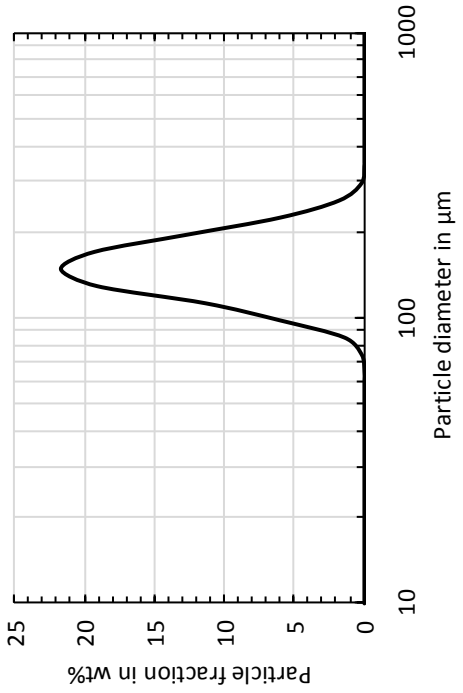

NiO-VITO II

Composition			
Nickel-oxide	NiO	41.3	wt%
Nickel-aluminate	$NiAl_2O_4$	41.4	wt%
	$MgAl_2O_4$	17.3	Wt%
Production method			
Spray-dried, sintered at 1400°C for 4h and sieved			
Particle size			
Mean particle diameter	d_p	129	µm
Particle diameter 10%	$d_{p,0.1}$	94	µm
Particle diameter 90%	$d_{p,0.9}$	176	µm
Density			
Apparent density	ρ_p	3250	kg/m^3
Bulk density	ρ_b	1700	kg/m^3
Fluiddynamic properties			
Voidage at incipient fluidization	ε_{mf}	0.45	-
Sphericity	ϕ	0.9	-
Physical properties			
Crushing strength		2.0	N
BET surface area		0.7	m^2/g

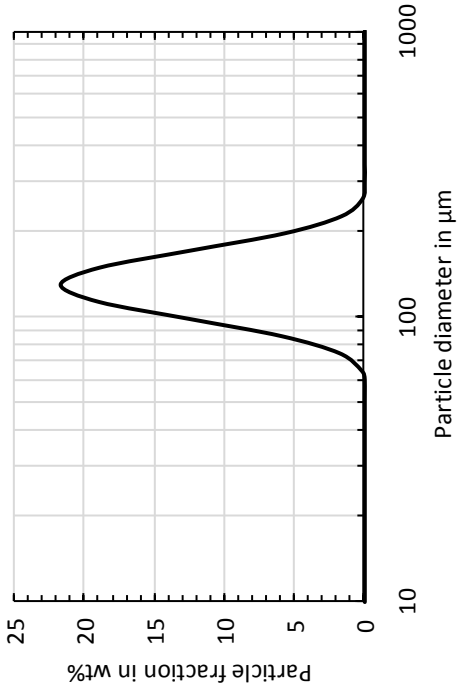

12.2 Summary of typical circulating fluidized bed riser heights

Reference	Capacity in MW_{th}	Riser height in m
(Höltl et al., 2009)	0.1	5
Confidential	0.1	12
(Kolbitsch, 2009)	0.14	4.1
(Cruz and Pugsley, 2008)	0.3	6.5
(Jia and Anthony, 2009)	0.8	6.6
DFB Biomass Gasification Plant Güssing	9	9.4
(Marx et al., 2012)	10	15
Confidential	10	22
CFB Chalmers University of Technology	12	13.5
CFB Biomass plant Fernwärme Wien	60	17
(Maryamchik and Wietzke, 2009)	275	30.2
(Mirek et al., 2009)	300	35
(Mirek et al., 2009)	300	38
(Lei et al., 2005)	300	34.7
(Stamatelopoulos and Darling, 2008)	335	32
(Robertson et al., 2009)	580	42
(Mirek et al., 2009)	600	54
(Robertson et al., 2009)	670	35
(Zhang et al., 2009)	670	40
(Cruz and Pugsley, 2008)	670	39
(Mirek et al., 2009)	670	50.9
(Sciazko et al., 2008)	670	44.8
(Stamatelopoulos and Darling, 2008)	775	36.65
(Robertson et al., 2009)	1700	49.98

12.3 Cyclone design reference

Taken from Hugi (1997)

Dimension diagram	Symbol	Value	Unit
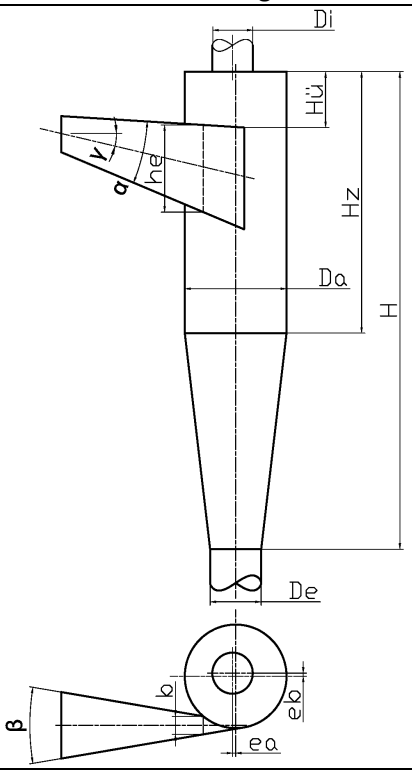	*Da*	630	mm
	Di	250	mm
	De	316	mm
	H	2905	mm
	Hz	1590	mm
	Hü	340	mm
	he	533	mm
	b	110	mm
	ea	0	mm
	eb	0	mm
	α	9.5	°
	β	9.5	°
	γ	13	°

12.4 Air reactor and fuel reactor cyclones

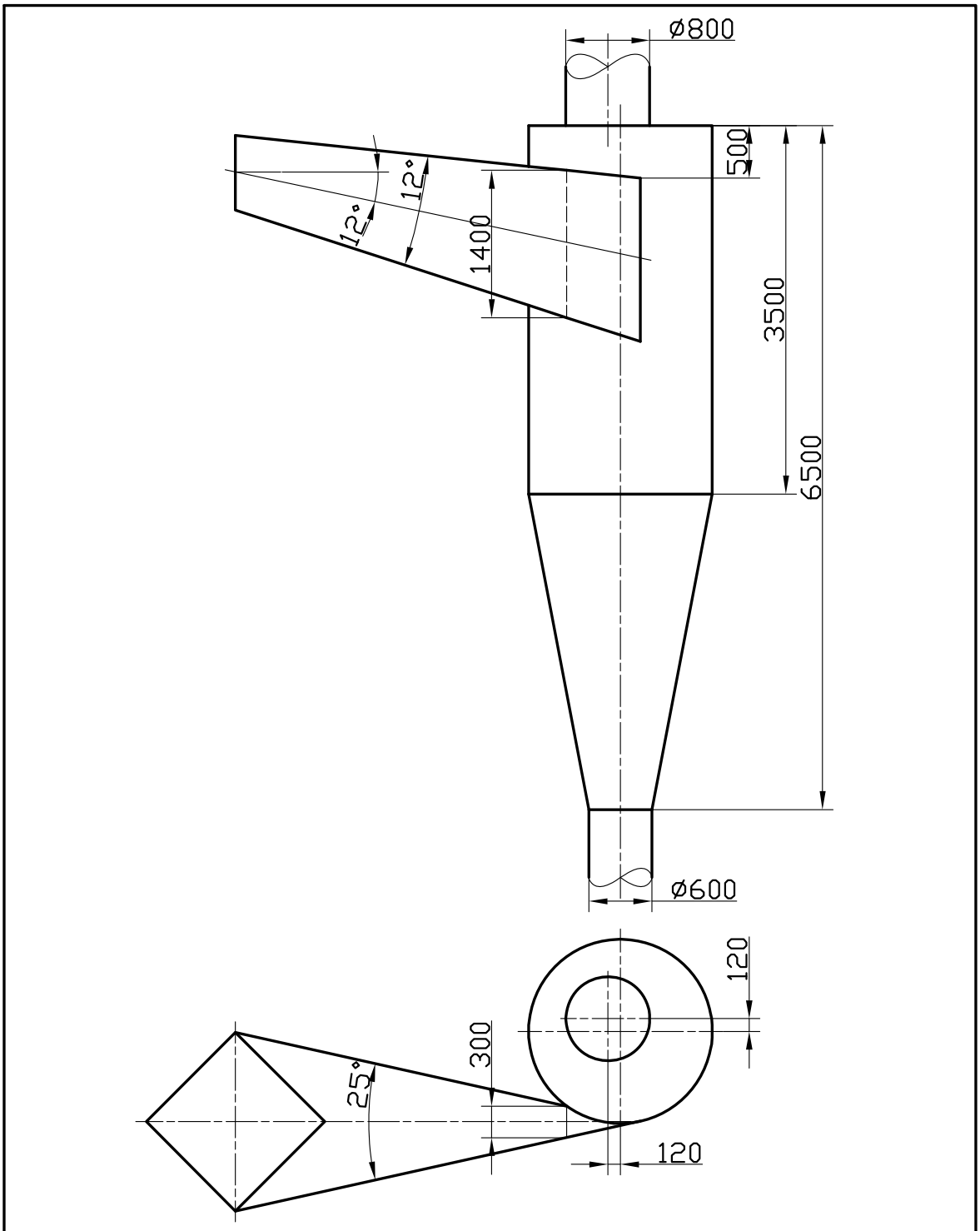

	Day	Name		
Draw.	22.08.2011		K. Marx	Vienna University of Technology Institute of Chemical Engineering Getreidemarkt 9/166 1060-Vienna
Proof				
NProof				
Scale 1:50	AR Cyclone			Drawing-Nr.:
Tolerance EN22768				Replacement:
				Filename: AR_Cyclone

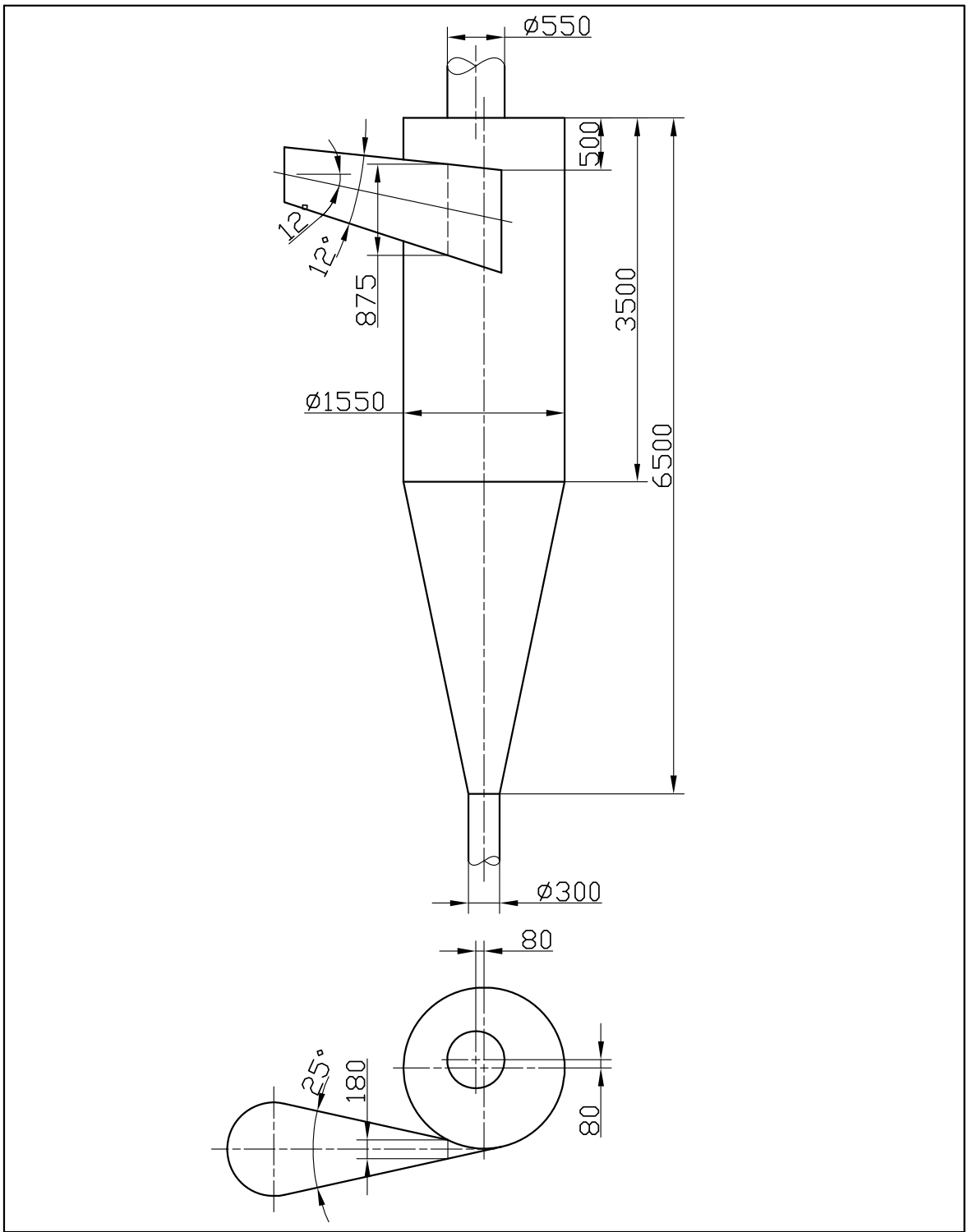

	Day	Name		
Draw.	22.08.2011		K. Marx	Vienna University of Technology Institute of Chemical Engineering Getreidemarkt 9/166 1060-Vienna
Proof				
NProof				
Scale 1:50	FR Cyclone			Drawing-Nr.:
Tolerance EN22768				Replacement:
				Filename: FR_Cyclone

12.5 3-dimensional reactor system setup

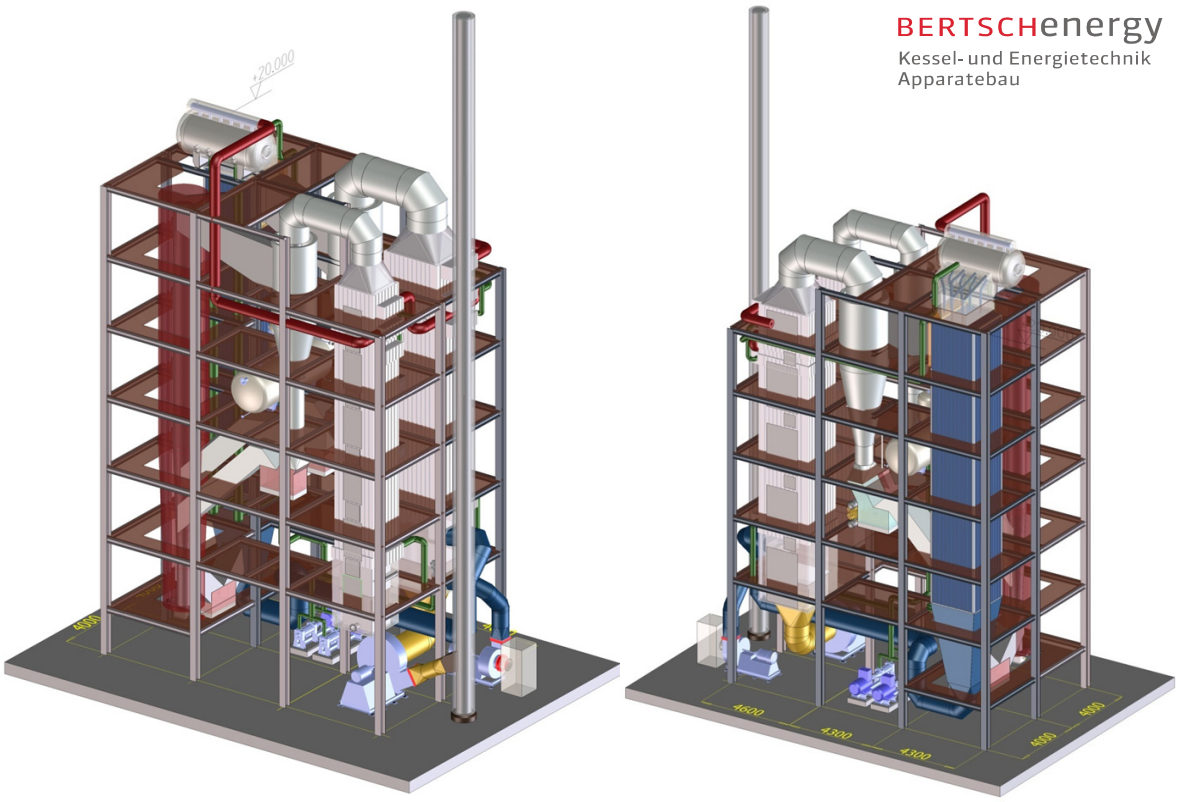

Source: Bertsch (2011).

12.6 Summary of air reactor cold flow model scaling parameters

Item	Unit	AR hot	Perfect match				Used	
			Full set		Simplified set			
U_s	m/s	7.67	3.45		2.43		3.23	
d_p	µm	200	40.5		34		50	
ρ_p	kg/m^3	3425	1.47E+04		1.47E+04		8900	
ρ_g	kg/m^3	0.28	1.19		1.19		1.19	
μ_g	Pa·s	4.6E-05	1.8E-05		1.8E-05		1.8E-05	
Dimensionless numbers			abs.	rel. ($^{hot}/_{cold}$)	abs.	rel. ($^{hot}/_{cold}$)	abs.	rel. ($^{hot}/_{cold}$)
Fr_p	-	3.0e+04	3.0E+04	1	1.7E+05	1.7	2.1E+04	1.44
Fr_D	-	5.0	5.0	1	5.0	1	8.9	0.56
ρ_p/ρ_g	-	1.24E+04	1.24E+04	1	1.24E+04	1	8.9E+03	1.64
Re_p	-	9.25	9.25	1	5.4	1.7	10.9	0.85
U_s/U_{mf}	-	350.5	350.5	1	350.5	1	350.5	1
D/d_p	-	6E+03	6E+03	1	3532	1.7	2.0E+03	2.9
Ψ	-	0.9	0.9	1	0.9	1	0.95	0.95
$Gs{\cdot}\rho_p^{-1}{\cdot}U_s^{-1}$	-	-	-	0.52	-	0.74	-	0.91
Scale	-	-	1:4.9		1:10		1:10	
Volumetric gas flow rate	m^3/h	39786	736		126		168	